U.S. DEPARTMENT OF THE INTERIOR
U.S. GEOLOGICAL SURVEY

Geology, Geophysics, Geochemistry, and Deep-Sea Mineral Deposits, Federated States of Micronesia: KORDI-USGS R.V. *Farnella* Cruise F11-90-CP

by

James R. Hein[1], Jung-Ho Ahn[2], Juliet C. Wong[1], Jung-Keuk Kang[2], Virginia K. Smith[1], Suk-Hoon Yoon[2], William M. d'Angelo[3], Sang-Ok Yoo[2], Ann E. Gibbs[1], Han-Joon Kim[2], Paula J. Quinterno[1], Moon-Young Jung[1], Alicé S. Davis[1], Byong-Kwon Park[2], Judy R. Gillison[3], Michael S. Marlow[1], Marjorie S. Schulz[1], David F. Siems[4], Joseph E. Taggart[4], Norma Rait[3], LedaBeth Gray[1], Mollie J. Malcolm[4], Marion G. Kavulak[3], Hsueh-Wen Yeh[5], Dennis M. Mann[1], Marlene Noble[1], George O. Riddle[4], Bruce H. Roushey[4], and Hezekiah Smith[3]

Open File Report 92-218

[1]U.S. Geological Survey, Menlo Park, CA
[2]Korea Ocean Research and Development Institute, Seoul
[3]U.S. Geological Survey, Reston, VA
[4]U.S. Geological Survey, Denver, CO
[5]University of Hawaii, Honolulu, HI

INTRODUCTION

From 15 October to 9 November 1990, the Korea Ocean Research and Development Institute (KORDI) and the U.S. Geological Survey (USGS) participated in a cooperative cruise (F11-90-CP) to the Federated States of Micronesia (FSM; Figs. 1-3). Eight scientists from KORDI, eleven from the USGS, and one observer from the FSM comprised the scientific staff (Table 1). The main objectives of the cruise were: 1. To determine the geological, oceanographic, and geochemical controls on the origin and evolution of Co-rich Fe-Mn oxyhydroxide crusts that occur on seamounts in the FSM Exclusive Economic Zone (EEZ), 2. Determine the origin of western Caroline Ridge and its potential for marine mineral deposits, 3. Complete a reconnaissance survey for hydrothermal Mn (and associated metals) and epithermal gold mineralization of the Yap arc, and 4. Study the effects of the collision of Caroline Ridge with the Yap arc.

Shipboard operations comprised 18 stations where 24 dredges and 11 CTD-oxygen profiles in the water column were taken (Table 2). In addition, 2577 km of 3.5 and 10 kHz bathymetry, single-channel 195 in^3 airgun, gravity, and magnetic surveys were completed (Table 3). This report presents all shipboard data and land-based laboratory data, including: 1. Maps with track lines, seismic-gravity-magnetic lines, stations, and bathymetry; 2. Location maps with geographic names; 3. Seismic, gravity, magnetic, and bathymetric profiles; 4. Temperature, oxygen, and salinity profiles of the water column; 5. Paleontological age dates of sediments and sedimentary rocks; 6. Descriptions of ferromanganese (Fe-Mn) and manganese (Mn) deposits and substrate rocks; 7. Mineralogy and major, minor, Pt-group, Au, and rare earth element chemistry of Fe-Mn and Mn deposits; 8. Statistical analyses of chemical compositions of Fe-Mn and Mn deposits; 9. Mineralogy and major element and Au compositions of substrate rocks; and 10. Discussions and comparisons with other data.

Dredges were collected from most of the physiographic and tectonic provinces that occur within the EEZ of the FSM. Three dredge hauls were recovered from two Cretaceous seamounts (Pali and Namonuito) and three dredges from two Tertiary seamounts (Sorol and Olapahd) located between Pohnpei Island and Yap arc (Figs. 1, 2; Table 2). Ten dredge hauls were recovered from Caroline Ridge and associated troughs located west of Chuuk Atoll (formerly called Truk Atoll). The age of this part of Caroline Ridge is probably Oligocene. One dredge haul was recovered from the north end of Eauripik Rise, where it abuts Caroline Ridge. Six dredge hauls were recovered from the Neogene Yap volcanic arc.

Pali, Olapahd, and Luhk seamounts were named by the FSM Government in Pohnpei. Names for other previously unnamed features discussed here were taken from nearby atolls or submarine features with well established names and are used informally.

GEOLOGICAL SETTING

FSM is divided into four states: Kosrae, Pohnpei, Chuuk, and Yap, from east to west. The main tectonic and physiographic features of the FSM EEZ include Caroline Ridge and associated narrow troughs, notably Sorol Trough; Yap trench-volcanic arc system; the southernmost end of the Mariana trench-arc system; southeastern edge of the Philippine Sea back-arc basin; isolated Cretaceous mid-plate seamounts; and the northernmost ends of Eauripik Rise and Mussau Trough (Figs. 1, 2). These tectonic ridges and troughs commonly display complex interactions, for example where Caroline Ridge collides with the Yap arc and where Eauripik Rise and Mussau Trough impinge on Caroline Ridge.

Caroline Ridge can be divided into three segments. The eastern third of the ridge extends from Kosrae Island to Chuuk Atoll and trends northwestward. This segment consists of isolated atolls and seamounts and has been shown to comprise a hot spot trace that was active between 12 and 1 Ma (Mattey, 1982; Keating et al., 1984). The central segment extends from Chuuk Atoll to

Ifalik Atoll-Tarang Bank and trends east-west. This segment consists of large carbonate(?) banks and atolls and is generally of less than 2500 m water depth. The western third of Caroline Ridge extends from Ifalik Atoll-Tarang Bank to the Yap trench and trends northwestward. This segment consists of a large shallow-water (<2500 m) ridge bounded by, and cut by, narrow troughs that represent strike-slip faults (southern margin; Hamilton, 1985), normal faults (northern margin; Andrews, 1971), and small spreading basins. Seismic profiles presented here show that both the north and south flanks of Caroline Ridge are block faulted. The origin of the western two-thirds of Caroline Ridge is unknown. West Caroline Ridge was proposed to be a relict island arc by Bracey and Andrews (1974). However, Hamilton (1985) disagreed with their interpretation and speculated that the ridge represents a leaky transform fault that connects the Mussau and Mariana trenches. Perfit and Fornari (1982) called on a combination of leaky transform fault and hot spot volcanism to form the ridge. Hegarty and Weissel (1988) suggested that the western part of Caroline Ridge, as well as Eauripik Rise, formed when a melting anomaly passed beneath the Pacific plate during the late Oligocene. Our work indicates that west Caroline Ridge, Sorol Trough, and associated topographic features may represent an extinct(?) spreading center-transform fault system. Vogt et al. (1976) suggested this possibility in passing, but provided no corroborative evidence. Eauripik Rise may also be an extinct spreading center, one of three in the Caroline Basin, which is located south of Caroline Ridge (Winterer et al., 1971; Erlandson et al., 1976; Mammerickx, 1978).

The Yap arc and trench represent an Oligocene(?) and Neogene convergent plate margin, but one that is distinct in many ways from other west and southwest Pacific arcs (Cole et al., 1960; Johnson et al., 1960; Hawkins and Batiza, 1977). For example, the distance between the arc summit and trench axis is very narrow and subduction may have ended in the late Miocene. Also, many of the rocks recovered from the arc (inner trench wall, summit, and summit islands) are metamorphic rocks of greenschist and amphibolite grade (Johnson et al., 1960; Shiraki, 1971). Many of the volcanic rocks have an oceanic crust compositional signature and thus may be obducted oceanic crust (Hawkins and Batiza, 1977; Working group, 1977). Other rocks belong to the calc-alkaline and island arc tholeiite series (Beccaluva et al., 1980; Crawford et al., 1986). Rocks dredged from the outer trench slope have a MORB-like composition and are about 7 m.y. old (Beccaluva et al., 1980). Hydrothermal mineralization of Quaternary sandstones collected by us from the central Yap arc indicate that the suggestions that subduction ended in the late Miocene and that back-arc basin crust was obducted onto the volcanic arc need to be modified, or at least must account for Quaternary hydrothermal activity at the summit of the arc (Hawkins and Batiza, 1977).

METHODS

The two main types of shipboard navigation used were GPS (the U.S. Navy's Global Positioning System) and an integrated navigation system to do direct ranging on Loran C stations (Gann, 1988). The Japanese Loran chain was used while in the FSM area. Seismic surveys included 3.5 and 10 kHz bathymetry and analog and digital single-channel seismics collected with a 195 in^3 airgun. The velocity of sound used to calculate sediment thicknesses was 1500 m/s. Sound velocity in sediment typically ranges from 1500-2200 m/s for the upper 1500 m of section. CTD-oxygen profiles and water samples were taken with a Neil Brown rosette. One to four water samples were taken per CTD cast and analyzed for oxygen content to calibrate the oxygen profiles. Standard Winkler titrations were performed to determine oxygen contents.

X ray diffraction analyses were conducted on a Phillips diffractometer, with Ni-filtered, Cu-kα radiation and a curved-crystal carbon monochromator. Abundances of major oxides in substrate rocks were determined by X ray fluorescence spectroscopy (Taggart et al., 1987), Fe(II) by colorimetric titration (Peck, 1964), CO_2 by coulometric titration (Engleman et al., 1985), H_2O^+ by water evolved at 950°C as determined coulometrically by Karl-Fischer titration (Jackson et al., 1987), and H_2O^- by sample weight difference at 110°C for greater than 1 hour (Shapiro, 1975).

The low totals for the phosphorite samples occur because fluorine and sulfur were not determined and therefore left out of the totals. High fluorine and sulfur contents are typical of marine carbonate fluorapatites (Cullen and Burnett, 1987; Burnett et al., 1987). For ferromanganese oxides, the concentrations of most major and minor elements were determined by inductively coupled plasma-atomic emission spectrometry, except those of K, Zn, and Pb, which were determined by flame atomic-absorption spectroscopy, and those of As, Cr, and Cd determined by graphite-furnace atomic absorption spectroscopy on air dried samples (Aruscavage et al., 1989). Concentrations of platinum-group elements for Fe-Mn deposits and substrate rocks and rare earth elements for Fe-Mn deposits were determined by inductively coupled plasma-mass spectrometry (Lichte et al., 1987a,b). Gold contents for Fe-Mn deposits and substrate rocks were determined by chemical separation and graphite-furnace atomic absorption spectroscopy (O'Leary and Meier, 1986).

For Q-mode factor analysis, each variable percentage was scaled to the percent of the maximum value before the values were row normalized and the cosine theta coefficients calculated. The factors were derived from orthogonal rotations of the principal component eigenvectors using the Varimax method (Klovan and Imbrie, 1971). All communalities are ≥0.97. The usual Pearson product moment correlation coefficient was used to calculate the correlation coefficient matrices.

BATHYMETRY AND GEOPHYSICS

Generally, two seismic lines were run at nearly right angles across each seamount and guyot studied in order to choose dredge sites. However, two lines are not enough to produce bathymetric maps. Our more detailed seismic and bathymetric survey, along with data from the National Geophysical Data Center, allowed us to construct a bathymetric map of west Caroline Ridge (Figs. 7-9; Appendices 1, 2). West Caroline Ridge is composed of northwest-southeast oriented ridges and troughs (Figs. 7-9; Appendix 2); it joins the western end of the northeast oriented central Caroline Ridge at nearly a right angle in the area of Ifalik Atoll, Gamen Reef, and Tarang Bank (Fig. 7; Appendix 2). West Caroline Ridge proper is about 130 km wide and 630 km long and has a summit platform supporting several islands: Ulithi Atoll, Fais Island, and Woleai Atoll; several basins and troughs also characterize the summit area, the largest being Fais Trough. The slope of the northern flank of the ridge is relatively gentle compared to the very steep south flank, which is also the north wall of Sorol Trough. Sorol Trough is about 80 km wide and narrows to the southeast. The trough is about 800 km long and is composed of a series of basins that range between 4000 and 5000 m water depth. South of Sorol Trough is Sorol Ridge and the north end of Eauripik Rise; the deep (>5000 m) Eauripik Trough separates the latter two ridges (Fig. 7; Appendix 2) and joins Sorol Trough to the West Caroline Basin (Figs. 1, 7). Eauripik Trough has an east-west orientation, unlike the northwest-southeast orientation of Sorol Trough, west Caroline Ridge, and Sorol Ridge. Sorol Atoll and Eauripik Atoll sit on the northern margins of Sorol Ridge and Eauripik Rise, respectively.

Airgun and 3.5 kHz Lines

In the following discussion, seismic reflection lines are grouped by geographic area. Each airgun line number is followed (in parentheses) by the direction of the line shown in the figures, e.g. (N-S) means the line is presented with north on the left and south on the right. The 3.5 kHz line orientations are reversed in several areas as listed in the figure captions.

Pali Seamount was crossed by lines 1-3. On LINE 1 (S-N; Figs. 4, 24, 25) the sediment thickness is variable and ranges from 400+ m adjacent to the base of the south flank to 200-300 m over the crest to 100 m on the north flank. The volcanic basement is exposed in places. Line 1 shows a 350 nT magnetic anomaly across the northern half of the line and a 77 mgal gravity anomaly centered over the seamount. LINE 2 (NW-SE; Figs. 4, 26, 27) crosses the northeastern flank of Pali Seamount and shows about 100 m of sediment on the flank that thickens to about 200 m at the base of the seamount. LINE 3 (W-E; Figs. 4, 28, 29) crosses the entire seamount and reveals about 300 m of abyssal sediment at the base of the seamount at each end of the line. The profile shows an asymmetrical 217 nT magnetic anomaly that increases to the west. The gravity anomaly of 129 mgal is symmetrically-centered over the seamount. The western flank of the seamount was dredged, recovering predominantly hyaloclastite and phosphorite (Dredge D1, Table 6). The north and west flanks may be underlain by slump deposits.

Namonuito Guyot was crossed by lines 4-6. LINE 4 (W-E; Figs. 5, 30, 31) shows 200 m of abyssal sediment beneath the eastern base of the guyot, 300 m beneath the western base, and about 100 m blanketing the top of the guyot. The nearly sediment-free eastern flank was dredged, recovering mudstone-siltstone, limestone, and phosphorite (Dredges D2, D3, Table 6). The guyot is characterized by a large negative magnetic anomaly of 814 nT centered over the western half of the guyot. The positive gravity anomaly is symmetrically centered over the feature. LINE 5 (SW-NE; Figs. 5, 32, 33) shows a basement knoll on the northwest flank of the guyot. The basement elsewhere on the line is veneered with less than 100 m of sediment. The central part of the line is characterized by a 787 nT magnetic anomaly. The gravity anomaly mimics the topography and rises to 107 mgals forming a 117 mgal anomaly at the northeastern end of the line. LINE 6 (S-N; Figs. 5, 34, 35) shows about 100 m of sediment on the summit and at the margins of the guyot. The south flank of another seamount was crossed at the north end of the line. A 637 nT magnetic anomaly is centered over the guyot. The gravity anomaly of 204 mgal is symmetrically centered over the structure.

Tarang Bank was crossed by 3.5 kHz line 7 and the northeast end of airgun line 8. The 3.5 kHz record (Figs. 6, 36) shows a steep slope and terraces at about 2250 m and 2630 m water depths. Dredges 4 and 5 on the lower flank recovered basalt capped by reef limestone.

Caroline Ridge and Sorol Trough were crossed by lines 8-14 and part of line 15. The southwest end of LINE 8 (SW-NE; Figs. 7, 18, 37A, 38A) crosses Eauripik Rise, covered by 600 m of sediment in low lying areas and thin sediment cover on topographic highs. Dredging of the northwest flank of the rise recovered mainly basalt and breccia (Dredge D19, Table 6). Line 8 continues to the northeast across Sorol Trough, which is characterized by a series of basement blocks and by a 58 mgal gravity low (Figs. 37B, 38B). To the northeast the profile crosses west Caroline Ridge, which is covered in places by up to 500 m of sediment, but is generally veneered with about 100 m of strata (Figs. 37C, 38C). The ridge is characterized by a negative magnetic anomaly of 118 nT. Northeast of the ridge are abyssal sediments more than 1000 m thick. The southern edge of the abyssal plain is notched by a channel that may be underlain by a fault zone (Figs. 37D, 38D). To the northeast, the profile crosses Tarang Bank, a basement ridge that was dredged along line 7. The bank is flanked by thick accumulations of sediment shown along line 8. The southern part of LINE 9 (SSW-NNE; Figs. 7, 18, 39A, 40A) crosses Eauripik Rise and Trough, which is filled with 300 m of sediment, and continues across Sorol Ridge and Trough. Flat-lying sediment to 200-300 m thick fills lows within Sorol Trough. The northern part of Sorol Trough is filled with about 600 m of sediment deposited during at least two distinct episodes as evidenced by discordant reflectors. Just north of Sorol Trough is Caroline Ridge, which is underlain by a few hundred meters of sediment and is characterized by a 194 nT magnetic high (Figs. 39B, 40B). The northern part of Caroline Ridge is underlain by a series of back-rotated and tilted blocks that are separated by high-angle normal faults that offset the sea floor. The morphology and subbottom structures suggest that this area is a zone of extension. Just north of the tilted blocks, the sea floor is underlain by 300 m of flat-lying sediment forming a broad mound. The southwestern end of LINE 10 (SW-NE; Figs. 7, 17, 41, 42) crosses part of Sorol Trough and the south flank of Caroline Ridge, where dredging recovered mainly metabasalt and limestone (Dredges D17 and D18, Table 6). The crest of Caroline Ridge is capped by nearly 600 m of sediment. The northern half of the ridge is down-faulted forming Fais Trough that is filled with discordant strata reflecting several periods of tectonism. The section is broken by high-angle normal faults in a fashion similar to those observed on line 9. The maximum sediment thickness is about 800 m in the area just south of the down-faulted Fais Trough, where the maximum sediment thickness reaches 500 m. The overall area is characterized by a 150 nT magnetic high. LINE 11 (SE-NW; Figs. 7, 17, 43, 44) traverses Sorol Trough and reveals between 200 and 300 m of sediment. The northern end of the line crosses a series of sediment-free hills that mark the base of the south flank of Caroline Ridge. LINE 12 (SSE-NNE; Figs. 7, 16, 17, 45, 46) crosses Caroline Ridge and Fais Trough. The crest of the ridge, at the southern end of the line, is capped by about 300 m of sediment. A small basement knoll crops out through the sediment layers and is characterized by a 340 nT negative magnetic anomaly. Near the center of the profile, the sea floor drops dramatically, forming Fais Trough, which is characterized by a series of fault-bounded and tilted blocks forming a graben. The faults are high angle normal faults that generally dip toward the central basin. Dredges D15 and D16, on the southern flank of Fais Trough, recovered basalt in the trough and basalt and siltstone that cap the ridge (Table 6). Caroline Ridge north of Fais Trough drops to the north in a series of stepped and faulted terraces blanketed by 100 to 300 m of sediment and characterized by a 190 nT magnetic high. The faults bounding the terraces are high-angled normal faults dipping to the north. LINE 13 (SW-NE; Figs. 7, 15, 47, 48) crosses a sediment-free trough located between Ulithi Atoll and Fais Island and then extends across Fais Island Ridge and Caroline Ridge. Dredge D14, from the southwest flank of Fais Island Ridge, recovered strongly recrystallized limestone. The ridges slope gently to the northeast and are capped by about 200 m of sediment, except where basement knolls are exposed. The line is characterized by a 220 nT magnetic high at its southern end and a 130 nT magnetic low near its northern end. Strata near the bedrock high (Day 297, 0800) appear to be disrupted by slumping. LINE 14 (SSE-NNW; Figs. 7, 15, 49, 50) is a longitudinal traverse through a trough between Ulithi Atoll and Fais Island Ridge. The trough is filled with more than 500 m of strata that are gently folded, possibly by sediment draping over bedrock highs, or from collision of Caroline Ridge with the Yap arc. LINE 15 (SE-NW; Figs. 7, 51, 52) continues in the trough on Caroline Ridge and crosses the north flank of Ulithi Atoll. The sedimentary section is about 200 m thick, but bedrock crops out in several places. Line 15 continues to the northwest across either thinly sediment draped or barren bedrock slopes that descend into the Yap trench.

Mariana-Yap arcs are crossed by part of airgun line 15, airgun line 16, and the summit area by airgun lines 17 and 18 and 3.5 kHz lines 19 and 20. On the continuation of LINE 15 (Figs. 7, 11, 51, 52), the northern, or arcward, side of the trench is characterized by hummocky topography devoid of sediment that may represent slump blocks. The arc summit was dredged, recovering mainly serpentinite (Dredge D7, Table 6). The crest of the arc is characterized by a 133 nT magnetic high. LINE 16 (SW-NE; Figs. 10, 11, 53, 54) begins in the southwest at the summit of north Yap arc and crosses the junction of the Yap and Mariana trenches to the summit of the southernmost Mariana arc. Both flanks of the trenches at the juncture are either devoid of sediment cover or thinly veneered. Small pockets of strata about 100 m thick are evident at the deepest southwestern and northeastern ends of the trench-trench juncture. At the northeastern end of the line, the southern Mariana arc is marked by a 250 nT magnetic anomaly. LINE 17 (SE-NW; Figs. 10, 55, 56) crosses the northeast flank of an unnamed seamount on the Mariana side of the Yap-Mariana arcs juncture crossed at the northeast end of line 16. The seamount is either devoid of sediment or has a thin cover. LINE 18 (N-S; Figs. 10, 57, 58) extends north-south across the same seamount as line 17 and also shows a surface barren of sediment except for a small pocket of less than 100 m near the southern end of the line. The flank of the seamount was dredged, recovering basalt (Dredge D6, Table 6). A 163 nT magnetic high occurs over the crest of the seamount. LINE 19 (W-E; 3.5 kHz only; Figs. 12, 59) crosses Hunter Bank showing two terraces on the upper east flank and little sediment cover. Dredge D8 on the middle west flank recovered basalt and breccia, whereas dredge D9 from the east summit recovered limestone. LINE 20 (NW-SE; 3.5 kHz only; Figs. 13, 60) crosses north Ngulu Ridge and shows two terraces on the upper west flank. Dredges D10 and D11 on the west flank recovered pebbly limestone, basalt, metamorphic and hydrothermal rocks, and serpentinite.

Sorol Guyot is crossed by lines 21-23. LINE 21 (W-E; Figs. 14, 61, 62) apparently crosses the crest of Sorol Guyot. Except for a bedrock knoll near the western end of the line, the guyot is uniformly blanketed with about 200 m of sediment. The bedrock knoll is characterized by a 212 nT magnetic low. The sedimentary strata at the eastern end of the line are broken by two high-angle reverse faults that appear to disrupt the sea floor. LINE 22 (SE-NW; Figs. 14, 63, 64) shows hummocky topography that is thinly veneered with sediment. A broad magnetic high of about 80 nT characterizes the central part of the line. Near the northern end of the line, a series of enigmatic subbottom reflectors dip to the northwest beneath the slope. LINE 23 (S-N; Figs. 14, 65, 66), unlike the previous two crossings of Sorol Guyot, shows a thick sedimentary cover on the south flank of the guyot. The maximum sediment thickness is about 400 m at the southern end of the line, which also shows evidence for the development of a channel and levee at the sea floor. The sediment layers are about 300 m thick on the north flank of the guyot. Bedrock crops out at the crest and north flank of the guyot. This flank was dredged at sites D12 and D13, where basalt was recovered (Table 6).

West Lanthe Bank was crossed by lines 24-26. LINE 24 (NW-SE; Figs. 19, 67, 68) shows that the bank is devoid of sediment except near the southern end of the line, where a veneer of sediment occurs. About 200 m of sediment flanks the edge of the bank. This region is also marked by a 250 nT magnetic high. LINE 25 (SE-NW; Figs. 19, 69, 70) shows strata as thick as 300-400 m at the south end. The lower sedimentary units dip to the south and discordantly underlie flat-lying upper beds. Sediment ponds containing about 200 m of sediment occur on the bank near the center and northern end of the line. The southern part of the bank on this line is characterized by a 342 nT magnetic high. LINE 26 (SW-NE; Figs. 19, 71, 72) imaged the most interesting structures beneath west Lanthe Bank. The central bank consists of a perched basin containing a thick sedimentary section, seen at the center of the profile. Stratigraphically lower beds in the basin dip to the south and are discordantly overlain by flat-lying upper units. The total thickness of both sections is about 500-600 m. The thinly veneered or bare bedrock flank and peak to the south are characterized by a 374 nT magnetic high. The northern flank of the basin is also thinly veneered or bare of sediment. The northern flank was dredged at sites D21 and D22, where basalt, limestone, and sandstone were recovered.

Condor Bank was crossed by 3.5 kHz line 27. LINE 27 (S-N; Figs. 20, 73) shows rugged topography with a double peak at the summit, which probably represent different positions of an outer reef margin. Rocks recovered in dredge D23 from the mid-south flank are solely limestone.

Chuuk B, an unnamed seamount on the Chase et al. (1988) map, was not found on 3.5 kHz lines 28-32. Either the seamount does not exist, or its location is significantly different from that indicated on the map. LINES 28-32 (Figs. 21, 74-78) show a number of small hills and levee and channel systems on the sediment-covered abyssal plain. A small 700 m high seamount is seen on lines 30-32, but is much smaller than the 2500+ m seamount indicated on the Chase et al. (1988) map.

The position of Luhk seamount as located on the Chase et al. (1988) map was crossed by 3.5 kHz line 33 (Figs. 22, 79), but the seamount was not found. Line 33 shows a sediment-covered abyssal plain that rises to the west, which may mark the lower east flank of Luhk Seamount.

Olapahd Seamount was crossed by 3.5 kHz line 34. LINE 34 (Figs. 23, 80) shows a rugged, sediment-draped summit with basement outcrops at the summit margins. Dredge 24 recovered limestone and minor basalt from the lower east flank.

WATER COLUMN STUDIES

Eleven CTD-oxygen profiles were taken over seamounts, banks, ridges, and troughs throughout the area of study (Figs. 81-91). The CTD stations were either over the summit or the upper flanks of the topographic features studied, in water depths between 2147 and 2930 m. Below 1500 m, the temperature, salinity, and oxygen values were fairly uniform over this large study region. However, the characteristics of the water column did vary with geographic location at shallower water depths. The water depth to the top of the oxygen-minimum zone varies from a low of 240 m over west Lanthe Bank, the southernmost station, to 400 m over the Mariana-Yap arcs junction, the northernmost station (Table 4). In fact, the water depth to the top of the oxygen-minimum zone has a weak positive correlation (coefficient = 0.599) with latitude of the 11 stations, that is it deepens to the north. From the 11 CTD stations, the regional mean water depth of the top of the oxygen-minimum zone is 289 m, 16 m shallower than it is in the Marshall Islands EEZ (Hein, Kang, et al., 1990).

The lowest minimum oxygen content measured in any of the profiles was over Olapahd Seamount, the station farthest to the east, and the highest minimum content was over the Mariana-Yap arcs juncture, the station farthest to the northeast. The three stations with the highest minimum oxygen contents occur along the Mariana-Yap arcs (Table 4). In fact, the degree of depletion in oxygen (lowest oxygen content at each station) has a weak positive (coefficient = 0.617) correlation with latitude and moderately strong negative (coefficient = -0.807) correlation with longitude. In other words, seawater is more depleted in oxygen to the east and south. This pattern is typical for this region of the equatorial Pacific. There is a core of generally low oxygen contents in water shallower than 250 m that extends from the South American coast westward across the Pacific, with the lowest oxygen values found to the east (Pickard and Emery, 1982). This pattern of oxygen content distribution is due to the equatorial zone of high biological productivity. The greater quantities of organic matter produced to the south and east are oxidized in the water column and, combined with zooplankton respiration, deplete the seawater in oxygen, thereby raising the top boundary of the oxygen-minimum zone.

In order to compare temperature profiles from the 11 stations, we looked at the water depth at each station corresponding to 10°C; the 10°C isotherm corresponds roughly to the boundary between the seasonal and permanent thermocline in the region and occurs at water depths near the top of the oxygen-minimum zone (Table 4). The deepest level of the 10°C isotherm is over Pali Seamount and the shallowest level is over west Lanthe Bank. However, this parameter does not correlate with latitude or longitude and overall varies little (61 m) throughout the area. In the Marshall Islands, the depth to this isothermal boundary varied by 110 m. The mean regional water depth of the 10°C isotherm for the EEZ of FSM is 288 m, compared to 247 m for the Marshall Islands EEZ.

Salinity profiles are similar throughout the region. Minimum values of about 33.9‰ occur at the sea surface (Figs. 81-91). Salinity increase rapidly to maximum values of about 34.9‰ at water depths that range from 100-140 m. The high salinity values are typical of equatorial waters that extend across the entire Pacific. These waters are among the most saline in the Pacific. The equatorial water is separate from, and does not mix with, the warmer less saline surface waters because of the strong density difference between them. Salinity then decreases rapidly to intermediate values of about 34.5‰ at water depths that range from 205-320 m. This low saline water represents the northward limit of the Antarctic Intermediate Water. Below 400 m, salinity then increases uniformly to the bottom of the profiles.

GEOLOGY, PETROLOGY, AND GEOCHEMISTRY

Rock and Sediment Ages

Unconsolidated sediment occurs throughout the area studied, but is thin in most areas. Sediment is most commonly white to brown foraminiferal-nannofossil ooze of Quaternary age, but may be as old as late Miocene in places (Table 5). Slightly calcareous or noncalcareous muds occur in several places, for example, Pliocene aged serpentine mud of mixed grey, blue, and green colors was recovered from the northern Yap arc (Table 5: D7-1); grey mud recovered from Hunter Bank on the central Yap arc is probably of similar composition and age. Green-brown volcaniclastic(?) mud was recovered from Sorol Trough.

Pali Seamount and Namonuito Guyot are probably part of the Cretaceous seamount province that occurs to the north and west of FSM. This is confirmed for Namonuito Guyot, where Cretaceous and late Paleocene or early Eocene limestones were recovered (Table 5: D3-5, 6, 7). Thus, even though Namonuito Guyot lies adjacent to the north flank of the Tertiary central Caroline Ridge, it is part of the older Pacific plate on which Caroline Ridge was superposed.

Central and western Caroline Ridge, including Tarang Bank, Sorol Guyot, Fais Island Ridge, and Fais Trough originated during the Oligocene, as indicated by middle to late Oligocene microfossils from siltstones and limestones recovered from those places (Table 5: D4, D13-D16). An Oligocene age assignment for western Caroline Ridge is consistent with the age of upper Oligocene chalk recovered at DSDP sites drilled during leg 6 (Fischer et al., 1971) on the north flank of Caroline Ridge. The basalt recovered from site 57, leg 6 is also of late Oligocene age, 23.5 m.y. old (based on the mean of two samples: 23.1 ± 0.95 and 23.9 ± 1.2; Ridley et al., 1974). Sedimentary rocks dredged on Condor Bank, south-central Caroline Ridge, are late Miocene in age and those from Sorol Trough are Miocene or Pliocene in age (Table 5).

The oldest sedimentary rocks of unquestionable age dredged from the Yap arc (Junction of Mariana-Yap arcs, north Yap arc, Hunter Bank, and north Ngulu Ridge) are middle Miocene, however, rocks may range in age from Eocene to Holocene (Table 5: D6-D11). For comparison, the oldest dated rocks from Yap Island are Miocene, based on microfossils, however, rocks may be as old as Oligocene, based on regional comparisons and geologic arguments (Cole et al., 1960; Johnson et al., 1960).

Rock Types, Petrography, Mineralogy, and Chemistry

Rock types in decreasing order of abundance are basalt-diabase-gabbro; limestone; metamorphic rocks including serpentinite, greenschist, metaigneous rocks, and amphibolite; mudstone-siltstone-sandstone; breccia; phosphorite; hyaloclastite and tuff (Tables 6, 7). Metamorphic rocks were recovered on the Yap arc and from Fais and Sorol troughs. Skarn deposits were recovered from north Ngulu Ridge and Fais Trough. To our knowledge, this is the first reported occurrence of deep-sea skarn deposits and the first reported occurrence of metamorphic rocks from Caroline Ridge.

Rocks recovered from Pali Seamount (D1) include yellow-green hyaloclastite, phosphorite, and minor altered basalt (Tables 6, 7). The hyaloclastite is in part phosphatized and the phosphorite and basalt occur as clasts in carbonate fluorapatite (CFA) cemented breccia. All the phosphorite is CFA and the hyaloclastite altered to phillipsite and smectite (Table 9). The CaO/P_2O_5 ratio for the phosphorite is 1.7 (Table 10), higher than the range expected (1.5-1.6) for theoretical chemical compositions of CFA (Manheim and Gulbrandsen, 1979). The ratio 1.7 falls within the range determined for phosphorites from the Marshall Islands (1.6-1.9; Hein, Kang, et al., 1990) and the Johnston Island area (1.6-1.7; Hein et al., 1990a). The excess Ca over P is apparently typical of seamount phosphorites and is probably due to Ca associated with plagioclase, phillipsite, and calcite.

Rocks recovered from Namonuito Guyot (D2, D3) include mudstone-siltstone, limestone, basalt, and minor pebbly sandstone and breccia (Tables 6, 7). The siltstones are volcaniclastic with grains of volcanic rock fragments, feldspar, magnetite, pyroxene, and sparse quartz and foraminifera in a tabular phillipsite and/or CFA cement. Phillipsite and CFA may also replace grains and fill voids and fractures. Smectite occurs in the matrix. Pebbly sandstone is a coarser-grained variety of the siltstone, but also contains recrystallized or micritized (by algal borings) reef bioclasts. The breccia has similar clasts to those in the siltstone and sandstone; clasts support a radial-fibrous rim cement followed by calcite cement filling the remaining pore space. The siltstone from D2 has the highest K_2O content (6.31%) and the siltstone from D3 the highest Fe_2O_3 content (15.2%) of any rocks analyzed from FSM (Table 10). The high potassium is reflected by the high K-feldspar content (Table 9) and may indicate potassium metasomatism in places on the guyot.

The Cretaceous limestone is composed of recrystallized foraminifera in calcite cement. The first stage in cementation was a rim cement and then the remaining pore space was filled. The calcite chamber fill and cement are texturally identical. Much of the limestone was partly to completely phosphatized (Tables 9, 10). The phosphorite has a CaO/P_2O_5 ratio of 1.8, and contains very little aluminosilicate detritus. In addition to foraminifera, sparse reef bioclasts and fish debris occur in a fine-grained phosphorite cement. Oolitic iron oxides also occur.

Volcanic rocks are limited to centimeter-sized rock fragments. Hyaloclastite (peperite) consists of angular, highly altered glass shards in a calcite cement. Other volcanic rock fragments include olivine phyric basalt that is extremely altered, with the olivine microphenocrysts replaced by clay minerals and iron oxides. One strongly alkalic fragment (probably a melilitite or nephelinite) consists of rare clinopyroxene phenocrysts and titanomagnetite microphenocrysts in a groundmass of melilite microlites, clinopyroxene, and olivine pseudomorphs, all set in a matrix of bright-yellow palagonite. Radial-fibrous zeolite and calcite veins cut some of the samples; zeolite formation always preceded calcite precipitation. Microprobe analyses of minerals and whole rock chemical analysis of the volcanic rocks are in progress (Table 8).

Rocks recovered from Tarang Bank (D4, D5) include basalt, bioclastic-volcaniclastic siltstone, and limestone. The siltstone is composed of grains of volcanic rock fragments, foraminifera, magnetite, plagioclase, pyroxene, and quartz in calcite and phillipsite cement, which also fill vesicles in basalt grains, chambers in foraminifera, voids, and fractures. Calcite formed before phillipsite. Many grains altered to smectite.

The limestone is a lagoonal, or outer reef, bioclastic limestone composed of aragonite and magnesian calcite (Tables 7, 9).

Tholeiitic basalt contains abundant large plagioclase and clinopyroxene phenocrysts (to 2 cm) in a groundmass of brown clinopyroxene subophitically enclosing plagioclase microlites. Clinopyroxene phenocrysts are colorless and only slightly less abundant than plagioclase. Some clay mineral alteration occurs in the groundmass and phillipsite fills some vesicles. A similar basalt sample has plagioclase, clinopyroxene, and fresh olivine phenocrysts in an unaltered sideromelane groundmass. Plagioclase separates will be dated by K-Ar techniques (Table 8).

Rocks recovered from an unnamed seamount at the junction between the Yap and Mariana arcs (D6) include basalt, tuff and mudstone, and limestone. Tuff is composed of glass shards in a smectite and iron oxide matrix with scattered plagioclase and foraminifera and sparse pyroxene. The foraminifera are replaced, possibly by smectite. Extensive borings in the yellowish-white limestone are lined with Fe-Mn oxyhydroxides.

Tholeiitic basalt is moderately vesicular, plagioclase and clinopyroxene phyric, with low abundances of small plagioclase and clinopyroxene glomerocrysts in a glassy or cryptocrystalline groundmass peppered with magnetite and partly altered to smectite. Other samples have similar sparse glomerocrysts in a seriate or subtrachytic groundmass of plagioclase microlites with anhedral clinopyroxene. Some samples have glass rinds of sideromelane that are substantially altered to smectite. Some vesicles are filled with massive zeolite with a relict radial-fibrous texture. One sample is highly vesicular with pinhole-sized round vesicles.

Rocks recovered from the northern Yap arc (D7) include serpentinite, serpentinite breccia, layered serpentinite-magnetite rocks, metaigneous rocks, vein quartz, and minor epidosite, basalt, and sandstone. Many of the rocks have been strongly sheared. Serpentinite is dominantly composed of lizardite forming a mesh texture, which derives from the replacement of olivine (Wicks et al., 1977). However, all samples have various amounts of bastite (probably also lizardite), which is a pseudomorph predominantly after pyroxene, but less commonly after amphibole (Wicks and Whittaker, 1977). Veins are dominantly serrate serpentine, but in places are also fibrous with curved or straight fibers oriented perpendicular to fracture walls or rarely are composed of blocky lizardite crystals. Magnetite is ubiquitous and forms along grain margins, as lenses, as isolated grains, as anastomosing networks, and also along cleavage planes or fractures in pseudomorphed pyroxene grains. In some samples, elongate magnetite grains show a preferred orientation and in other rocks form layers alternating with serpentinite layers. Very fine-grained garnet(?) occurs along hairline fractures in some pseudomorphed pyroxene grains. Chlorite veins also cut the serpentinites. Iron content is generally high (mean 6% Fe_2O_3) compared to other serpentines (Faust and Fahey, 1962), which reflects the high contents of magnetite. MgO and SiO_2 average 35.8% and 37.3%, respectively. Of the platinum-group elements (PGEs), Rh, Ru, and Ir are more concentrated in the serpentinites than they are in any of the other substrate rock type analyzed (Table 10); Pt contents are also relatively high.

Basalt, diabase, and microgabbro are aphyric, holocrystalline, and fine- to medium-grained, with subophitic texture of brown anhedral clinopyroxene partially enclosing plagioclase and a small amount of olivine (pseudomorphed by smectite and iron oxides). Most samples have been metamorphosed and contain amphibole, quartz, and chlorite. Rare large irregularly shaped vugs occur in some samples and may be partly filled with smectite; opaque minerals are abundant in all samples. Plagioclase is cloudy and partly altered; smectite is abundant in the groundmass. Some basalt samples are highly altered, plagioclase phyric, with variolitic texture and some have palagonite rinds. Altered tuff breccia is composed of palagonite lapilli, plagioclase, amphibole, and clinopyroxene. Some glass has been preserved, but most is altered to smectite. Quartz, smectite, and analcite fill vesicles in the glass shards. Metagabbro sample D7-6-1 has the highest Pt (7.6 ppb) and Pd (17 ppb) contents of the analyzed substrate rocks (Table 10). In contrast, Rh, Ru, and Ir contents are very low in this sample.

Epidosite has a cataclastic texture and is composed of large analcite grains, plagioclase, and quartz in an epidote matrix. Thick chlorite and thin quartz veins are common. Epidote replaced analcite and chlorite veins cut quartz veins. The paragenesis is quartz-analcite-epidote-quartz-chlorite.

Large fragments of quartz-plagioclase veins are translucent and milky with high sodium contents (Table 10), which indicates that the mineralizing fluid was probably seawater or a seawater-derived brine.

Rocks recovered from Hunter Bank (D8, D9) on the Yap arc include limestone, basalt, diabase, gabbro, breccia, and minor metagreywacke, mudstone-siltstone, and cataclastic quartz-serpentinite rock. Reef framework limestone is most common, with minor clastic limestone and *Halimeda* limestone of lagoonal facies. The limestone is composed of aragonite and calcite, indicating that it had probably not been subjected to meteoric diagenesis before the reef subsided. Rare pebbly limestone is composed of reef debris, basalt, and quartz clasts in calcite cement.

A wide variety of breccia occurs, but is most commonly composed of basalt clasts in a matrix of crushed clay- and silt-sized grains. Other clast types include altered volcanic glass, serpentinite, andesite, quartz, magnetite, and amphibole, which may occur in a matrix of serpentine, quartz, and chlorite that was clearly metamorphosed and hydrothermally altered along with the clasts. Quartz fills some vesicles, vugs, and fractures and, along with calcite, forms a cement.

Sandstone-siltstone-mudstone may be laminated, where laminae are defined by iron oxide content, grain size, and carbonate content. Coarser laminae are graded and contain more foraminifera. Metagreywacke and altered siltstone are composed mostly of grain-supported pyroxene and amphibole crystals, mosaic quartz, and volcanic rock fragments altered to smectite, chlorite, zeolite, and iron oxides in a smectite cement. Some chlorite occurs as cement and chlorite, calcite, quartz, smectite, and analcite fill vesicles. Rare recrystallized foraminifera(?) are present. These metamorphosed and hydrothermally altered volcaniclastic rocks are strongly deformed and sheared and are about 7-13 times enriched in gold (3-6 ppb, Table 10) over oceanic basalts ($\approx$0.45 ppb; Keays and Scott, 1976; Nesbitt et al., 1987).

Fine, medium, and coarse grained gabbro is composed predominantly of plagioclase, clinopyroxene, and minor olivine pseudomorphed by clay minerals and iron oxide. Biotite is a minor component in some and opaque minerals are an abundant accessory phase in all samples. Gabbro samples have secondary minerals characteristic of lower greenschist facies metamorphism, with chlorite and traces to moderate amounts of actinolite. Volcanic rocks consist of highly altered ankaramite basalt with large unaltered clinopyroxene phenocrysts and pseudomorphs of olivine in a groundmass of partly altered (not greenschist facies) plagioclase, clinopyroxene, and glass altered to smectite. Another volcanic rock type consists of highly vesicular, strongly altered basalt with clinopyroxene and olivine microphenocrysts in a glass groundmass, largely altered to smectite. In another sample (D8-14-1), calcite replaces grains and, along with chlorite and smectite, replaces the groundmass. Mordenite, heulandite, quartz, chlorite, and smectite fill vesicles and fractures. Vesicle fill parageneses include smectite-analcite, smectite-heulandite-mordenite, chlorite-quartz, and quartz-smectite-quartz.

Rocks recovered from north Ngulu Ridge (D10, D11) include breccia and sandstone; basalt, andesite; serpentinite, amphibolite, and metaigneous rocks; pebbly limestone; and skarn deposits. Pebbly limestone is composed of grains of altered and metamorphosed basalt and other igneous rock fragments, amphibole-quartz-mica schist, pyroxene-mica-plagioclase schist, mica-chlorite schist, serpentinite, amphibolite, hornblende, chlorite, magnetite, hematite, quartz, pyroxene, foraminifera, coral, calcareous algae, limestone, echinoid spines, and rare fish debris in calcite cement, or more rarely in nannofossil-foraminifera matrix. Moldic porosity is high.

Sandstone and breccia are composed of clasts or grains of volcanic rock fragments, mica, serpentine, pyroxene, smectite-replaced volcanic glass shards, chlorite schist, amphibole, fish debris, foraminifera overgrown by calcite, and limestone in a phillipsite cement. Calcite cement occurs locally. Some deposits are cemented by, and contain stratiform layers of, hydrothermal manganese oxyhydroxides, which will be discussed in the next section.

Serpentinite is much like that from dredge D7, with mesh texture being dominant, indicating replacement of olivine. The cell walls are composed of microfibrous serpentine in places, and in sample D11-11, the cell walls and interiors are laminated serpentine-magnetite. Bastite pseudomorphs of pyroxene occur in various amounts. Both fibrous and non-fibrous serpentine occur in veins. Magnetite is ubiquitous and abundant in some samples. Some samples (D11-8-1; D11-26) are highly fractured and the pyroxene clasts have only been partly replaced by serpentine, mostly along fractures. The MgO contents (mean 35.4%) are comparable to those of serpentinites in dredge D7, but the SiO_2 contents are greater (mean 39.4%) in dredge D11 samples. The Fe_2O_3 content is also greater (mean 8.2%) in D11 samples, which reflects the generally high magnetite contents and high goethite and magnetite in D11-26. Serpentinized greenschist consists of mesh textured serpentine grains, hornblende surrounded by chlorite, and tremolite-actinolite, all embedded in prehnite, and in places chlorite; the rock is laced with magnetite along all fractures. Thin quartz veins cut the rock.

Skarn deposits consist of vesuvianite, garnet (probably andradite), chlorite, and minor serpentine (Table 9), which formed in limestone. Vesuvianite forms columnar aggregates and, along with fibrous serpentine and feathery chlorite-serpentine grains, is embedded in a very fine-grained matrix of vesuvianite, garnet, and chlorite. The matrix has a relict radial-fibrous texture.

Fine, medium, and coarse grained gabbro with fractured olivine phenocrysts are mildly serpentinized and contain pyroxene replaced by tremolite; one sample contains biotite. Magnetite fills fractures and chlorite occurs interstitially. Andesite is quartz phyric, peppered with magnetite, and contains pyroxene and plagioclase in a groundmass altered to smectite. Amphibolite is banded and consists chiefly of green hornblende, sodic plagioclase, alkali feldspar, and pyroxene, with interstitial prehnite, chlorite, and serpentine. Some bands are nearly pure amphibole, others serpentine.

Rocks recovered from Sorol Guyot (D12, D13) include alkalic basalt and gabbro, with very minor limestone and breccia. Medium- to coarse-grained gabbro consists of purplish-brown clinopyroxene, plagioclase, and olivine pseudomorphs replaced by smectite and iron oxides. Smectite-hematite-calcite fill vugs in that order of occurrence. Volcanic rocks consist of vesicular, sparsely plagioclase-phyric basalt with plagioclase in seriate textured groundmass. One basalt sample is non-vesicular, aphyric, strongly altered, and sheared. Smectite fills vesicles.

Rocks recovered from Fais Island Ridge (D14) include chiefly limestone, with minor tuff, basalt, gabbro, and volcaniclastic sandstone, siltstone, and breccia. Limestone is composed of foraminifera, ostracods, pelecypods, and micritized (by boring algae) clasts of coral, calcareous algae, and echinoids, in a coarse- to fine-grained calcite cement. Some samples consist of single large recrystallized coral. Limestone fracture breccia contains many microfaults and fractures filled with mosaic quartz. Limestone fragments can be fit back together. Large fragments of coral and calcareous algae occur. Some clasts are recrystallized, while others are micritized. Intra- and inter-clast calcite cement is common. Some samples are dominantly foraminifera, others reef debris.

Tuff is composed of glass shards altered to smectite and zeolites, sparse to moderate amounts of plagioclase crystals, sparse pyroxene, moderate to sparse calcite and zeolite vesicle fill, hematite veins, and abundant anatase. Porosity is high.

Tholeiitic basalt is highly vesicular, moderately altered, with intersertal to subophitic texture; clinopyroxene partly encloses plagioclase that looks cloudy or mildly altered. Magnetite is abundant and smectite alteration of the groundmass is common. A sample of non-vesicular basalt contains similar minerals and has a similar intersertal to subophitic texture as the vesicular samples;

rarely, the vesicles are filled with smectite and calcite. Hydrothermally altered basalt contains coarse-grained quartz with undulatory extinction and quartz in the groundmass. Gabbro is composed of very coarse-grained plagioclase, coarse-grained magnetite, and pyroxene and is strongly altered to smectite and iron oxides.

Rocks recovered from Fais Trough (D15, D16) include basalt, volcaniclastic mudstone-siltstone-sandstone-breccia, and limestone with associated skarn deposits. Limestone varieties include burrowed micrite, pebbly limestone, and foraminiferal limestone. This latter type contains skarn deposits and grades from red limestone, the least altered, to grey limestone, and finally to yellow-green calcareous siltstone (skarn), which is the most altered and composed predominantly of andradite garnet. The garnets are close-packed, 5-25 μm in diameter (predominantly about 10 μm), and are concentrated in smectite-rich patches in calcite. The contact of the skarn with the underlying limestone is highly irregular, but relatively sharp. In the limestone adjacent to the skarn, the bioclasts (foraminifera, coral, gastropods, pelecypods) are recrystallized, tightly packed and squashed, and show a preferred orientation roughly parallel to the contact. Farther away from the contact (about 2 centimeters) with the skarn, the limestone has higher porosity, contains more smectite and altered volcanic glass, and has a preferred orientation of grains, but is less deformed and altered. Small pyroxene crystals are scattered through out the rock, which is cut by calcite veins. Oxygen and carbon isotope data for the green, grey, and red limestones are as follows:

Limestone/siltstone	$\delta^{13}C_{PDB}$ ‰	$\delta^{18}O_{smow}$ ‰
Green, with garnets	1.6	18.8
Grey	0.0	21.9
Red	0.5	24.4

The temperature of contact metamorphism was calculated assuming an initial limestone with 20% porosity, $\delta^{18}O$ of 0‰ for porewaters (seawater), and $\delta^{18}O$ of 31‰ for the biogenic limestone (Savin and Yeh, 1981). The contact metamorphism shifted the porewater $\delta^{18}O$ to about 18‰. The temperature of re-equilibration for the limestones ranged from about 300°C for the red limestone to about 500°C for the garnet-rich green calcareous skarn (fractionation factor from O'Neil et al., 1969). These temperatures indicate that a very steep thermal gradient existed, about 200°C over 3 or 4 cm interval. These temperatures of re-equilibration for the limestones are comparable with the lower end of the temperature range for the formation of andradite garnet. The lack of a change in the $\delta^{13}C$ values from those of biogenic carbonates (Savin and Yeh, 1981) indicates that contact metamorphism took place within a closed or semi-closed system, with little available organic carbon.

Volcaniclastic rocks were deposited by turbidites and reworked by bottom currents. Phillipsite and calcite form cements, volcanogenic grains are altered, mostly to smectite, and carbonate bioclasts are common.

Tholeiitic basalt is sparsely porphyritic and sparsely vesicular, with plagioclase and rare clinopyroxene glomerocrysts. Smectite replaces much of the groundmass, and some vugs, vesicles, and fractures are filled with smectite and minor calcite and zeolites; in places, calcite replaces smectite. Other basalt samples are fine-grained and holocrystalline, with rare plagioclase glomerocrysts and olivine pseudomorph microphenocrysts. Diabase or microgabbro consists mostly of plagioclase subophitically enclosed by brown clinopyroxene. Fresh olivine and plagioclase phyric basalt has a glass rind of sideromelane.

Rocks recovered from Sorol Trough (D17, D18) include metabasalt, other metaigneous rocks, greenschist, and very minor limestone. All the igneous rocks were metamorphosed to the greenschist facies, with characteristic chlorite, fibrous amphibole, and epidote (Table 9); minor prehnite and pumpellyite may also occur in some rocks. Original textures are weakly- to moderately-well preserved and many rocks are sheared. Relict textures indicate that some rocks were vesicular basalts with variolitic texture and others were fine- to medium-grained gabbros. Chlorite fills vesicles and in places formed long the margins of interlocking crystals. Chlorite also replaced the groundmass and some coarse-grained plagioclase. Penninite is the most common variety of chlorite. Epidote fills fractures, voids, replaced the groundmass, and rarely fills vesicles, where it may have replaced zeolites. Tremolite and actinolite replaced pyroxene and the groundmass, and in places replaced chlorite, as did hematite. Prehnite fills some vesicles lined with chlorite. Quartz fills some vesicles, replaced groundmass, and hosts abundant fibers of actinolite(?). Magnetite is common in all the rocks.

Rocks recovered from north Eauripik Rise (D19) include breccia and basalt. Breccia is composed of grey and brown basalt clasts in a phosphorite cement and altered hyaloclastite matrix. Breccia varies from clast supported to cement supported varieties.

Alkalic pillow basalt is highly vesicular (with pinhole-sized vesicles), with pristine olivine microphenocrysts and plagioclase microlites in a glass groundmass altered to smectite and iron oxides; some fresh glass rind with olivine crystals is still present. Some vesicles are filled with phillipsite.

Rocks recovered from west Lanthe Bank (D21, D22) include interbedded sandy limestone and calcareous volcaniclastic sandstone-breccia and basalt. The sandstone was deposited by turbidity currents on the limestone, but both rock types are commonly mixed. The sandstone consists of grains of altered volcanic rock fragments (vesicular glass and basalt are most common), pyroxene, plagioclase, recrystallized foraminifera, and recrystallized and micritized reef debris. The rock is grain supported with minor smectite and calcite cement. The limestone is composed of foraminifera, reef debris, and various amounts of the volcanogenic grains found in the sandstone. Breccia consists of basalt clasts in closely packed glass shards (hyaloclastite matrix), some of which are fresh and others replaced by phillipsite and smectite. Sparse grains of olivine, plagioclase, and pyroxene also occur. Smectite and calcite are cements.

Alkalic basalt is highly vesicular, with unaltered olivine and plagioclase phenocrysts in a glass groundmass replaced by smectite and iron oxides. Vesicles are rarely lined with phillipsite or smectite. In one sample (D22-5-1) plagioclase laths occur in brown pyroxene and the groundmass contains ilmenite needles.

Rocks recovered from Condor bank (D23) include limestone and minor pumice. The limestone consists of recrystallized foraminifera in a fine-grained calcite cement. Some laminae contain silt-size grains of altered volcanic rock fragments, pyroxene, and plagioclase. Other laminae contain abundant benthic foraminifera.

Rocks recovered from Olapahd Seamount (D24) include limestone and basalt. The limestone is composed of foraminifera and reef debris in a calcite cement.

Alkalic basalt is non-vesicular sparsely porphyritic hawaiite, with plagioclase and clinopyroxene phenocrysts in a trachytic groundmass of plagioclase microlites, tiny anhedral clinopyroxene, and rare olivine pseudomorphed by iddingsite. Titanomagnetite is abundant.

MANGANESE AND FERROMANGANESE DEPOSITS

Ferromanganese deposits include hydrogenetic oxyhydroxide crusts and hydrothermal oxide cement in sandstone. Manganese deposits consist of hydrothermal oxide and oxyhydroxide stratiform submetallic layers and lenses in sandstone. The hydrothermal deposits were recovered only from dredge D11 on north Ngulu Ridge.

Fe-Mn crusts have been studied in some detail during the past ten years, mostly from the central Pacific region (e.g., Halbach et al., 1982; Aplin and Cronan, 1985; Hein et al., 1985a, b; DeCarlo et al., 1987; Le Suave et al., 1989), but also from the Atlantic (Varentsov et al., 1991). Hydrogenetic crusts from the FSM vary in thickness from a patina to 75 mm, with the greatest average thickness being 50 mm (D1, Pali Seamount; see Table 6). This contrasts to the maximum thickness of crusts recovered from the adjacent Marshall Islands of 180 mm, the thickest Co-rich crust known (Hein, Kang, et al., 1990). However, only two Cretaceous seamounts have been sampled in FSM; others may yield thicker crusts. The thicker crusts recovered in the FSM are composed of two or more layers, six being the maximum and two being the most common. Layers are laminated, massive and dense, massive and microfractured, porous and Fe stained, and porous with empty vugs. Layers may contain columnar structures, inclusions of substrate grains, large fractures, or may be minutely fractured (Tables 6, 7). However, most crusts are thin, consisting of one massive or one porous layer. CFA veins, layers, and inclusions are not common in crusts from FSM, as they are from other areas, occurring only in dredge D1 samples from Pali Seamount.

The surface texture of crusts is predominantly botryoidal. Many botryoidal surfaces have been smoothed, polished, or fluted by bottom current activity. All gradations from high relief botryoids to uniformly smooth surfaces are found. Surfaces may be dense or granular and porous. Other surface textures include granular, which is the predominant texture on the sides and underside of substrate rocks; lizard skin, which consists of very fine-scale botryoids; irregular; and smooth.

Dredge D1 from Pali Seamount includes several hundred kilograms of Fe-Mn nodules. Nodules range from 20 to 130 mm in diameter and average 45 mm. Seventy-five percent of the nodules have a small nucleus or no discernable nucleus, 20% have a medium-sized rock nucleus, and 5% have a large rock nucleus. This contrasts with most seamount nodules, where the nuclei are most commonly large and represent Fe-Mn encrusted rock talus (Hein et al., 1985a, b). Nuclei are composed of hyaloclastite (about 75%), phosphorite (about 20%), and basalt (about 5%). Fractures and pores in the nodules are infilled with CFA.

Dredge D11 from north Ngulu Ridge recovered about 85 kg of pale grey to black hydrothermal Fe-Mn oxyhydroxide-cemented sandstone and breccia interbedded with 3 kg of stratiform grey, steel-grey, and brown-grey submetallic hydrothermal Mn oxide. Some Mn layers are disrupted. Fine-scale metallic botryoids line some voids. Mn layers are composed of alternating porous massive and very porous fibrous oxide laminae. In polished sections the stratiform oxide laminae occur as repeating couplets composed of an early formed porous massive lamina that becomes massive and dense at the base and finally grew downward into columns or bubble trains of oxides; abundant pore space occurs between the columns. The columns are composed of botryoidal Mn oxide with the growth direction downward (convex downward). These couplets are identical to those described by Hein et al. (1990b). Each couplet shows axially elongated growth from a point source and decreases in porosity and increases in crystallinity from bottom to top of each composite layer. Also the reflected-light colors grade from grey to brown to black from bottom to top of each column and from bottom to top of the immediately overlying massive dense layer. These couplets indicate formation from a supersaturated solution with decreasing saturation and rate of precipitation with time. Each stratiform layer represents several repetitions of the process. The couplets probably formed by the rhythmic pulsation of hydrothermal solutions, which is supported by the mineralogy and chemical compositions (see next sections; Hein et al., 1990b).

The Mn oxyhydroxide-cemented Quaternary sandstone and breccia consist of volcanic rock fragments, pyroxene, quartz, and serpentine grains in a massive cement; some layers contain predominantly foraminifera. Rocks may be either grain supported or cement supported; the latter may grade into massive silty stratiform layers. The cement is in part botryoidal, forming cauliflowerlike structures in foraminifera-rich beds that were cemented and replaced by Mn oxyhydroxides.

Growth Rates and Ages

Growth rates were determined by using the Co, Fe, and Mn contents of the hydrogenetic and hydrothermal deposits and the equation (growth rate in mm/m.y. = $6.8 \times 10^{-1}/(Co^n)^{1.67}$, where Co^n = normalized cobalt content = Co x 50/Fe + Mn) of Manheim and Lane-Bostwick (1988). Crust growth rates varied from 0.9 to 5.8 mm/m.y., comparable to those reported for hydrogenetic crusts from other areas (Hein et al., 1990a; Hein, Kang, et al., 1990). Growth rates generally decrease with increasing distance from the Mariana and Yap volcanic arcs, with the maximum rates calculated for Sorol Guyot crusts and the minimum rates for crusts from Pali Seamount. Presumably, the higher growth rates reflect input of hydrothermally produced metal hydroxides at the island arcs. Consequently, some of the crusts may have formed by a combination of hydrogenetic and low-temperature hydrothermal processes. Using the equation (R = 1.28/Co-0.24 for Co contents > 0.24%) of Puteanus and Halbach (1988) developed for Co-rich crusts, the growth rates range from 3.7 to >130 mm/m.y. Based on results from other areas, we suspect that the rates produced by the Puteanus and Halbach equation may be too fast and those produced by the Manheim and Lane-Bostwick equation may be too slow for mixed hydrogenetic-hydrothermal crusts, but the regional trends in growth rates should remain the same (Hein et al., 1990b). Growth rates can be determined directly by Sr isotope analysis (Futa et al., 1988; Ingram et al., 1990) or Be isotope analysis (Segl et al., 1984; Mangini et al., 1986).

Growth rates of stratiform deposits from Ngulu Ridge vary from about 30 to 560 mm/m.y. These growth rates may be too slow in that the Co contents of the deposits are anomalously high compared to stratiform Mn deposits from the Mariana arc (Hein et al., 1987b) and the Tonga-Lau region (Hein et al., 1990b).

The approximate ages of the crusts are determined from the calculated growth rates and the thicknesses of the crusts. Crusts are about 10 to 30 m.y. old from the Cretaceous Pali Seamount and Namonuito Guyot, and Eauripik Rise (unknown age); about 2 and 16 m.y. old from the Oligocene and younger Mariana-Yap arcs junction; about 3 and 6 m.y. old from west Lanthe Bank (minimum age of late Miocene) and the Oligocene and younger north Yap arc and north Ngulu Ridge; about 2-3 m.y. old from Tarang Bank; and less than 1 m.y. old on the Oligocene Sorol Guyot. These ages of initiation of crust growth are minimum ages because the technique does not take into account dissolution and erosional unconformities, which can add another several million years to the age of the crusts (Futa et al., 1988; Ingram et al., 1990). Even with moderate increases in the age of initiation of crust growth, crusts at all locations formed much later than the formation of the volcanic edifices that support them, especially those that occur on the Cretaceous seamounts.

The age of the stratiform Mn layers is Quaternary, as they occur in volcaniclastic rocks of that age. The duration of formation of each layer is estimated by dividing the thickness by the growth rate. This calculation indicates that stratiform layers took from 9,000 to 70,000 y to form. These durations of formation are longer than those calculated for stratiform Mn deposits from the Tonga-Lau region (Hein et al., 1990b) and for durations of individual hydrothermal events measured at oceanic spreading centers and determined from associated deposits (days to 1000 y; for example Rona et al., 1984; Kadko and Moore, 1988; Shimmield and Price, 1988; Lalou et al., 1990). Again, this is probably the result of anomalously high Co contents in the Yap arc deposits that decrease the calculated growth rates.

X ray Diffraction Mineralogy

Great care was taken in sampling crusts and stratiform Mn deposits for chemical and mineralogical analyses. All contamination from recent sediment was removed, which was especially critical in the porous crust layers. Also, special attention was paid to obtaining a clean separation of the lower crust layers from the substrate. Any minerals or elements determined to exist in the various deposits were incorporated into those layers during deposition or diagenesis and are not due to sampling procedures or post-depositional infiltration of sediment. Finally, all encrusting organisms and other debris were cleaned from the crust surfaces before sampling. Bulk always refers to the entire crust thickness whether composed of layers or not.

Bulk crusts and nodules and layers of crusts are composed of 92 to 100% δ-MnO_2 (vernadite), which has only two X ray reflections at about 2.42Å and 1.41Å (Table 11). On Pali Seamount the δ-MnO_2 is well crystallized in nodules relative to crusts formed nearby. X ray amorphous Fe oxyhydroxide epitaxially intergrown with δ-MnO_2 is also a dominant phase. The Fe phase crystallized to goethite in the older layers of sample D1-8 and, in the oldest layer, was replaced by CFA; goethite also occurs in crust D3-3-3, probably in the older layers (Table 11). The CFA also composes a small percentage of the Fe-Mn nodules, mostly as veins and layers in the inner (older) parts of large diameter nodules. Detrital and eolian minerals make up the remainder of the crusts, including quartz (to 3%), plagioclase (to 6%), and calcite (to 6%). In general, crusts from the Yap arc contain more clastic debris (mean 4.9%) than crusts from other areas (mean 1.2%). Most of the quartz and part of the plagioclase are eolian and the remainder of the plagioclase and the calcite are reworked from local outcrops and incorporated into the crusts during precipitation of the Fe-Mn oxyhydroxides. Some of the quartz in the Yap arc crusts may also derive from local outcrops. In the open-ocean setting, no local source for quartz exists. Calcite is rare in crusts and most commonly dissolves before accretion of more than a millimeter of crust (Hein, Kang, et al., 1990).

The hydrothermal stratabound deposits from north Ngulu Ridge are composed of pyrolusite, todorokite, birnessite, and probably δ-MnO_2. The presence of δ-MnO_2 is difficult to determine if it is not the dominant phase when mixed with todorokite and birnessite because its two X ray reflections also occur in the patterns of the other two. Consequently, the percentages are difficult to determine and Mn minerals are listed in order of relative abundance in Table 11. Todorokite also has X ray reflections at about 9.4Å, 4.8Å, and 3.3Å and birnessite at about 7.2Å and 3.5Å. Birnessite is always accompanied by todorokite and is more abundant than todorokite in only one sample, a cement in sandstone (Table 11). Pyrolusite solely composes some layers and is mixed with todorokite in other layers. This is the first study that we are aware of that has found pyrolusite in hydrothermal Mn deposits in the ocean basins. Previously, it was found in insular Mn deposits in the Tonga Islands, but not in the offshore deposits (Hein et al., 1990b). Pyrolusite formed at sites with a high oxidation potential either by precipitation directly from hydrothermal fluids, or by oxidation of primary todorokite. Consequently, pyrolusite probably formed very near the sea floor. Rancieite ($[Ca, Mn]Mn_4O_9.3H_2O$) may occur in one sample.

Major and Minor element Chemistry

Crusts

Chemical analyses for 24 bulk crusts, 11 crust layers, a composite of 2 large nodules, a composite of 8 small nodules, 7 stratiform layers, and 2 Fe-Mn oxide cemented sandstones are presented in Tables 12 and 13 and basic statistics for the various groups in Tables 14-16. Compositions from Table 12 were recalculated on a hygroscopic water-free (0% H_2O^-) basis (Table 13). The mean Fe and Mn contents of 24 bulk crusts are 16.9% and 16.4%, respectively, yielding a Mn/Fe ratio of 1.0 (Table 14). The Mn/Fe ratio is lower than the average ratio for the Marshall Islands (1.54) and for the entire central Pacific region (1.46); Fe and Mn are respectively higher than and lower than their regional means of 15.7% and 23.0% (based on analyses of 311 bulk crusts from central Pacific seamounts and ridges; Hein et al., 1987a, 1991). Most other metals are also below the central Pacific regional mean. Exceptions include elements that reflect eolian and clastic input, such as Al (Table 17). Phosphorus is significantly lower than its regional mean and much lower yet than the very high P contents in Marshall Islands crusts. The mean contents of the potential economically important metals Co (0.32%) and Ni (0.29%) are much below their regional means of 0.79% and 0.47%, respectively. Pt (167 ppb) is slightly below the regional mean (240 ppb) and only half of the Marshall Islands mean of 489 ppb.

Little variability exists in the composition of crusts of different thicknesses (Table 17). Cobalt, P, Cu, Mo, and Ni are somewhat more concentrated in thicker crusts and Fe in thinner crusts. This small variability is partly due to the limited range in thicknesses of crusts, but nevertheless contrasts with trends from other areas, where the metals, especially Co, are less concentrated as crust thicknesses increase (Hein, Kang, et al., 1990). Aluminum concentrations are low in thin crusts and very low for the outermost surface (0-0.5 mm) of the crusts (Table 17).

Nodules from Pali Seamount generally have lower Fe and Mn and higher P contents than do the crusts (Tables 12, 17). Phosphorous increases with increasing nodule diameter.

Little variability exists in the composition of crusts from different geographic areas. The Mn/Fe ratios vary from 0.8 to 1.2 and the highest Fe and Mn contents occur in crusts from Sorol Guyot and west Lanthe Bank; the lowest Fe and Mn contents occur in crusts from the north Yap and Mariana arcs (Table 17). Aluminum is highest in crusts from the Mariana-Yap arcs junction and lowest in Tarang Bank crusts. Cobalt, Ni, and Cu are generally lowest in Mariana and Yap arcs crusts. Chromium is very strongly enriched (380 ppm) in a crust from north Ngulu Ridge on the Yap arc. Based on Co+Ni+Cu x10, Fe, and Mn contents plotted on a Bonatti et al. (1972) ternary diagram, the crusts from FSM fall within the low trace metal half of the central Pacific crust field (Fig. 92). No bulk crust or crust layer composition falls outside the central Pacific bulk crust field.

It has been well established that Co and Ni contents in general decrease from outer crust layers to inner crust layers (Halbach et al., 1982; Hein et al., 1985b). This relationship is not noted here for two crusts (D6-5; D19-19), where the inner half is more enriched in Co and Ni than the outer half (Table 12). On the other hand, six layers analyzed from crust D1-8 (Table 12) show fluctuating Co and Ni contents in each successive layer, but overall, the inner half of the crust is depleted in Co and enriched in Ni relative to the outer half. Copper is also enriched in the inner half of the crust and P increases in the innermost two layers, which is typical of thick central Pacific Co-rich crusts. The highest Co content measured (0.63%) was for the outermost surface (0-0.5 mm) scraped from crust D1-9. Maximum Co contents typically occur in this surface layer of crusts (Hein, Kang, et al., 1990). Other metals also vary with depth in typical central Pacific crusts. Manganese commonly decreases and Fe and Pt increase toward the substrate. For crust D1-8, Fe contents are greatest for layers in the inner half (except for the innermost 5 mm), but Mn shows no trend with depth in the crust. Platinum, Rh, and Ir are also enriched in the inner half, whereas Ru and Pd occur in nearly constant concentrations throughout the crust.

Adsorbed water (H_2O^-) measured in the crusts varies with the humidity in the laboratory where the samples were analyzed. Unless all samples are analyzed in the same laboratory at the same time, H_2O^-, and consequently the abundances of the other elements, will vary accordingly. Therefore, compositions normalized to 0% H_2O^- can be more readily compared and may indicate the composition of ore if the crusts are eventually mined and can be easily separated form their substrates. The mean compositions of Fe, Mn, P, Co, Cu, Ni, and Pt for bulk crusts normalized for adsorbed water are 22.1%, 21.5%, 0.52%, 0.43%, 0.11%, 0.39%, and 223 ppb, respectively (Table 14). These concentrations are lower than their regional mean concentrations (including adsorbed water), except for Fe, which is much higher. Also Mo and Cr have higher concentrations than their regional means.

Hydrothermal Deposits

Submetallic stratiform layers show a strong fractionation between Fe and Mn, with a mean Mn/Fe ratio of 20.4 (Table 15); Mn contents are as high as 49% (Table 12). Trace metal contents are also very high, with, in decreasing abundance in ppm: Ni (4119), Ba (2843), Cu (2403), Zn (1477), Sr (780), V (487), Co (410), Cr (402), and Mo (297). Lead is relatively low (80 ppm). These high trace metal contents contrast with other marine hydrothermal manganese deposits, where commonly only one or two trace metals are enriched, such as Mo or Zn (Table 17; Hein, Kang, et al., 1990). Low trace metal contents have commonly been used as a criterion to distinguish hydrothermal from hydrogenetic and hydrogenous Mn deposits. The Yap arc deposits show that this criterion may not always be applicable. The types of rocks leached by the hydrothermal fluids, temperatures of the fluids, and the precipitation of proximal sulfides at depth determine the concentration and types of trace metals that accumulate in the distal hydrothermal Mn deposits. The trace metals indicate that the mineralizing fluids were relatively hot (high Co), that serpentinites and mafic igneous rocks (high Cr, Ni, Cu, Zn) and to a lesser extent intermediate to silicic igneous rocks (high Mo, V) were leached, and that little sulfide was precipitated at depth (high Cu and Zn). Compared with similar deposits from other volcanic arcs, Co, Cu, Ni, Cr, and

Pt are enriched from one to two orders of magnitude in the Yap arc deposits (Table 17); only Mo is relatively depleted. Iron, Mn, P, Al, and other elements fall within the range of other volcanic arc hydrothermal Mn deposits. On the Bonatti et al. (1972) diagram, the statiform deposits fall within the hydrothermal field at the Mn apex (Fig. 92). This contrasts with deposits from the Mariana and Tonga arcs, where the stratiform deposits plot predominantly in the hydrothermal field along the base of the triangle (Hein et al., 1987b, 1990b).

Iron and Mn are not strongly fractionated in the Fe-Mn cemented sandstones (Tables 12, 15), unlike similar deposits from the Mariana arc, where Mn is two to three times enriched over Fe (Table 17; Hein et al., 1987b). Silicon (18%), Mg (13%), Ni (1400 ppm), and Cr (8250 ppm) are strongly enriched in the Yap arc deposits. The high Ni and Cr indicate the presence of Ni- and Cr-rich grains in the sandstone and/or leaching of serpentinites and incorporation of these metals in the Fe-Mn cement. The high Si and Mg reflect the detrital component. Normalization of the composition of the sandstone for the detrital fraction yields a Fe-Mn oxide composition much different from that of the stratiform layers, indicating that different fluids or different stages in the evolution of a single hydrothermal fluid produced the stratiform layers and sandstone cement. Even though the bulk compositions of the Fe-Mn cemented sandstones plot within the crust field on the Bonatti et al. (1972) diagram, the cements are clearly of hydrothermal origin.

Platinum Group Elements (PGEs) and Gold

We report the concentrations of Pt, Pd, Rh, Ru, Ir, and Au for 10 bulk crusts, 8 crust layers, 2 submetallic stratiform layers, and 1 Fe-Mn cemented sandstone (Table 12). Gold is less than its limit of detection of 10 ppb in all samples analyzed (Table 12). This is the second report of Ru and Ir in Fe-Mn crusts (see Hein, Kang, et al., 1990 for the first report) and the first report of Ru and Ir in hydrothermal Mn and Fe-Mn deposits.

Crusts

PGEs in bulk crusts and crust layers from FSM show significant enrichments over lithospheric and seawater abundances, but not over solar system abundances (mean composition of C1 chondrites). Relative to the lithosphere (Parthé and Crocket, 1978), the mean composition of bulk crusts is enriched in Pt, Ru, Rh, and Ir by 84, 40, 30, and 10 times, respectively, whereas Pd and probably Au concentrations are depleted by 2 to about 4 times. The enrichments of PGEs in the crusts are about the same if the PGE data for substrate rocks from the Yap arc (Table 10) are used. Ruthenium, Ir, Pt, Pd and Au are enriched over surface seawater (Hodge et al., 1986; Goldberg, 1987) by about 8×10^6, 3×10^6, 2×10^6, 9×10^4, and 3×10^4 times, respectively (Fig. 93b). Most of these metals may increase in seawater with increasing water depth, so at about 1500 to 2000 m water depth, where many of the crusts formed, the enrichment factors may be less by as much as one-half (Hodge et al., 1986; Goldberg, 1987). However, Colodner et al. (1991) found no increase in Pt with increasing water depth and determined a mean Pt concentration in seawater of 260 fM (standard deviation of 70 fM). This seawater concentration would increase the enrichment of Pt in the crusts over seawater by an additional 9×10^5 times. The concentration of Rh in seawater has not been reported in the literature. However, based on the ratios of PGEs in Fe-Mn crusts and seawater, Hein, Kang, et al. (1990) suggested that 6 pg/l may closely approximate its seawater concentration. Ratios of PGEs determined here and those from Hein, Kang, et al. (1990) suggest that Rh concentrations in seawater may fall between about 2.5 and 12 pg/l in the 1500-3000 m water depth range. Ruthenium shows a positive anomaly and Pd and possibly Au large negative anomalies on a seawater normalized plot (Fig. 93b). This trend is closely comparable to that for crusts from the Marshall Islands (Hein, Kang, et al., 1990).

Mean concentrations of Pd, Au, Ir, Ru, Rh, and Pt in the solar system (equivalent to C1 chondrites; Anders and Ebihara, 1982) are enriched relative to bulk Fe-Mn crusts by 330, 139, 117, 45, 11, and 6 times, respectively (Fig. 93a). Palladium and possibly Au show negative anomalies on a plot normalized to solar system abundances (Fig. 93a). This trend is similar to that for crusts from the Marshall Islands, but the Marshall Islands crusts show a negative Ru anomaly.

The highest Pt, Rh, and Ir concentrations occur in the inner layers of crust D1-8 (Table 12). The inner half of crust D19-19 also shows strong enrichments in these metals relative to the outer half. Enrichment of these metals in the inner parts is common for central Pacific crusts. The highest Pd and Ru concentrations occur in crusts from the Yap and Mariana arcs as do elements indicative of clastic input.

Comparisons of the ratios of each PGE to Ir and Pt for crusts, seawater, the lithosphere, and the solar system indicate that Pt, Ir, and probably Rh are derived predominantly from seawater and that Pd, and to a lesser extent Ru, are derived from both seawater and clastic debris. The extraterrestrial component (meteorite debris) in the bulk crusts must be very small, certainly no more than about 15% of the PGEs could have been derived from an extraterrestrial source. However, meteorite debris may be concentrated locally in various horizons or layers in the crusts by formation of dissolution unconformities, or by proximity of the crust to meteorite fallout during formation of the layer. These localized extraterrestrial debris-rich horizons, however, do not significantly alter the overall hydrogenetic signature of the crusts. A similar result was found for PGEs in crusts from the Marshall Islands (Hein, Kang, et al., 1990).

Hydrothermal Deposits

All of the PGEs except Pd are more enriched in crusts than they are in hydrothermal stratabound deposits (Tables 12-15). Ruthenium and Pd are also more enriched in the Fe-Mn cemented sandstones than they are in the submetallic stratiform deposits. In addition, the seawater and solar system normalized patterns (Fig. 94b) are comparable to those of crusts except that the negative Pd anomaly is less pronounced for the hydrothermal deposits. These relationships support the idea derived from the crust data that Pt, Rh, and Ir are derived predominantly from seawater and that Pd, and to a lesser extent Ru, are derived from seawater and clastic debris. Also, the mineralizing fluid for the hydrothermal deposits must have been chiefly seawater. The PGE ratios indicate that Pt in hydrothermal deposits, as compared to crusts, is enriched relative to the other PGEs (except Pd) in decreasing order Ir, Rh, and Ru. This indicates that Pt in the hydrothermal deposits partly derives from hydrothermal processes, probably from leaching of ultramafic rocks.

Submetallic stratiform Mn deposits are enriched over seawater concentrations of Ru, Pt, Ir, Rh, and Pd by 2×10^6, 7×10^5, 6×10^5, 5×10^5, and 1.5×10^5 times, respectively. The PGEs are also enriched over their lithospheric abundances by 2 to 34 times, except for Pd which is slightly depleted.

Rare Earth Elements (REEs)

Twenty-one samples, 8 bulk crusts, 8 crust layers, 4 submetallic stratiform Mn layers, and 1 Fe-Mn cemented sandstone were analyzed for REEs (Table 18).

Crusts

For bulk crusts, ΣREEs ranges from 0.16% to 0.10%, with a mean of 0.13%. About the same range is found for crust layers (Table 18). For the six layers of crust D1-8, the individual REEs have their highest concentrations in the outermost layer, except for Ce, which is highest at the center. The second highest contents for La, Ho, Er, Tm, and Yb occur in the innermost layer; for the other REEs, the second through fourth outer layers have uniform concentrations for each respective element that are somewhat depleted relative to the outermost layer of highest concentrations. For the two layers of crust D19-19, the outer half has the highest concentration of all the REEs except Ce.

Chondrite-normalized REE patterns (Haskin et al., 1968) are shown in Figures 95-100. Different REEs are enriched in crusts from about 100 to 1100 times over chondrites and vary over a narrow range (Fig. 95). Most of the chondrite-normalized patterns for FSM crusts are typical of Fe-Mn oxyhydroxide crusts and nodules (Piper, 1974; Elderfield et al., 1981; Aplin, 1984; Hein et al., 1988, 1990a), with heavy REE (HREE) depletion, nearly flat HREE pattern, and small positive Gd anomaly (the occurrence of the Gd anomaly has been reported only for crusts; Hein et al., 1988). However, unlike typical crusts and nodules, crusts from FSM do not have a pronounced positive Ce anomaly, but rather either a small positive or small negative anomaly (Table 18; Figs. 95-100). Twenty-one percent of the crusts analyzed from the Marshall Islands located just to the northeast also have similar Ce anomaly patterns (Hein, Kang, et al., 1990). Crusts that formed farther to the east in the central Pacific all have positive Ce anomalies. These Ce anomaly variations are related to geographic position and the associated oxidation potential of the water mass in which the crusts formed. The chondrite-normalized patterns have an aspect in common with seawater (Gd anomaly), another opposite to seawater (HREE depletion), and another between these extremes (Ce anomaly). These variations in characteristics relative to the seawater pattern indicate that the REEs were scavenged by several different phases within the crusts, predominantly Fe and Mn oxyhydroxides, zeolites, barite, CFA, and others, and probably formed in seawater of different oxidation potential then crusts formed in the central Pacific.

Unlike the other REEs, soluble Ce^{+3} is oxidized to insoluble Ce^{+4} at the Fe-Mn surface and fixed in predominantly Fe and Mn phases, thus creating a large positive Ce anomaly on both shale- and chondrite-normalized plots (Goldberg et al., 1963; Piper, 1974). The Ce anomaly, Ce* (normalized 2Ce/La+Pr), ranges from 0.63 to 1.32 for all crust samples analyzed from the FSM and averages 0.81 for bulk crusts. Values greater than one indicate a positive anomaly and those less than one a negative anomaly.

Nearly all the crusts have a small positive Gd anomaly. This characteristic is similar to that obtained for crusts from the Marshall Islands (Hein et al., 1988; Hein, Kang, et al., 1990), but contrasts with the results for crusts from the Johnston Island EEZ in the central Pacific, where the Gd anomaly is rarely present (Hein et al., 1990a). A small negative Tb anomaly also occurs in patterns of some Marshall Islands crusts, but was not found here or in patterns of central Pacific crusts. DeBaar et al. (1985) attributed the Gd/Tb fractionation in seawater to anomalous properties associated with the shift from an exactly half-filled 4f electron shell.

The HREE depletion results from the formation of more stable complexes by the HREEs in seawater than by the light REEs (LREEs), and consequently the HREEs are more difficult to fix in the crusts than are the LREEs (Cantrell and Byrne, 1987).

Hydrothermal Deposits

Concentrations of REEs are consistently lower in hydrothermal deposits than they are in crusts, with ΣREEs ranging from 20 to 271 ppm (Table 18; Figs. 95, 99). The Fe-Mn cemented sandstone has the lowest ΣREEs. Cerium is not the dominant REE as it is with crusts, but rather La is predominant and Nd second in abundance.

The chondrite-normalized patterns are characterized by HREE depletion, small negative Eu anomalies, and large negative Ce anomalies (Fig. 99). The Fe-Mn cemented sandstone does not show the Eu anomaly, but shows several small anomalies in the HREEs that may result from analytical error. Hydrothermal Mn deposits from spreading centers commonly have large negative Ce anomalies (Toth, 1980), however those from volcanic arcs commonly have no Ce anomaly, or only a small negative anomaly (Morten et al., 1980; Hein et al., 1987b, 1990b). This Ce anomaly pattern may be due to mixing of the hydrothermal Mn oxide with small amounts of hydrogenetic Fe-Mn oxyhydroxides, to leaching of a variety of rock types that occur in volcanic arcs, and/or to fractionation of the REEs at depth in hydrothermal fluids of different oxidation states. If the magnitude of the negative Ce anomaly results from fluid mixing, then the Mn deposits from the Yap arc reflect hydrothermal components ranging from 95% to 100%; in contrast, similar deposits from the Mariana and Tonga arcs reflect hydrothermal components ranging from 85% to 90%, using the theoretical mixing curves of Fleet (1983). This supports the conclusion based on the mineralogy and chemical compositions mentioned earlier that the Yap arc deposits are relatively high-temperature proximal deposits compared to similar deposits sampled from other volcanic arcs. The small negative Eu anomalies may reflect the types of rocks leached by the hydrothermal fluids, such as ferromagnesian-rich rocks rather than felsic rocks.

Interelement Relationships: Correlation Coefficient Matrix

Correlation coefficient matrices were calculated from the compositions of 24 bulk crusts (Table 19), from 6 layers of crust D1-8 (Table 20), and from 7 hydrothermal stratiform layers (Table 21). In addition to 29 elements, all three matrices include H_2O^+, H_2O^-, CO_2, LOI and the matrix for bulk crusts also includes latitude, longitude, water depth, and crust thickness.

Crusts

For the 24 bulk crusts, statistically significant strong to moderate positive correlations are found among the following selected elements, listed in order of decreasing significance for each element (Table 19): **Mn:** Ni, Cd, Mo, As, Sr, Co; **Fe:** V, Zn; **Si:** Al, K; **Ca:** P, Y; **Co:** Ni, Mn, Pb; **Ni:** Mn, Mo, Co, Cd; **Cu:** Ba, Zn, V; **V:** Zn, Ba, Fe, Cu; **Cr:** Mg; **Sr:** Mo, Mn, As; **Pt:** Rh, Ir, Ru; **Pd:** none; **Ru:** CO_2, Pt, Rh, Ir; **latitude:** weak correlation with Al. Latitude also shows a moderate negative correlation with water depth and weak negative correlations with Mn, Cd, Co, and Ce. The correlations with latitude indicate an increase in clastic debris in the crusts formed at more northerly latitudes, in the direction of the Mariana volcanic arc, and an increase in Mn and manganophile elements to the south. **Longitude:** Ba, weak with Zn, P, V, Mo, Ti, Pb, Sr. Longitude shows weak negative correlations with Mg, Si, Al, K, Na, supporting evidence presented earlier for an increase in clastic debris in crusts to the west, towards the Yap volcanic arc. Correlations with longitude also indicate increasing contributions from biogenic debris in crusts with increasing longitude, eastwardly. Manganese in crusts generally increases and Si and Al decrease with increasing **water depth**. Platinum, Rh, and Ir show very weak positive correlations with **crust thickness**.

All of the elements are associated with one or more mineral phase(s) in the crusts. We interpret the correlations in Table 19 to indicate the following phases and their associated elements: **δ-MnO_2:** Mn, Ni, Co, Cd, Mo, Pb, As, Sr, Ce, Ti(?); **Fe oxyhydroxide:** Fe, Cu(?); **aluminosilicate:** Si, Al, K, Na, Mg, Ru, Pd; **CFA:** Ca, P, Y, CO_2, Sr; **residual biogenic:** Ba, Zn, V, Cu, Fe, Ce, Sr, Ti(?); **Cr-spinel** (or other Cr-rich phase): Cr, Mg. Elements of the δ-MnO_2 and residual biogenic phases vary inversely with the aluminosilicate and Cr-spinel phases. In general, these interelement associations are similar to those determined for crusts from other areas of the central Pacific, although regional differences do occur (Hein et al., 1990a, 1991; Hein, Kang, et al., 1990).

Other than Ce and Ce*, the **REEs** are not correlated with any of the other elements, indicating that the REEs in bulk crusts must be distributed among most of the constituent phases. The ΣREEs is negatively correlated with Al and Si. Cerium and Ce* have positive correlations with elements characteristic of the δ-MnO_2, residual biogenic, and Fe oxyhydroxide phases. The individual REEs and ΣREEs show strong positive correlations among themselves, except Ce, which has only a strong positive correlation with ΣREEs and moderate correlation with La. The statistical significance of the correlations among the REEs is generally relatively high for correlations with Dy and generally low for correlations with La and Tm, although most correlations are strong. For other individual REEs, generally the strongest correlations are with the adjacent REEs in the periodic table, then the significance decreases through the remaining REEs of higher and lower atomic numbers. Lanthanum, Ce, Eu, Ho, Tm, Yb, and ΣREEs have very weak negative correlations with latitude, that is REEs increase toward the equator, and a very weak positive correlation with water depth. As water depth and latitude are negatively correlated, it is uncertain which of these control the REE distributions, although both water depth and latitude have been shown to control the distribution of REEs in the central Pacific (Aplin, 1984; Hein, Kang, et al., 1990; DeCarlo and McMurtry, in press).

PGEs are apparently distributed among most of the different crust phases because they are not strongly correlated with any elements outside the Pt group per se. A strong association exists among Pt-Rh-Ir and to a lesser extent Ru. This group may show a slight preference to the CFA phase and Pt also for the aluminosilicate phase. Palladium may show a slight preference to the Cr-spinel phase.

The six **layers** from crust D1-8 show interelement correlations somewhat different from those of bulk crusts (Tables 19, 20). The differences are chiefly concerned with fewer correlations for each element in the coefficient matrix of crust layer compositions. Fewer correlations in this matrix partly result from the requirement of larger coefficients for the correlations to be statistically significant at the 95% confidence level. However, some notable differences do occur: 1) Ti and Cr accompany Si, Al, K, and Na in the aluminosilicate phase; a separate Cr-rich phase is not evident. 2) The CFA phase includes Ce, Cd, and Pd. 3) The Fe oxyhydroxide phase includes As and probably Ru. 4) The residual biogenic phase also includes Rh, Ir, Mg, and probably Pt. These relationships are typical of hydrogenetic crusts from central Pacific Cretaceous seamounts, and thus consistent with the location of dredge D1 on the Cretaceous Pali Seamount. The aluminosilicate phase is typical of that derived from these seamounts, whereas the aluminosilicate phase defined by the 24 bulk crusts is a combination of mid-plate island and volcanic arc suites. In addition, crust D1-8 has a well-defined CFA mineralogy, unlike crusts from many of the locations sampled.

The REEs in the six crust layers show many more correlations than they do in the matrix for the 24 bulk crusts. For example, negative correlations exist among Fe: Er, Tm, Yb; Cu: Pr, Nd, Sm, Eu, Gd, Tb, Dy, ΣREEs; Zn: Dy, Ho, Er, Tm, Yb; and Ba: Tb, Dy. These correlations indicate that the REEs vary inversely with the residual biogenic phase, and perhaps also with the Fe oxyhydroxide phase. Ce is positively correlated with Co and Pb, elements characteristic of the δ-MnO_2 phase. Among the REEs, La, Gd, Tb, and Dy have positive correlations with all the other REEs, whereas, Pr, Nd, Sm, and Eu correlate generally only with other LREEs and Ho, Er, Tm, and Yb only with other HREEs.

Hydrothermal Deposits

Interelement associations are much different for stratiform hydrothermal deposits compared to bulk crusts. Statistically significant strong to moderate positive correlations are found among the following selected elements, listed in order of decreasing significance for each element (Table 21): **Fe:** Ti, Ce, P, Pb, Y, Co; **Co:** P, Ce, Ti, Pb, Y, Fe, As; **Ni:** Na, K, Cu, Zn, Cd; **Cu:** Ni, K, Cd; **Ba:** V; **Pb:** P, Ce, As, Fe, Ti, Co; **Al:** Y; **K:** Cd, Na, Ni, Zn, Mg, Cu; **Ca:** Y; **P:** Ce, Fe, Pb, Ti, Y, Co, As; **Ti:** Fe, P, Ce, Y, Pb, Co, As. Manganese, Mo, Sr, and Si do not show significant positive correlations with other elements. Many other weak correlations and negative correlations exist among the elements.

All of the elements are associated with one or more mineral or X ray amorphous phases within the stratiform Mn deposits. We interpret the correlations in Table 21 to indicate the following associations and their accompanying elements: 1) Hydrothermal Mn oxide-hydroxide association: Mn; 2) hydrothermal Fe oxide-hydroxide association: Fe, Ti, Ce, P, Pb, Y, As, Co; 3) hydrothermally leached elements that do not covary with either Mn or Fe: Zn, Cd, Ni, Cu, Mo, K, Na; this group of elements are probably associated, at least in part, with Mn oxide phase (see next section on Q-mode factor analysis); 4) aluminosilicate phase: Si, Al, Mg, Ti, Ca, Y; 5) Cr-spinel or other Cr-rich phase derived from leaching of serpentinite: Cr, Mg; and 6). hydrothermally leached biogenic component of sediment: Ba, Sr, V, CO_2. These element associations can be compared with the dominant mean oxide composition of 64.4% MnO_2 and 2.9% Fe_2O_3; aluminosilicate-related oxides make up about 17% and water makes up 13.6% of the deposits (Table 15). None of the elements increase with increasing Mn, but many of them show a moderate to weak negative correlation with Mn, especially those elements associated with the Fe and aluminosilicate phases.

The HREEs, ΣREEs, and Ce* have strong positive correlations and the LREEs weak positive correlations with Fe. The REEs also have positive correlations with elements associated with the hydrothermal Fe oxide phase (number 2 above), including Ti, P, Co, Pb, and As. This indicates that the REEs are also associated primarily with the Fe phase. The REEs also have positive correlations among themselves, with several general patterns evident in the distribution of the level of statistical significance. Cerium has very low (the lowest among the REEs) or no statistical correlation with the other REEs. The statistical significance of the correlations for La and Pr decrease going to REEs of higher atomic numbers, then remain constant at relatively low values for the heaviest REEs; Yb has the opposite pattern. Gadolinium correlations decrease in significance in a V-shaped pattern going to REEs of lower and higher atomic numbers. Neodymium, Sm, Eu, Tb, and Dy correlations all decrease in significance going to REEs of lower and higher atomic numbers, but the correlations going to higher atomic numbers become constant at relatively moderate to low values for correlations with the heaviest REEs; Ho, Er, and Tm show the opposite pattern. These are very similar to the inter-REE correlation patterns found for crusts.

Grouping of Elements: Q-Mode Factor Analysis

Q-mode factor analysis was completed for the 24 bulk crusts, 6 layers of crust D1-8, and 7 hydrothermal stratiform layers (Figs. 101-105).

Crusts

The elements grouped by Q-mode factor analysis for bulk crusts can be assigned to five of the six groups interpreted from the correlation coefficient matrix. Q-mode does not distinguish an Fe oxyhydroxide factor. The five factors are interpreted to be the following (elements added or omitted compared to those grouped by interpretation of the correlation coefficient matrix are in parentheses): **δ-MnO_2**: Co, Ni, Cd, Mo, Mn, As, Pb (Fig. 101) (Sr and Ti omitted); **aluminosilicate**: Al, Si, K, Na, Mg (Fig. 101) (Ru and Pd were not included in the Q-mode analysis); **residual biogenic**: Cu, Ba, Zn, V, Ce, Ti, Fe, Pb (Fig. 101) (Pb added, Sr omitted); **CFA**: CO_2, Ca, P, Y (Fig. 102) (Sr omitted); **Cr-spinel**: Cr, Mg, As (Fig. 102) (As added). Overall, the two different analyses produce closely comparable results. Nearly 68% of the variance in the data set is accounted for by the δ-MnO_2 and aluminosilicate factors (Figs. 101, 102).

Four factors were determined for the six layers of crust D1-8, which account for 99.7% of the data set (Fig. 103). These factors are interpreted to represent the following crust phases: **δ-MnO_2**: Co, Pb, Mn, Mo, Ni, As, which differs from bulk crusts from FSM only by the omission of Cd; **aluminosilicate**: Cr, Al, Ti, Si, K, Na, which includes Cr in this detrital phase rather than producing a separate Cr-spinel detrital phase as for bulk crusts; this factor also differs from bulk crusts by including Ti; **residual biogenic**: Cu, As, Ba, Zn, Fe, Mo, V, which differs from bulk crusts by omission of Ti and Ce and addition of As and Mo; **CFA**: P, Ca, CO_2, Y, Ce, Ni, Cd, Mn, Sr, Cu, which differs from the bulk crusts from FSM by addition of the last five elements and from bulk crusts from the central Pacific by addition of Ni, Cd, and Mn, typically manganophile elements. Why these elements are grouped with those typical of the CFA phase is uncertain, but may be related to preferential replacement of the Fe oxyhydroxide phase by CFA in the inner layers of the crust.

Hydrothermal Deposits

The elements grouped by Q-mode factor analysis for submetallic stratiform Mn oxide layers can be assigned to five of the six groups interpreted from the correlation coefficient matrix (Figs. 104, 105). The only difference in the groupings is that the Mn oxide phase and hydrothermally leached elements that do not covary with either Mn or Fe are grouped together by Q-mode analysis and are interpreted to represent the Mn oxide phase. In contrast to crusts, most elements occur in more than one factor and Mg and Al occur in three of the five Q-mode factors (Figs. 104, 105). The five factors are interpreted to represent: **hydrothermal Mn oxide**: Zn, Cd, Na, K, Ni, Mo, Mg, Cu, Mn, Ca (Fig. 104), which adds Mg and Ca to the two phases interpreted from correlation coefficients; **hydrothermal Fe oxide**: Ce, Pb, Fe, Ti, P, Co, CO_2, Y, As, Al, Cu (Fig. 104), which includes Al and Cu in contrast to the group interpreted from the correlation matrix; **hydrothermally leached biogenic debris**: Si, Sr, CO_2, Mn, Ca, Ba, V (Fig. 104), which adds Si, Mn, and Ca to the group derived from the correlation matrix; this factor represents leaching of biogenic carbonate, silica, and probably organic matter from the host sediment; **aluminosilicate**: Al, Si, Fe, Zn, Mg (Fig. 105), which adds Fe and Zn, but omits Ti, Ca, and Y compared to the grouping derived from the correlation matrix; **Cr-rich phase**, probably derived from leaching of serpentinite: Cr, As, Ba, Ti, V, Al, Mg (Fig. 105); note that all the elements except Cr show very low factor scores, indicating that Cr is the dominant element of this group.

Many of the phases that make up the hydrothermal deposits and crusts are similar, but the elements that belong to the various phases may differ. Notable examples include Co and Pb, which are invariably part of the δ-MnO_2 phase in crusts in contrast to being part of the Fe oxide phase in hydrothermal deposits; phosphorous makes up part of the CFA phase in crusts and the Fe oxide phase in hydrothermal deposits. On the other hand, many of the elements are associated with similar phases in crusts and hydrothermal deposits. For example, Zn, Cd, Ni, and Mo are associated with Mn in both deposit types; Cu and As are associated with Fe in both deposit types; and Sr, Ca, and V are associated with a biogenic phase in both deposit types.

RESOURCE CONSIDERATIONS

The potential deep-sea resources considered here include 1) cobalt, nickel, manganese, and platinum from Fe-Mn crusts, 2) epithermal gold from veins and shear zone breccias on the Yap arc, 3) nickel, copper, and manganese from hydrothermal stratiform Mn oxide deposits on the Yap arc, and 4) nickel and chromium from Fe-Mn cemented sandstones from the Yap arc. Significant accumulations of phosphorite were not found. The small amount of data and samples collected within the vast EEZ of the FSM during this short cruise are not enough to make resource assessments for the deposit types listed. Several additional cruises would be needed to delineate the variety and general distributions of the mineral deposits that occur in the FSM EEZ. During this short cruise, new marine mineral deposit types were discovered including chromium-rich hydrothermal deposits, offshore epithermal vein systems, nickel- and copper-rich hydrothermal manganese deposits, and a seamount nodule field consisting of nodules with internal structures like those found on abyssal plains. All of these new discoveries have important resource implications. In addition, the first deep-sea skarn deposits were discovered. A variety of ores are known to form as skarns, suggesting that the areas where skarns were found warrant further investigations.

We consider the FSM EEZ as having a moderate potential for Co-rich crusts (Table 22) based on the limited information acquired here and the eleven criteria developed for the exploration for and exploitation of Co-rich crusts (Hein et al., 1988, 1991). The commonly cited cut off grade for potential economic development is 0.8% cobalt. On a hygroscopic water-free basis, crusts from FSM have relatively low mean concentrations of cobalt (0.43%) and phosphorous (0.52%) and moderate concentrations of manganese (21.5%), nickel (0.39%), copper (0.11%), and platinum (0.22 ppm). The commonly cited cut off thickness for potential economic development is 40 mm. Dredges with mean crust thicknesses greater than 40 mm were recovered from only Pali Seamount (mean 50 mm). This is half the mean thickness of crusts recovered from a seamount in the Marshall Islands (Hein, Kang, et al., 1990). Because the mining of crusts from the rugged flanks and summit of seamounts and ridges will be a difficult endeavor, crust thickness (tonnage) may turn out to be a more important factor in economic and site selection considerations than grade. However, surveys within FSM have not been extensive enough to delineate the distribution of crust thicknesses or grade. Only two of the more than 12 Cretaceous seamounts that occur in the FSM EEZ have been sampled. The seamount that perhaps offers the greatest potential is located north of Kosrae at the boundary of the EEZ, which has subdued topography, large size, and occurs near seamounts known to host thick crusts. One favorable aspect of Pali Seamount deposits is that Fe-Mn nodules are abundant. In addition, the nodules have small nuclei like abyssal nodules, rather than large rock nuclei like most seamount nodules. Consequently, the crust component (potential ore) dominates the rock component. It is well known that the mining of nodules is technologically much less complex than the mining of crusts and mining systems for nodules are presently available. The nodules also have higher mean nickel (0.47%) and copper (0.13%) grades compared to their means for crusts, but an identical mean cobalt content (0.43%).

Gold occurs in epithermal quartz veins and mineralized breccias on the islands of Yap and Palau. The gold is very fine grained (up to 20 μm), occurs as native gold, electrum, and gold-silver telluride, and is concentrated up to 13 ppm (Rytuba and Miller, 1990). It is possible that epithermal gold deposits also occur on the submerged portions of the Palau and Yap arcs, and we chose our dredge sites on the Yap arc with this in mind. Remarkably, two of the six dredges taken on the Yap arc contained vein quartz, but none of the vein quartz was mineralized. Breccia and hydrothermally altered siltstone associated with the vein quartz in dredge D8 do contain somewhat elevated gold contents of 6 ppb and 3 ppb, respectively. Recovery of the appropriate host rocks and slightly elevated gold contents in associated rocks indicate that additional surveys are warranted. The most serious problem for offshore exploration for epithermal gold is the poor quality of available bathymetric, geologic, and structural maps of the Yap arc. This makes it difficult to choose dredge sites where epithermal gold deposits are most likely to be recovered. Detailed offshore mapping should greatly enhance the results of future exploration. Even if rich deposits were found in the areas sampled here, they would offer only a long term resource potential because of the significant water depths involved. Exploration in more near-shore environments might identify more viable deposits with a shorter term resource potential.

Hydrothermal Mn deposits were recovered in only one dredge, although they are common in other volcanic arcs. However, the Yap arc hydrothermal deposits are unique in their high trace metal contents, especially the stratiform deposits with 0.45% nickel, 0.26% copper, 0.16% zinc, 0.04% cobalt, and 0.04% chromium and high but typical contents of manganese (44.2%), barium (0.31%), molybdenum (0.03%), and vanadium (0.05%). The Fe-Mn cemented sandstones are also remarkably high in chromium (0.86%) and moderately high in nickel (0.15%). These high metal contents contrast with those that occur in deposits from the Tonga arc and Lau back-arc basin, which have high trace metal contents for titanium (0.14%), strontium (0.13%), molybdenum (0.15%), and vanadium (0.15%). However, not more than one of these trace metals is concentrated in the Mn deposits from any one location (Hein et al., 1990b). Even though the Yap arc hydrothermal deposits are strongly enriched in manganese and other economically and strategically important trace metals, their distribution and bulk tonnage are unknown. Detailed mapping and sampling are required to delineate the extent and grade of these deposits. If the tonnage and grade were good, these deposits would offer only a long term resource potential because of the water depths and remote location. This is especially true for the sandstones with high chromium contents (maximum 1.16%, Table 14) because chromium resources in layered ultramafic intrusions on land are relatively abundant and high grade (DeYoung et al., 1984).

SUMMARY AND CONCLUSIONS

1. The distributions of ridges, troughs, faults, and rock types show that a complex geologic and tectonic evolution of plate boundaries has taken place in the western EEZ of the FSM. Western Caroline Ridge may represent a system of small spreading centers and long transform

faults that originated in the Oligocene, and is presently impinging on the Yap arc to the west. The Yap arc is an Oligocene(?) and Neogene volcanic arc composed of serpentinite and metamorphic and igneous rocks. Quaternary hydrothermal activity occurred on the central summit region of the arc. Rocks recovered from the western end of the Caroline ridge are deformed and sheared, presumable from the collision of the ridge with the arc; reefal limestones from that same area are strongly recrystallized.

2. The first occurrences of deep-sea skarn deposits were found. They were recovered from Caroline Ridge and are composed of vesuvianite and garnet. The skarns probably formed at about 500°C when high-level magmas were intruded into limestones on the ridge. As ore deposits are commonly associated with skarns on land, further exploration for skarn ores is warranted in the FSM EEZ.

3. Metamorphic rocks were recovered from Caroline Ridge for the first time, indicating that the ridge has been subjected to significant tectonic or deformational stresses. Rocks in places on the ridge were also strongly altered by hydrothermal fluids.

4. Hydrothermal stratiform Mn and stratabound Fe-Mn cemented sandstone were recovered from the central Yap arc. The deposits are unique in that they have high trace metal contents, especially, Ni, Ba, Cu, Zn, Sr, V, Co, Cr, and Mo. Chromium in the Fe-Mn cemented sandstones reaches a maximum of 1.16%. These deposits also have a unique mineral composition and are the subject of the first reported occurrence of marine hydrothermal manganese composed of pyrolusite; they are also composed of todorokite and birnessite. The unique composition of these deposits results from the types of rocks leached by the hydrothermal fluids, the temperature of the fluid, and the paucity of polymetallic sulfides deeper in the hydrothermal system. REE compositions and chondrite-normalized patterns, mineralogy, and chemical compositions indicate that the Yap arc deposits are relatively high-temperature proximal deposits compared to similar deposits sampled from other volcanic arcs.

5. Co-rich Fe-Mn crusts occur throughout the FSM EEZ and are thickest on the Cretaceous Pali Seamount in the eastern part of the EEZ. Trace metals are lower than they are in crusts from other regions of the central Pacific. However, an Fe-Mn oxyhydroxide nodule field on Pali Seamount offers a greater potential resource than the crusts. Only two of the more than twelve Cretaceous seamounts that occur in the FSM EEZ have been sampled, and more field work is required to determine the distribution and grade of crusts in the FSM.

6. Q-mode factor analysis and correlation coefficients indicate that bulk crusts are composed of six phases with characteristic associated elements: δ-MnO_2: Co, Ni, Cd, Mo, Mn, As, Pb; Fe oxyhydroxide: Fe, Cu, As; aluminosilicate: Al, Si, K, Na, Mg, Ru, Pd; residual biogenic: Cu, Ba, Zn, V, Ce, Ti, Fe, Pb; CFA: CO_2, Ca, P, Y; and Cr-spinel: Cr, Mn, As.

7. Many of the phases that make up the hydrothermal deposits and crusts are similar, but the elements that belong to the various phases may differ. Notable examples include Co and Pb, which are invariably part of the δ-MnO_2 phase in crusts in contrast to being part of the Fe oxide phase in hydrothermal deposits; phosphorous makes up part of the CFA phase in crusts and the Fe oxide phase in hydrothermal deposits. On the other hand, many of the elements are associated with similar phases in crusts and hydrothermal deposits. For example, Zn, Cd, Ni, and Mo are associated with Mn in both deposit types; Cu and As are associated with Fe in both deposit types; and Sr, Ca, and V are associated with a biogenic phase in both deposit types.

8. The PGEs (Pt, Rh, Pd, Ru, and Ir) in bulk crusts show significant enrichments over their lithospheric averages and over seawater abundances. PGE ratios indicate that most of the Pt, Ir, and Rh are derived from seawater and that Pd, and to a lesser extent Ru, are derived from seawater and clastic debris. In the hydrothermal Mn deposits, some Pt derives from hydrothermal sources, probably from leaching of ultramafic rocks.

9. ΣRREs ranges from 0.10-0.16% for bulk crusts. Chondrite-normalized REE patterns do not show the typical large positive Ce anomaly, but rather show a small positive or small negative Ce anomaly, probably reflecting redox conditions of the water column. ΣREEs ranges from 20-271 ppm for hydrothermal Mn deposits. Large negative Ce and small negative Eu anomalies characterize the chrondrite-normalized REE patterns. The Eu anomalies may reflect the types of rocks leached by the hydrothermal fluids, such as ferromagnesian-rich rocks rather than

felsic rocks. The Ce anomalies indicate that the stratiform deposits formed from fluids with a 95-100% hydrothermal component and 0-5% hydrogenetic component.

10. Phosphorites and CFA mineralization are not common in the FSM as they are in the adjacent EEZ of the Marshall Islands.

11. Oxygen content of the seawater may influence the composition of Fe-Mn crusts, especially in regards to redox sensitive elements. Oxygen contents decrease to the south and east in the area studied, thereby raising the top boundary of oxygen-minimum zone in those areas.

12. Vein quartz and cataclastic breccias were recovered in dredges from the Yap arc. The breccia is enriched in gold relative to MORB, although mineralization comparable to that on islands of Yap and Palau was not found. However, additional surveys for offshore gold are warranted after good bathymetric, geologic, and structural maps are made of the offshore areas.

ACKNOWLEDGMENTS

We thank the Honorable Marcelino K. Actouka, Secretary of the Department of Resources and Development, Federated States of Micronesia for help in coordination of our program with the FSM Government and in arranging for the research cruise. Mr. Aurelio P. Joab, Division of Labor, FSM provided valuable help during and after the cruise and Mr. Peter Sitan, Micronesian Maritime Authority, provided needed clearances. We thank the Government and people of the Federated States of Micronesia for their kindness, help, and encouragement of our work. We thank Captain John Cannan and the crew of the R.V. Farnella for excellent support. We thank Carolyn H. Degnan, Henry Chezar, Shawn V. Dadisman, Kaye L. Kinoshita, Michael E. Boyle, Walter P. Olson, Richard W. Viall, and Ransome W. Rideout of the U.S. Geological Survey and Suk-Ki Kim and Yong Joo of the Korea Ocean Research and Development Institute for technical help on various aspects of this project. Randolph Koski, U.S. Geological Survey, kindly and bravely reviewed this large report.

REFERENCES CITED

Anders, E. and Ebihara, M., 1982, Solar-system abundances of the elements: Geochimica et Cosmochimica Acta, v. 46, p. 2363-2380.

Andrews, J.E., 1971, Gravitational subduction of a western Pacific crustal plate: Nature, Physical Science, v. 233, p. 81-83.

Aplin, A.C., 1984, Rare earth element geochemistry of central Pacific ferromanganese encrustations: Earth and Planetary Science Letters, v. 71, p. 13-22.

Aplin, A.C. and Cronan, D.S., 1985, Ferromanganese oxide deposits from the central Pacific, I. Encrustations from the Line Islands Archipelago: Geochimica et Cosmochimica Acta, v. 49, p. 427-436.

Aruscavage, P.J., Kirschenbaum, H., and Brown, F., 1989, Analytical methods: The determination of 27 elements in ferromanganese materials: in Manheim, F.T. and Lane-Bostwick, C.M. (eds.), Chemical Composition of Ferromanganese Crusts in the World Ocean: A Review and Comprehensive Database. U.S. Geological Survey Open File Report 89-020, 200 p. plus 3 appendices.

Beccaluva, L., Macciotta, G., Savelli, C., Serri, G., and Zeda, O.,1980, Geochemistry and K/Ar ages of volcanics dredged in the Philippine Sea (Mariana, Yap, and Palau trenches and Parece Vela basin): in Hayes, D.E. (ed.), The Tectonic and Geologic Evolution of Southeast Asian Seas and Islands, American Geophysical Union Geophysical Monograph 23, Washington, D.C., p. 247-268.

Bonatti, E., Kraemer, T., and Rydell, H., 1972, Classification and genesis of submarine iron-manganese deposits: in Horn, D.R. (ed.), Ferromanganese Deposits On the Ocean Floor. Washington, D.C., National Science Foundation, p. 149-166.

Bracey, D.R. and Andrews, J.E., 1974, Western Caroline Ridge: Relic Island Arc?: Marine Geophysical Researches, v. 2, p. 111-125.

Burnett, W.C., Cullen, D.J., and McMurtry, G.M., 1987, Open-ocean phosphorites--in a class by themselves?: in Teleki, P.G., Dobson, M.R., Moore, J.R., and von Stackelberg, U., Marine Minerals, D. Reidel, Dordrecht, p. 119-134.

Cantrell, K.J. and Byrne, R.H., 1987, Rare earth element complexation by carbonate and oxalate ions: Geochimica et Cosmochimica Acta, v. 51, p. 597-605.

Chase, T.E., Seekins, B.A., and Young, J.D., 1988, Marine topography of the Republic of the Marshall Islands, Federated States of Micronesia, Republic of Palau, Commonwealth of the Northern Mariana Islands, and Territory of Guam: U.S. Geological Survey unpublished map that was modified from Chase, T.E. and Menard, H.W. (compilers), 1973, Bathymetric atlas of the North Pacific Ocean: U.S. Naval Oceanographic Office, Washington, D.C., Publication 1301-2-3.

Cole, W.S., Todd, R., and Johnson, C.G., 1960, Conflicting age determinations suggested by foraminifera on Yap, Caroline Islands: Bulletins of American Paleontology, v. 41, no. 186, p. 77-113.

Colodner, D.C., Boyle, E.A., and Edmond, J.M., 1991, Platinum in seawater: Abstracts and Program, 1992 Ocean Sciences Meeting, EOS, Transactions of the American Geophysical Union, v. 72, no. 51, p. 44.

Cook, H.E., Johnson, P.D., Matti, J.C., and Zemmels, I., 1975, Methods of sample preparation and X-ray diffraction data analysis (X-ray mineralogy laboratory, Deep Sea Drilling Project, University of California Riverside): in Hays, D.E., Frakes. L.A., et al., Initial Reports of the Deep Sea Drilling Project, U.S. Government Printing Office, Washington, D.C., v. 28, p. 999-1007.

Crawford, A.J., Beccaluva, L., Serri, G., and Dostal, J., 1986, Petrology, geochemistry and tectonic implications of volcanics dredged from the intersection of the Yap and Mariana trenches: Earth and Planetary Science Letters, v. 80, p. 265-280.

Cullen, D.J. and Burnett, W.C., 1986, Phosphorite associations on seamounts in the tropical southwest Pacific Ocean: Marine Geology, v. 71, p. 215-236.

DeBaar, H.J.W., Brewer, P.G., and Bacon, M.P., 1985, Anomalies in rare earth distributions in seawater: Gd and Tb: Geochimica et Cosmochimica Acta, v. 49, p. 1961-1969.

DeCarlo, E.H. and McMurtry, G.M., in press, Rare earth element geochemistry of ferromanganese crusts from the Hawaiian Archipelago: Chemical Geology.

DeCarlo, E.H., McMurtry, G.M., and Kim, K.H., 1987, Geochemistry of ferromanganese crusts from the Hawaiian Archipelago--I. Northern survey areas: Deep Sea Research, v. 34, p. 441-467.

DeYoung, J.H., Jr., Lee, M.P., and Lipin, B.R., 1984, International strategic minerals inventory summary report--Chromium: U.S. Geological Survey Circular 930-B, 41 p.

Elderfield, H., Hawkesworth, C.J., Greaves, M.J., and Calvert, S.E., 1981, Rare earth element geochemistry of oceanic ferromanganese nodules and associated sediments: Geochimica et Cosmochimica Acta, v. 45, p. 513-528.

Engleman, E.E., Jackson, L.L., and Norton, D.R., 1985, Determination of carbonate carbon in geological materials by coulometric titration: Chemical Geology, v. 53, p. 125-128.

Erlandson, D.L., Orwig, T.L., Kiilsgaard, G., Mussells, J.H., and Kroenke, L.W., 1976, Tectonic interpretations of the East Caroline and Lyra Basins from reflection-profiling investigations: Geological Society of America Bulletin, v. 87, p. 453-462.

Faust, G.T. and Fahey, J.J., 1962, The serpentine-group minerals: U.S. Geological Survey Professional Paper 384-A, 92 p.

Fleet, A.J., 1983, Hydrothermal and hydrogenous ferro-manganese deposits: Do they form a continuum? The rare earth element evidence: in Rona, P.A., Boström, K, Laubier, L, and Smith, K.L. (eds.) Hydrothermal Processes at Seafloor Spreading Centers, Plenum, New York, p. 535-555.

Fischer, A.G., et al., 1971, Initial reports of the Deep Sea Drilling Project, v. 6: Washington, U.S. Government Printing Office, 1329 p.

Futa, K., Peterman, Z. E., and Hein, J.R., 1988, Sr and Nd isotopic variations in ferromanganese crusts from the central Pacific: Implications for age and source provenance: Geochimica et Cosmochimica Acta, v. 52, p. 2229-2233.

Gann, J.T., 1988, Integrated GPS, range-range and hyperbolic Loran C marine navigation system for use on IBM AT or compatible microcomputer: U.S. Geological Survey Open File Report 88-562.

Goldberg, E.D., Koide, M., Schmitt, R.A., and Smith R.H., 1963, Rare earth distribution in the marine environment: Journal of Geophysical Research, v. 68, p. 4209-4217.

Goldberg, E.D., 1987, Heavy metal analyses in the marine environment--approaches to quality control: Marine Chemistry, v. 22, p. 117-124.

Halbach, P., Manheim, F.T., and Otten, P., 1982, Co-rich ferromanganese deposits in the marginal seamount regions of the central Pacific basin--results of the Midpac '81: Erzmetall, v. 35, p. 447-453.

Hamilton, W., 1985, Tectonics of the Indonesian Region: U.S. Geological Survey Professional Paper 1078, 345 p.

Haskin, L.A., Haskin, M.A., Frey, F.A., and Wildeman, T.R., 1968, Relative and absolute terrestrial abundances of the rare earths: in Ahrens, L.H. (ed.), Origin and Distribution of the Elements, 1, Pergamon, Oxford, p. 889-911.

Hawkins, J. and Batiza, R., 1977, Metamorphic rocks of the Yap arc-trench system: Earth and Planetary Science Letters, v. 37, p. 216-229.

Hegarty, K.A. and Weissel, J.K., 1988, Complexities in the development of the Caroline plate region, western equatorial Pacific: in, Nairn, A.E.M., Stehli, F.G., and Uyeda, S. (eds.) The Ocean Basins and Margins, Plenum, New York, p. 277-301.

Hein, J.R., Fleishman, C.L., Morgenson, L.A., Bloomer, S.H., and Stern, R.J., 1987b, Submarine ferromanganese deposits from the Mariana and Volcano volcanic arcs, west Pacific: U.S. Geological Survey Open File Report 87-281, 67 p.

Hein, J.R., Kang, J-K., et al., 1990, Geological, geochemical, geophysical, and oceanographic data and interpretations of seamounts and Co-rich ferromanganese crusts from the Marshall Islands, KORDI-USGS R.V. *Farnella* cruise F10-89-CP: U.S. Geological Survey Open File Report 90-407, 246 p.

Hein, J.R., Manheim, F.T., Schwab, W.C., and Davis, A.S., 1985a, Ferromanganese crusts from Necker Ridge, Horizon Guyot, and S.P. Lee Guyot: Geological considerations: Marine Geology, v. 69, p. 25-54.

Hein, J.R., Manheim, F.T., Schwab, W.C., Davis, A.S., Daniel, C.L., Bouse, R.M., Morgenson, L.A., Sliney, R.E., Clague, D.A., Tate, G.B., and Cacchione, D.A., 1985b, Geological and geochemical data for seamounts and associated ferromanganese crusts in and near the Hawaiian, Johnston Island, and Palmyra Island Exclusive Economic Zones: U.S. Geological Survey Open-File Report 85-292, 129 p.

Hein, J.R., Morgenson, L.A., Clague, D.A., and Koski, R.A., 1987a, Cobalt-rich ferromanganese crusts from the Exclusive Economic Zone of the United States and nodules from the oceanic Pacific: in Scholl, D.W., Grantz, A., and Vedder, J.G. (eds.), Geology and Resource Potential of the Continental Margin of Western North America and Adjacent Ocean Basins-Beaufort Sea to Baja California. Circum-Pacific Council for Energy and Mineral Resources, Earth Science Series, Houston, Texas, v. 6, p. 753-771.

Hein, J.R., Schwab, W.C. and Davis, A.S., 1988, Cobalt and platinum-rich ferromanganese crusts and associated substrate rocks from the Marshall Islands: Marine Geology, v. 78, p. 255-283.

Hein, J.R., Kirschenbaum, H., Schwab, W.C., Usui, A., Taggart, J.E., Stewart, K.C., Davis, A.S., Terashima, S., Quinterno, P.J., Olson, R.L., Pickthorn, L.G., Schulz, M.S., Morgan, C.L., 1990a, Mineralogy and geochemistry of Co-rich ferromanganese crusts and substrate rocks from Karin Ridge and Johnston Island, *Farnella* Cruise F7-86-HW, 80 p.

Hein, J.R., Schulz, M.S. and Kang, J.K., 1990b, Insular and submarine ferromanganese mineralization of the Tonga-Lau region: Marine Mining, v. 9, p. 305-354.

Hein, J.R., Schulz, M.S., and Gein, L.M., 1991, Central Pacific cobalt-rich ferromanganese crusts: Historical perspective and regional variability: in Keating, B. and Bolton, B. (eds.), Geology and Offshore Mineral Resources of the Central Pacific Region, Circum-Pacific Council for Energy and Mineral Resources, Earth Science Series, Houston, Texas, in press.

Hodge, V., Stallar, M., Koide, M., and Goldberg, E.D., 1986, Determination of platinum and iridium in marine waters, sediments, and organisms: Analytical Chemistry, v. 58, p. 616-620.

Ingram, B.L., Hein, J.R., and Farmer, G.L., 1990, Age determinations and growth rates of Pacific ferromanganese deposits using strontium isotopes: Geochimica et Cosmochimica Acta, v. 54, p. 1709-1721.

Jackson, L.L., Brown, F.W., and Neil, S.T., 1987, Major and minor elements requiring individual determination, classical whole rock analysis, and rapid rock analysis: in, Baedecker, P.A. (ed) Methods for Geochemical Analysis, U.S. Geological Survey Bulletin 1770, p. G1-G23.

Johnson, C.G., Alvis, R.J., and Hetzler, R.L., 1960, Military geology of Yap Islands, Caroline Islands: U.S. Army Engineers, Pacific, Intelligence Dossier Strategic Study Carolines, 164 p.

Kadko, D. and Moore, W., 1988, Radiochemical constraints on the crustal residence time of submarine hydrothermal fluids: Endeavour Ridge: Geochimica et Cosmochimica Acta, v. 52, p. 659-668.

Keating, B.H., Mattey, D.P., Helsley, C.E., Naughton, J.J., Epp, D., Lazarewicz, A., and Schwank, D., 1984, Evidence for a hot spot origin of the Caroline Islands: Journal of Geophysical Research, v. 89, p. 9937-9948.

Keays, R.R., and Scott, R.B., 1976, Precious metals in ocean-ridge basalts: Implications for basalts as source rocks for gold mineralization: Economic Geology, v. 71, p. 705-720.

Klovan, J.E. and Imbrie, J., 1971, An algorithm and FORTRAN-IV program for large-scale Q-mode factor analysis and calculation of factor scores: Mathematical Geology, v. 3, p. 61-77.

Lalou, C., Thompson, G., Arnold, M., Brichet, E., Druffel, E., and Rona, P.A., 1990, Geochronology of TAG and Snakepit hydrothermal fields, Mid-Atlantic Ridge: witness to a long and complex hydrothermal history: Earth and Planetary Science Letters, v. 97, p. 113-128.

Le Suave, R., Pichocki, C., Pautot, G., Hoffert, M. Morel, Y., Voisset, M., Monti, S., Amosse, J., and Kosakevitch, A., 1989, Geological and mineralogical study of Co-rich ferromanganese crusts from a submerged atoll in the Tuamotu Archipelago (French Polynesia): Marine Geology, v. 87, p. 227-247.

Lichte, F.E., Golightly, D.W., and Lamothe, P.J., 1987a, Inductively coupled plasma-atomic emission spectrometry: in Baedecker, P.A. (ed.), Methods for Geochemical Analysis. U.S. Geological Survey Bulletin 1770, p. B1-B10.

Lichte, F.E., Meier, A.L., and Crock, J.G., 1987b, Determination of the rare eath elements in geological materials by inductively coupled plasma-mass spectrometry: Analytical Chemistry, v. 59, p. 1150-1157.

Mammerickx, J., 1978, Re-evaluation of some geophysical observations in the Caroline basins: Geological Society of America Bulletin, v. 89, p. 192-196.

Mangini, A., Segl, M., Kudrass, H., Wiedicke, M., Bonani, G., Hofmann, H.G., Morenzoni, E., Nessi, M., Suter, M., and Wölfli, W., 1986, Diffusion and supply rates of ^{10}Be and ^{230}Th radioisotopes in two manganese encrustations from the South China Sea: Geochimica et Cosmochimica Acta, v. 50, p. 149-156.

Manheim, F.T. and Gulbrandsen, R.A., 1979, Marine Phosphorites: in Burns, R.G. (ed.), Marine Minerals, Mineralogical Society of America Short Course Notes, v. 6, p. 151-173.

Manheim, F.T. and Lane-Bostwick, C.M., 1988, Cobalt in ferromanganese crusts as a monitor of hydrothermal discharge on the Pacific sea floor: Nature, v. 335, p. 59-62.

Mattey, D.P., 1982, The minor and trace element geochemistry of volcanic rocks from Truk, Ponape and Kusaie, eastern Caroline Islands; the evolution of a young hot spot trace across old Pacific Ocean crust: Contributions to Mineralogy and Petrology, v. 80, p. 1-13.
Morten, L., Landini, F., Bocchi, G., Mottana, A., and Brunfelt, A.O., 1980, Fe-Mn crusts from the southern Tyrrhenian Sea: Chemical Geology, v. 28, p. 261-278.
Nesbitt, B.E., St. Louis, R.M., and Muehlenbachs, K., 1987, Distribution of gold in altered basalts of DSDP hole 504B: Canadian Journal of Earth Sciences, v. 24, p. 201-209.
O'Leary, R.M. and Meier, A.L., 1986, Analytical methods used in geochemical exploration, 1984: U.S. Geological Survey Circular 948, p. 23-27.
O'Neil, J.R., Clayton, R.N., and Mayeda, T.K., 1969, Oxygen isotope fractionation in divalent metal carbonates: Journal of Chemical Physics, v. 51, p. 5547-5558.
Parthé, E. and Crocket, J.H., 1978, Platinum group: in Wedepohl, K.H. (ed.) Handbook of Geochemistry, v. II/5, Springer-Verlag, Berlin, p. 78-A1-78-O7.
Peck, L.C., 1964, Systematic analysis of silicates: U.S. Geological Survey Bulletin 1170, 89 p.
Perfit, M.R. and Fornari, D.J., 1982, Mineralogy and geochemistry of volcanic and plutonic rocks from the boundaries of the Caroline plate: Tectonic implications: Tectonophysics, v. 87, p. 279-313.
Piper, D.Z., 1974, Rare earth elements in ferromanganese nodules and other marine phases: Geochimica et Cosmochimica Acta, v. 38, p. 1007-1022.
Puteanus, D. and Halbach, P., 1988, Correlation of Co concentration and growth rate: a method for age determination of ferromanganese crusts: Chemical Geology, v. 69, p. 73-85.
Ridley, W.I., Rhodes, J.M., Reid, A.M., Jakes, P., Shih, C., and Bass, M.N., 1974, Basalts from Leg 6 of the Deep-Sea Drilling Project: Journal of Petrology, v. 15, p. 140-159.
Rona, P.A., Thompson, G., Mottl, M.J., Karson, J.A., Jenkins, W.J., Graham, D., Mallette, M., Von Damm, K., and Edmond, J.M., 1984, Hydrothermal activity at the Trans-Atlantic Geotraverse hydrothermal field, Mid-Atlantic Ridge crest at 26° N: Journal Geophysical Research, v. 89, p. 11,365-11,377.
Rytuba, J.J. and Miller, W.R., 1990, Geology and geochemistry of epithermal precious metal vein systems in the intra-oceanic arcs of Palau and Yap, western Pacific: Journal of Geochemical Exploration, v. 35, p. 413-447.
Savin S.M. and Yeh, H-W., 1981, Stable isotopes in ocean sediments: in Emiliani, C. (ed.), The Sea, v. 7, Wiley-Interscience, New York, p. 1521-1554.
Schulz, M.S. and Hein, J.R., 1991, Petrography and chemistry of hydrothermal manganese oxyhydroxides from the Mariana and Izu-Bonin volcanic arcs, West Pacific: U.S. Geological Survey Open File Report 91-557, 80 p.
Segl, M., Mangini, A., Bonani, G., Hofmann, H.G., Nessi, M., Suter, M., Wölfli, W., Friedrich, G., Plüger, W.L., Wiechowski, A., and Beer, J., 1984, ^{10}Be-dating of a manganese crust from the central North Pacific and implication for ocean paleo-circulation: Nature, v. 309, p. 540-543.
Shapiro, L., 1975, Rapid analysis of silicate, carbonate, and phosphate rocks--revised edition: U.S. Geological Survey Bulletin 1401, 76 p.
Shimmield, G.B. and Price, N.B., 1988, The scavenging of U, ^{230}Th and ^{231}Pa during pulsed hydrothermal activity at 20°S, East Pacific Rise: Geochimica et Cosmochimica Acta, v. 52, 669-667.
Shiraki, K., 1971, Metamorphic basement rocks of Yap Islands, western Pacific: Possible oceanic crust beneath an island arc: Earth and Planetary Science Letters, v. 13, p. 167-174.
Taggart, J.E., Lindsay, J.R., Scott, B.A., Vivit, D.V., Bartel, A.J., and Stewart, K.C., 1987, Analysis of geologic materials by wavelength-dispersive X-ray fluorescence spectrometry: in Baedecker, P.A. (ed.), Methods for Geochemical Analysis. U.S. Geological Survey Bulletin 1770, p. E1-E19.
Toth, J.R., 1980, Deposition of submarine crusts rich in manganese and iron: Geological Society of America Bulletin, v. 9, p. 44-54.

Varentsov, I., Drits, V.A., Gorshkov, A.I., Sivtsov, A.V., and Sakharov, B.A., 1991, Mn-Fe oxyhydroxide crusts from Krylov Seamount (Eastern Atlantic): Mineralogy, geochemistry, and genesis: Marine Geology, v. 96, p. 53-70.

Vogt, P.R., Lowrie, A., Bracey, D.R., and Hey, R.N., 1976, Subduction of aseismic oceanic ridges: Effects on shape, seismicity, and other characteristics of consuming plate boundaries: Geological Society of America Special Paper 172, Boulder, Colorado, 59 p.

Wicks, F.J. and Whittaker, E.J.W., 1977, Serpentine textures and serpentinization: Canadian Mineralogist, v. 15, p. 459-488.

Wicks, F.J., Whittaker, E.J.W., and Zussman, J., 1977, An Idealized model for serpentine textures after olivine: Canadian Mineralogist, v. 15, p. 446-458.

Winterer, E.L., et al., 1971, Initial Reports of the Deep Sea Drilling Project, v. 7: Washington, U.S. Government Printing Office, pt. 1, 844 p., pt. 2, 912 p.

Working Group, IGCP on Ophiolites, 1977, Initial report of the geological study of oceanic crust of the Philippine Sea floor: Ofioliti, v. 2, p. 137-167.

Table 1. Scientific personnel on R.V. *Farnella* cruise F11-90-CP

James R. Hein	Chief Scientist	USGS[1]
Jung-Ho Ahn	Chief Scientist	KORDI[2]
Michael E. Boyle	Electronics technician	USGS
Henry Chezar	Photographer	USGS
Shawn V. Dadisman	Geologist	USGS
Aurelio P. Joab	Observer	FSM[3]
Yong Joo	Marine technician	KORDI
Moon-Young Jung	Resource analyst	KORDI
Han-Joon Kim	Geophysicist	KORDI
Suk-Ki Kim	Ships captain	KORDI
Kaye L. Kinoshita	Geologist	USGS
Walter P. Olson	Marine technician	USGS
Dong-Won Park	Electronics technician	KORDI
LedaBeth Gray	Geologist	USGS
Ransome W. Rideout	Marine technician	USGS
Marjorie S. Schulz	Geologist	USGS
Virginia K. Smith	Geologist	USGS
Juliet C. Wong	Geologist	USGS
Sang-Ok Yoo	Geologist	KORDI
Suk-Hoon Yoon	Geologist	KORDI

[1]United States Geological Survey; [2]Korea Ocean Research and Development Institute; [3]Federated States of Micronesia

Table 2. Stations and operations for R.V. *Farnella* cruise F11-90-CP

Station	Location	Operation	Station	Location	Operation
01	Pali Seamount	D1	10	Sorol Guyot	D12
01	Pali Seamount	CTD 1	10	Sorol Guyot	D13
02	Namonuito Guyot	D2	12	Fais Island Ridge	D14
03	Namonuito Guyot	D3	13	Fais Trough	D15
04	Namonuito Guyot	CTD 2	13	Fais Trough	D16
05	Tarang Bank	D4	13	Fais Trough	CTD 8
05	Tarang Bank	D5	14	Sorol Trough	D17
05	Tarang Bank	CTD 3	14	Sorol Trough	D18
06	Mariana-Yap arcs join	D6	15	North Eauripik Rise	D19
06	Mariana-Yap arcs join	CTD 4	16	West Lanthe Bank	CTD 9
07	North Yap Arc	D7	16	West Lanthe Bank	D20
08	Hunter Bank	D8	16	West Lanthe Bank	D21
08	Hunter Bank	CTD 5	16	West Lanthe Bank	D22
08	Hunter Bank	D9	17	Condor Bank	CTD 10
09	North Ngulu Ridge	D10	17	Condor Bank	D23
09	North Ngulu Ridge	CTD 6	18	Olapahd Seamount	CTD 11
09	North Ngulu Ridge	D11	18	Olapahd Seamount	D24
10	Sorol Guyot	CTD 7			

D = dredge; CTD = temperature, salinity, oxygen profiles

Table 3. Single-channel airgun and 3.5 kHz bathymetry lines for R.V. *Farnella* cruise F11-90-CP

Line	Location	Equipment[1]	Length (km)
01	Pali Seamount	SC/bathy	54.8
02	Pali Seamount	SC/bathy	24.4
03	Pali Seamount	SC/bathy	52.0
04	Namonuito Guyot	SC/bathy	93.2
05	Namonuito Guyot	SC/bathy	45.8
06	Namonuito Guyot	SC/bathy	60.6
07	Tarang Bank	bathy	25.6
08	Caroline Ridge-Sorol Trough	SC/bathy	225.4
09	Caroline Ridge-Sorol Trough	SC/bathy	287.1
10	Caroline Ridge-Sorol Trough	SC/bathy	114.5
11	Caroline Ridge-Sorol Trough	SC/bathy	39.8
12	Caroline Ridge-Sorol Trough	SC/bathy	161.9
13	Caroline Ridge	SC/bathy	179.6
14	Caroline Ridge	SC/bathy	63.2
15	Yap trench-arc	SC/bathy	223.9
16	North Yap arc	SC/bathy	187.2
17	Mariana-Yap arcs juncture	SC/bathy	23.9
18	Mariana-Yap arcs juncture	SC/bathy	29.0
19	Hunter Bank	bathy	25.6
20	North Ngulu Ridge	bathy	50.0
21	Sorol Guyot	SC/bathy	84.5
22	Sorol Guyot	SC/bathy	57.2
23	Sorol Guyot	SC/bathy	71.9
24	West Lanthe Bank	SC/bathy	53.5
25	West Lanthe Bank	SC/bathy	36.3
26	West Lanthe Bank	SC/bathy	62.7
27	Condor Bank	Bathy	27.9
28	Chuuk B	Bathy	34.6
29	Chuuk B	Bathy	23.1
30	Chuuk B	Bathy	43.0
31	Chuuk B	Bathy	12.4
32	Chuuk B	Bathy	21.3
33	Luhk Seamount	Bathy	34.1
34	Olapahd Seamount	Bathy	47.3
Total	--	--	2577.3

SC = single-channel 195 in^3 airgun; bathy = 3.5 kHz and 10 kHz bathymetry

Table 4. Oxygen and temperature data from CTD casts

	Location	Top of O_2 minimum zone (m)	Lowest O_2 contents (ml/l)	Water depth of lowest O_2 (m)	Water depth of 10°C isotherm (m)
CTD 1	Pali Seamount	300	1.27	347	311
CTD 2	Namonuite Guyot	250	1.32	303	264
CTD 3	Tarang Bank	260	1.43	315	298
CTD 4	Mariana-Yap arcs junture	400	1.82	431	302
CTD 5	Hunter Bank-Yap arc	280	1.62	307	284
CTD 6	North Ngulu Ridge-Yap arc	320	1.67	337	286
CTD 7	Sorol Guyot	300	1.40	362	307
CTD 8	Fais Trough	300	1.37	349	303
CTD 9	West Lanthe Bank	240	1.47	270	250
CTD 10	Condor Bank	250	1.17	262	254
CTD 11	Olapahd Seamount	280	1.02	323	309

Table 5. Foraminifer and calcareous nannofossil ages of sediments and sedimentary rocks

Sample	Lithology	Nannofossils	Foraminifers	Age	Comments
D3-5	Volcaniclastic-bioclastic pebbly sandstone	*Microrhabdulus decoratus* *Watznauria barnesae*	*Globotruncana* sp. aff. *G. augusticarinata* *G.* sp. aff. *G. ventricosa* *Heterohelix* sp.	Late Cretaceous	nannos sparse; microfossils poorly preserved
D3-6	Foraminiferal limestone	*Quadrum*? sp. *Watznauria* sp.	*Globotruncana* sp. aff *G. bulloides* *G.* spp.	Cretaceous	nannos sparse and poorly preserved
D3-7	Limestone	*Chiasmolithus gigas* *Discoaster mohleri* *Sphenolithus anarrhopus* *S.* sp. aff. *S. radians*	*Globigerina senni* *Morozovella* sp. aff. *M. subbotinae*	late Paleocene or early Eocene	—
D4-2A	Volcaniclastic-bioclastic pebbly siltstone	*Coccolithus miopelagicus* *Cyclicargolithus abisectus* *C. floridanus* *Dictyococcites bisectus* *Discoaster deflandrei* *Helicosphaera euphratis* *Ilselithina* sp. aff. *I. fusca* *Sphenolithus* sp. aff. *S. conicus*	*Globigerina sellii* *Globoquadrina tripartita* *G.* sp. aff. *G. praedehiscens*	Oligocene	—
D4-4	Pale brown foraminiferal-nannofossil ooze	*Ceratolithus cristatus* *C. telesmus* *Calcidiscus leptoporus* *Gephyrocapsa* sp. aff. *G. oceanica* *Gephyrocapsa* sp. aff.*G. Caribbeanica*	not analyzed	Quaternary	discoasters rare; probably reworked
D5-3	Brown foraminiferal-nannofossil ooze	*Calcidiscus leptoporus* *C. macintyrei* *Ceratolithus cristatus* *C. telesmus* *Gephyrocapsa caribbeanica* *G.* sp. aff. *G. oceanica* *Rhabdosphaera claviger* *Helicosphaera kamptneri* *H. sellii*	not analyzed	Quaternary	—
D6-3A	Reworked tuff	*Discoaster* sp. aff. *D. deflandrei or D. saundersi* *D.* sp. aff. *D. sublodoensis* *Sphenolithus* sp. aff. *S. orphanknollensis*	not analyzed	Eocene to early Miocene (questionably Eocene)	Smear slide was barren, identifications made from a thin, thin section

Sample	Lithology	Nannofossils	Foraminifers	Age	Comments
D6-3D	Reworked tuff	*Cyclicargolithus floridanus* *Discoaster* sp. aff. *D. challengeri* *D.* sp. aff. *D. dilatus* *D.* sp. aff. *D. druggi* *D.* sp. aff. *D. exilis* *D.* sp. aff. *D. saundersi* *Dictyococcites* sp. aff. *D. scrippsae?* *Umbilicosphaera* sp.	not analyzed	Miocene, possibly early Miocene	Different layer from same rock as D6-3A
D6-4B	Limestone	*Discoaster* spp.	not analyzed	Tertiary	nannos sparse, broken
D6-12	Foraminiferal-nannofossil ooze	*Amaurolithus delicatus* *Calcidiscus leptoporus* *C. macintyrei* *Coccolithus pelagicus* *Discoaster asymmetricus* *D. blackstockae* ? *D. brouweri* *D. challengeri* *D. pentaradiatus* *D. quinqueramus* *D. surculus* *D. variabilis*	*Dentoglobigerina altispira* *Globigerina nepenthes* *Globigerinoides sacculifer* *G.* sp. aff. *G. extremus* *Globorotalia menardii* *Globoquadrina venezuelana* *Orbulina bilobata* *Sphaeroidinellopsis seminulina*	late Miocene or early Pliocene	discoasters abundant
D7-1	Grey-blue-green pebbly serpentine mud	*Discoaster pentaradiatus* ? *D.* sp. aff. *D. variabilis*	*Globigerinoides ruber* *Neogloboquadrina dutertrei* *Pulleniatina obliquiloculata* *P. primalis* *Sphaeroidinella dehiscens*	Pliocene	nannos sparse
D8-1	White foraminiferal-nannofossil ooze	*Calcidiscus leptoporus* ? *Ceratolithus cristatus* *Gephyrocapsa* sp. aff. *G. oceanica* *Helicosphaera wallichi*	not analyzed	Quaternary	—
D8-8A	Pebbly clastic limestone	*Discoaster* spp. *Sphenolithus* spp.	not analyzed	Neogene	nannos sparse, poorly preserved
D8-16-2	Laminated mudstone-siltstone	*Discoaster* sp. aff. *D. deflandrei* *D.* sp. aff. *D. tani*?	not analyzed	Eocene to middle Miocene (very questionably Oligocene)	—
D9-11	*Halimeda* clastic limestone	*Calcidiscus leptoporus* *Ceratolithus* sp. *Gephyrocapsa caribbeanica* *G. oceanica* *G.* sp. *Pontosphaera* sp. *Rhabdosphaera claviger*	not analyzed	Quaternary	—

Sample	Lithology	Nannofossils	Foraminifers	Age	Comments
D10-2B	Pebbly clastic limestone	*Coccolithus pelagicus* *Discoaster asymmetricus* *D. brouweri* *D. intercalaris* ? *D. pentaradiatus* *D. variabilis* *Helicosphaera kamptneri*	non diagnostic	late Miocene-Pliocene	nannos sparse
D10-4	Foraminiferal limestone	*Calcidiscus leptoporus* *Discoaster brouweri* *D. pentaradiatus* *Emiliania annula* ? Small "*gephyrocapsids*"	*Globigerinoides fistulosus* *G. sacculifer* *Globoquadrina altispira* *Orbulina universa* *Pulleniatina obliquiloculata* *Sphaeroidinella dehiscens*	late Pliocene	—
D11-1A	Pale brown foraminiferal-nannofossil ooze	*Calcidiscus leptoporus* *Discoaster asymmetricus* *D. brouweri* *D. pentaradiatus* *Sphenolithus* sp. aff. *S. abies* *S.* sp. aff. *S. neoabies* Small"*gephyrocapsids*"	not analyzed	Pliocene	—
D11-1B	White foraminiferal-nannofossil ooze	*Cyclicargolithus abisectus* *Discoaster* sp. *Fasciculithus* ? *Sphenolithus moriformis* ? *S.* sp.	not analyzed	Tertiary	nannos sparse and poorly preserved
D11-5	Foraminiferal limestone	*Calcidiscus leptoporus* *Ceratolithus rugosus* *Discoaster brouweri* *D. challengeri* *D. pentaradiatus* *D. triradiatus* ? *D. variabilis* *Sphenolithus abies* *S. neoabies* small "*gephyrocapsids*"	*Globorotalia tumida flexuosa* *Sphaerodinella dehiscens* *Sphaeroidinellopsis seminulina* *S. seminulina vars.* *S. paenedehiscens*	Pliocene	nannos abundant but poorly preserved
D11-9-8	Mn cemented foraminiferal sandstone	*Ceratolithus* fragment *Discoaster* sp. aff. *D. brouweri* *D.* sp. *Gephyrocapsa* sp. aff. *G. oceanica* *Helicosphaera* sp.	not analyzed	Quaternary ?	nannos sparse
D11-14-1	Pebbly limestone	*Cyclicargolithus* sp. aff. *C. abisectus* *C.* sp. aff. *C. floridanus* *Sphenolithus heteromorphus*	not analyzed	Miocene (possibly early Miocene)	—

Sample	Lithology	Nannofossils	Foraminifers	Age	Comments
D11-32	Mudstone	*Discoaster brouweri* *D. challengeri* *D. pansus* *D. variabilis*	not analyzed	middle Miocene to Pliocene	nannos sparse
D13-1	White foraminiferal-nannofossil ooze	*Coccolithus pelagicus* *Cyclicargolithus abisectus* *C. floridanus* *Discoaster* sp. aff. *D deflandrei* *Sphenolithus* sp. aff. *S. moriformis* *S.* sp. aff. *S. neoabies* *S. tribulosus* *Triquetrorhabdulus carinatus*	*Globigerina binaiensis* *G. tripartita* *Globigerinoides conglobatus* *G. fistulosus* *G. sacculifer* *Neogloboquadrina dutertrei* *Globorotalia crassiformis* *G. tosaensis* *G. truncatulinoides* *Pulleniatina obliquiloculata* *Sphaeroidinella dehiscens*		Nannos indicate late Oligocene or early Miocene. Forams are a mixture of Oligocene, early Miocene, and Quaternary. A white clast within the mud yielded a rich late Oligocene or early Miocene nanno flora. A brown clast was barren. The age of the mud is probably Quaternary; the white clasts, late Oligocene or early Miocene.
D13-6A	Limestone fracture fill in basalt	*Cyclicargolithus* ? *Dictyococcites* ? *Fasciculithus* ?	not analyzed	Early Tertiary	nannos sparse and poorly preserved
D13-11-1	White limestone	*Coccolithus eopelagicus* ? *Cyclicargolithus abisectus* *C. floridanus* *Dictyococcites bisectus* *D.* sp. aff. *D. scrippsae* *Discoaster* sp. aff. *D. deflandrei* *Sphenolithus obtusus* *S. primus* *S. tribulosus*	non-diagnostic	middle Oligocene	—
D14-1A	White stiff sparsely pebbly foraminiferal-nannofossil ooze	*Calcidiscus leptoporus* *C. macintyrei* *Ceratolithus rugosus* *Coccolithus pelagicus* *Discoaster asymmetricus* *D. blackstockae* *D. brouweri* *D.*sp. aff. *D. intercalaris* *D. pentaradiatus* *D.* sp. aff. *D. surculus* *Helicosphaera* sp. aff. *H. sellii*	*Globigerinoides fistulosus* *Globorotalia flexuosa* *G. tosaensis* *Sphaeroidinella dehiscens*	middle or late Pliocene	—
D14-4-1	Foraminiferal limestone	*Coccolithus pelagicus* *Dictyococcites bisectus* *Sphenolithus* sp. aff. *anarrhopus* *S.* sp. aff. *S. primus* *Toweius gammation*	non-diagnostic	Eocene ?	—

Sample	Lithology	Nannofossils	Foraminifers	Age	Comments
D14-6	Clastic limestone	*Coccolithus pelagicus* *Dictyococcites bisectus* *Fasciculithus* ?	not analyzed	Early Tertiary	nannos sparse and poorly preserved
D15-1A	Brown clast within mud D15-1B	*Cyclicargolithus abisectus* *Dictyococcites scrippsae* *Discoaster* sp. aff. *D. deflandrei* *Reticulofenestra* sp. *Sphenolithus ciperoensis* *S. pseudoradians* *S. tribulosus*	not analyzed	late Oligocene	—
D15-1B	Brown foraminiferal-nannofossil ooze	*Cyclicargolithus abisectus* *Discoaster* sp. aff. *D. deflandrei* *Gephyrocapsa* spp. *Sphenolithus abies* ? *Triquetrorhabdulus carinatus*	*Beella digitata* *Orbulina universa* *Pulleniatina obliquiloculata* *Sphaeroidinella dehiscens*	Quaternary	nannos a mixture of late Oligocene and Quaternary
D15-15-1	Limestone	*Cyclicargolithus* sp. aff. *C. abisectus* *C.* sp. aff. *C. floridanus* *Sphenolithus* sp. aff. *S. moriformis*	not analyzed	Eocene to Miocene (possibly late Oligocene or early Miocene	—
D16-1A	White foraminiferal limestone	*Coccolithus eopelagicus* *C. pelagicus* *Cyclicargolithus abisectus* *Dictyococcites bisectus* *Discoaster deflandrei* *Sphenolithus ciperoensis* *S.* sp. aff. *S. capricornutus*	*Globoquadrina binaiensis* *G. tripartita* *Pulleniatina primalis* *P.* sp. aff. *P. spectabilis* *Sphaeroidinella dehiscens* *Sphaeroidinellopsis* sp. aff. *S. seminulina*	late Oligocene with some late Miocene or early Pliocene forams.	—
D16-13-1	Pale brown bioturbated limestone	*Coccolithus pelagicus* *Cyclicargolithus abisectus* *C. floridanus* *Discoaster* sp. *Helicosphaera* sp. aff. *H. euphratis* *Sphenolithus* sp. aff. *S. distentus* *S. tribulosus*	not analyzed	middle Oligocene	—

Sample	Lithology	Nannofossils	Foraminifers	Age	Comments
D16-15	Dark brown limestone	*Coccolithus pelagicus* *Cyclicargolithus abisectus* *C. floridanus* *Dictyococcites scrippsae* *Discoaster* sp. aff. *D. gemmifer* *D. tani* var. *ornatus* ? *Discolithina* ? *Helicosphaera euphratis* *Sphenolithus distentus* ? *S. predistentus* *S. tribulosus*	not analyzed	middle Oligocene	—
D17-1	White foraminiferal limestone	*Gephyrocapsa* sp. *Sphenolithus neoabies* ? small "*gephyrocapsids*"	not analyzed	earliest Pleistocene?	nannos sparse
D18-1-2	Brown foraminiferal-nannofossil ooze	*Calcidiscus leptoporus* *Ceratolithus cristatus* *C. telesmus* *Coccolithus pelagicus* *Gephyrocapsa caribbeanica* ? *G. oceanica* ? *Helicosphaera sellii* small "*gephyrocapsids*"	not analyzed	Quaternary	—
D21-2A	Foraminiferal limestone	*Calcidiscus leptoporus* *C. macintyrei* *Coccolithus pelagicus* *Discoaster bellus* ? *D. brouweri* *D. pentaradiatus* *D. variabilis* *Helicosphaera euphratis* ? *Sphenolithus* sp. aff. *S. abies*	not analyzed	Miocene or Pliocene	—
D21-4	Pale brown foraminiferal-nannofossil ooze	*Calcidiscus leptoporus* *Ceratolithus cristatus* ? *Gephyrocapsa caribbeanica* ? many small "*gephyrocapsids*" *Helicosphaera kamptneri* *H. sellii*	not analyzed	Quaternary	an overgrown reworked sphenolith

Sample	Lithology	Nannofossils	Foraminifers	Age	Comments
D22-1	White pebbly and sandy limestone	*Calcidiscus leptoporus* *C. macintyrei* *Coccolithus pelagicus* *Discoaster brouweri* *D. pentaradiatus* *D.* sp. aff. *D. pansus* *D. variabilis* *Sphenolithus* sp. aff. *S. abies* *Triquetrorhabdulus* sp. aff. *T. rugosus*	not analyzed	Miocene or Pliocene	nannos poorly preserved
D22-3	Massive white limestone	*Calcidiscus macintyrei* *Ceratolithus* sp. *Coccolithus pelagicus* *Discoaster bellus* ? *D. brouweri* *D.* sp. aff. *D. challengeri* *D. pansus* *D. pentaradiatus* *D.* sp. aff. *D. tamalis* *Sphenolithus* sp. aff. *S. abies* *Sphenolithus* sp. aff. *S. neoabies* *Triquetrorhabdulus* sp. aff. *T. milowii*	not analyzed	Pliocene	nannos abundant but poorly preserved
D22-10-1	White pebbly and sandy limestone	*Amaurolithus* sp. aff. *A. amplificus* *Calcidiscus macintyrei* *Coccolithus pelagicus* *Discoaster brouweri* *Helicosphaera euphratis* ? *Sphenolithus* sp. aff *S. abies* *S.* sp. aff. *S. neoabies* *Triquetrorhabdulus carinatus* ? *T.* sp. aff. *T. milowii*	not analyzed	Miocene or Pliocene	few, poorly preserved nannos
D23-1A	Pale brown foraminiferal-nannofossil ooze	*Ceratolithus telesmus* *Discoaster* sp. aff. *D. asymmetricus* *D. quinqueramus*? *D. brouweri* *D. challengeri* *D.* sp. aff. *D. neorectus* *D. pentaradiatus* *D. surculus* *Triquetrorhabdulus* sp. *Sphenolithus* sp. aff. *S. abies* *S. moriformis* small "*gephyrocapsids*"	not analyzed	late Miocene mixed with Quaternary	—

Sample	Lithology	Nannofossils	Foraminifers	Age	Comments
D23-1B	White foraminiferal-nannofossil ooze	*Calcidiscus leptoporus* *Discoaster asymmetricus* *D. brouweri* *D. quinqueramus* *D. variabilis* *Sphenolithus abies* ? *S. neoabies* ? many small "*gephyrocapsids*"	not analyzed	late Miocene	—
D23-4-1	Poorly lithified white foraminiferal limestone	*Amaurolithus* sp. aff. *A. amplificus* *Discoaster asymmetricus* *D. brouweri* *D.* sp. aff. *D. exilis* *D. quinqueramus* *D. surculus* *Sphenolithus* sp.	not analyzed	late Miocene	—

The following samples are barren or contain indeterminate microfossils:

D1-4A: Phosphorite breccia
D2-1A: Phosphorite
D2-4A: Siltstone
D2-5A: Phosphorite
D3-2-1A: Phosphatized mudstone
D3-4-1A: Siltstone

D5-1-2: Bioclastic reefal limestone
D8-2A: Grey mud
D9-12: Bioclastic reefal limestone
D11-2B: Pebbly Mn sandstone
D11-4: Breccia

D14-2-3: Reefal limestone
D14-7-1: Reworked tuff
D14-8-1: Siltstone
D18-1-1: Stiff green-brown mud
D24-1: Bioclastic limestone

Table 6. Summary of dredges from R.V. *Farnella* cruise F11-90-CP

Dredge Number	Seamount	Water Depth on/off Bottom (m)	Water Depth of Recovery (m)	Recovery (Kg)	Percent from Outcrop	Percent Covered by Crust	Crust Thickness (Ave. mm.)	Crust Thickness (max. mm)	Dominant Substrate Type	Comments
D1	Pali Seamount	2200-2105	2180-2105	425	90	100	50	75	Hyaloclastite, phosphorite	90% Fe-Mn nodules, ave. 40 mm diameter
D2	Namonuito Guyot	2335-2115	2335-2300 (lifted) 2050-1980 (restarted)	20	100	100	10	34	Limestone	Partly phosphatized
D3	Namonuito Guyot	2650-2633	2650-2580	250	90	90	3	26	Mudstone-siltstone	Some fossil crusts; phosphorite
D4	Tarang Bank	3195-2774	2900-2774	40	100	100	1	10	Basalt	Large augite & plagioclase
D5	Tarang Bank	2745-2595	2745-2600	6	95	50	1	2	Reef limestone	Framework corals
D6	Mariana-Yap arcs juncture	2050-1865	2050-1840	300	20	50, 50 patina	5	50	Basalt	Serpentinite
D7	North Yap arc	2315-2055	2315-2020	300	50	5, 95 patina	Patina	20	Serpentinite	Vein quartz, sheared
D8	Hunter Bank	2000-1500	2000-1500	50	40	0	Patina	Patina	Basalt, breccia	Gabbro, diabase
D9	Hunter Bank	830-770	820-760	60	80	0	Patina	Patina	Reef Limestone	Much biology: sponge, coral, etc
D10	N. Ngulu Ridge	1380-1300	1380-1300	20	90	0	Patina	Patina	Pebbly limestone	Amphibolite, serpentinite
D11	N. Ngulu Ridge	2380-2260	2300-2280	300	60	50, 50 patina	8	12	Breccia, basalt	Hydrothermal Mn; metamorphic rocks; serpentinite; skarn
D12	Sorol Guyot	2660-1835	2660-1835	<1	50	20	1	2	Basalt	9 small pebble-sized fragments
D13	Sorol Guyot	3000-2930	3000-2700	450	100	80, 20 patina	2	10	Basalt	Gabbro
D14	Fais Island Ridge	2740-1800	2700-2500	140	90	0, 50 patina	Patina	Patina	Limestone	Strongly recrystallized limestone
D15	Fais Trough	3140-2400	3140-2500	110	100	0	Patina	Patina	Basalt	Pillow basalt, fresh glass; skarn
D16	Fais Trough	1440-1385	1950-1385	240	60%, mudstone	0	Patina	Patina	Basalt, siltstone	Bedded & bioturbated sed. rocks
D17	Sorol Trough	2330-1980	2330-2050	1.5	100	30	1	3	Limestone, basalt	Green metaigneous rocks
D18	Sorol Trough	2950-2800	2950-2600	400	90	25	1	3	Basalt	Green metaigneous rocks; greenschist
D19	N. Eauripik Rise	3050-2650	3050-2850	120	90	100	35	60	Basalt, breccia	basalt maybe clasts from breccia
D20	W. Lanthe Bank	2930-2000	--	0	--	--	--	--	--	Lost Bag
D21	W. Lanthe Bank	2910-2700	2800-2780	4	100	95	5	8	Basalt	--
D22	W. Lanthe Bank	2580-1800	2550-2100	275	100	50, 50 patina	2	10	Limest., basalt, sandstone	Volcaniclastic sandstone turbidites
D23	Condor Bank	2460-2000	2460-2200	25	100	5	Patina	Patina	Limestone	Carbonate ooze
D24	Olapahd Seamount	3120-3100	3120-3100	7	100	30	Patina	Patina	Limestone	--

Table 7. Location and description of dredges from R.V. *Farnella* cruise F11-90-CP

Dredge number	Latitude (°N)[1]	Longitude (°E)	Water Depth (m)[2]	Recovery (kg)	Ferromanganese Deposits	Substrate Rocks
D1	10°27.29' 10°27.02'	156°40.93' 156°41.80'	2180-2105	425	95% nodules, 20-130mm diameter (ave. 45), 75% with small or no nucleus, 20% medium-sized nucleus, & 5% nucleus dominates; dominantly botryoidal surfaces, some smooth; 5% crusts, most without substrate, few enrusted cobbles; 1 to 6 layers: black, dense & massive to porous & brown, more rarely laminated, columnar, & dendritic; most porous layers are Fe stained, some vuggy, some filled with sediment; thickness: max=75mm, ave=50mm	60% completely altered yellow-green hyaloclastite; 35% pale to dark brown phosphorite; 5% altered, basalt with phosphorite and rarely calcite amygdules; the phosphorite & basalt occur as clasts in phosphorite cemented breccia; nucleus of nodules are same 3 rock types in about same relative proportions; 5% of nodules have older nodule fragments as nucleus; overall, little substrate recovered
D2	09°50.90' 09°51.12' lifed & restarted 09°50.99' 09°50.99'	148°28.02' 148°28.13' lifted & restarted 148°27.02' 148°27.13'	2335-2300 lifted & restarted 2050-1980	20	Thin crusts on limestone with granular, smooth, botryoidal, & subdued botryoidal surfaces; 1 or 2 layers: black massive dense, black massive porous; lines animal borings in host rock & shows diffusion fronts below crust, along fractures, & next to borings; 1 nodule; thickness: max=34mm, ave=10mm	98% bioclastic limestone: 1. clasts of reefal debris, recrystallized, moldic porosity, 2. clasts of pelagic foraminifera, both friable & partly phosphatized, minor pebbly limestone with basalt clasts; 1% altered massive basalt, 7 pumice pebbles; 1% greenish-grey volcaniclastic siltstone with shell fragments
D3	09°50.00' 09°51.16'	148°31.69' 148°30.95'	2650-2580	250	Thin crusts on mudstone with botryoidal, granular, & smooth surfaces, some botryoids stand in very high relief; patina or 1 layer, black, massive, more rarely porous; microfractures & vugs Fe stained; lines animal borings in host rock & shows diffusion fronts below crust, along fractures, & next to borings in host rock; rarely fossil crust overlain by siltstone turbidite; thickness: max=26mm, ave=3mm	90% siltstone-mudstone, pale to dark brown & yellowish brown, massive to crudely layered, slightly to moderately calcareous, bioturbated & microbored at margins with crusts, poorly to moderately indurated, fractures & borings lined with Mn oxides; 5% bioclastic limestone like that in D2; 5% altered basalt, massive, fine & medium grained varieties, 2 pebbles of pumice; 1% coarse-grained pebbly volcani-clastic sandstone, with calcite rim cement & some shell debris & red coral; 1 small cobble of cement-supported breccia with clasts of basalt in calcite cement
D4	08°33.08' 08°31.96'	144°59.84' 145°00.45'	2900-2774	40	Mostly thin granular crust, thicker in lows, porous black; some smooth or botryoidal surfaces; dendrites & clastic grains in tuff; thickness: max=10mm, ave=1mm	95% basalt boulder with olivine to 8mm altered to iddingsite, plagioclase and clinopyroxene phyric, some fresh glass, calcite amygdules; 5% calcarous (foraminiferal) siltstone with crystals of clinopyroxene & plagioclase to 2mm & rare altered basalt pebbles; 6 pumice pebbles; 6kg foraminiferal-nannoplankton ooze
D5	08°30.54' 08°29.77'	145°02.41' 145°03.79'	2745-2600	6	Patchy thin granular patina, thicker in lows; thickness: max=2mm, ave=1mm	99% limestone, framework reef limestone, predominantly coral, minor solitary corals & bioclastic limestone, lagoonal or outer reef facies; 17 pebbles of pumice; 20gm foraminiferal-nannoplankton ooze

Table 7 continued

Dredge number	Latitude (°N)	Longitude (°E)	Water Depth (m)	Recovery (kg)	Ferromanganese Deposits	Substrate Rocks
D6	11°27.15' 11°28.83'	139°49.01' 139°48.94'	2050-1840	300	50% of rocks have crusts, granular, small botryoidal, & smooth-abraded surfaces, black, porous Fe stained outer layer & black massive dense inner layer, or 1 porous layer; sedimentary rocks peppered with Mn, limestone impregnated with Mn for 4mm below crust & animal borings lined with Mn; max=50mm, ave=15mm; 50% rocks with smooth patina	63% basalt: 1. grey to greenish with wavy parallel fractures; 2. fresh-grey to altered greenish-brown vesicular; 3. highly altered greenish massive; 4. same as 3, but with glass rinds; 23% tuff & mudstone, waxy mottled white-green, some pebbles & cobbles of basalt, some fine-grained laminated; 7% thin plates of limestone, yellowish-white, extensively bored; 7% mudstone, mottled brown by bioturbation
D7	10°59.17' 10°57.57'	138°31.43' 138°32.99'	2315-2020	300	5% of rocks have crusts, granular & smooth surfaces, mostly with 1 porous black or brown layer, 1 with inner black massive layer also; max=20mm, ave=10mm; 95% of rocks with smooth to granular patina; dendrites on fracture surfaces in some rocks	1 kg of grey-blue-green serpentine-chlorite mud with embedded pebbles; about 65kg boulder of pale to dark green serpentinite, fibrous in places, in a black matrix laced with white serpentine, small patches of red-brown iddingsite, calcite crystals to 3mm at base; cobbles to pebbles of serpentinite breccia & serpentinized basalt & peridotite; layered serpentinite & magnetite rock; 40kg quartz vein pebbles & cobbles with minor serpentine; mixed quartz (fracture-fill)-serpentinite rocks; altered basalt cobbles; minor pumice and sandstone
D8	10°00.01' 09°59.97'	138°12.37' 138°13.23'	2000-1500	50	Smooth patina on most rocks	55% basalt, gabbro, & diabase, massive, grey, plagioclase & pyroxene phyric, plagioclase glomerocrysts, magnetite-rich, some minor sulfides; some altered to Fe oxides & serpentine; others are vesicular with calcite & quartz amygdules; minor serpentinitite & quartz veins; 38% breccia, brown to greenish subangular to subrounded clasts of mostly vesicular basalt in finer-grained matrix of same crushed rock & clay minerals; clear quartz & green analcite? crystals; 7% limestone: 1. quartz & serpentinite pebble clasts in foraminiferal matrix, 2. framework coral; minor: 1. laminated mudstone-siltstone, 2.cataclastic quartz-serpentinite rock, 3.coarse-grained, strongly cemented metagreywacke; 0.5kg white mud, 0.5kg grey mud; 2 glass sponges, corals, pelecypod

Table 7 continued

Dredge number	Latitude (°N)	Longitude (°E)	Water Depth (m)	Recovery (kg)	Ferromanganese Deposits	Substrate Rocks
D9	10°00.00' 10.00.02'	138°15.69' 138°15.95'	820-760	60	Smooth, rarely granular, patina on most rocks	70% reef framework coral limestone; minor *Halimeda* limestone, clastic limestone of reef debris, coral & reefal gravel; 25% breccia: 1. brown vesicular basalt clasts (some fractured & cemented by calcite) in calcite cement & serpentine, chlorite, and quartz matrix; 2. clasts of basalt hydrothermally alter to Fe oxides, blue-grey altered basalt in Fe oxide-clay mineral matrix; rare serpentinized volcaniclastic rocks; 5% basalt: brown, vesicular, disseminated magnetite, zeolite & quartz amygdules, rarely calcite; minor pumice; glass sponge, coral, other organisms
D10	08°53.60' 08°52.70'	137°43.71' 137°43.66'	1380-1300	20	Minor smooth to granular patina	100% limestone: 1. pebbly to cobbly clastic limestone, rounded to angular clasts of basalt, diabase, gabbro, green amphibolite, & siltstone in matrix of sand-sized reefal debris and calcite cement; 2. recrystallized brown coral fragments; 3. foraminiferal limestone; minor pumice; sea anenome
D11	08°55.51' 08°54.90'	137°40.93' 137°41.09'	2300-2280	300	50% of rocks have crusts with granular surface on large-relief to subdued botryoids, 1 black porous layer, max=12mm, ave=8mm; 50% of rocks with smooth patina; 85kg of pale grey to black hydrothermal Mn-cemented breccia & sandstone (volcaniclastic & bioclastic); 3kg stratabound submetallic (grey, steal-grey, brown-grey) hydrothermal Mn oxide, fine botryoids in voids, fibrous laminae alternating with massive laminae, & Mn-sandstone layers alternating with submetallic layers, some chaotic-disrupted layers, some fragments have black to brown hydrogenetic crusts on the outer surface; greatest thickness=60mm	70% breccia & sandstone: 1. grey to black crudely layered pebbly (basalt, siltstone) sandstone with mudstone lenes and Mn-oxide cement & clay matrix, grains of basalt, siltstone, limestone, 2. yellow-brown pebbly sandstone with grain supported pebbly layers-probably same as #1 without the Mn cement, 3. greenish breccia with angular to subrounded clasts of basalt, metamorphic rock, limestone, hydrothermally altered clasts, breccia, serpentine in greenish serpentine mud & basaltic sand matrix with white calcite in places; patches of waxy sheared clays, rare quartz veins, 4. brown & white breccia with hydrothermally altered brown basalt clasts in calcite cement; 5. metamorphic & serpentine clasts in calcite cement & fine clastic grains or in Fe-oxide rich clay matrix; 30% basalt, aphanitic, slightly vesicular, grey, sparsely plagioclase phyric, rarely analcite amygdules; some hydrothermally altered to Fe oxides, others serpentinized with calcite veins, some metavolcanic rocks including blue-grey crudely gneissic rocks; <1% foraminiferal limestone; <1% hydrothermal prehnite-quartz-laumontite(?) rock & strongly altered rocks of unknown origin; traces of white nannoplankton ooze & pale brown foraminiferal ooze
D12	08°43.47' 08°41.60'	138°53.04' 138°53.03'	2660-1835	<1	Minor porous granular crust on 1 of 9 small pebbles; max=2mm, ave=1mm	9 small pebbles: 2 pumice, 2 sandstone, 1 Mn coated bone, 4 volcanic rocks; possible that pebbles are from D11 and bag was not thoroughly cleaned

Table 7 continued

Dredge number	Latitude (°N)	Longitude (°E)	Water Depth (m)	Recovery (kg)	Ferromanganese Deposits	Substrate Rocks
D13	08°45.06' 08°45.10'	138°52.96' 138°53.60'	3000-2700	450	20% granular (some smooth) patina; 80% crusts with botryoidal current modified & polished or granular surfaces, 1 layer, porous black with Fe staining; max-=10mm, ave=2mm	>99% basalt & gabbro: vesicular, altered, grey to brown, olivine & plagioclase phyric, olivine altered to Fe oxides & clay minerals, vesicles filled with calcite and zeolites, some magnetite-rich samples; <1% coralline & foraminiferal limestones, breccia, pumice, white carbonate ooze
D14	09°31.63' 09°32.18'	140°17.95' 140°19.75'	2700-2500	140	Patchy smooth to granular patina	84% stongly recrystallized reef limestone, framework and bioclastic, minor to moderate moldic porosity, rare chert lenses & burrow fill; 7% sparcely pebbly white foraminiferal limestone; beige foraminiferal limetstone; cataclastic-shear limestone breccia, some clasts can be fit together, calcite cement; foraminiferal & reefal bioclastic limestones; 3% greenish-brown calcareous volcaniclastic sandstone & sandy siltstone; greenish-brown breccia; 6%: 3 pebbles of coarse-grained stongly altered magnetite-rich gabbro; grey, massive basalt; vesicular basalt, plagioclase phyric, some peppered with magnetite, some olivine phyric; pumice
D15	09°10.25' 09°09.88'	141°34.21' 141°33.79'	3140-2500	110	Patchy granular to smooth patina commonly Fe stained	>99% basalt: pillow basalt, fresh to altered, grey to brown, yellowish-green alteration rind, glass rind-some only partly altered, plagioclase phyric, disseminated and fracture lined sulfides (pyrite & calcopyrite); grey to black, tiny vesicles, very fine grained, pale-colored sulfide-marcasite(?); coarse-grained massive, greenish-grey, plagioclase phyric, sulfides; some samples with calcite amygdules; <1% breccia, stronly altered, sheared matrix; brown mud
D16	09°09.16' 09°09.50'	141°34.03' 141°33.66'	1950-1385	240	Patina, smooth or granular, Fe stained	45% basalt: fresh, grey, plagioclase phyric, very small vesicles filled with Mn oxides(?); pillow basalt, fresh glass margin, alteration rind, plagioclase phyric, minor vesicles, some filled with calcite; massive, coarse-grained, altered, olivine & plagioclase phyric; 45% bedded sedimentary rocks: extensively burrowed volcaniclastic mudstone-siltstone-sandstone, greenish-brown, friable, graded beds, some burrows filled with calcareous sediment, bed thickness in centimeter-size range; 10% extensively burrowed carbonate mudstone (micrite), yellowish-brown; massive pebbly limestone; white & brown foraminiferal limestones
D17	08°24.70' 08°24.82'	141°49.02' 141°48.97'	2330-2050	1.5	30% rocks with crusts with granular surface, or patina with smooth surface; porous, Fe stained; max=3mm, ave=1mm	60% white foraminiferal limestone; 35% pale grey-green volcanic & intrusive rocks altered to greenschist, vesicles filled with green clay; 5% coarse-grained basalt pebbles

Table 7 continued

Dredge number	Latitude (°N)	Longitude (°E)	Water Depth (m)	Recovery (kg)	Ferromanganese Deposits	Substrate Rocks
D18	08°24.04' 08°24.38'	141°48.28' 141°48.10'	2950-2600	400	70% smooth, rarely granular, patina; 30% granular crust, porous, Fe stained; max=3mm, ave=<1mm	60% grey metabasalt, plagioclase & olivine phyric, coarse-grained, amphibole, some with sulfides (pyrite); porphyroblasts of quartz, vesicular with green mineral lining vesicles with the remainder being filled with quartz; dense, very fine-grained dark grey aphanitic metabasalt; medium-grained, grey, plagioclase & pyroxene phyric, with titanomagnatite; minor brown strongly altered basalt; 38% pale green metamorphosed volcanic rocks, greenschist, quartz & sulfides(?) in vesicles, felty groundmass, grey feldspar, green chlorite & amphibole, black pyroxene; very fine-grained variety of previous rock; stiff green mud, calcareous brown mud
D19	06°35.66' 06°36.20'	142°16.91' 142°17.72'	3050-2850	120	Crusts with botryoidal, subdued botryoidal smoothed and/or polished by currents, subdued elongate botryoidal, or smooth & granular surfaces, commonly with a lizard skin-like textured finish; granular, porous, Fe stained on sides of rocks; 1 to 3 layers; outer dense black or laminated, middle porous, in places columnar, Fe stained, in places fractured, inner dense black microfractured, in places Fe stained; in places in some crusts the middle layer extends to the substrate; boundaries between layers are gradational; single crusts may consist of only layer 1 or 2;	46% breccia: clasts of strongly altered grey to brown vesicular basalt & massive olivine-plagioclase phyric basalt, both surrounded by Mn in phosphorite cement & hyaloclastite matrix; phosphorite fills fractures; 43% basalt: vesicular (Mn fills most, phosphorite some, rarely lined with quartz), brown, altered, aphanitic, rarely plagioclase &/or olivine phyric; pillow basalt, brown, altered, aphanitic, rarely plagioclase &/or olivine phyric, glass margin, alteration rind, some vesicles filled with phosphorite; 11% crust fragments without substrate; <<1% pumice; glass sponge
~~D20~~	~~06°09.50'~~ 06°11.30'	~~144°57.54'~~ 144°58.10'	~~2930-2000~~	~~0~~	~~lost bag~~	lost bag
D21	06°09.62' 06°09.96'	144°57.83' 144°58.03'	2800-2780	4 does not include mud	Granular patina; crusts with granular, lizard skin, or small botryoidal surfaces; 1 black, dense massive layer, Fe stained in places; phosphorite layer between crust & substrate; max=8mm, ave=5mm	92% vesicular basalt with fresh black glass margin, reddish-brown alteration rind, small plagioclase & olivine phyric with olivine altered to Fe oxides; phosphorite in some vesicles; 4% pumice; 4% limestone: pebbly limestone, foraminiferal limestone, & coral fragments; 7kg beige carbonate mud

Table 7 continued

Dredge number	Latitude (°N)	Longitude (°E)	Water Depth (m)	Recovery (kg)	Ferromanganese Deposits	Substrate Rocks
D22	06°10.23' 06°11.14'	144°57.74' 144°58.69'	2550-2100	275	Granular patina; cru$ts with granular, subdued botryoidal, smooth, & lizard skin surfaces; 1 layer, black, dense, massive; disseminated in some limestones; lines animal borings in limestones	41% limestone, 24% volcaniclastic sandstone-breccia are interbedded with sharp contacts that may be undulatory, also each occurs as lenses in the other and as clasts in the other; white limestone is sandy to pebbly, massive, foraminifera-rich, rarely burrowed, commonly bored, & is a matrix for the sandstone; yellow-brown sandstone-breccia is composed of basalt, volcanic glass, shell, & limestone grains, graded bedding, channalized in places, and is also dispersed in the limestone; 1 cobble or recrystallized clastic limestone composed of reef debris with moldic porosity; 28% vesicular basalt, aphanitic, sparcely to moderately plagioclase & olivine phyric, olivine altered to Fe oxides, some vesicles filled with calcite, fresh black glass margins occur on some with an alteration rind; 6% breccia, clasts of above basalt in calcite cement & altered hyaloclastite matrix
D23	07°17.74' 07°19.50'	148°16.02' 148°16.40'	2460-2200	25	Granular to smooth patina on 1 cobble of limestone, also lines fractures & borings; some disseminated in massive white limestone	98% limestone & carbonate ooze: white, stiff but friable foraminiferal limestone, massive; white, carbonate ooze; brown carbonate ooze; moderately well lithified white & brown mottled (burrowed) foraminiferal limestone, relict cross bedding; 2% pumice
D24	05°16.99' 05°16.49'	158°17.48' 158°17.16'	3120-3100	7	Smooth to granular patina, patchy; lines borings in limestone; rarely botryoidal	90% limestone: bioclastic with foraminifera, coral, & shell fragments; recrystallized coral fragments; 10% volcanic: pale to dark grey pumice; brown basalt altered to clay minerals; red altered alkalic basalt with phenocrysts altered to green clay, subaerially erupted; grey olivine phyric altered basalt

Table 8. Igneous rock samples being processed for analyses

Sample	WR by XRF	REE by ICP-MS	Microprobe	K-Ar dating
D2-2	X	X	Minerals	--
D4-1c	X	X	Minerals	X?
D4-2	--	X	Glass	--
D6-6	X	X	Minerals	X
D6-7	X	X	--	X
D6-11-1	X	X	Glass, minerals	--
D7-6-1	X	X	--	--
D7-11-1	X	X	Minerals	--
D7-12	X	X	--	X?
D8-11-1	X	--	--	X
D8-11-2,3	X	X	Minerals	--
D8-13	X	X	--	--
D9-5a	X	X	--	--
D9-7-1	X	X	Minerals	--
D10-2A	X	X	Minerals	--
D10-2B	--	--	--	X
D11-6-1	X	X	Minerals	X
D11-12A	X	X	Minerals	--
D11-13	X	X	Minerals	--
D13-2-1	X	X	Minerals	X
D13-5	X	X	--	--
D13-6B	X	X	--	X
D13-15	X	X	--	--
D14-9-1	X	X	Minerals	X?
D14-10-1	X	X	Minerals	X?
D14-11-3	X	X	--	--
D15-3	X	X	--	--
D15-7-1	X	X	--	--
D15-9-1	X	X	Minerals	--
D15-18	X	X	--	--
D16-3-1	X	X	--	X
D16-8-1A	X	X	Glass, minerals	X?
D18-8-1	X	X	Minerals	--
D18-10-1	X	X	--	--
D19-20-1	X	X	--	--
D21-1-2	X	X	Minerals	X?
D22-5-1	X	X	--	X?
D22-7-1	--	--	Glass	--
D22-9-1	--	--	Glass	--
D24-6-1	X	X	Minerals	X?

Whole rock (WR) chemistry by X ray fluorescence (XRF); rare earth element (REE) chemistry by induction-coupled plasma mass spectrometry (ICP-MS)

Table 9. X-ray diffraction mineralogy of substrate rocks from cruise F11-90-CP

Sample	Major[1]	Moderate	Minor/Trace	Rock/Sediment
D1-4B-1	CFA[2]	--	--	Phosphorite breccia
D1-6	CFA, Phillipsite	--	Smectite	Phosphatized altered hyaloclastite
D2-1A	CFA	--	--	Phosphorite: replaced bioclastic limestone
D2-2	Plagioclase, pyroxene	--	Magnetite	Basanite
D2-4	Phillipsite	K-feldspar, magnetite	Quartz, smectite	Siltstone
D2-5A	CFA	--	Calcite	Phosphorite: replaced foraminiferal limestone
D2-6	Calcite	--	--	Bioclastic limestone
D3-1-1A	Phillipsite	K-feldspar, halite	Quartz, smectite	Pale brown mudstone
D3-1-1B	K-feldspar	Smectite, halite	quartz?	Grey mudstone
D3-1-2	CFA	K-feldspar, phillipsite	Quartz, calcite?	Pale yellow phosphatized siltstone
D3-1-3	CFA	--	K-feldspar	Pale brown phosphorite: replaced siltstone
D3-1-4	CFA	K-feldspar, phillipsite	Quartz	Pale brown phosphatized siltstone
D3-2-1A	Phillipsite, CFA	K-feldspar	Magnetite	Phosphatized mudstone
D3-3-2	Pyroxene	Magnetite, plagioclase	X-ray amorphous	Grey basanite
D3-4-1A	Phillipsite	Smectite, plagioclase	Calcite?	Siltstone
D3-5	Phillipsite	Calcite, plagioclase	Smectite	Volcaniclastic-bioclastic pebbly sandstone, phillipsite cemented
D3-6	Calcite	--	CFA?	Bioclastic foraminiferal limestone
D3-8-1A	Calcite	--	Phillipsite	Calcite & phillipsite cement from breccia
D4-1B	Plagioclase, pyroxene	--	Smectite	Tholeiitic basalt
D4-1D	Plagioclase, pyroxene	K-feldspar, smectite	--	Altered glassy rind on basalt
D4-2A	Pyroxene, plagioclase	Calcite, phillipsite	Smectite	Volcaniclastic-bioclastic pebbly siltstone
D4-2B	Phillipsite, plagioclase	Quartz, smectite, calcite	Pyroxene	Greenish-brown layer in siltstone
D4-2C	Pyroxene, phillipsite	Plagioclase	Smectite	Basalt pebble from siltstone
D4-2D	Pyroxene	--	--	Black crystals in siltstone
D5-1-1	Aragonite	Mg-calcite	--	Bioclastic reefal limestone
D6-1A	Smectite, plagioclase	Pyroxene	K-feldspar, halite	Altered tuff matrix of breccia
D6-1B	Plagioclase	Pyroxene	Smectite	Tholeiitic basalt clast in breccia
D6-3A	Smectite, plagioclase	Pyroxene	Calcite, phillipsite?	Altered waxy reworked tuff
D6-6-1	Plagioclase	Pyroxene	Smectite	Basalt with parallel wavy fracture
D6-7-1	Plagioclase, pyroxene	--	Smectite	Tholeiitic basalt
D6-7-2	Plagioclase, pyroxene	--	Smectite	Tholeiitic basalt
D6-8-1	Plagioclase, pyroxene	--	Smectite	Green-brown tholeiitic basalt
D6-10-2A	Phillipsite, K-feldspar	Smectite	--	Bioturbated, mottled mudstone: pale brown mottle
D6-10-2B	Plagioclase, pyroxene	Smectite	--	Same as 2A: dark brown mottle
D6-10-2C	Plagioclase	Smectite, halite	Phillipsite	Same as 2A: red-brown mottle
D6-10-2D	Phillipsite	Smectite	--	Same as 2A: drusy vug fill
D6-11-1	Plagioclase, pyroxene	--	Smectite	Vesicular tholeiitic basalt
D6-12	Calcite	--	Plagioclase	Foraminiferal-nannofossil ooze
D7-1	Serpentine	Plagioclase, chlorite, magnetite	Quartz, smectite, marcasite?, calcite	Grey-blue-green pebbly serpentine mud
D7-4	Serpentine	Magnetite	--	Serpentinite
D7-5A	Quartz, plagioclase	--	Chlorite	Milky vein quartz
D7-5B	Quartz, plagioclase	--	--	Translucent vein quartz
D7-6-1	Plagioclase	Quartz, amphibole	Chlorite	Altered metagabbro
D7-8-1	Serpentine	Magnetite	--	Serpentinite
D7-8-2	Serpentine	--	Magnetite	Serpentinite

D7-8-3	Serpentine	--	--	Serpentinite
D7-8-4	Epidote	Quartz, calcite, plagioclase	Chlorite, analcite	Epidosite, cataclastic, quartz & chlorite veins
D7-8-5	Plagioclase, quartz	Amphibole	Chlorite	Greenschist
D7-8-6	Pyroxene	Chlorite	--	Lavender vein fill
D7-8-7	Chlorite or Chlorite-serpentine mixed layer	Pyroxene, garnet	--	Vein fill in serpentinite
D7-11-1	Pyroxene	Plagioclase, smectite	--	Dark grey alkalic basalt
D7-12	Plagioclase, pyroxene	Amphibole	Smectite	Alkalic basalt
D7-13	Serpentine, magnetite	--	--	Layered serpentinite-magnetite
D7-14	Smectite, plagioclase	Quartz, amphibole	Analcite	Green-brown reworked tuff
D8-2A	Plagioclase	Quartz, calcite, serpentine	Smectite	Grey mud
D8-4-1	Smectite	Analcite, quartz	--	Greenish-brown breccia
D8-5	Plagioclase, pyroxene	Analcite	Amphibole, chlorite, smectite	Cataclastic rock
D8-6	Smectite, Pyroxene	Plagioclase, quartz	Chlorite, analcite	Metagreywacke
D8-7-1	Plagioclase, quartz	--	Chlorite	Vein quartz
D8-8A	Calcite	--	Plagioclase, quartz, analcite	Pebbly (basalt & quartz) clastic limestone
D8-11-1	Mica	Pyroxene, magnetite, plagioclase, amphibole, smectite	Chlorite	Dark grey tholeiitic metadiabase
D8-11-2	Pyroxene, plagioclase	Magnetite, mica, smectite	Chlorite	Medium grey tholeiitic metadiabase
D8-11-3	Pyroxene	Plagioclase, Chlorite, magnetite	Smectite, quartz, amphibole, analcite	Pale grey tholeiitic metadiabase
D8-12-1	Plagioclase	Quartz, pyroxene, chlorite, hematite	Analcite, amphibole, smectite, calcite	Hydrothermally altered siltstone
D8-13	Plagioclase	Pyroxene, magnetite, mica, Chlorite	smectite, analcite	Altered vesicular diabase
D8-14-1	Plagioclase	Quartz, calcite, chlorite	Smectite	Amygdaloidal basaltic andesite
D8-16-1	Plagioclase	Amphibole	Smectite	Pale green mudstone
D8-16-2	Plagioclase	Quartz, calcite	Analcite, chlorite, amphibole	Reddish-brown laminated mudstone-siltstone
D8-16-3	Plagioclase	Pyroxene, Quartz, calcite, smectite	Amphibole, chlorite	Grey siltstone
D9-1A	Calcite	--	Smectite, halite	Cement in breccia
D9-4-1	Plagioclase	Quartz, magnetite, smectite	Celadonite, hematite, amphibole, calcite, CFA?	Hydrothermally altered breccia
D9-5A	Plagioclase, pyroxene	Mordenite	Heulandite	Brown amygdaloidal alkalic basalt
D9-5B	Mordenite	--	Heulandite	Vesicle fill in basalt
D9-6B	Plagioclase, quartz, calcite	Magnetite	Smectite	Vesicle fill in basalt
D9-7-1	Pyroxene, plagiocase	Smectite	--	Pebbly volcaniclastic sandstone
D9-11	Aragonite	Calcite	--	*Halimeda* clastic limestone
D9-12	Calcite	Aragonite	--	Clastic limestone
D10-2A	Amphibole, prehnite	pyroxene, plagioclase, serpentine, chlorite	--	Amphibolite clast from clastic limestone
D10-2B	Calcite	Amphibole	Plagioclase, K-feldspar, serpentine	Pebbly clastic limestone
D10-3	Calcite	--	Amphibole	Recrystallize coral fragments
D10-5	Calcite, goethite	--	--	silt in worm tube
D11-3A	Smectite, calcite	--	--	Waxy clay on shear planes in breccia
D11-3B	Phillipsite, calcite	Pyroxene	Smectite, plagioclase	Calcareous sandstone, phillipsite cement

D11-6-1	Plagioclase, smectite	Pyroxene, quartz	phillipsite?	Altered andesite
D11-7-1A	Serpentine	--	--	Serpentinite (was basalt?)
D11-7-1B	Serpentine	--	--	Serpentinite (was glass rind)
D11-8-1	Serpentine	Plagioclase, pyroxene	Epidote?	Serpentinite (was basalt)
D11-11	Serpentine	Magnetite	Hematite	Serpentinite, dark brown (was basalt?)
D11-12-1A	Amphibole, pyroxene, plagioclase	--	Serpentine?, magnetite? chlorite?	Altered metadiabase or metagabbro
D11-12-1B	Amphibole, pyroxene	Plagioclase, chlorite	Serpentine?, magnetite	Red oxidized margin of metadiabase
D11-13-1	Pyroxene, plagioclase	Magnetite, serpentine	Chlorite	Grey-blue metagabbro, aligned minerals
D11-13-2A	Chlorite	--	Serpentine, pyroxene	Outer green-white rim of 13-1
D11-13-2B	Pyroxene, plagioclase	Magnetite, chlorite	Serpentine	adjacent to 13-2A, reddish rim
D11-13-2C	Pyroxene, plagioclase	Magnetite, serpentine	Chlorite	Grey-blue igneous rock, aligned minerals, adjacent to 13-2B
D11-14-1	Phillipsite, pyroxene	plagioclase, calcite	smectite, magnetite, chlorite	Pebbly limestone
D11-15	Plagioclase, calcite	Chlorite, quartz	--	Altered diorite?
D11-18	Vesuvianite	Chlorite, garnet	Serpentine	Skarn
D11-19	Plagioclase	Pyroxene, Serpentine	Smectite, magnetite	Cataclastite
D11-20	Calcite	Amphibole, halite	--	Sandy, micrite limestone
D11-21	Serpentine	--	Calcite, halite	Fracture fill in basalt
D11-22	Serpentine, prehnite	Chlorite, quartz, plagioclase, amphibole	Magnetite, pumpellyite?, halite?	Serpentinized greenschist
D11-26	Serpentine	--	Magnetite, goethite, ?, maghemite?	Serpentinite (was basalt?)
D11-27-2	Pyroxene, serpentine	--	Smectite	Serpentinized gabbro
D13-2-1	Pyroxene, plagioclase	--	Smectite, analcite, calcite	Alkalic gabbro
D13-7-1	Plagioclase, pyroxene	--	Olivine, magnetite?	Alkalic basalt
D13-15A	Plagioclase, pyroxene	--	Magnetite, smectite	Altered basalt, parallel fractures
D14-3-1	Calcite	Quartz	--	Bioclastic limestone breccia
D14-7-1	Plagioclase	Calcite, smectite, mordenite, anatase	Analcite, pyroxene, hematite	Reworked tuff
D14-10-1	Pyroxene, plagioclase	Smectite	Laumonite? or talc?	Tholeiitic basalt
D14-12	Plagioclase	Pyroxene, amphibole	--	Volcaniclastic breccia
D14-13-1	Phillipsite	Smectite, analcite	Plagioclase	Brown volcaniclastic breccia
D14-14-1	Plagioclase	Pyroxene, quartz, smectite	Magnetite	Hydrothermally altered vesicular tholeiitic basalt
D15-3	Pyroxene, plagioclase	--	Smectite	Tholeiitic pillow basalt
D15-4	Smectite, pyroxene	Plagioclase	--	Tholeiitic pillow basalt
D15-5	Plagioclase, pyroxene	Smectite, calcite	Magnetite	Tholeiitic pillow basalt
D15-7-1	Plagioclase, pyroxene	Smectite	Magnetite, wairakite?	Tholeiitic pillow basalt
D15-8	Smectite, plagioclase, pyroxene	--	Magnetite	Basalt
D15-9-1	Plagioclase, pyroxene	Smectite	Magnetite	Basalt
D15-9-2	Plagioclase, pyroxene	Smectite	Magnetite, calcite	Basalt
D15-10-1	Pyroxene, plagioclase	--	Magnetite	Tholeiitic basalt
D15-15-1	Garnet[4]	Smectite, calcite	--	Yellow-green calcareous mudstone-siltstone gradational to grey limestone; skarn deposit
D15-15-2	Calcite	--	K-feldspar, smectite	Red-brown limestone adjacent to grey limestone
D16-2-1B	Pyroxene, plagioclase	--	Smectite, magnetite	Basalt
D16-3-1	Pyroxene, plagioclase	--	Magnetite	Tholeiitic basalt
D16-7-1	Pyroxene, plagioclase	--	Smectite	Tholeiitic basalt
D16-8-1C	Calcite, phillipsite	--	--	Glassy rind on basalt
D16-9-1	Plagioclase, pyroxene	--	Magnetite, smectite	Tholeiitic basalt

D16-12-1	Phillipsite, calcite	--	Smectite, plagioclase?	Greenish-brown calcareous sandstone
D16-12-2	Calcite	Phillipsite, smectite	Analcite	Olive-green burrow infilling
D16-12-3	Calcite, phillipsite	--	Smectite, analcite	Yellowish burrow infilling
D16-12-4	Calcite, smectite	--	--	Dark green calcareous mudstone
D16-12-5	Phillipsite	Calcite, smectite	Analcite	Bedded, yellow-brown, calcareous sandstone-siltstone
D16-13-1	Calcite	--	Phillipsite	Pale brown, bioturbated limestone
D17-2	Plagioclase, quartz	Chlorite	Ilmenite? pumpellyite?	Greenschist (was basalt?)
D18-5-1	Plagioclase, pyroxene	Chlorite, amphibole, epidote	Hematite	Grey-green metadiabase
D18-6-1	Plagioclase	Amphibole, pyroxene, chlorite	--	Metabasalt
D18-7-1	Chlorite, plagioclase	Pyroxene, amphibole	Magnetite, epidote?	Metadiabase
D18-8-1	Pyroxene, plagioclase	Chlorite, amphibole	Magnetite, calcite	Metadiabase
D18-9-1	Plagioclase, pyroxene	Chlorite, amphibole	Epidote, magnetite	Pale green metabasalt
D18-10-1	Pyroxene, plagioclase	Chlorite, amphibole	Magnetite, calcite	Alkalic metabasalt
D18-11A	Chlorite, epidote	Amphibole, pyroxene, pyrite	Smectite, heulandite?	Greenschist, sheared
D18-13A	Pyroxene	Plagioclase, quartz, chlorite, epidote	Prehnite	Whitish-pale green metabasalt
D19-20-1	Pyroxene, plagioclase	--	Smectite, phillipsite	Brown vesicular alkalic pillow basalt
D21-1-2	Plagioclase, pyroxene	--	Olivine, phillipsite	Dark brown vesicular alkalic basalt
D22-1	Calcite	--	Plagioclase	White sandy & pebbly limestone
D22-3	Calcite	--	--	Massive white limestone
D22-5-1	Plagioclase, pyroxene	--	Ilmenite, smectite	Brown vesicular alkalic basalt
D22-7-1	Phillipsite	Smectite, plagioclase	Anatase?	Hyaloclastite breccia
D22-9-1	Calcite, plagioclase	Pyroxene	Smectite	Volcaniclastic-bioclastic sandstone
D22-10-1	Calcite	--	Halite, plagioclase	White pebbly & sandy limestone
D23-2A	Calcite	--	Smectite, plagioclase	White bedded limestone
D23-2B	Calcite	--	Smectite, plagioclase	Pale brown limestone
D24-1	Calcite	--	--	Clastic limestone
D24-3-1	Plagioclase, pyroxene	Quartz	Smectite	Brown, altered basalt?
D24-5-1	CFA, smectite	Hematite	--	Red, altered basalt?
D24-6-6	Plagioclase, pyroxene	--	Smectite, magnetite	Grey alkalic basalt

[1]Major: > 25%, Moderate: > 5% to < 25 %, Minor: < 5 %
[2]CFA is Carbonate Fluorapatite
[3]All breccias are sedimentary, and most are volcaniclastic
[4]Garnet is probably andradite, but maybe goldmanite or uvarovite

Table 10. Chemical composition in weight percent of substrate rocks, except Au and PGEs in ppb; PGEs are listed separately at end of table

	D1-4B-1	D1-6	D2-1A	D2-2	D2-4	D2-5A	D3-2-1A	D3-3-2	D3-4-1A	D3-5	D3-6	D4-1B	D4-2A
SiO_2	6.20	33.4	3.25	36.4	47.5	1.06	34.1	36.9	45.1	27.3	0.64	45.6	34.8
Al_2O_3	1.94	10.8	1.15	18.6	15.3	0.28	11.8	15.2	13.5	9.74	0.24	16.0	8.41
FeO	< 0.01	< 0.01	< 0.01	3.3	-	< 0.01	0.28	4.3	< 0.01	0.56	< 0.01	3.2	-
Fe_2O_3	1.40	8.56	0.92	11.2	10.1	0.69	10.0	9.52	15.2	7.91	0.17	6.94	9.55
MgO	0.70	2.10	0.65	3.53	1.54	0.60	1.36	5.07	3.02	1.39	0.72	6.31	3.35
CaO	48.2	16.3	49.6	9.03	1.79	50.9	14.3	11.2	3.11	21.2	55.3	13.4	14.5
Na_2O	0.87	1.91	0.84	2.15	3.05	0.65	2.64	1.37	3.74	2.11	< 0.15	2.35	2.80
K_2O	0.36	2.16	< 0.02	0.73	6.31	< 0.02	3.84	0.94	1.80	2.18	< 0.02	0.41	1.34
TiO_2	0.26	1.56	0.08	4.86	3.43	0.03	3.13	4.62	2.75	2.29	< 0.02	1.59	1.88
P_2O_5	28.1	8.30	27.3	1.80	0.88	28.0	8.59	2.04	0.20	0.69	0.63	0.31	0.37
MnO	0.06	0.05	0.23	0.18	0.67	0.06	0.15	0.22	0.83	0.07	< 0.02	0.12	0.57
LOI 925°C	8.57	13.6	11.6	7.53	8.92	13.8	8.82	8.08	10.2	24.1	43.1	3.45	22.0
Total	96.7	98.7	95.6	99.3	99.5	96.1	99.0	99.5	99.5	99.5	100.8	99.7	99.6
H_2O^+	1.9	6.1	1.6	4.4	3.7	1.9	4.2	5.1	5.6	4.4	0.20	0.55	4.9
H_2O^-	1.3	6.7	1.4	5.3	6.3	1.2	4.8	5.7	7.6	5.1	0.44	2.4	7.6
CO_2	6.3	3.4	8.5	0.13	0.09	6.1	1.3	0.14	0.03	16.0	42.3	0.94	9.8
Au	-	-	-	-	-	-	-	-	-	-	-	-	-
Rock Type	Phosphorite breccia	Phosphatized altered hyaloclastite	Phosphorite (replaced limestone)	Basanite	Siltstone	Phosphorite (replaced limestone)	Phosphatized mudstone	Basanite	Siltstone	Bioclastic-volcaniclastic sandstone	Bioclastic foraminiferal limestone	Tholeiitic basalt	Volcaniclastic -bioclastic siltstone

	D6-1A	D6-1B	D6-3A	D6-6-1	D6-7-1	D6-7-2	D6-8-1	D6-11-1	D7-4	D7-5A	D7-5B	D7-6-1	D7-8-1
SiO_2	45.3	48.1	45.8	48.5	47.3	48.8	48.8	48.9	39.1	78.5	76.0	61.6	39.6
Al_2O_3	14.1	17.7	14.9	17.4	16.3	16.6	17.5	16.6	0.69	10.9	12.6	9.40	0.68
FeO	< 0.01	5.2	0.16	5.0	5.6	5.9	5.7	6.1	1.3	0.24	0.48	5.5	1.3
Fe_2O_3	11.0	7.62	11.0	7.54	6.98	6.94	6.67	6.52	6.81	0.79	0.60	1.32	6.13
MgO	3.46	3.43	3.61	3.36	4.15	4.28	3.71	4.59	37.9	0.88	1.49	8.52	38.2
CaO	1.58	8.34	2.45	7.78	10.9	9.67	8.72	9.27	0.23	1.44	1.45	7.38	0.08
Na_2O	3.39	2.60	2.51	2.68	2.50	2.64	2.66	2.61	0.30	4.94	5.07	3.28	0.35
K_2O	2.47	0.67	1.98	0.66	0.46	0.47	0.46	0.63	< 0.02	0.16	0.36	0.10	< 0.02
TiO_2	0.75	1.05	0.69	1.03	0.93	0.95	1.04	0.93	0.04	0.37	0.32	0.45	< 0.02
P_2O_5	0.05	0.15	0.06	0.11	1.12	0.24	0.38	0.13	< 0.05	0.07	0.08	0.08	< 0.05
MnO	0.31	0.18	<0.02	0.16	0.18	0.17	0.16	0.18	0.08	< 0.02	< 0.02	0.19	0.07
LOI 925°C	17.4	4.92	16.2	5.51	3.37	2.72	4.08	3.10	13.1	0.79	1.11	1.24	13.3
Total	99.8	100.0	98.4	99.7	99.8	99.4	99.9	99.6	99.6	99.1	99.6	99.1	99.7
H_2O^+	6.3	2.6	9.2	2.3	2.8	1.2	1.6	1.6	11.9	0.18	0.50	1.3	11.9
H_2O^-	11.8	4.1	10.0	4.9	1.6	2.9	3.9	3.1	2.0	0.71	0.74	0.69	2.1
CO_2	0.10	0.01	0.44	0.04	0.14	0.02	0.04	0.01	0.03	0.02	< 0.01	< 0.01	< 0.01
Au	-	-	-	-	-	-	-	-	N 2	N 2	N 2	N 2	N 2
Rock Type	Altered tuff matrix of breccia	Tholeiitic basalt clast in breccia	Altered tuff waxy, reworked	Tholeiitic basalt, wavy fracture	Tholeiitic basalt	Tholeiitic basalt	Tholeiitic basalt	Vesicular tholeiitic basalt	Serpentinite	Milky vein quartz	Translucent vein quartz	Altered metagabbro	Serpentinite

Table 10. Continued

	D7-8-3	D7-8-5	D7-11-1	D7-12	D7-13	D7-14	D8-4-1	D8-5	D8-7-1	D8-11-1	D8-11-2	D8-11-3	D8-12-1
SiO_2	32.4	55.5	43.6	47.7	37.9	50.9	48.9	53.9	76.2	34.9	38.7	50.3	57.9
Al_2O_3	13.5	12.4	15.6	16.8	1.97	11.5	11.0	12.8	11.7	9.56	11.4	12.4	13.3
FeO	3.6	5.6	4.3	3.2	1.4	2.0	1.0	4.0	0.48	11.7	10.7	6.8	3.7
Fe_2O_3	2.23	3.88	7.52	6.23	8.84	7.98	8.61	2.28	0.78	11.3	9.41	2.94	4.58
MgO	32.2	6.71	9.15	6.05	34.8	9.94	10.1	8.09	1.85	11.3	8.83	10.2	3.94
CaO	1.12	9.80	6.96	8.31	1.40	3.50	2.97	8.71	1.48	6.82	7.18	9.44	4.65
Na_2O	0.31	2.40	2.56	4.25	0.37	2.93	4.06	4.97	4.68	1.99	2.90	1.63	5.36
K_2O	< 0.02	0.21	1.23	0.87	0.03	2.06	1.04	0.86	0.30	0.75	0.67	2.40	0.36
TiO_2	0.18	0.54	1.51	1.85	0.12	0.44	0.39	0.33	0.33	6.03	5.44	0.39	0.58
P_2O_5	< 0.05	0.16	0.24	0.47	< 0.05	0.11	0.14	0.08	0.08	0.49	0.71	0.08	0.13
MnO	0.42	0.20	0.22	0.18	0.22	0.10	0.09	0.13	< 0.02	0.27	0.26	0.16	0.17
LOI 925°C	13.9	2.03	6.62	3.62	12.5	7.94	11.1	3.49	1.34	3.75	2.85	2.73	4.51
Total	99.9	99.4	99.5	99.5	99.6	99.4	99.4	99.6	99.2	98.9	99.1	99.5	99.2
H_2O^+	12.3	1.7	3.8	1.9	11.9	4.1	6.1	2.5	0.98	3.4	2.9	2.5	2.5
H_2O^-	1.6	1.1	4.7	2.2	2.0	6.2	7.4	1.3	0.48	2.1	1.6	1.0	1.9
CO_2	0.62	0.01	< 0.01	0.32	< 0.01	< 0.01	0.01	< 0.01	0.02	0.02	0.01	<0.01	0.88
Au	< 2	-	-	-	-	-	-	6	N 2	< 2	< 2	2	3
Rock Type	Serpentinite	Greenschist	Dark grey alkalic basalt	Alkalic basalt	Layered serpentinite-magnetite	Reworked tuff	Greenish-brown breccia	Cataclastic rock	Vein quartz	Dark grey tholeiitic metadiabase	Med. grey tholeiitic metadiabase	Pale grey tholeiitic metadiabase	Hydrotherm-ally altered siltstone

	D8-14-1	D9-4-1	D9-5A	D10-2A	D11-2B	D11-6-1	D11-7-1A	D11-8-1	D11-11	D11-12-1A	D11-13	D11-18	D11-22
SiO_2	51.7	57.6	45.2	46.1	39.3	52.3	39.9	41.4	39.4	46.8	46.9	34.9	40.3
Al_2O_3	13.6	13.6	14.1	15.9	6.86	15.5	0.88	1.51	0.56	12.0	16.5	14.7	7.91
FeO	5.0	2.4	3.2	4.6	-	2.4	0.84	1.3	0.68	5.0	3.2	1.8	2.8
Fe_2O_3	3.38	6.31	7.14	2.26	8.45	5.22	6.65	7.77	7.08	1.81	1.12	1.99	5.61
MgO	3.34	3.48	3.08	12.5	20.7	7.85	35.5	32.7	38.1	16.7	13.5	21.5	26.3
CaO	7.77	7.19	12.8	15.4	3.45	10.0	0.52	1.87	0.18	12.9	16.2	15.1	5.52
Na_2O	3.93	2.95	2.72	1.17	2.00	2.36	0.42	0.47	0.34	0.96	0.76	< 0.15	0.33
K_2O	1.15	1.22	1.41	0.03	0.74	0.28	< 0.02	0.04	< 0.02	0.09	0.08	< 0.02	0.04
TiO_2	0.49	0.64	0.76	0.20	0.25	0.51	< 0.02	0.05	< 0.02	0.28	0.1	0.23	0.06
P_2O_5	0.09	1.15	3.85	< 0.05	0.06	0.05	< 0.05	< 0.05	< 0.05	< 0.05	< 0.05	0.15	< 0.05
MnO	0.12	0.15	0.14	0.12	5.57	0.09	0.09	0.14	0.15	0.12	0.09	0.26	0.12
LOI 925°C	8.39	2.80	4.85	0.80	11.2	3.41	14.5	12.2	13.1	2.12	2.05	8.91	10.5
Total	99.0	99.5	99.3	99.1	98.6	100.0	99.3	99.5	99.6	98.8	100.5	99.5	99.5
H_2O^+	2.5	1.8	2.0	1.2	8.9	1.5	13.5	9.8	13.2	2.3	1.8	8.7	11.1
H_2O^-	1.1	1.4	3.4	0.71	3.7	2.6	3.0	2.6	1.9	0.57	0.51	1.0	1.4
CO_2	5.4	0.17	0.58	< 0.01	< 0.01	0.01	0.05	0.57	< 0.01	0.12	0.02	0.28	0.05
Au	-	< 2	-	-	-	< 2	< 2	< 2	-	< 2	< 2	< 2	< 2
Rock Type	Amygdaloidal basaltic andesite	Hydrotherm-ally altered breccia	Altered brown amygdaloidal alkalic basalt	Amphibolite cobble from limestone	Manganifer-ous sandstone	Andesite	Serpentinite	Serpentinite	Serpentinite	Altered metadiabase	Grey-blue metagabbro	Tactite (skarn)	Serpentin-ized greenschist

Table 10. Continued

	D11-26	D13-2-1	D13-7-1	D14-10-1	D14-14-1	D15-3	D15-4	D15-5	D15-7-1	D15-10-1	D15-18	D16-3-1	D16-7-1
SiO_2	36.8	47.9	48.1	48.1	49.4	47.3	46.9	44.7	47.8	48.8	47.4	48.6	47.7
Al_2O_3	0.54	17.3	17.8	13.7	12.5	15.1	13.8	13.6	13.5	15.7	14.0	14.8	14.9
FeO	0.6	5.0	2.6	7.4	3.2	6.3	5.2	4.7	7.0	6.7	5.2	8.0	5.5
Fe_2O_3	11.23	4.07	7.09	6.28	12.24	4.40	7.32	5.98	6.22	3.75	6.62	3.80	6.89
MgO	35.2	7.23	4.83	6.80	5.88	7.33	7.38	6.70	6.71	6.87	7.53	6.32	5.48
CaO	1.04	8.77	8.99	10.7	6.32	12.6	11.1	14.9	10.8	12.6	11.8	12.2	12.4
Na_2O	0.35	3.47	3.89	2.84	3.34	2.41	2.94	2.68	3.08	2.38	2.89	2.53	2.57
K_2O	< 0.02	0.83	1.04	0.15	0.31	0.08	0.12	0.12	0.31	0.08	0.12	0.09	0.33
TiO_2	0.02	1.63	1.72	1.82	2.51	1.57	1.64	1.56	2.39	1.46	1.58	1.81	1.89
P_2O_5	< 0.05	0.26	0.34	0.21	0.30	0.14	0.17	0.16	0.24	0.13	0.16	0.16	0.18
MnO	0.15	0.15	0.13	0.23	0.14	0.17	0.13	0.16	0.19	0.17	0.14	0.17	0.17
LOI 925°C	13.7	2.76	2.84	3.74	1.5	2.36	3.3	4.54	1.47	1.23	2.67	1.01	1.83
Total	99.6	99.4	99.4	102.0	97.6	99.8	100.0	99.8	99.7	99.9	100.1	99.5	99.8
H_2O^+	12.5	2.0	1.2	0.75	1.8	0.90	1.1	0.89	0.93	0.93	0.14	0.54	0.19
H_2O^-	1.6	1.5	2.5	1.4	2.9	2.4	2.6	1.4	1.5	1.2	3.0	2.1	2.4
CO_2	0.74	0.08	< 0.01	< 0.01	0.01	0.01	0.19	2.8	< 0.01	< 0.01	0.21	0.01	0.02
Au	< 2	-	-	-	-	-	-	-	-	-	-	-	-
Rock Type	Serpentinite	Alkalic gabbro	Vesicular alkalic basalt	Tholeiitic basalt	Vesicular tholeiitic basalt	Tholeiitic pillow basalt	Tholeiitic pillow basalt	Tholeiitic pillow basalt	Pillow basalt	Tholeiitic basalt	Greenish-grey altered basalt	Tholeiitic basalt	Tholeiitic basalt

	D16-8-1B	D16-9-1	D17-2	D18-5-1	D18-6-1	D18-7-1	D18-8-1	D18-9-1	D18-10-1	D18-13-A	D19-20-1	D21-1-2	D22-5-1
SiO_2	47.9	48.5	50.5	49.6	48.2	47.7	46.4	47.5	48.0	45.9	45.9	45.8	48.1
Al_2O_3	15.0	14.5	13.9	13.2	14.1	13.9	14.5	14.3	13.9	15.6	16.9	17.9	19.0
FeO	5.5	4.4	6.8	7.6	9.6	10.4	8.2	8.7	8.9	7.0	2.4	3.1	3.2
Fe_2O_3	6.79	6.81	2.74	2.95	2.23	2.14	3.69	2.73	3.01	4.22	7.43	5.31	6.33
MgO	5.37	6.53	6.77	7.23	8.79	7.58	7.27	9.29	7.92	6.84	4.76	4.50	3.14
CaO	12.3	12.5	9.99	11.9	9.08	9.97	11.8	8.89	12.1	14.3	10.4	9.25	9.27
Na_2O	2.66	2.59	4.11	3.25	2.78	2.93	2.72	3.14	2.29	1.48	3.15	3.56	3.96
K_2O	0.31	0.38	0.03	0.04	0.06	0.23	0.26	0.10	0.09	< 0.02	0.99	1.50	1.28
TiO_2	1.90	1.65	1.43	1.31	1.21	1.69	1.38	1.21	1.15	1.22	1.96	2.27	2.17
P_2O_5	0.18	0.17	0.14	0.15	0.11	0.08	0.11	0.14	0.11	0.11	1.29	1.09	0.57
MnO	0.16	0.14	0.16	0.25	0.27	0.26	0.29	0.21	0.26	0.17	0.13	0.11	0.14
LOI 925°C	1.81	2.05	3.05	2.06	2.61	2.49	2.49	3.35	1.84	2.86	4.40	5.11	2.75
Total	99.9	100.2	99.6	99.5	99.0	99.4	99.1	99.6	99.6	99.7	99.7	99.5	99.9
H_2O^+	0.44	0.19	2.7	2.2	3.1	3.0	2.2	3.3	2.0	2.7	1.7	2.1	1.3
H_2O^-	2.1	2.0	0.99	0.59	0.55	0.42	0.36	0.97	0.80	0.82	3.0	3.4	1.9
CO_2	0.09	0.30	< 0.01	0.01	0.01	0.04	0.90	0.02	0.03	< 0.01	0.12	0.07	0.04
Au	-	-	-	-	-	-	-	-	-	-	-	-	-
Rock Type	Tholeiitic pillow basalt	Tholeiitic basalt	Greenschist	Grey-green metadiabase	Metabasalt	Metadiabase	Metagabbro	Pale green metabasalt	Alkalic metabasalt	Whitish-pale green metabasalt	Alkalic pillow basalt	Vesicular alkalic basalt	Vesicular alkalic basalt

Table 10. Continued

	D22-7-1	D24-6-1
SiO_2	41.4	45.7
Al_2O_3	14.8	15.7
FeO	1.6	2.9
Fe_2O_3	7.88	9.08
MgO	4.31	5.88
CaO	2.40	10.4
Na_2O	3.19	2.73
K_2O	2.52	1.09
TiO_2	2.05	3.01
P_2O_5	0.16	0.56
MnO	0.16	0.17
LOI 925°C	19.4	2.82
Total	99.9	100.0
H_2O^+	5.5	1.9
H_2O^-	14.2	1.4
CO_2	0.02	0.02
Au	-	-
Rock Type	Hyaloclastite breccia	Alkalic basalt

PGEs	D7-4	D7-5A	D7-5B	D7-6-1	D7-8-1	D7-8-3	D8-5	D8-7-1	D8-11-1	D8-11-2	D8-11-3	D9-4-1
Pt	7.2	<0.5	<0.5	9.1	7.6	6.6	3.9	<0.5	1.6	0.5	7.9	2.3
Pd	2.0	<0.5	<0.5	17	3.7	2.8	4.4	<0.5	1.2	1.0	13	2.4
Rh	0.7	<0.5	<0.5	0.5	0.7	<0.5	<0.5	<0.5	<0.5	<0.5	<0.5	<0.5
Ru	6.0	<0.5	<0.5	<0.5	5.6	1.1	<0.5	<0.5	<0.5	<0.5	<0.5	<0.5
Ir	3.3	<0.5	<0.5	<0.5	3.9	<0.5	<0.5	<0.5	<0.5	<0.5	<0.5	<0.5

- Sample D11-27-1, a quartz vein, contains N 4 ppb Au
- Major oxides by X-ray fluorescence; LOI = Loss On Ignition at 925 °C
- Gold determined by Graphite-Furnace Atomic Absorption Spectroscopy
- PGEs determined by Inductively Coupled Plasma-Mass Spectrometry
- Analysts: J.E. Taggart, D.F. Siems, and B.H. Roushey, J.R. Gillison, M.G. Kavulak, C.A. Motooka, J.H. Bullock
- < indicates that the element was detected below the limit of quantitation
- N indicates that the concentration is below the limit of detection

Table 11 . X ray diffraction mineralogy of ferromanganese and manganese deposits from cruise F11-90-CP

Sample Number	Type & Interval (mm)[1]	δ-MnO_2 (%)[2]	Others (%)
D1-1-1A	Composite 8 bulk small nodules (<30 mm diameters)	98	<1-CFA, <1-quartz, <1-plagioclase
D1-1-1B	Composite 2 bulk large nodules (60 mm diameters)	95	5-CFA
D1-8A	Bulk crust (0-55)	100	--
D1-8B	Crust layer (0-15)	99	1-quartz
D1-8C	Crust layer (15-27)	98	2-plagioclase
D1-8D	Crust layer (27-34)	100	--
D1-8E	Crust layer (34-44)	98	2-goethite, <1-quartz
D1-8F	Crust layer (44-50)	98	2-goethite
D1-8G	Crust layer (50-55)	95	5-CFA
D1-9A	Crust surface (≤0.5)	99	≈1-calcite, <1-quartz
D1-9B	Bulk crust (0-40)	100	--
D2-1B	Bulk crust (0-12)	99	1-plagioclase, <1-quartz
D2-5B	Bulk crust (0-23)	93	6-calcite, 1-quartz
D2-7	Bulk crust (0-20)	97	2.5-K-feldspar, <1-quartz
D3-2-1B	Bulk crust (0-25)	99	1-quartz
D3-3-3	Bulk crust (0-18)	97	2-goethite, 1-quartz
D3-4-1B	Bulk fossil crust (0-20)	100	--
D4-1A	Bulk crust (0-8)	98	1.5-calcite, <1-quartz
D6-1C	Bulk crust (0-19)	95	3-plagioclase, 2-quartz
D6-3B	Bulk crust (0-17)	96	3-plagioclase, 1 quartz
D6-4A	Bulk crust (0-10)	94	3-plagioclase, 3-quartz
D6-5A	Bulk curst (0-33)	95	4-plagioclase, 1-quartz
D6-5B	Crust layer (0-18)	92	6-plagioclase, 2-quartz
D6-5C	Crust layer (18-33)	94	5-plagioclase, 1-quartz
D7-10A	Bulk crust (0-15)	96	3-calcite (contamination by infiltered sed.), 1-quartz
D11-2A	Bulk crust (0-10)	>99	<1-quartz
D11-2B	Bulk manganiferous sandstone	60	Birnessite, phillipsite, todorokite, plagioclase, pyroxene
D11-9-1	Bulk stratabound manganese	?	Todorokite, birnessite
D11-9-2	Porous stratabound manganese layer	?	Todorokite, plagioclase, pyroxene, halite
D11-9-3	Steel-grey, metallic stratabound manganese layer	0	100-pyrolusite
D11-9-4	Steel-grey stratabound manganese layer	0	Pyrolusite, todorokite, <1-amphibole?
D11-9-5	Botryoidal, steel-grey stratabound manganese layer	0?	Todorokite, pyrolusite
D11-9-6	Bulk stratabound manganese	?	Todorokite, birnessite
D11-9-7	Laminated, grey-brown stratabound manganese	?	Todorokite, birnessite

D11-9-9	Bulk, submetallic, manganese crust, 3 layers	?	Pyrolusite, todorokite
D11-9-10A	Crust in 9-9 (0-1)	?	Pyrolusite
D11-9-10B	Crust in 9-9 (1-6)	?	Pyrolusite, todorokite, plagioclase, pyroxene, rancieite?
D11-9-10C	Crust in 9-9 (6-17)	?	Todorokite, pyrolusite
D11-10A	Manganiferous breccia	48	15-serpentine, 15-phillipsite 15-plagioclase, 5-todorokite 2-calcite
D13-8A	Bulk crust (0-3)	100	--
D13-16B	Bulk crust (0-3)	99	1-quartz
D19-4-1	Bulk crust (0-32)	>98	1-plagioclase, <1-quartz
D19-6	Bulk crust (0-42)	>98	<1-plagioclase, <1-quartz
D19-13-1	Bulk, porous, brown, side crust (0-35)	>99	<1-quartz
D19-13-2	Bulk crust (0-32)	>99	<1-quartz
D19-19A	Layer (0-30)	100	--
D19-19B	Layer (30-52)	>98	1-plagioclase, <1-quartz
D19-19C	Bulk crust (0-53)	100	--
D21-1-1	Bulk crust (0-7)	98	1-plagioclase, 1-quartz
D22-6-1	Bulk crust (0-6)	98	1-plagioclase, 1-quartz

[1]Intervals measured from the outer surface of crusts and nodules

[2]Percentages were determined by using the following weighting factors relative to quartz set at 1: δ-MnO_2 75; todorokite 10; birnessite 12 (Hein et al., 1988); carbonate fluorapatite 3.1; plagioclase 2.8; calcite 1.65; smectite 3.0; goethite 7.0; phillipsite 17.0; illite 6.0; pyroxene 5.0; halite 2.0 (From Cook et al., 1975); the limit of detection for each mineral falls between 0.2 and 1.0%, except the manganese minerals which are greater, perhaps as much as 10% for δ-MnO_2; apatite always refers to carbonate fluorapatite

Table 12. Chemical composition of ferromanganese and manganese oxyhydroxide deposits in weight percent for major elements, ppm for minor elements, and ppb for gold and platinum group elements

	D1-1-1A[1]	D1-1-1B	D1-8A	D1-8B	D1-8C	D1-8D	D1-8E	D1-8F	D1-8G	D1-9A	D1-9B	D2-1B
Fe Wt %	14	12	16	15	16	18	22	20	13	16	16	17
Mn	16	13	17	18	15	19	15	19	19	21	15	18
Mn/Fe	1.1	1.1	1.1	1.2	0.9	1.1	0.7	1.0	1.5	1.3	0.9	1.1
Si	3.7	3.2	2.6	2.8	4.2	2.9	3.1	2.6	1.9	2.9	2.9	4.0
Na	1.3	1.2	1.3	1.3	1.4	1.4	1.3	1.3	1.3	1.8	1.3	1.4
Al	1.1	0.89	0.54	0.45	1.0	0.65	0.72	0.68	0.45	0.32	0.69	0.79
K	0.50	0.42	0.36	0.39	0.46	0.42	0.33	0.38	0.38	0.39	0.38	0.43
Mg	0.88	0.72	0.81	0.83	0.80	0.88	0.86	0.92	0.82	1.1	0.80	0.90
Ca	2.2	7.3	2.3	2.0	1.9	2.1	1.8	2.4	8.6	2.7	5.2	2.1
Ti	0.81	0.73	0.99	0.96	1.4	1.4	0.93	0.89	0.73	0.74	0.90	0.96
P	0.41	2.3	0.43	0.33	0.29	0.33	0.36	0.45	2.6	0.44	1.5	0.37
H_2O^+	7.4	6.6	7.9	8.0	7.7	9.0	9.3	8.1	7.3	4.6	7.5	8.0
H_2O^-	22.3	22.0	21.7	22.3	21.0	13.6	16.7	12.2	10.7	14.0	18.3	15.9
CO_2	0.43	1.1	0.45	0.48	0.35	0.43	0.37	0.44	1.4	0.97	0.86	0.52
LOI	35.6	33.0	35.0	35.6	33.3	27.9	30.2	26.9	24.5	30.2	31.4	29.6
Ni ppm	3500	3000	3200	3300	2700	3400	2700	3800	4100	3900	2800	3400
Cu	780	1000	690	420	720	1000	1100	1200	1000	250	830	1300
Zn	650	590	680	570	680	820	920	890	670	590	650	660
Co	3600	2400	3800	4900	3300	4700	2700	3400	2500	6300	3400	3600
Ba	1300	1600	1700	1300	1600	2100	2200	2200	1800	1000	1500	1600
Mo	310	270	430	430	270	420	460	510	460	370	340	390
Sr	1100	1200	1400	1400	1300	1600	1400	1600	1600	1400	1400	1400
Ce	560	690	700	690	710	860	570	850	1000	720	640	720
Y	160	220	150	160	130	130	120	130	320	180	290	130
V	480	460	610	570	490	650	790	530	580	670	560	600
Pb	1100	900	1200	1400	1200	1200	960	1200	1100	1400	960	1300
Cr	12	7.4	8.2	5.6	18	12	10	8.6	8.5	5.5	5.0	16
Cd	2.3	1.4	1.9	1.8	1.7	2.0	1.7	2.1	2.3	5.4	1.6	2.2
As	170	110	220	230	180	230	280	270	160	270	180	240
Au ppb	-	-	< 10	< 10	< 10	< 10	< 10	< 10	< 10	-	-	< 10
Pt	-	-	210	120	250	320	270	300	370	-	-	200
Pd	-	-	1	0.9	1	1	1	1	2	-	-	2.3
Rh	-	-	14	8.9	14	22	18	20	17	-	-	12
Ru	-	-	13	15	14	15	15	17	13	-	-	19
Ir	-	-	4.8	3.6	4.2	6.1	5.4	6.4	6.5	-	-	3.9
Interval[2]	B 8 small	B 2 large	B 0-55	L 0-15	L 15-27	L 27-34	L 34-44	L 44-50	L 50-55	S 0-0.5	B 0-40	B 0-12
Type	Nodules	Nodules	Crust	Crust	Crust	Crust	Crust	Crust	Crust	Crust	Crust	Crust

Table 12 Continued

	D2-5B	D2-7	D3-2-1B	D3-3-3	D3-4-1B	D4-1A	D6-1C	D6-3B	D6-4A	D6-5A	D6-5B	D6-5C
Fe Wt %	15	15	15	18	23	17	16	17	16	15	16	16
Mn	18	16	18	14	16	20	14	13	12	13	12	12
Mn/Fe	1.2	1.1	1.2	0.8	0.7	1.2	0.9	0.8	0.8	0.9	0.8	0.8
Si	3.6	4.2	3.1	3.8	3.9	2.7	6.5	5.6	9.4	7.5	7.5	9.4
Na	1.5	1.3	1.3	1.3	1.2	1.6	1.6	1.4	1.8	1.6	1.6	1.9
Al	0.70	1.1	0.52	0.97	1.0	0.45	1.8	1.5	2.7	2.2	2.2	2.8
K	0.44	0.48	0.38	0.38	0.39	0.35	0.54	0.47	0.62	0.70	0.55	0.90
Mg	0.85	0.90	0.80	0.78	0.91	0.99	0.90	0.82	1.0	0.91	0.89	1.1
Ca	2.1	1.7	2.0	2.1	1.9	3.1	2.2	1.9	2.6	2.0	2.2	2.0
Ti	0.94	1.3	0.77	0.61	1.5	0.89	0.66	0.79	0.65	0.85	0.77	1.3
P	0.31	0.30	0.30	0.46	0.36	0.37	0.34	0.32	0.33	0.29	0.31	0.24
H_2O^+	8.7	7.1	6.9	6.6	9.5	9.3	6.9	8.0	8.5	7.8	7.6	9.1
H_2O^-	19.1	21.2	24.6	22.6	10.9	13.7	18.2	19.9	10.2	17.7	16.3	9.3
CO_2	0.63	0.37	0.49	0.37	0.35	1.3	0.52	0.39	0.51	0.33	0.37	0.27
LOI	33.0	33.8	37.3	35.4	25.5	29.9	29.4	32.0	22.5	29.4	27.9	21.4
Ni ppm	3700	3700	3300	2600	2900	3500	2200	2000	1900	2300	2000	2300
Cu	590	700	620	1800	1600	620	580	580	480	750	590	850
Zn	540	730	520	670	1100	500	460	500	470	450	460	500
Co	5500	3800	3400	1900	2200	2900	2300	2500	1900	2900	2400	2900
Ba	1200	1400	1200	2100	2500	1000	1100	1200	1100	1100	1100	1300
Mo	350	320	420	310	350	330	270	270	210	230	220	160
Sr	1300	1200	1300	1100	1500	1400	1200	1200	1200	1100	1200	1100
Ce	700	550	520	840	620	680	510	590	500	610	560	740
Y	120	130	140	120	150	170	150	160	130	140	140	130
V	540	550	570	730	780	540	490	480	480	430	460	410
Pb	1200	1100	1100	1200	1100	960	990	1100	1000	1000	940	1100
Cr	15	28	15	35	16	2.3	16	15	26	22	18	27
Cd	2.3	2.4	2.1	1.3	1.9	2.6	1.6	1.6	1.8	1.6	1.8	1.9
As	210	170	230	180	230	270	220	220	210	180	190	140
Au ppb	-	-	< 10	-	-	-	< 10	-	-	-	-	-
Pt	-	-	110	-	-	-	140	-	-	-	-	-
Pd	-	-	2	-	-	-	2.6	-	-	-	-	-
Rh	-	-	6.5	-	-	-	10	-	-	-	-	-
Ru	-	-	13	-	-	-	15	-	-	-	-	-
Ir	-	-	3.1	-	-	-	3.6	-	-	-	-	-
Interval	B 0-23	B 0-20	B 0-25	B 0-18	B 0-20	B 0-8	B 0-19	B 0-17	B 0-10	B 0-33	L 0-18	L 18-33
Type	Crust	Crust	Crust	Crust	Fossil Crust	Crust	Crust	Crust	Crust	Crust	Crust	Crust

Table 12 Continued

	D7-10A	D11-2A	D11-2B	D11-9-1	D11-9-2	D11-9-3	D11-9-4	D11-9-5	D11-9-6	D11-9-7	D11-10	D13-8A
Fe Wt %	16	16	5.8	2.6	1.7	1.3	2.8	0.6	4.3	0.6	5.6	17
Mn	15	16	3.3	38	38	49	39	45	35	41	5.6	20
Mn/Fe	0.9	1.0	0.6	14.6	22.4	37.7	13.9	72.6	8.1	67.2	1.0	1.2
Si	4.6	4.3	18.2	2.0	2.9	8.9	2.7	0.4	2.9	1.2	17.8	3.5
Na	1.2	1.4	1.1	2.1	1.9	0.7	1.5	1.6	2.0	2.4	1.4	1.6
Al	1.3	0.88	2.5	1.4	1.4	0.60	0.99	0.47	1.2	0.72	3.6	0.66
K	0.41	0.41	0.44	1.1	1.1	0.40	0.87	0.98	0.98	1.1	0.96	0.41
Mg	0.90	1.2	14.0	2.5	2.4	1.6	2.4	1.9	2.2	2.4	11.0	1.0
Ca	2.8	2.2	1.9	1.7	1.3	1.2	1.4	1.3	1.5	1.3	2.3	2.3
Ti	0.75	0.63	0.12	0.10	0.088	0.046	0.12	0.032	0.17	0.034	0.14	0.80
P	0.32	0.33	0.031	0.078	0.058	0.042	0.071	0.051	0.12	0.049	0.028	0.37
H_2O^+	7.8	5.8	10.2	10.2	8.4	4.2	9.3	9.6	6.5	9.4	6.1	8.8
H_2O^-	20.4	20.7	2.1	6.5	5.2	2.3	4.9	5.1	7.6	6.2	2.9	13.0
CO_2	1.5	0.62	0.11	0.17	0.08	0.23	0.12	0.20	0.24	0.07	0.05	0.60
LOI	33.7	33.5	12.6	24.1	22.3	15.8	21.2	22.3	24.2	24.7	11.3	28.7
Ni ppm	2600	2900	1600	4500	5600	830	2800	3900	5800	5400	1200	3600
Cu	670	640	72	2700	3400	420	1800	3200	3300	2000	210	610
Zn	450	460	180	2300	1600	230	810	1400	1600	2400	180	500
Co	2300	2700	100	320	490	180	380	340	870	290	130	3000
Ba	950	950	100	2000	3800	2600	2900	3500	3000	2100	460	890
Mo	260	330	11	290	270	140	350	341	280	410	24	370
Sr	1200	1200	100	580	890	1100	740	870	800	520	120	1400
Ce	480	530	< 20	54	< 20	< 20	46	< 20	120	< 20	< 20	690
Y	140	150	5	43	38	24	32	27	48	26	6	170
V	440	510	110	310	590	440	520	700	520	330	180	560
Pb	830	900	< 15	100	34	17	110	84	200	17	< 15	960
Cr	14	380	5500	210	840	13	1500	110	81	62	11000	8.2
Cd	1.8	2.2	3.1	58	44	3.8	30	52	40	51	1.2	2.6
As	190	240	13	38	40	23	65	49	69	32	10	280
Au ppb		< 10	-	-	-	< 10	-	-	< 10	-	< 10	-
Pt	260	120	-	-	-	26	-	-	110	-	7.2	-
Pd	1	2.6	-	-	-	2.5	-	-	3.2	-	2.9	-
Rh	17	7.6	-	-	-	1.6	-	-	3.8	-	1.4	-
Ru	23	13	-	-	-	2.3	-	-	5.7	-	5.5	-
Ir	5.4	2.9	-	-	-	0.7	-	-	1.1	-	2.6	-
Interval	B 0-15	B 0-10	B	B	B	B	B	B	B	B	B	B 0-3
Type	Crust	Crust	Mn Sst[3]	Stb Mn[3]	Stb Mn	Stb Mn	Stb Mn	Stb Mn	Stb Mn	Stb Mn	Mn Sst	Crust

Table 12 Continued

	D13-16B	D19-4-1	D19-6	D19-13-1	D19-13-2	D19-19A	D19-19B	D19-19C	D21-1-1	D22-6-1
Fe Wt %	20	16	16	18	16	17	18	17	19	18
Mn	16	14	16	18	19	20	19	19	17	19
Mn/Fe	0.8	0.9	1.0	1.0	1.2	1.2	1.1	1.1	0.9	1.1
Si	5.1	6.1	3.7	4.3	3.2	2.8	4.2	3.7	4.2	3.7
Na	1.4	1.4	1.3	1.5	1.4	1.4	1.6	1.5	1.4	1.5
Al	1.2	1.8	0.76	1.0	0.55	0.43	0.99	0.80	0.86	0.65
K	0.44	0.64	0.42	0.48	0.39	0.38	0.52	0.46	0.40	0.43
Mg	1.0	0.88	0.81	0.97	0.89	0.91	0.95	0.94	0.93	0.94
Ca	2.3	1.8	1.8	2.0	2.0	2.1	2.2	2.1	2.0	2.3
Ti	0.70	0.82	0.91	0.93	0.81	0.77	1.4	1.0	0.79	0.90
P	0.39	0.29	0.29	0.33	0.32	0.34	0.30	0.32	0.38	0.38
H_2O^+	9.1	7.2	6.8	5.6	9.4	8.9	9.3	10.5	10.2	8.1
H_2O^-	13.1	18.6	22.0	13.5	17.3	15.1	11.9	11.4	13.2	14.2
CO_2	0.63	0.45	0.41	0.46	0.46	0.53	0.44	0.52	0.49	0.75
LOI	27.3	31.4	34.7	28.5	32.1	29.8	27.3	27.6	28.1	29.1
Ni ppm	2200	2400	3000	3200	3200	3500	3800	3700	2700	3300
Cu	620	1000	780	1200	810	600	740	970	590	340
Zn	550	490	560	540	540	550	650	570	590	550
Co	2000	2800	3200	4200	3900	3800	4200	4300	3300	5900
Ba	1000	1000	1300	1100	1200	1200	1600	1400	1200	1100
Mo	2[illegible]0	210	360	320	440	520	390	430	360	360
Sr	1300	1000	1300	1200	1300	1400	1400	1400	1400	1400
Ce	670	590	650	740	650	620	820	720	630	780
Y	170	140	160	180	180	190	150	180	180	180
V	600	440	510	530	560	620	550	570	610	580
Pb	960	880	1100	1100	1100	1200	1300	1200	1300	1400
Cr	15	20	21	13	9.3	11	20	7.8	5.8	3.9
Cd	2.3	1.9	1.8	2.3	2.1	2.2	2.1	2.2	2.2	2.6
As	260	170	200	210	240	250	220	230	250	260
Au ppb	-	-	< 10	-	-	-	-	-	-	-
Pt	-	-	150	-	-	110	270	220	110	150
Pd	-	-	1	-	-	< 1	1	2	1	< 1
Rh	-	-	12	-	-	8.6	19	17	7.3	13
Ru	-	-	14	-	-	15	16	17	13	19
Ir	-	-	4.3	-	-	3.8	5.8	5.7	2.9	4.8
Interval	B 0-3	B 0-32	B 0-42	B 0-35	B 0-32	L 0-30	L30-52	B 0-53	B 0-7	B 0-6
Type	Crust	Crust	Crust	Crust	Crust	Crust	Crust	Crust	Crust	Crust

- Major and minor elements determined by Inductively Coupled Plasma-Atomic Emission Spectrometry (ICP-AES): except K, Zn, Pb by Flame Atomic Absorption Spectroscopy, and As, Cr, Cd by Graphite-Furnance Atomic Absorption Spectroscopy; Pt group elements determined by ICP-Mass Spectroscopy and Au by fire assay
- Analysts: W.M. d'Angelo, N. Rait, H. Smith, J.R. Gillison, M.G. Kavulak, J.W. Marinenko, G.O. Riddle, and M.J. Malcolm

[1]Sample numbers that are identical except for suffixes -A, -B, -C, and -D represent different sample intervals from the same crust

[2]Intervals are measured from the outer surface of the crust; B=bulk, the entire crust thickness was sampled and analyzed; N=nodule; S=scraped surface, ≤ 0.5mm of the surface was analyzed

[3]Mn SSt = Mn-Fe oxyhydroxide cemented sandstone; Stb Mn = stratabound Mn oxide & oxyhydroxide

Table 13. Hygroscopic water-free (0% H_2O^-) composition of ferromanganese and manganese oxyhydroxides from Table 12

	D1-1-1A	D1-1-1B	D1-8A	D1-8B	D1-8C	D1-8D	D1-8E	D1-8F	D1-8G	D1-9A	D1-9B	D2-1B
Fe Wt%	20.2	17.2	22.7	21.4	22.5	22.2	28.4	24.1	15.4	20.1	21.4	21.8
Mn	23.1	18.6	24.1	25.7	21.1	23.4	19.4	22.9	22.4	26.4	20.0	23.1
Si	5.4	4.6	3.7	3.9	5.8	3.6	4.0	3.2	2.3	3.7	3.9	5.2
Na	1.9	1.7	1.8	1.9	2.0	1.7	1.7	1.6	1.6	2.2	1.7	1.8
Al	1.6	1.3	0.77	0.64	1.4	0.80	0.93	0.82	0.53	0.40	0.92	1.0
K	0.72	0.60	0.51	0.56	0.65	0.52	0.43	0.46	0.45	0.49	0.51	0.55
Mg	1.3	1.0	1.2	1.2	1.1	1.1	1.1	1.1	0.97	1.4	1.1	1.2
Ca	3.2	10.5	3.3	2.9	2.7	2.6	2.3	2.9	10.2	3.4	6.9	2.7
Ti	1.2	1.1	1.4	1.4	2.0	1.7	1.2	1.1	0.86	0.93	1.2	1.2
P	0.59	3.3	0.61	0.47	0.41	0.41	0.46	0.54	3.1	0.55	2.0	0.47
H_2O^+	10.7	9.5	11.2	11.4	10.8	11.1	12.0	9.8	8.6	5.8	10.0	10.3
H_2O^-	0.0	0.0	0.0	0.0	0.0	0.0	0.0	0.0	0.0	0.0	0.0	0.0
CO_2	0.62	1.58	0.64	0.69	0.49	0.53	0.48	0.53	1.65	1.22	1.15	0.67
Ni ppm	5055	4303	4532	4713	3795	4193	3484	4587	4843	4898	3742	4365
Cu	1127	1434	977	600	1012	1233	1420	1449	1181	314	1109	1669
Zn	939	846	963	814	956	1011	1187	1074	791	741	869	847
Co	5200	3442	5382	6999	4638	5797	3484	4105	2953	7913	4544	4621
Ba	1878	2295	2408	1857	2249	2590	2839	2656	2126	1256	2005	2054
Mo	448	387	609	614	379	518	594	616	543	465	454	501
Sr	1589	1721	1983	2000	1827	1973	1807	1932	1890	1758	1871	1797
Ce	809	990	991	986	998	1061	736	1026	1181	904	855	924
Y	231	316	212	229	183	160	155	157	378	226	388	167
V	693	660	864	814	689	802	1019	640	685	842	748	770
Pb	1589	1291	1699	2000	1686	1480	1239	1449	1299	1758	1283	1669
Cr	17	11	12	8.0	25	15	13	10	10	6.9	6.7	21
Cd	3.3	2.0	2.7	2.6	2.4	2.5	2.2	2.5	2.7	6.8	2.1	2.8
As	246	158	312	329	253	284	361	326	189	339	241	308
Pt ppb	-	-	297	171	351	395	348	362	437	-	-	257
Pd	-	-	1.4	1.3	1.4	1.2	1.3	1.2	2.4	-	-	3.0
Rh			20	13	20	27	23	24	20			15
Ru	-	-	18	21	20	19	19	21	15	-	-	24
Ir	-	-	6.8	5.1	5.9	7.5	7.0	7.7	7.7	-	-	5.0

Table 13 Continued

	D2-5B	D2-7	D3-2-1B	D3-3-3	D3-4-1B	D4-1A	D6-1C	D6-3B	D6-4A	D6-5A	D6-5B	D6-5C
Fe Wt%	20.3	21.2	22.3	26.0	27.1	20.9	21.5	23.5	18.9	20.0	20.9	18.6
Mn	24.3	22.6	26.7	20.2	18.8	24.6	18.8	17.9	14.1	17.3	15.7	13.9
Si	4.9	5.9	4.6	5.5	4.6	3.3	8.8	7.7	11.0	10.0	9.8	10.8
Na	2.0	1.9	1.9	1.8	1.4	1.9	2.1	1.9	2.1	2.2	2.0	2.2
Al	0.95	1.6	0.77	1.4	1.2	0.55	2.4	2.1	3.2	2.9	2.9	3.2
K	0.59	0.68	0.56	0.55	0.46	0.43	0.73	0.65	0.73	0.93	0.72	1.0
Mg	1.2	1.3	1.2	1.1	1.1	1.2	1.2	1.1	1.2	1.2	1.2	1.3
Ca	2.8	2.4	3.0	3.0	2.2	3.8	3.0	2.6	3.1	2.7	2.9	2.3
Ti	1.3	1.8	1.1	0.88	1.8	1.1	0.89	1.1	0.77	1.1	1.0	1.5
P	0.42	0.42	0.45	0.67	0.42	0.46	0.46	0.44	0.39	0.39	0.41	0.28
H_2O^+	11.8	10.0	10.2	9.5	11.2	11.5	9.3	11.0	10.0	10.4	9.9	10.6
H_2O^-	0.0	0.0	0.0	0.0	0.0	0.0	0.0	0.0	0.0	0.0	0.0	0.0
CO_2	0.85	0.52	0.73	0.53	0.41	1.60	0.70	0.54	0.60	0.44	0.48	0.31
Ni ppm	4999	5232	4897	3759	3414	4309	2955	2761	2240	3064	2616	2668
Cu	797	990	920	2603	1883	763	779	801	566	999	772	986
Zn	730	1032	772	969	1295	616	618	690	554	599	602	580
Co	7431	5374	5045	2747	2590	3570	3090	3451	2240	3863	3139	3364
Ba	1621	1980	1781	3036	2943	1231	1478	1657	1297	1465	1439	1508
Mo	473	453	623	448	412	406	363	373	248	306	288	186
Sr	1756	1697	1929	1591	1766	1724	1612	1657	1415	1465	1569	1276
Ce	946	778	772	1215	730	837	685	815	589	813	732	858
Y	162	184	208	174	177	209	201	221	153	186	183	151
V	730	778	846	1056	918	665	658	663	566	573	602	476
Pb	1621	1556	1632	1735	1295	1182	1330	1519	1179	1332	1229	1276
Cr	20	40	22	51	19	2.8	22	21	31	29	24	31
Cd	3.1	3.4	3.1	1.9	2.2	3.2	2.1	2.2	2.1	2.1	2.4	2.2
As	284	240	341	260	271	332	296	304	248	240	248	162
Pt ppb	-	-	163	-	-	-	188	-	-	-	-	-
Pd	-	-	3.0	-	-	-	3.5	-	-	-	-	-
Rh	-	-	9.6	-	-	-	13	-	-	-	-	-
Ru	-	-	19	-	-	-	20	-	-	-	-	-
Ir	-	-	4.6	-	-	-	4.8	-	-	-	-	-

Table 13 Continued

	D7-10A	D11-2A	D11-2B	D11-9-1	D11-9-2	D11-9-3	D11-9-4	D11-9-5	D11-9-6	D11-9-7	D11-10	D13-8A
Fe Wt%	22.1	22.5	6.0	2.9	1.8	1.3	3.0	0.7	4.9	0.7	5.9	20.8
Mn	20.7	22.5	3.4	41.9	41.2	50.6	42.1	48.6	39.5	45.1	5.9	24.5
Si	6.4	6.0	18.9	2.2	3.1	9.2	2.9	0.5	3.2	1.3	18.7	4.3
Na	1.6	2.0	1.2	2.3	2.1	0.8	1.6	1.7	2.3	2.6	1.5	2.0
Al	1.8	1.2	2.6	1.5	1.5	0.62	1.1	0.51	1.4	0.79	3.8	0.81
K	0.57	0.58	0.46	1.2	1.2	0.41	0.94	1.1	1.1	1.2	1.0	0.50
Mg	1.2	1.7	15	2.8	2.6	1.7	2.6	2.1	2.5	2.6	12	1.2
Ca	3.9	3.1	2.0	1.9	1.4	1.2	1.5	1.4	1.7	1.4	2.4	2.8
Ti	1.0	0.89	0.12	0.11	0.10	0.048	0.13	0.035	0.19	0.037	0.15	0.98
P	0.44	0.46	0.032	0.086	0.063	0.043	0.077	0.055	0.14	0.054	0.029	0.45
H_2O^+	10.8	8.2	10.6	11.2	9.1	4.3	10.0	10.4	7.3	10.3	6.4	10.8
H_2O^-	0.0	0.0	0.0	0.0	0.0	0.0	0.0	0.0	0.0	0.0	0.0	0.0
CO_2	2.07	0.87	0.11	0.19	0.09	0.24	0.13	0.22	0.27	0.08	0.05	0.73
Ni ppm	3589	4078	1657	4962	6076	858	3020	4213	6550	5944	1262	4402
Cu	925	900	75	2977	3689	434	1941	3457	3727	2201	221	746
Zn	621	647	186	2536	1736	238	874	1512	1807	2642	189	611
Co	3175	3797	104	353	532	186	410	367	983	319	137	3668
Ba	1311	1336	104	2205	4123	2687	3128	3781	3388	2311	484	1088
Mo	359	464	11	320	293	145	377	368	316	451	25	452
Sr	1656	1687	104	640	966	1137	798	940	904	572	126	1712
Ce	663	745	~101	60	~11	~10	50	~11	136	~11	~11	844
Y	193	211	5	47	41	25	35	29	54	29	6	208
V	607	717	114	342	640	455	561	756	587	363	189	685
Pb	1146	1266	~8	110	37	18	119	91	226	19	~8	1174
Cr	19	534	5697	232	912	13	1618	119	92	68	11571	10
Cd	2.5	3.1	3.2	64	48	3.9	32	56	45	56	1.3	3.2
As	262	337	13	42	43	24	70	53	78	35	11	342
Pt ppb	359	169	-	-	-	27	-	-	124	-	8	-
Pd	1.4	3.7	-	-	-	2.6	-	-	3.6	-	3.1	-
Rh	23	11	-	-	-	1.7	-	-	4.3	-	1.5	-
Ru	32	18	-	-	-	2.4	-	-	6.4	-	5.8	-
Ir	7.5	4.1	-	-	-	0.7	-	-	1.2	-	2.7	-

Table 13 Continued

	D13-16B	D19-4-1	D19-6	D19-13-1	D19-13-2	D19-19A	D19-19B	D19-19C	D21-1-1	D22-6-1
Fe Wt%	24.4	21.7	23.0	22.4	21.0	21.5	21.5	20.3	23.3	22.4
Mn	19.5	19.0	23.0	22.4	24.9	25.3	22.7	22.6	20.8	23.6
Si	6.3	8.2	5.4	5.3	4.2	3.5	5.0	4.5	5.1	4.6
Na	1.7	1.9	1.9	1.8	1.8	1.8	1.9	1.8	1.7	1.8
Al	1.5	2.4	1.1	1.2	0.72	0.54	1.2	1.0	1.1	0.81
K	0.54	0.87	0.60	0.60	0.51	0.48	0.62	0.55	0.49	0.53
Mg	1.2	1.2	1.2	1.2	1.2	1.2	1.1	1.1	1.1	1.2
Ca	2.8	2.4	2.6	2.5	2.6	2.7	2.6	2.5	2.4	2.9
Ti	0.85	1.1	1.3	1.2	1.1	0.97	1.7	1.2	0.97	1.1
P	0.48	0.39	0.42	0.41	0.42	0.43	0.36	0.38	0.47	0.47
H_2O^+	11.1	9.8	9.8	7.0	12.3	11.3	11.1	12.5	12.5	10.1
H_2O^-	0.0	0.0	0.0	0.0	0.0	0.0	0.0	0.0	0.0	0.0
CO_2	0.77	0.61	0.59	0.57	0.60	0.67	0.53	0.62	0.60	0.93
Ni ppm	2685	3251	4305	3986	4192	4428	4548	4410	3305	4105
Cu	757	1354	1119	1495	1061	759	886	1156	722	423
Zn	671	664	804	673	707	696	778	679	722	684
Co	2441	3792	4592	5232	5109	4807	5027	5125	4039	7339
Ba	1221	1354	1865	1370	1572	1518	1915	1669	1469	1368
Mo	330	284	517	399	576	658	467	512	441	448
Sr	1587	1354	1865	1495	1703	1771	1676	1669	1714	1741
Ce	818	799	933	922	851	784	981	858	771	970
Y	208	190	230	224	236	240	180	215	220	224
V	732	596	732	660	734	784	658	679	747	721
Pb	1172	1192	1578	1370	1441	1518	1556	1430	1591	1741
Cr	18	27	30	16	12	14	24	9.3	7.1	4.9
Cd	2.8	2.6	2.6	2.9	2.8	2.8	2.5	2.6	2.7	3.2
As	317	230	287	262	314	316	263	274	306	323
Pt ppb	-	-	215	-	-	139	323	262	135	187
Pd	-	-	1.4	-	-	0.6	1.2	2.4	1.2	0.6
Rh	-	-	17	-	-	11	22	20	8.9	16
Ru	-	-	20	-	-	19	19	20	16	24
Ir	-	-	6.2	-	-	4.8	6.9	6.8	3.5	6.0

[1]Less than values were normalized from one half their respective limits of detection

Table 14. Statistics for 24 bulk Fe-Mn crusts from the Federated States of Micronesia, data from Table 12

ELEMENT	N	MEAN	MEDIAN	SD[1]	MIN[2]	MAX[3]	NM[4]
Fe Wt %	24	16.9	16.0	1.8	15.0	23.0	22.1
Mn	24	16.4	16.0	2.3	12.0	20.0	21.5
Mn/Fe	24	1.0[5]	1.0	0.2	0.7	1.2	-
Si	24	4.4	4.0	1.6	2.6	9.4	5.8
Na	24	1.4	1.4	0.1	1.2	1.8	1.9
Al	24	1.1	0.9	0.6	0.5	2.7	1.4
K	24	0.45	0.43	0.09	0.35	0.70	0.59
Mg	24	0.91	0.90	0.90	0.78	1.20	1.19
Ca	24	2.3	2.1	0.7	1.7	5.2	3.0
Ti	24	0.87	0.84	0.20	0.61	1.50	1.14
P	24	0.39	0.33	0.24	0.29	1.50	0.52
H_2O^+	24	8.0	8.0	1.3	5.6	10.5	10.5
H_2O^-	24	17.1	18.0	4.1	10.2	24.6	0.0
CO_2	24	0.58	0.50	0.28	0.33	1.50	0.76
LOI	24	30.8	30.7	3.5	22.5	37.3	-
Ni ppm	24	2929	2950	561	1900	3700	3857
Cu	24	680	783	350	340	1800	1063
Zn	24	572	540	137	450	1100	752
Co	24	3237	3100	1038	1900	5900	4261
Ba	24	1283	1200	380	890	2500	1691
Mo	24	330	335	67	210	440	435
Sr	24	1283	1300	124	1000	1500	1685
Ce	24	638	645	93	480	840	839
Y	24	159	150	34	120	290	208
V	24	553	555	82	430	780	727
Pb	24	1081	1100	143	830	1400	1422
Cr	24	30	15	75	2.3	380	41
Cd	24	2.0	2.1	0.4	1.3	2.6	2.7
As	24	220	220	32	170	280	269
Pt ppb	10	167	150	52	110	260	223
Pd	10	1.7	1.5	0.7	1.0	2.6	2.2
Rh	10	12	12	3.8	6.5	17	16
Ru	10	16	15	3	13	23	21
Ir	10	4.1	4.1	1.0	2.9	5.7	5.5
Depth[6]	24	2467	2470	391	1945	2950	-
Thickness[7]	24	22	20	15	3	55	-

[1]Standard deviation
[2]Minimum
[3]Maximum
[4]Mean of hygroscopic water free data (0% H_2O^-) for bulk crusts from Table 13; less than values were normalized from the values of one half their respective limits of detection
[5]Ratio of the Fe and Mn means, not a mean of the summation of ratios
[6]Water depth in meters
[7]Crust thickness in millimeters

Table 15. Statistics for 7 stratabound manganese samples from the Federated States of Micronesia, data from Table 12

ELEMENT	N	MEAN	MEDIAN	SD[1]	MIN[2]	MAX[3]	NM[4]
Fe Wt %	7	2.0	1.7	1.3	0.6	4.3	2.2
Mn	7	40.7	39.0	4.8	35.0	49.0	44.2
Mn/Fe	7	20.45[5]	22.4	26.4	8.1	72.6	-
Si	7	3.0	2.7	2.8	0.4	8.9	3.2
Na	7	1.7	1.9	0.6	0.7	2.4	1.9
Al	7	0.97	0.99	0.38	0.47	1.40	1.06
K	7	0.93	0.98	0.25	0.40	1.10	1.02
Mg	7	2.2	2.4	0.3	1.6	2.5	2.4
Ca	7	1.4	1.3	0.2	1.2	1.7	1.5
Ti	7	0.084	0.088	0.051	0.032	0.170	0.093
P	7	0.067	0.058	0.027	0.042	0.120	0.074
H_2O^+	7	8.2	9.3	2.1	4.2	10.2	9.0
H_2O^-	7	5.4	5.2	1.7	2.3	7.6	0.0
CO_2	7	0.16	0.17	0.07	0.07	0.24	0.17
LOI	7	22.1	22.3	3.1	5.8	24.7	-
Ni ppm	7	4119	4500	1799	830	5800	4518
Cu	7	2403	2700	1079	420	3400	2632
Zn	7	1477	1600	771	230	2400	1621
Co	7	410	340	223	180	870	450
Ba	7	2843	2900	670	2000	3800	3089
Mo	7	297	290	85	140	410	324
Sr	7	786	800	197	520	1100	851
Ce[6]	7	43	20	37	20	120	36
Y	7	34	32	9	24	48	37
V	7	487	520	139	310	700	529
Pb	7	80	84	66	17	200	88
Cr	7	402	110	561	13	1500	436
Cd	7	40	44	18	4	58	44
As	7	45	40	17	23	69	49
Pt ppb	2	68	68	59	26	110	76
Pd	2	2.9	2.9	0.5	2.5	3.2	3.1
Rh	2	2.7	2.7	1.6	1.6	3.8	3.0
Ru	2	4.0	4.0	2.4	2.3	5.7	4.4
Ir	2	0.9	0.9	0.3	0.7	1.1	1.0
Depth[7]	7	2290	2290	2290	0	2290	-

[1]Standard deviation
[2]Minimum
[3]Maximum
[4]Mean of hygroscopic water free data (0% H_2O^-) for deposits listed in Table 13
[5]Ratio of the Fe and Mn means, not a mean of the summation of ratios
[6]Less than values were normalized from values of one half their respective limits of detection
[7]Water depth in meters

Table 16. Statistics for 2 manganiferous sandstones from the Federated States of Micronesia, data from Table 12

ELEMENT	N	MEAN	MEDIAN	SD[1]	MIN[2]	MAX[3]	NM[4]
Fe Wt %	2	5.7	5.7	0.1	5.6	5.8	6.0
Mn	2	4.5	4.5	1.6	3.3	5.6	4.7
Mn/Fe	2	0.8[5]	0.8	0.3	0.6	1.0	-
Si	2	18.0	18.0	0.3	7.8	18.2	18.8
Na	2	1.3	1.3	0.2	1.1	1.4	1.3
Al	2	3.1	3.1	0.8	2.5	3.6	3.2
K	2	0.70	0.70	0.37	0.44	0.96	0.74
Mg	2	13	13	2	11	14	13
Ca	2	2.1	2.1	0.3	1.9	2.3	2.2
Ti	2	0.13	0.13	0.01	0.12	0.14	0.14
P	2	0.03	0.03	0.00	0.03	0.03	0.03
H_2O^+	2	8.2	8.2	2.9	6.1	10.2	8.5
H_2O^-	2	2.5	2.5	0.6	2.1	2.9	0.0
CO_2	2	0.08	0.08	0.04	0.05	0.11	0.08
LOI	2	12.0	12.0	0.9	11.3	12.6	-
Ni ppm	2	1400	1400	283	1200	1600	1461
Cu	2	141	141	98	72	210	148
Zn	2	180	180	0	180	180	188
Co	2	115	115	21	100	130	120
Ba	2	280	280	255	100	460	294
Mo	2	18	18	9	11	24	18
Sr	2	110	110	14	100	120	115
Ce[6]	2	~10	~10	0	~10	~10	~10
Y	2	6	6	1	5	6	6
V	2	145	145	50	110	180	152
Pb	2	15	15	0	15	15	8
Cr	2	8250	8250	3889	5500	11000	8638
Cd	2	2.2	2.2	1.3	1.2	3.1	2.2
As	2	12	12	2	10	13	12
Pt ppb	1	7.2	7.2	-	7.2	7.2	7.6
Pd	1	2.9	2.9	-	2.9	2.9	3.1
Rh	1	1.4	1.4	-	1.4	1.4	1.5
Ru	1	5.5	5.5	-	5.5	5.5	5.8
Ir	1	2.6	2.6	-	2.6	2.6	2.7
Depth[7]	2	2290	2290	0	2290	2290	-

[1]Standard deviation
[2]Minimum
[3]Maximum
[4]Mean of hygroscopic water free data (0% H_2O^-) for samples listed in Table 13
[5]Ratio of the Fe and Mn means, not a mean of the summation of ratios
[6]Less than values were normalized from values of one half their respective limits of detection
[7]Water depth in meters

Table 18. Concentrations of rare earth elements (ppm) in ferromanganese and manganese deposits

	D1-8A	D1-8B	D1-8C	D1-8D	D1-8E	D1-8F	D1-8G	D2-1B	D3-2-1B	D6-1C	D7-10A	D11-2A	D11-9-1
La	350	330	270	280	290	230	300	250	300	240	270	310	35
Ce	640	640	560	650	450	600	520	490	400	310	420	450	9.9
Pr	59	55	48	49	48	38	44	43	54	43	45	59	5.7
Nd	270	260	220	220	220	170	200	200	250	200	210	280	29
Sm	49	47	42	41	41	33	36	38	49	39	40	54	5.6
Eu	13	12	10	10	10	8.2	9.7	11	13	10	11	15	1.4
Gd	54	53	43	44	44	35	45	43	54	45	46	61	7.4
Tb	8.8	8.9	7.3	7.4	7.0	5.7	7.2	7.1	8.9	7.3	7.4	9.6	1.2
Dy	54	56	44	44	44	36	49	43	54	44	45	59	7.5
Ho	11	12	8.5	8.7	8.4	7.4	11	8.5	11	8.9	9.1	11	1.5
Er	30	32	25	25	23	21	32	23	30	26	25	30	4.4
Tm	4.3	4.6	3.3	3.3	3.1	2.7	4.5	3.2	3.9	3.4	3.8	4.2	0.61
Yb	28	30	24	23	21	19	30	22	28	24	25	29	3.8
Σ REE	1571	1541	1305	1405	1210	1206	1288	1182	1256	1001	1157	1372	113
Ce*	0.92	0.98	1.02	1.15	0.78	1.32	0.91	0.98	0.65	0.63	0.78	0.70	0.14
Interval	B 0-55	L 0-15	L 15-27	L 27-34	L 34-44	L 44-50	L 50-55	B 0-12	B 0-25	B 0-19	B 0-15	B 0-10	Stb Mn

	D11-9-3	D11-9-4	D11-9-6	D11-10	D19-6	D19-19A	D19-19B	D19-19C
La	34	60	78	5.6	360	350	280	310
Ce	1.8	3.3	50	2.9	600	450	600	600
Pr	4.3	9.4	13	0.9	61	57	48	52
Nd	21	45	64	4.3	290	270	220	240
Sm	4.1	8.4	12	1.0	53	50	40	44
Eu	1.2	2.4	3.6	0.32	15	14	11	12
Gd	5.3	10	15	1.1	61	58	43	51
Tb	0.81	1.5	2.3	0.20	9.5	9.0	6.9	7.7
Dy	4.9	10	14	1.3	61	58	43	50
Ho	1.2	1.9	3.1	0.24	13	12	8.6	10
Er	3.4	5.1	7.5	0.78	34	31	23	27
Tm	0.44	0.68	1.1	0.08	5.0	4.6	3.4	4.2
Yb	2.7	4.3	7.7	1.0	32	29	22	27
Σ REE	85	162	271	20	1595	1393	1349	1435
Cc*	0.03	0.03	0.32	0.26	0.83	0.65	1.07	0.97
Interval	Stb Mn	Stb Mn	Stb Mn	Mn Sst	B 0-42	L 0-30	L 30-52	B 0-43

- Analyses by Inductively Coupled Plasma - Mass Spectrometry (ICP-MS); analyst: M. J. Malcolm
- Intervals are measured from the outer surface of the crust; B = bulk, the entire crust thickness was sampled and analyzed; L = layer, a layer was sampled and analyzed
- Mn Sst = Fe-Mn oxyhydroxide cemented sandstone; Stb Mn = stratabound Mn oxide & oxyhydroxide
- Ce* = 2Ce/La+Pr from chondrite normalized data

Table 19. Correlation coefficient matrix for 24 bulk crusts listed in Table 12; n = 24, except for Pt, Pd, Rh, Ru, and Ir = 10; the zero correlations for 24 points and 10 points at the 95% confidence level are |0.403| and |0.631|

	Depth	Lat.	Long.	Fe	Mn	Fe/Mn	Si	Na	Al	K	Mg	Ca	Ti	P	H_2O^+	H_2O^-	CO_2	LOI	Ni
Lat.	-0.813																		
Long.	-0.132	0.115																	
Fe	0.361	-0.230	-0.004																
Mn	0.537	-0.573	0.167	0.105															
Fe/Mn	0.211	-0.318	0.179	-0.493	0.798														
Si	-0.415	0.378	-0.547	-0.118	-0.750	-0.558													
Na	-0.128	0.042	-0.433	-0.217	-0.003	0.144	0.550												
Al	-0.440	0.441	-0.472	-0.123	-0.820	-0.619	0.982	0.454											
K	-0.293	0.193	-0.440	-0.282	-0.598	-0.328	0.872	0.527	0.878										
Mg	0.105	-0.180	-0.579	0.163	0.175	0.036	0.220	0.430	0.126	0.115									
Ca	-0.207	0.237	0.378	-0.101	-0.037	-0.057	-0.177	-0.004	-0.126	-0.242	-0.071								
Ti	0.056	-0.077	0.453	0.342	0.254	0.075	-0.324	-0.361	-0.261	-0.148	-0.172	-0.123							
P	-0.163	0.160	0.551	-0.011	-0.096	-0.148	-0.256	-0.198	-0.192	-0.254	-0.255	0.902	0.011						
H_2O^+	0.229	-0.188	0.002	0.375	0.336	0.076	-0.096	0.166	-0.130	-0.152	0.046	0.028	0.241	-0.054					
H_2O^-	-0.252	0.268	0.262	-0.577	-0.224	0.158	-0.237	-0.521	-0.173	-0.152	-0.486	-0.072	-0.191	0.033	-0.620				
CO_2	-0.036	0.069	-0.081	-0.094	0.230	0.171	-0.222	-0.026	-0.197	-0.323	0.191	0.557	-0.186	0.214	0.127	-0.059			
LOI	-0.036	0.066	0.325	-0.511	0.065	0.358	-0.502	-0.586	-0.445	-0.373	-0.462	-0.062	-0.118	0.026	-0.499	0.948	0.047		
Ni	0.323	-0.395	0.382	-0.124	0.858	0.829	-0.748	-0.132	-0.770	-0.506	0.011	-0.058	0.481	-0.048	0.148	0.015	0.105	0.262	
Cu	0.271	-0.040	0.286	0.449	-0.079	-0.324	-0.172	-0.399	-0.094	-0.123	-0.252	-0.129	0.312	0.070	-0.130	-0.010	-0.305	0.017	0.051
Zn	0.077	0.025	0.575	0.636	0.076	-0.251	-0.343	-0.533	-0.276	-0.355	-0.247	-0.043	0.797	0.177	0.206	-0.153	-0.299	-0.113	0.227
Co	0.061	-0.458	0.316	-0.229	0.615	0.674	-0.450	0.051	-0.502	-0.170	-0.109	-0.050	0.303	0.009	0.097	-0.008	-0.017	0.148	0.695
Ba	-0.031	0.165	0.617	0.499	-0.096	-0.324	-0.273	-0.506	-0.193	-0.313	-0.438	-0.034	0.568	0.198	0.092	0.029	-0.368	0.031	0.094
Mo	0.339	-0.381	0.470	0.043	0.772	0.652	-0.806	-0.304	-0.848	-0.712	-0.166	-0.034	0.311	0.070	0.267	0.074	-0.097	0.296	0.755
Sr	0.173	-0.192	0.409	0.432	0.648	0.308	-0.591	-0.121	-0.637	-0.657	0.022	0.268	0.457	0.258	0.580	-0.415	0.174	-0.240	0.514
Ce	0.382	-0.436	0.328	0.322	0.465	0.212	-0.476	-0.002	-0.492	-0.328	-0.185	-0.023	0.120	0.112	0.150	-0.190	-0.151	-0.013	0.408
Y	0.181	-0.251	0.253	0.122	0.194	-0.002	-0.331	-0.072	-0.314	-0.284	-0.036	0.748	0.029	0.809	0.146	-0.229	0.230	-0.150	0.047
V	0.274	-0.123	0.515	0.702	0.296	-0.114	-0.498	-0.404	-0.488	-0.597	-0.168	-0.050	0.415	0.142	0.269	-0.176	-0.254	-0.060	0.279
Pb	0.012	-0.317	0.410	0.210	0.359	0.238	-0.318	-0.060	-0.382	-0.269	-0.305	-0.295	0.274	-0.111	0.242	-0.090	-0.377	-0.002	0.385
Cr	-0.120	0.024	-0.277	-0.116	-0.103	-0.033	0.036	-0.044	-0.010	-0.049	0.648	-0.067	-0.259	-0.083	-0.411	0.220	-0.020	0.183	-0.049
Cd	0.379	-0.512	-0.093	0.101	0.808	0.654	-0.383	0.224	-0.482	-0.277	0.513	-0.137	0.240	-0.257	0.297	-0.395	0.235	-0.185	0.676
As	0.319	-0.305	-0.220	0.392	0.660	0.353	-0.301	0.291	-0.430	-0.444	0.480	-0.067	-0.096	-0.202	0.483	-0.495	0.185	-0.332	0.276
Pt	-0.099	0.375	0.083	-0.331	-0.286	-0.203	-0.213	-0.488	0.325	-0.174	-0.342	0.386	0.172	0.213	0.107	0.156	0.607	0.229	-0.125
Pd	-0.250	0.385	0.084	-0.510	-0.057	0.215	-0.028	0.276	-0.064	0.220	0.296	0.253	-0.085	0.271	-0.139	0.058	-0.119	0.023	0.315
Rh	0.131	0.056	-0.058	-0.211	-0.022	-0.020	-0.193	-0.247	0.207	0.062	-0.320	0.164	0.283	0.017	0.203	0.012	0.459	0.116	0.068
Ru	-0.205	0.204	-0.170	-0.093	-0.236	-0.323	0.164	-0.285	0.515	0.103	-0.171	0.492	-0.093	0.282	0.046	-0.069	0.879	-0.051	-0.240
Ir	0.170	-0.034	-0.077	-0.124	0.138	0.100	-0.182	-0.149	0.144	0.158	-0.320	0.039	0.382	-0.092	0.246	-0.074	0.370	0.033	0.184
Thick	0.102	-0.110	0.407	-0.298	-0.020	0.132	-0.203	-0.243	-0.119	0.065	-0.477	0.060	0.274	0.202	-0.109	0.278	-0.277	0.297	0.183

	Cu	Zn	Co	Ba	Mo	Sr	Ce	Y	V	Pb	Cr	Cd	As	Pt	Pd	Rh	Ru	Ir
Zn	0.611																	
Co	-0.240	-0.019																
Ba	0.759	0.894	-0.112															
Mo	0.087	0.315	0.540	0.293														
Sr	-0.057	0.477	0.333	0.307	0.700													
Ce	0.427	0.241	0.436	0.337	0.404	0.296												
Y	-0.134	0.033	0.167	-0.067	0.223	0.414	0.148											
V	0.601	0.812	0.001	0.810	0.496	0.547	0.530	0.034										
Pb	0.143	0.336	0.613	0.398	0.552	0.426	0.607	-0.071	0.504									
Cr	-0.058	-0.163	-0.156	-0.157	-0.052	-0.214	-0.262	-0.120	-0.110	-0.279								
Cd	-0.351	-0.051	0.537	-0.372	0.381	0.457	0.211	0.043	0.057	0.198	0.042							
As	-0.298	-0.059	0.137	-0.217	0.430	0.644	0.224	0.128	0.267	0.219	0.064	0.655						
Pt	-0.017	-0.098	-0.197	0.063	-0.141	-0.121	-0.258	0.216	-0.402	-0.470	-0.323	-0.521	-0.597					
Pd	0.391	-0.047	-0.039	0.055	0.012	-0.203	-0.125	0.063	-0.079	-0.324	0.457	-0.048	-0.204	-0.194				
Rh	-0.152	-0.166	0.051	-0.014	-0.011	-0.047	-0.037	0.137	-0.352	-0.245	-0.380	-0.279	-0.410	0.923	-0.342			
Ru	-0.235	-0.384	0.000	-0.371	-0.573	-0.212	-0.260	0.313	-0.547	-0.386	-0.302	-0.206	-0.430	0.716	-0.221	0.694		
Ir	-0.098	-0.109	0.147	0.041	0.100	0.044	0.107	0.050	-0.257	-0.086	-0.430	-0.150	-0.273	0.853	-0.414	0.978	0.638	
Thick	0.214	0.125	0.265	0.264	0.322	-0.024	0.130	0.223	-0.071	0.076	-0.179	-0.340	-0.478	0.541	0.066	0.548	-0.061	0.522

Table 20. Correlation coefficient matrix for 6 layers from crust D1-8 listed in Table 12; the zero correlation for 6 points at the 95% confidence level is |0.813|

	Fe	Mn	Fe/Mn	Si	Na	Al	K	Mg	Ca	Ti	P	H_2O^+	H_2O^-	CO_2	LOI	Ni	Cu	Zn	Co
Mn	-0.335																		
Fe/Mn	-0.843	0.741																	
Si	0.237	-0.774	-0.697																
Na	-0.078	-0.196	-0.189	0.652															
Al	0.375	-0.698	-0.716	0.886	0.633														
K	-0.464	-0.023	0.129	0.558	0.828	0.490													
Mg	0.679	0.449	-0.244	-0.315	-0.205	-0.107	-0.378												
Ca	-0.633	0.430	0.798	-0.693	-0.327	-0.516	-0.144	-0.297											
Ti	0.081	-0.293	-0.371	0.764	0.959	0.667	0.765	-0.130	-0.573										
P	-0.610	0.398	0.773	-0.692	-0.351	-0.514	-0.182	-0.303	0.999	-0.593									
H_2O^+	0.816	-0.250	-0.670	0.179	0.118	0.150	-0.403	0.495	-0.610	0.273	-0.589								
H_2O^-	-0.087	-0.603	-0.365	0.695	0.198	0.305	0.313	-0.524	-0.593	0.383	-0.588	0.012							
CO_2	-0.663	0.461	0.834	-0.727	-0.360	-0.589	-0.167	-0.308	0.995	-0.594	0.994	-0.603	-0.557						
LOI	-0.034	-0.537	-0.374	0.655	0.162	0.253	0.273	-0.424	-0.651	0.368	-0.647	0.068	0.992	-0.609					
Ni	-0.430	0.909	0.820	-0.868	-0.386	-0.688	-0.134	0.301	0.714	-0.550	0.690	-0.484	-0.726	0.726	-0.696				
Cu	0.571	0.162	-0.206	-0.312	-0.126	0.122	-0.410	0.657	0.187	-0.220	0.197	0.330	-0.833	0.124	-0.826	0.278			
Zn	0.896	-0.106	-0.612	-0.004	-0.046	0.305	-0.453	0.752	-0.294	-0.006	-0.276	0.693	-0.497	-0.345	-0.462	-0.123	0.870		
Co	-0.112	0.338	0.092	0.122	0.321	-0.208	0.362	0.145	-0.512	0.464	-0.540	0.205	0.419	-0.447	0.501	-0.051	-0.561	-0.327	
Ba	0.748	0.083	-0.392	-0.186	-0.035	0.178	-0.429	0.747	-0.066	-0.063	-0.054	0.586	-0.703	-0.119	-0.675	0.093	0.955	0.963	-0.376
Mo	0.315	0.586	0.205	-0.827	-0.754	-0.683	-0.797	0.705	0.247	-0.740	0.257	0.225	-0.621	0.272	-0.541	0.609	0.517	0.432	-0.096
Sr	-0.030	0.876	0.532	-0.797	-0.194	-0.540	-0.230	0.621	0.484	-0.331	0.464	-0.013	-0.898	0.482	-0.847	0.856	0.601	0.312	-0.002
Ce	-0.547	0.802	0.814	-0.635	0.025	-0.405	0.216	0.116	0.749	-0.208	0.718	-0.543	-0.738	0.735	-0.748	0.892	0.295	-0.158	-0.098
Y	-0.733	0.427	0.854	-0.684	-0.351	-0.591	-0.119	-0.398	0.983	-0.578	0.981	-0.658	-0.459	0.993	-0.514	0.689	0.011	-0.448	-0.406
V	0.584	-0.261	-0.396	-0.152	-0.230	-0.160	-0.719	0.221	-0.135	-0.157	-0.097	0.817	-0.140	-0.119	-0.121	-0.311	0.353	0.548	-0.160
Pb	-0.480	0.386	0.361	0.063	0.125	-0.242	0.503	-0.100	-0.234	0.212	-0.269	-0.377	0.475	-0.177	0.529	0.167	-0.738	-0.673	0.804
Cr	0.052	-0.561	-0.415	0.795	0.829	0.903	0.690	-0.331	-0.247	0.769	-0.254	-0.007	0.203	-0.317	0.123	-0.546	0.047	0.093	-0.185
Cd	-0.389	0.836	0.776	-0.827	-0.267	-0.566	-0.107	0.275	0.788	-0.477	0.768	-0.437	-0.851	0.781	-0.843	0.964	0.439	-0.004	-0.211
As	0.896	-0.096	-0.661	0.020	-0.325	0.030	-0.586	0.758	-0.652	-0.111	-0.633	0.765	0.006	-0.643	0.099	-0.259	0.354	0.708	0.161
Pt	0.040	0.291	0.226	-0.375	0.121	0.044	-0.066	0.245	0.584	-0.107	0.581	-0.041	-0.892	0.521	-0.934	0.462	0.814	0.473	-0.584
Pd	-0.589	0.351	0.735	-0.639	-0.278	-0.440	-0.142	-0.320	0.993	-0.531	0.995	-0.566	-0.603	0.981	-0.670	0.648	0.236	-0.239	-0.578
Rh	0.501	0.281	-0.154	-0.214	0.224	0.157	-0.140	0.668	0.067	0.127	0.063	0.446	-0.797	0.012	-0.779	0.247	0.902	0.809	-0.242
Ru	0.694	0.190	-0.459	0.023	-0.194	0.087	-0.230	0.861	-0.626	-0.015	-0.632	0.418	-0.061	-0.628	0.045	0.009	0.307	0.561	0.312
Ir	0.206	0.525	0.237	-0.608	-0.138	-0.201	-0.314	0.578	0.495	-0.307	0.492	0.094	-0.990	0.452	-0.981	0.631	0.895	0.605	-0.430

	Ba	Mo	Sr	Ce	Y	V	Pb	Cr	Cd	As	Pt	Pd	Rh	Ru
Mo	0.498													
Sr	0.519	0.705												
Ce	0.096	0.260	0.797											
Y	-0.233	0.204	0.400	0.699										
V	0.508	0.380	0.031	-0.427	-0.169									
Pb	-0.704	-0.184	-0.087	0.094	-0.102	-0.641								
Cr	0.059	-0.827	-0.427	-0.133	-0.312	-0.231	-0.217							
Cd	0.240	0.543	0.890	0.945	0.728	-0.235	-0.042	-0.375						
As	0.549	0.534	0.047	-0.538	-0.694	0.537	-0.166	-0.333	-0.329					
Pt	0.674	0.233	0.657	0.661	0.431	0.112	-0.646	0.223	0.675	-0.234				
Pd	-0.013	0.201	0.450	0.716	0.964	-0.083	-0.328	-0.165	0.750	-0.657	0.637			
Rh	0.922	0.360	0.669	0.375	-0.100	0.324	-0.566	0.185	0.421	0.278	0.814	0.115		
Ru	0.437	0.467	0.208	-0.226	-0.673	0.016	0.184	-0.260	-0.104	0.837	-0.209	-0.665	0.279	
Ir	0.791	0.595	0.863	0.662	0.346	0.200	-0.541	-0.126	0.773	0.076	0.907	0.516	0.869	0.120

Table 21. Correlation coefficient matrix for 7 stratiform manganese layers listed in Table 12; the zero correlation for 7 points at the 95% confidence level is |0.753|

	Fe	Mn	Fe/Mn	Si	Na	Al	K	Mg	Ca	Ti	P	H_2O^+	H_2O^-	CO_2	LOI	Ni	Cu	Zn	Co
Mn	-0.715																		
Fe/Mn	-0.879	0.622																	
Si	0.044	0.520	-0.249																
Na	0.130	-0.729	0.022	-0.798															
Al	0.646	-0.819	-0.805	-0.148	0.451														
K	0.090	-0.728	0.007	-0.899	0.934	0.498													
Mg	0.315	-0.830	-0.367	-0.636	0.813	0.713	0.823												
Ca	0.637	-0.671	-0.572	-0.374	0.496	0.672	0.490	0.600											
Ti	0.985	-0.792	-0.880	-0.041	0.201	0.700	0.190	0.406	0.601										
P	0.934	-0.782	-0.681	-0.204	0.361	0.574	0.304	0.350	0.670	0.926									
H_2O^+	-0.158	-0.405	0.176	-0.888	0.679	0.216	0.813	0.723	0.442	-0.083	-0.028								
H_2O^-	0.511	-0.854	-0.236	-0.726	0.881	0.519	0.821	0.693	0.680	0.551	0.739	0.504							
CO_2	0.362	0.264	-0.156	0.409	-0.507	-0.225	-0.534	-0.671	0.141	0.237	0.373	-0.567	-0.112						
LOI	0.234	-0.766	-0.014	-0.876	0.969	0.429	0.944	0.775	0.577	0.300	0.485	0.717	0.944	-0.361					
Ni	0.236	-0.779	-0.069	-0.718	0.913	0.527	0.899	0.682	0.379	0.330	0.479	0.482	0.876	-0.375	0.905				
Cu	0.265	-0.669	-0.108	-0.746	0.654	0.481	0.817	0.484	0.402	0.358	0.486	0.517	0.740	-0.114	0.751	0.835			
Zn	-0.017	-0.566	0.130	-0.740	0.953	0.392	0.882	0.713	0.531	0.023	0.225	0.678	0.793	-0.430	0.906	0.827	0.585		
Co	0.770	-0.747	-0.509	-0.247	0.376	0.491	0.361	0.266	0.338	0.816	0.887	-0.105	0.694	0.242	0.478	0.629	0.645	0.188	
Ba	-0.018	-0.037	-0.002	-0.098	-0.205	0.022	0.059	-0.187	-0.409	0.088	-0.004	-0.081	-0.125	0.005	-0.121	0.137	0.487	-0.332	0.358
Mo	-0.150	-0.403	0.349	-0.886	0.741	-0.050	0.743	0.632	0.171	-0.067	0.049	0.818	0.586	-0.586	0.766	0.557	0.409	0.637	0.075
Sr	-0.079	0.560	-0.034	0.711	-0.857	-0.296	-0.749	-0.810	-0.584	-0.105	-0.225	-0.761	-0.714	0.510	-0.827	-0.581	-0.287	-0.844	-0.044
Ce	0.938	-0.685	-0.672	-0.096	0.259	0.480	0.166	0.249	0.650	0.905	0.984	-0.122	0.661	0.469	0.384	0.347	0.338	0.135	0.826
Y	0.847	-0.857	-0.763	-0.239	0.463	0.852	0.478	0.523	0.777	0.863	0.887	0.113	0.733	0.184	0.538	0.600	0.635	0.389	0.790
V	-0.072	0.109	0.161	-0.171	-0.285	-0.230	-0.019	-0.336	-0.402	0.004	-0.018	-0.031	-0.146	0.183	-0.143	0.003	0.428	-0.394	0.285
Pb	0.858	-0.632	-0.552	-0.280	0.218	0.361	0.230	0.205	0.624	0.841	0.935	0.050	0.647	0.501	0.409	0.321	0.479	0.085	0.804
Cr	0.233	-0.328	-0.439	-0.115	-0.067	0.334	0.111	0.450	0.013	0.335	0.021	0.304	-0.095	-0.490	-0.044	-0.083	0.029	-0.263	0.030
Cd	-0.036	-0.547	0.172	-0.920	0.872	0.332	0.944	0.672	0.538	0.026	0.218	0.852	0.771	-0.364	0.909	0.791	0.778	0.901	0.210
As	0.709	-0.633	-0.443	-0.419	0.212	0.262	0.299	0.306	0.359	0.759	0.756	0.203	0.547	0.176	0.397	0.321	0.497	-0.021	0.750

	Ba	Mo	Sr	Ce	Y	V	Pb	Cr	Cd
Mo	-0.107								
Sr	0.568	-0.796							
Ce	-0.107	-0.015	-0.188						
Y	0.057	-0.033	-0.253	0.818					
V	0.933	-0.019	0.554	-0.087	-0.071				
Pb	0.093	0.108	-0.146	0.933	0.751	0.189			
Cr	0.332	0.220	-0.039	-0.031	0.064	0.244	0.069		
Cd	-0.046	0.717	-0.745	0.103	0.383	-0.037	0.210	-0.095	
As	0.347	0.348	-0.139	0.723	0.544	0.432	0.870	0.443	0.191

Table 22. Suggested resource potential of Co-rich crusts within the EEZ of Pacific nations, Hawaii, and U.S. territories and possessions

Area	Relative Ranking	Potential[1]
Republic of the Marshall Islands	1	High
Johnston Atoll	2	High
French Polynesia	3	High
Kiribati (Line & Phoenix Islands)	4	High
Hawaiian Islands	5	Medium
Federated States of Micronesia	6	Medium
Kingman-Palmyra Islands	7	Medium
Howland-Baker Islands	8	Medium
Wake Island	9	Medium
Commonwealth Northern Mariana Is.	10	Low
Jarvis Island	11	Low
Tokelau Islands	12	Low
Kiribati (Gilbert Islands)	13	Low
Republic of Palau	14	Low
Guam	15	Low
American Samoa	16	Low

[1]Based on 11 criteria presented by Hein et al. (1988, 1991)

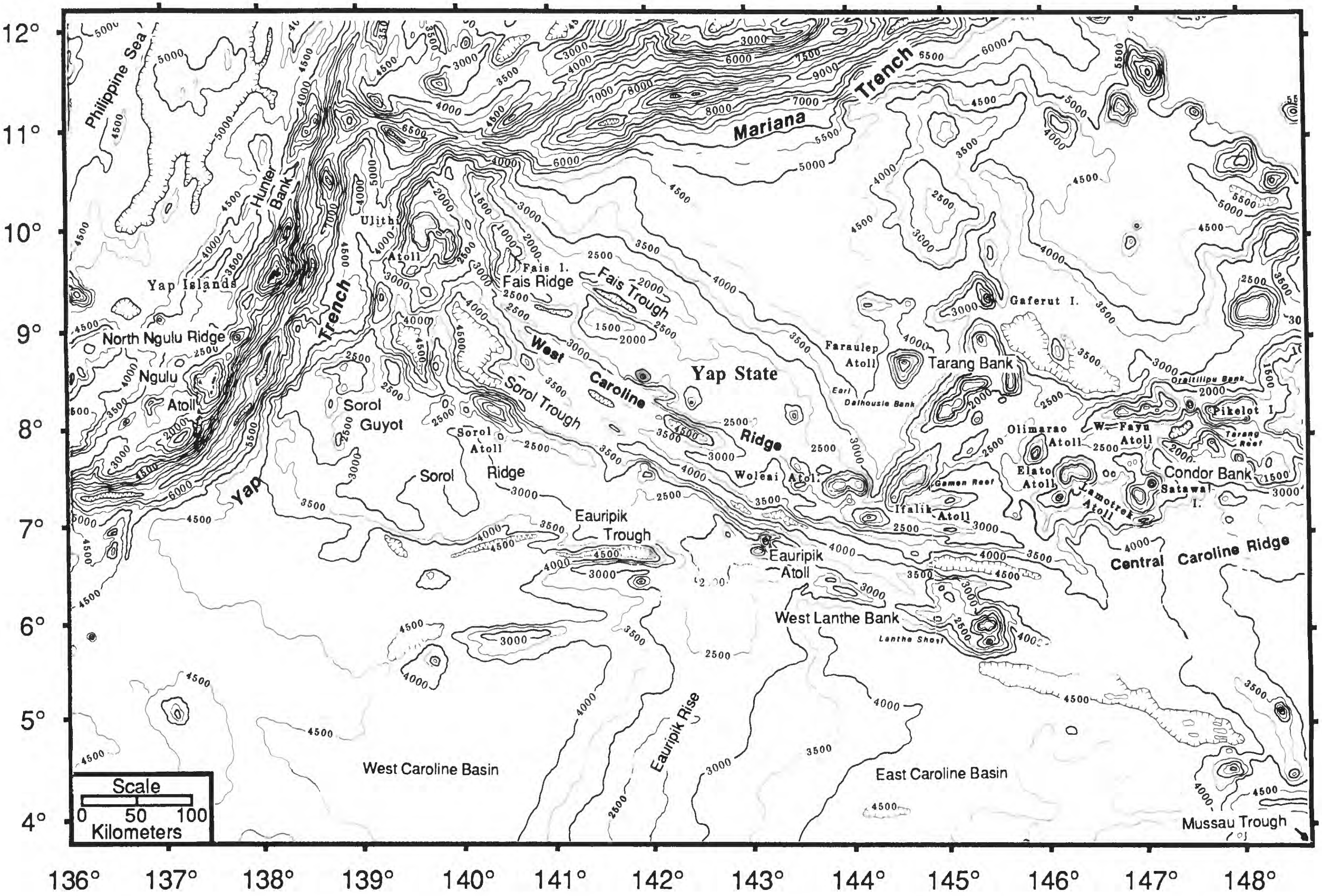

Figure 1. Atoll, island, and seamount names within the Exclusive Economic Zone of the western Federated States of Micronesia, including the Yap Arc-Trench and the west and central Caroline Ridge. Hatchured lines are basins. Contour interval = 500 m, modified from Chase, Seekins and Young (1988).

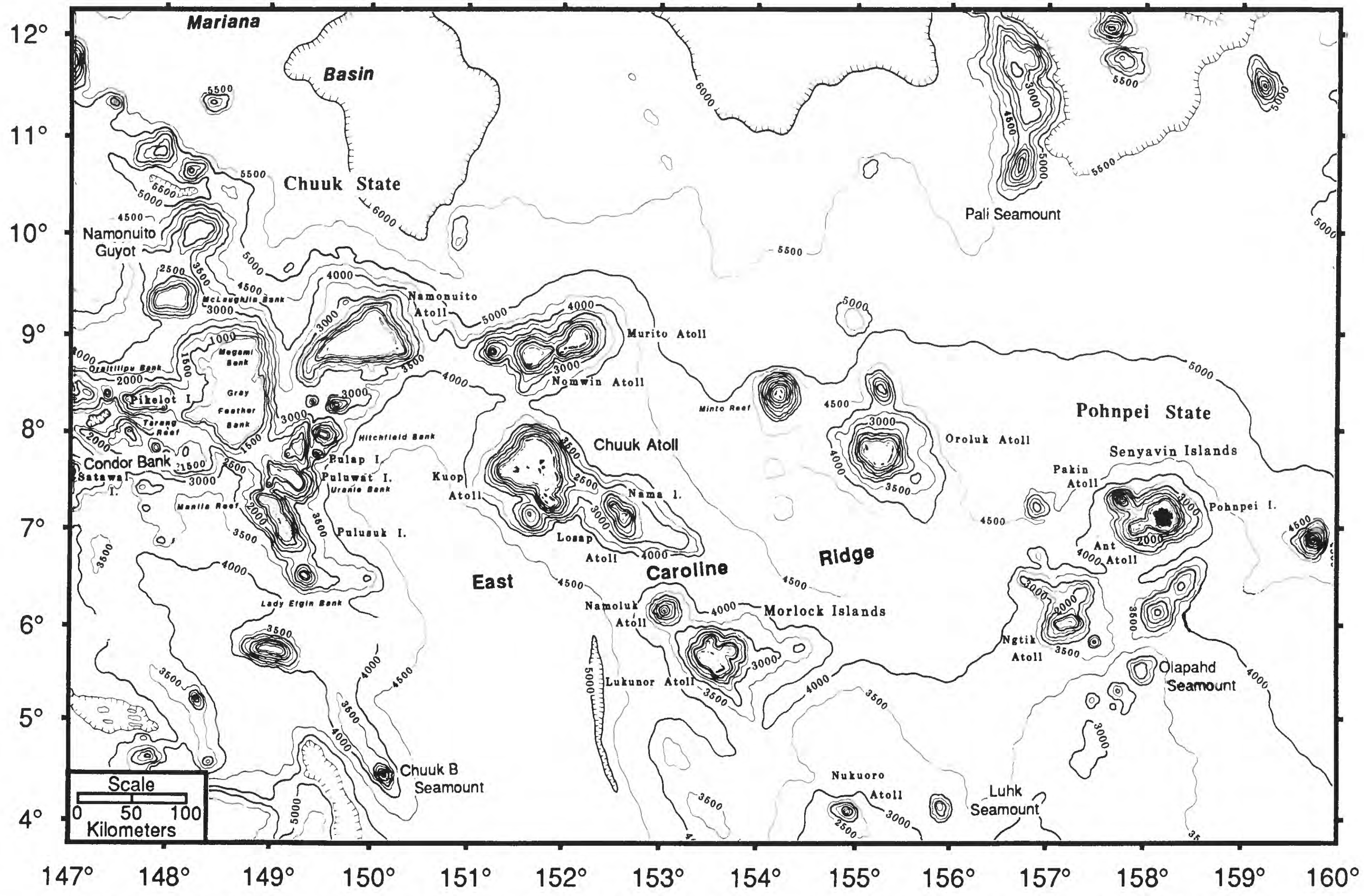

Figure 2. Atoll, island, and seamount names within the Exclusive Economic Zone of the eastern Federated States of Micronesia, including the east Caroline Ridge. Kosrae State is off the map to the east. Hatchured lines are basins. Contour interval = 500 m, modified from Chase, Seekins and Young (1988).

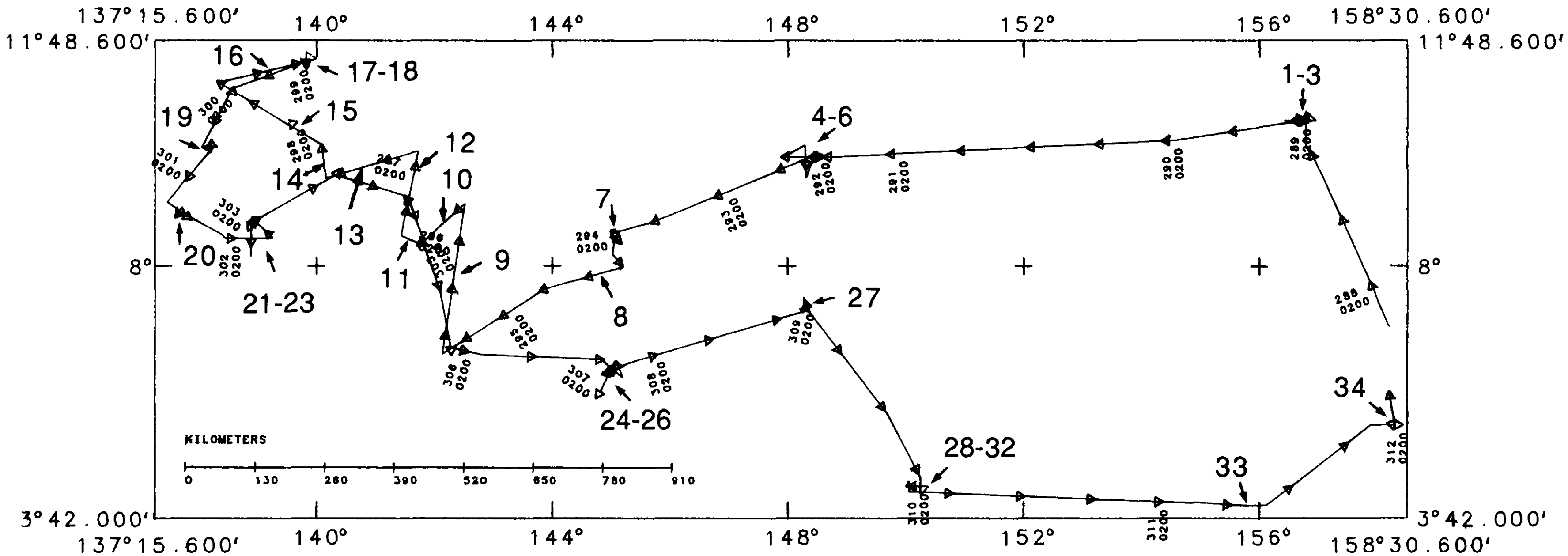

Figure 3. Trackline chart of cruise F11-90-CP. Large numbers indicate the location of individual seismic lines and tracklines. Smaller numbers along the trackline are the Julian day and hour of passage.

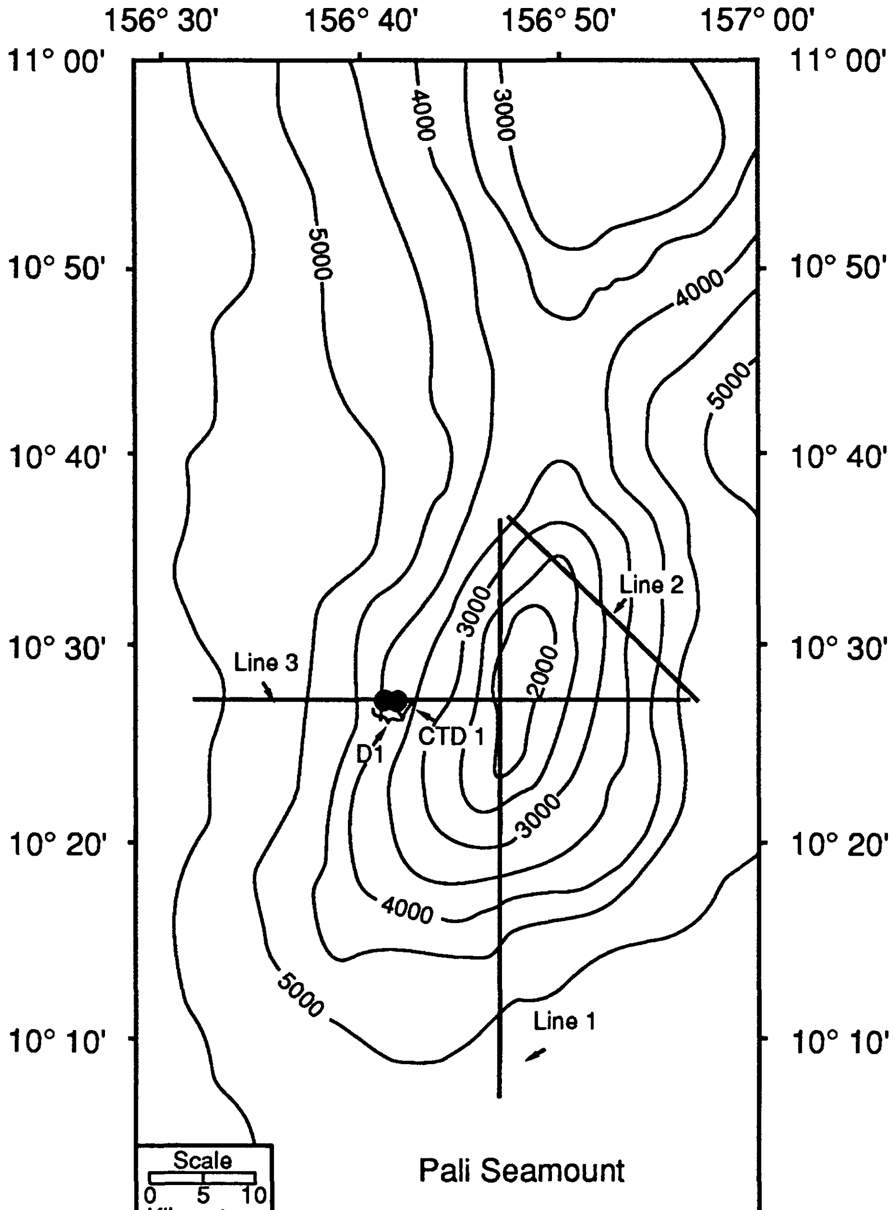

Figure 4. Trackline and Station map for Pali Seamount; bathymetry from Chase, Seekins, and Young (1988). Bathymetry is inaccurate, seamount consists of 2, possibly 3 peaks. D = Dredge, CTD = Temperature-salinity-oxygen profile. Contour interval is 500 m.

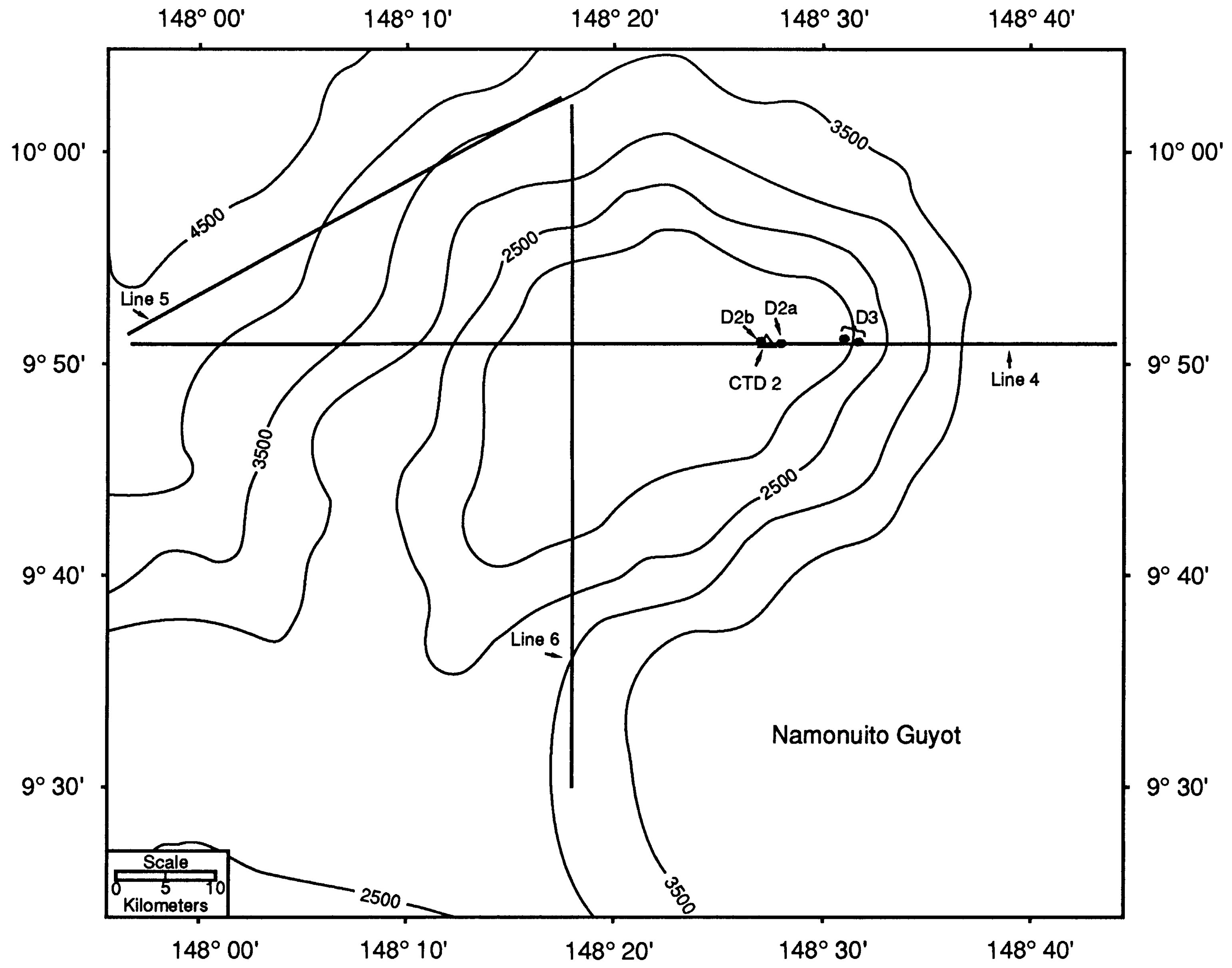

Figure 5. Trackline and station map for Namonuito Guyot; bathymetry from Chase, Seekins, and Young (1988). Lines 5 and 6 (Figs. 32-35) indicate that another seamount or guyot occurs adjacent to the northern flank of Namonuito Guyot. The bathymetry used in this figure does not accurately represent the topography as determined here. D = Dredge, CTD = Temperature-salinity-oxygen profile. Contour interval is 500 m.

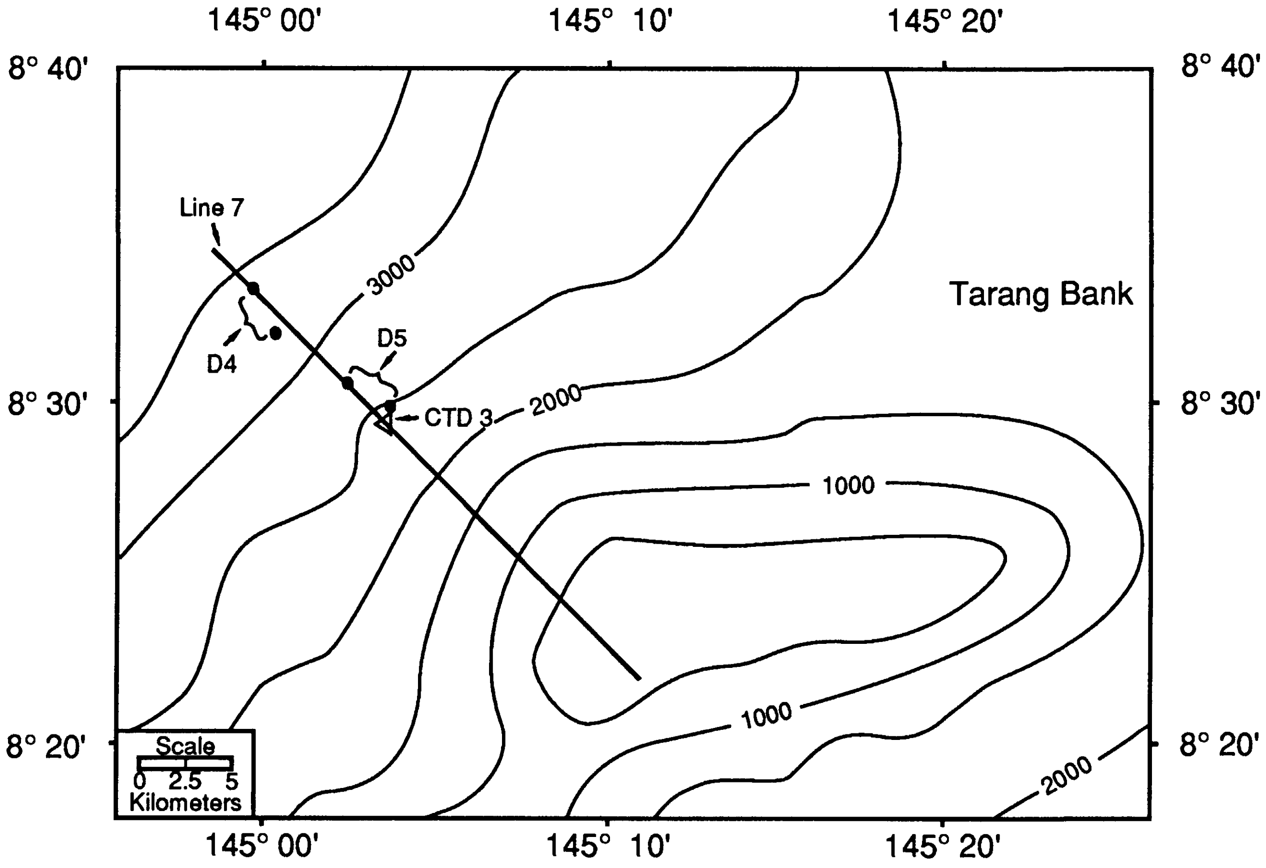

Figure 6. Trackline and Station map for Tarang Bank; bathymetry from Chase, Seekins, and Young (1988). D = Dredge, CTD = Temperature-salinity-oxygen profile. Contour interval is 500 m.

West Caroline Ridge Bathymetry

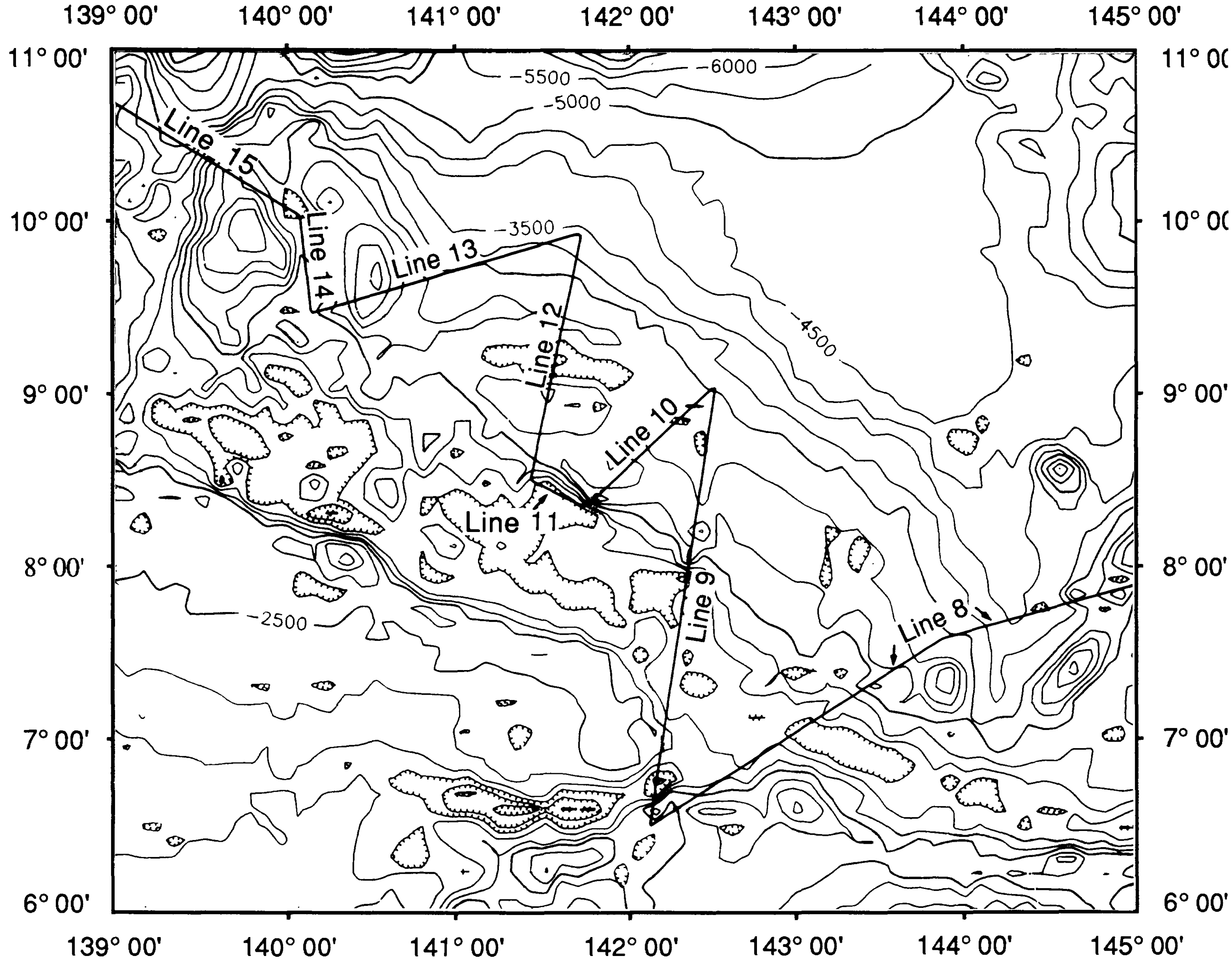

Figure 7. Bathymetry and single-channel seismic lines for west Caroline Ridge. The bathymetry is from our seismic and transit lines and from lines obtained from the the National Geophysical Data Center (NGDC; see Appendix 1 for all tracklines and Appendix 2 for names of topographic features). Areas of no data were filled in with NGDC, ETOPO5. Contour interval is 500m.

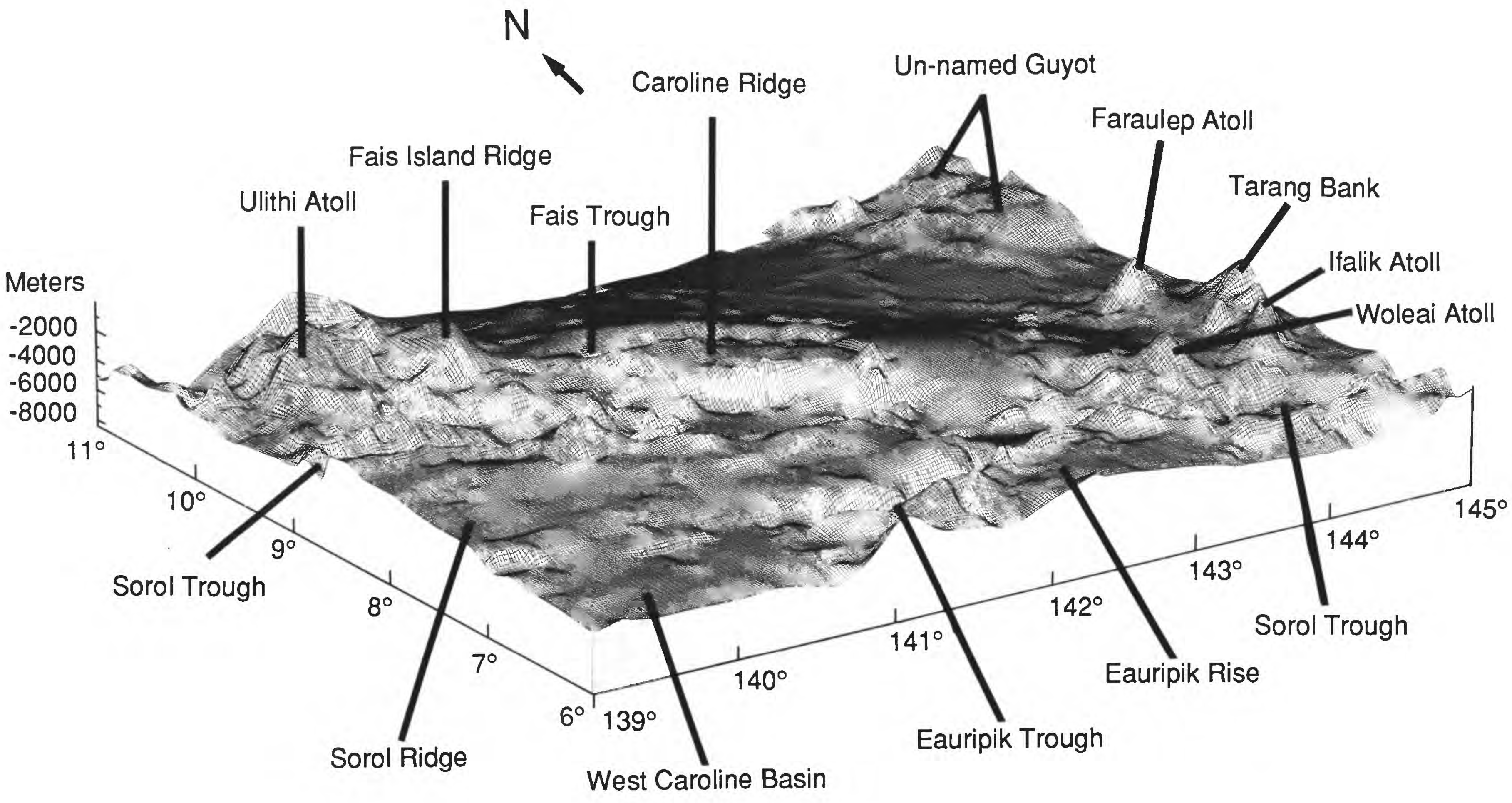

Figure 8. Computer generated physiographic map of Caroline Ridge derived from the bathymetry in Figure 7. View looking to the northeast from 215° azimuth at 20° elevation; vertical exaggeration is 10 times. Note that several, very low relief, linear features are artifacts of ship track lines.

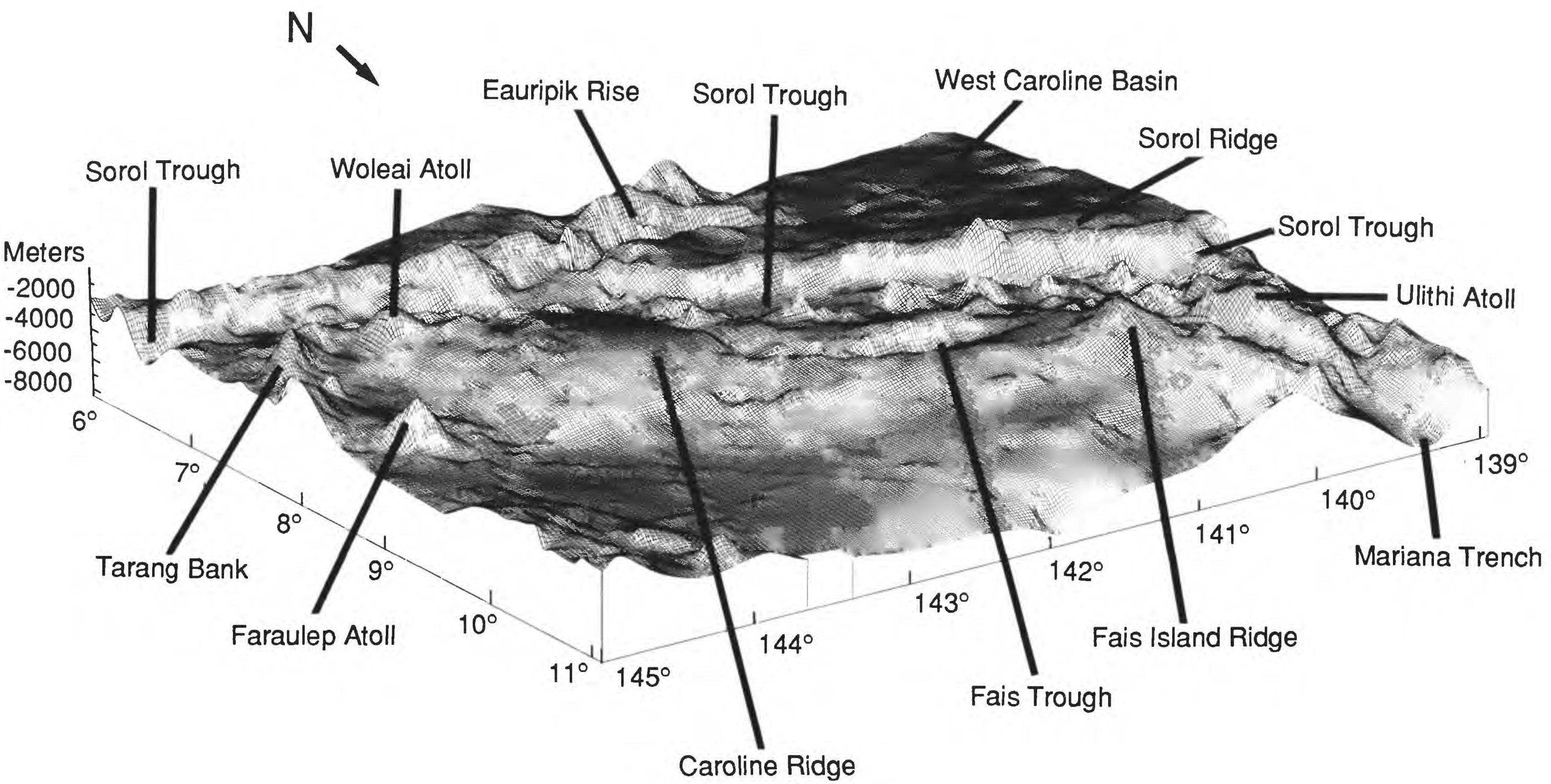

Figure 9. Computer generated physiographic map of Caroline Ridge derived from the bathymetry in Figure 7. View looking to the southwest from 35° azimuth at 20° elevation; vertical exaggeration is 10 times. Note that several, very low relief, linear features are artifacts of ship track lines.

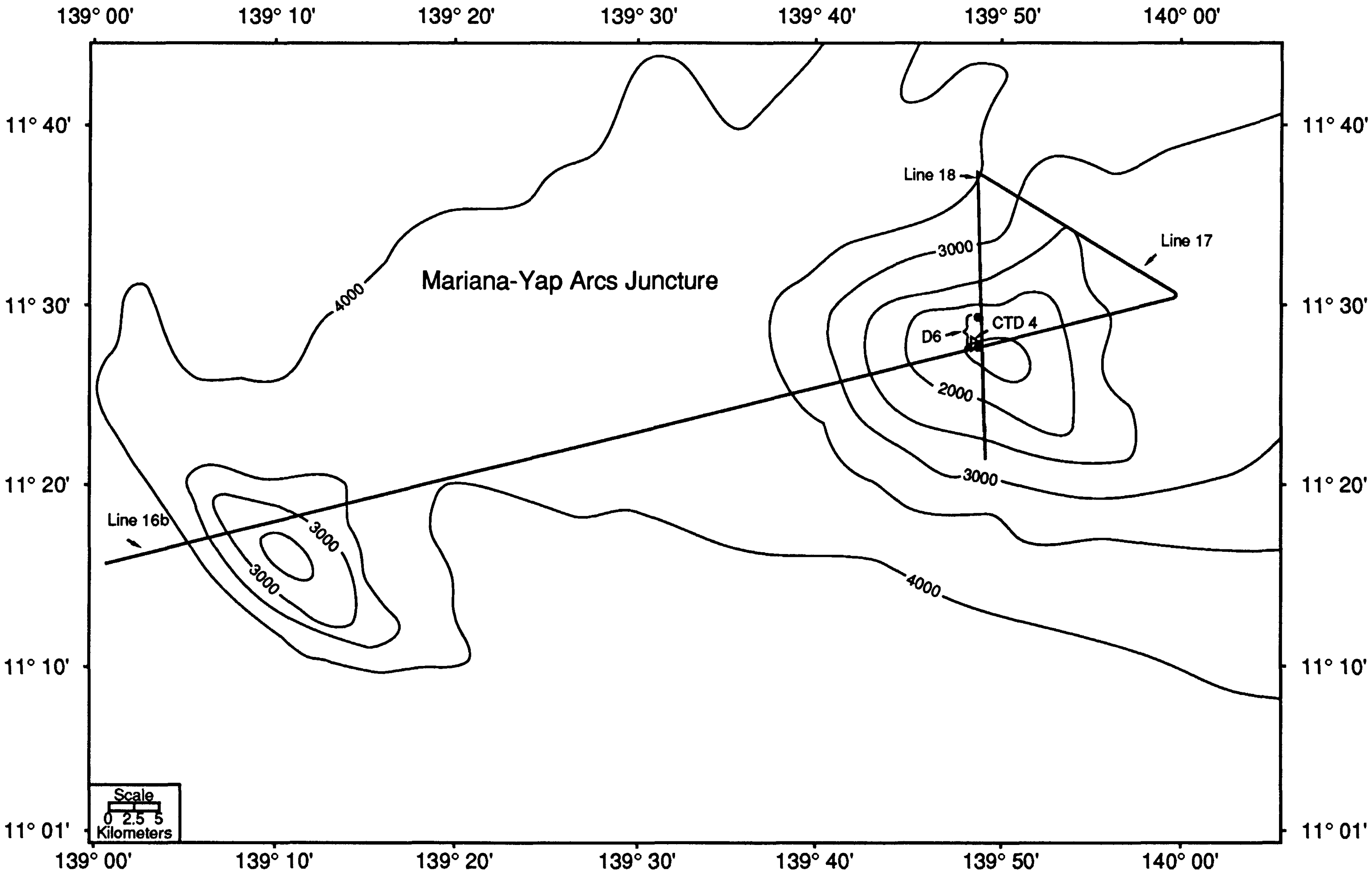

Figure 10. Trackline and Station map for the Mariana - Yap Arcs Juncture; bathymetry from Chase, Seekins, and Young (1988). D = Dredge, CTD = Temperature-salinity-oxygen profile. Contour interval is 500 m.

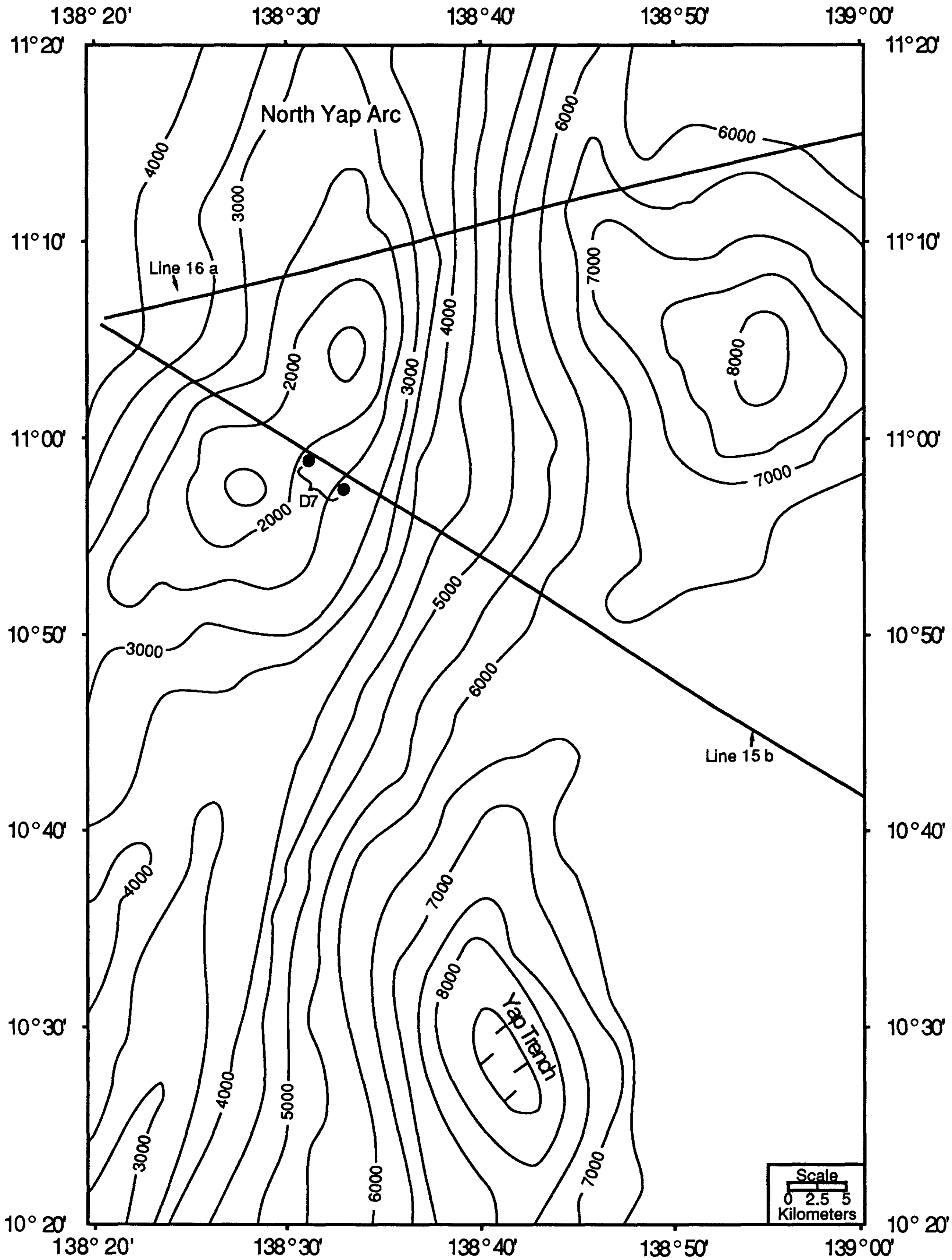

Figure 11. Trackline and Station map for North Yap Arc; bathymetry from Chase, Seekins, and Young (1988). D = Dredge, a and b = divisions of Lines 15 and 16. Contour interval is 500 m.

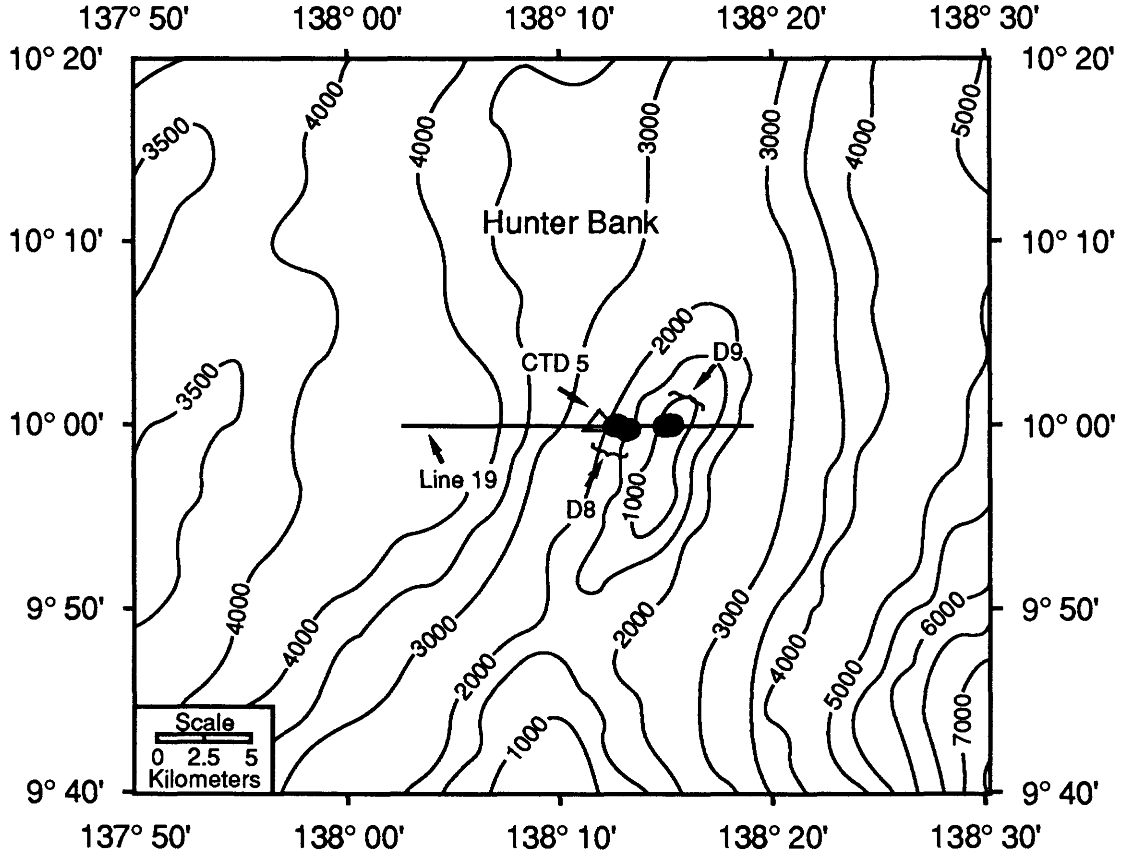

Figure 12. Trackline and station map for Hunter Bank, Yap Arc; bathymetry from Chase, Seekins, and Young (1988). D = Dredge, CTD = Temperature-salinity-oxygen profile. Contour interval is 500 m.

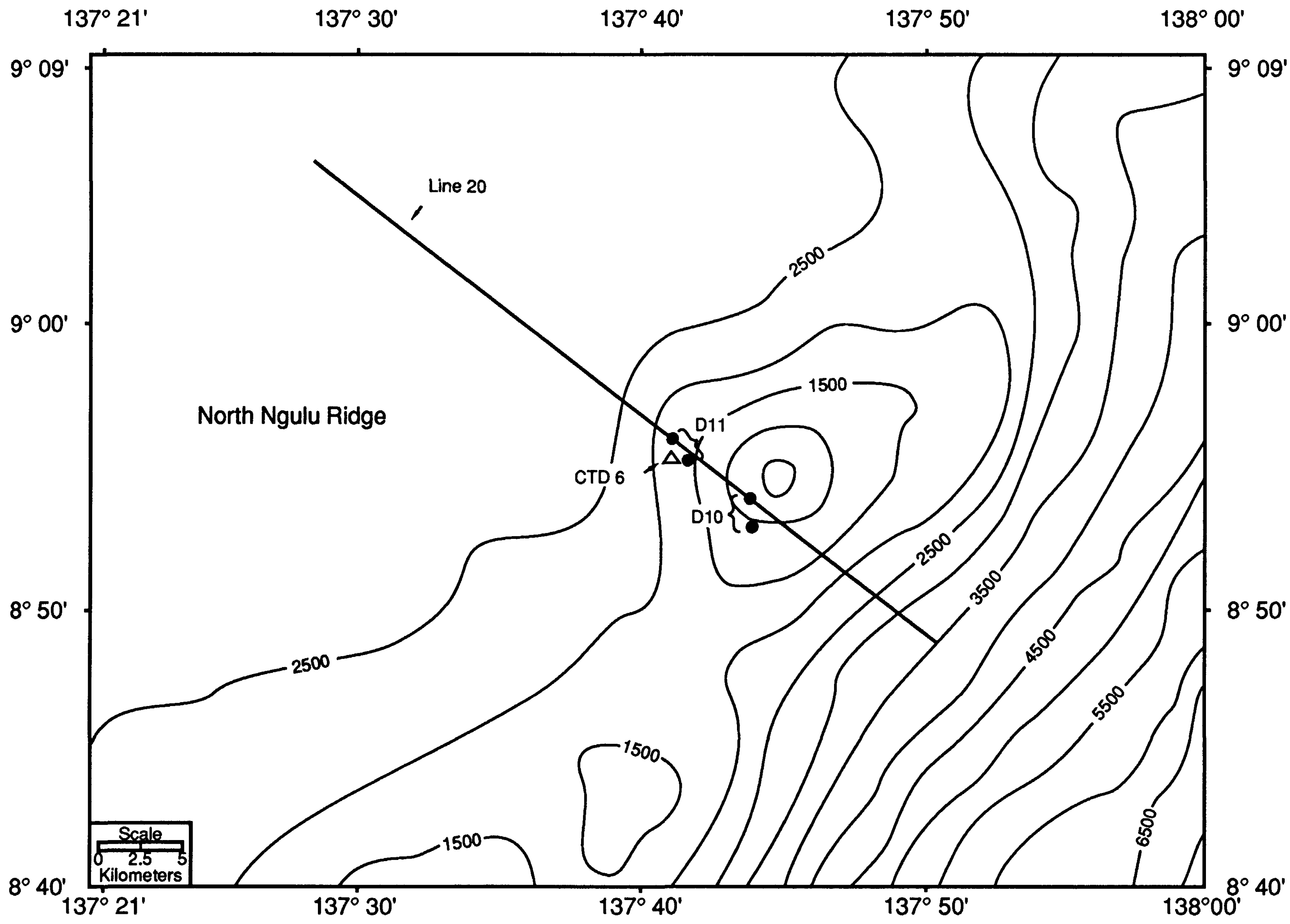

Figure 13. Trackline and Station map for north Ngulu Ridge and Yap Arc; bathymetry from Chase, Seekins, and Young (1988). D = Dredge, CTD = Temperature-salinity-oxygen profile. Contour interval is 500 m.

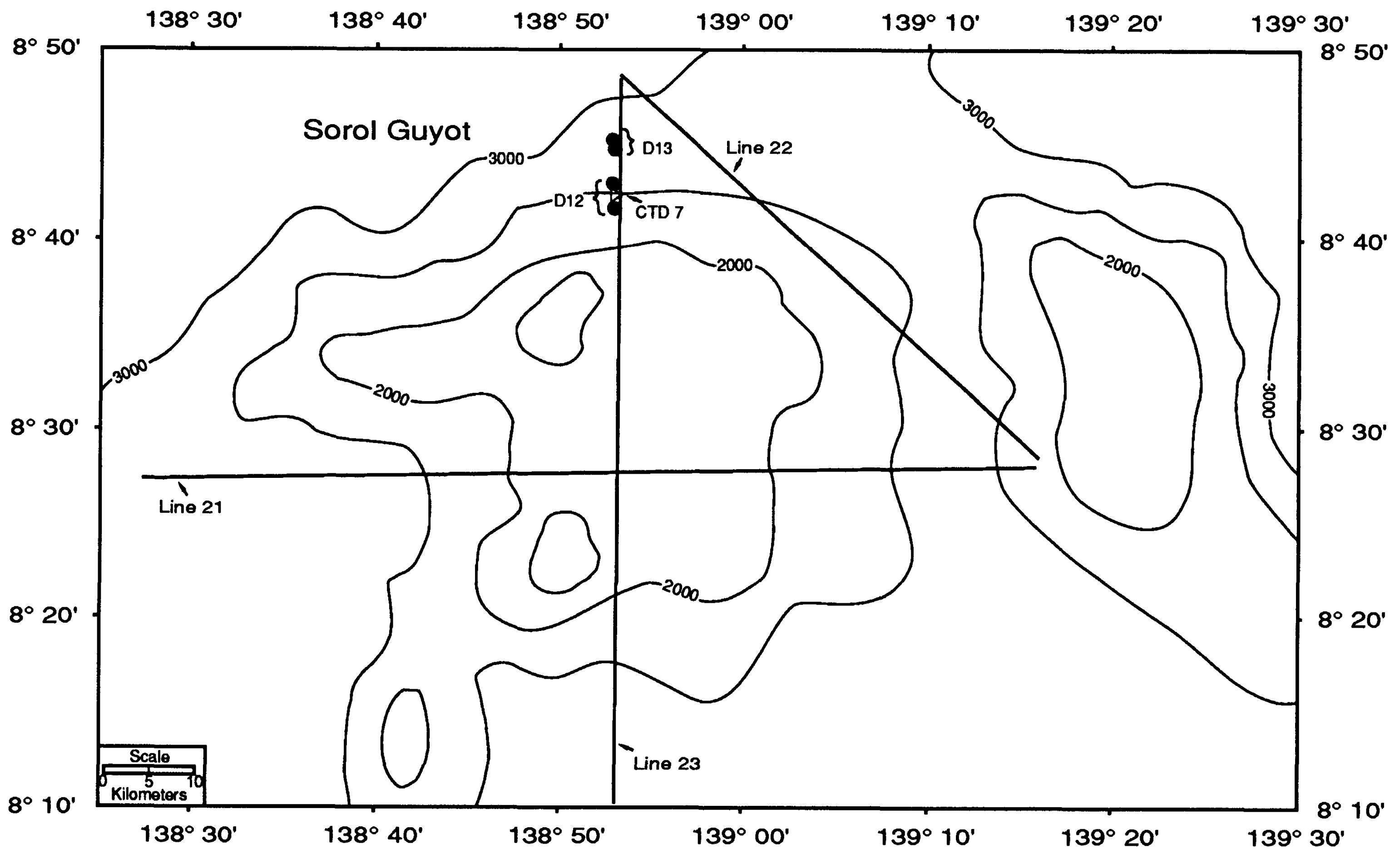

Figure 14. Trackline and Station map for Sorol Guyot; bathymetry from Chase, Seekins, and Young (1988). D = Dredge, CTD = Temperature-salinty-oxygen profile. Contour interval is 500 m.

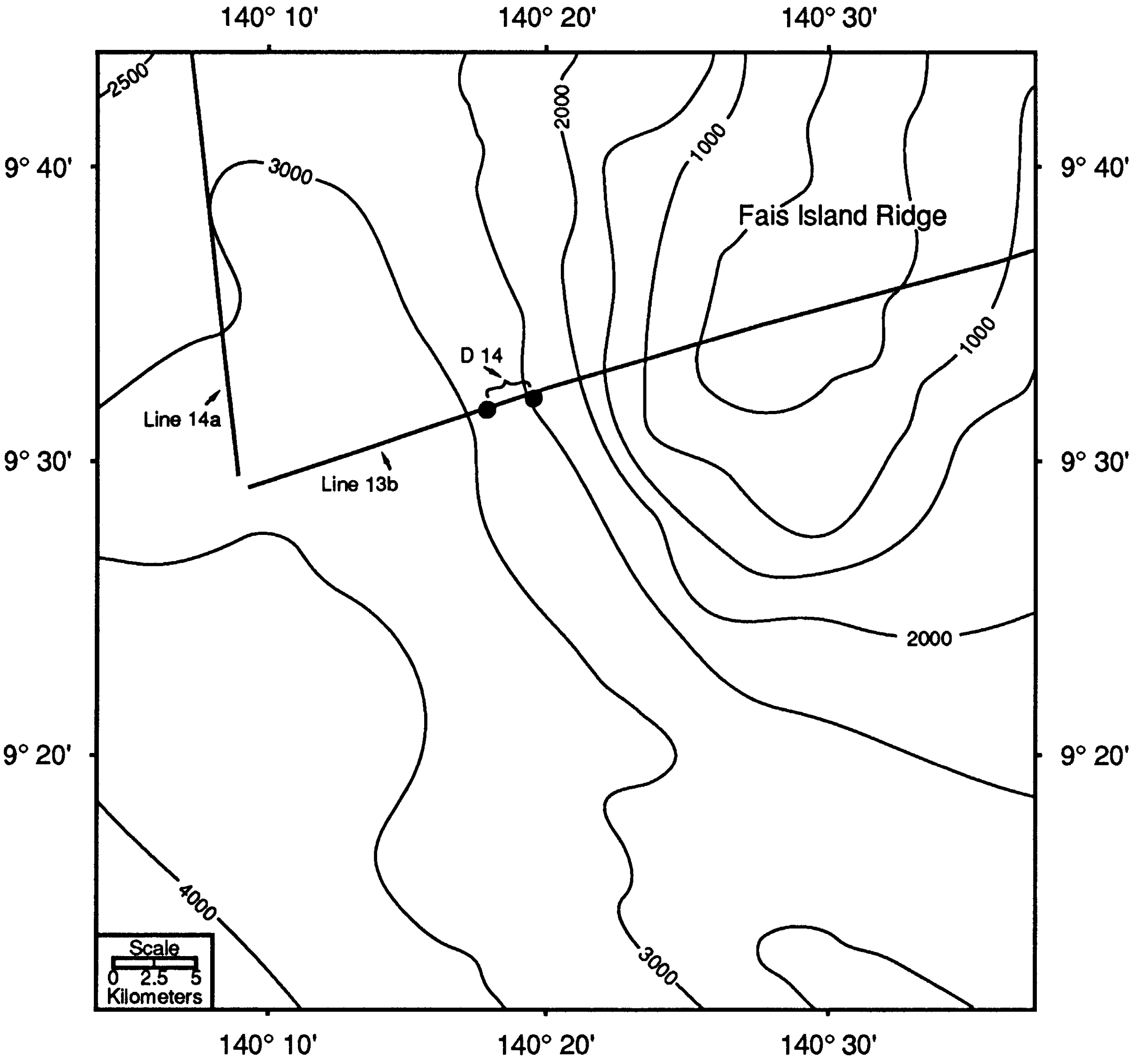

Figure 15. Trackline and Station map for Fais Island Ridge; bathymetry from Chase, Seekins, and Young (1988). D = Dredge. Contour interval is 500 m.

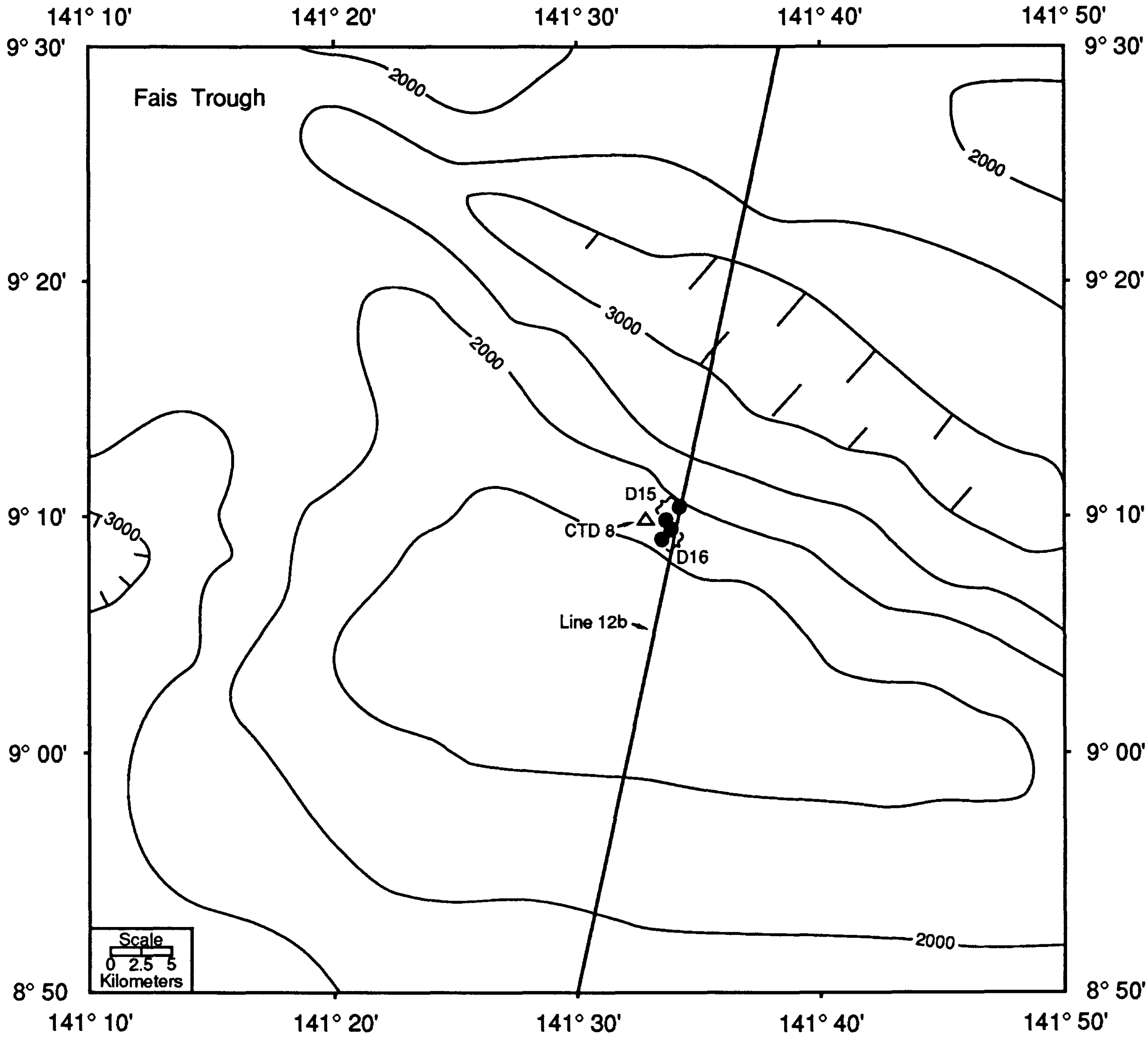

Figure 16. Trackline and Station map for Fais Trough; bathymetry from Chase, Seekins, and Young (1988). D = Dredge, CTD = Temperature-salinity-oxygen profile, b = divisions of bathymetry line. Contour interval is 500 m.

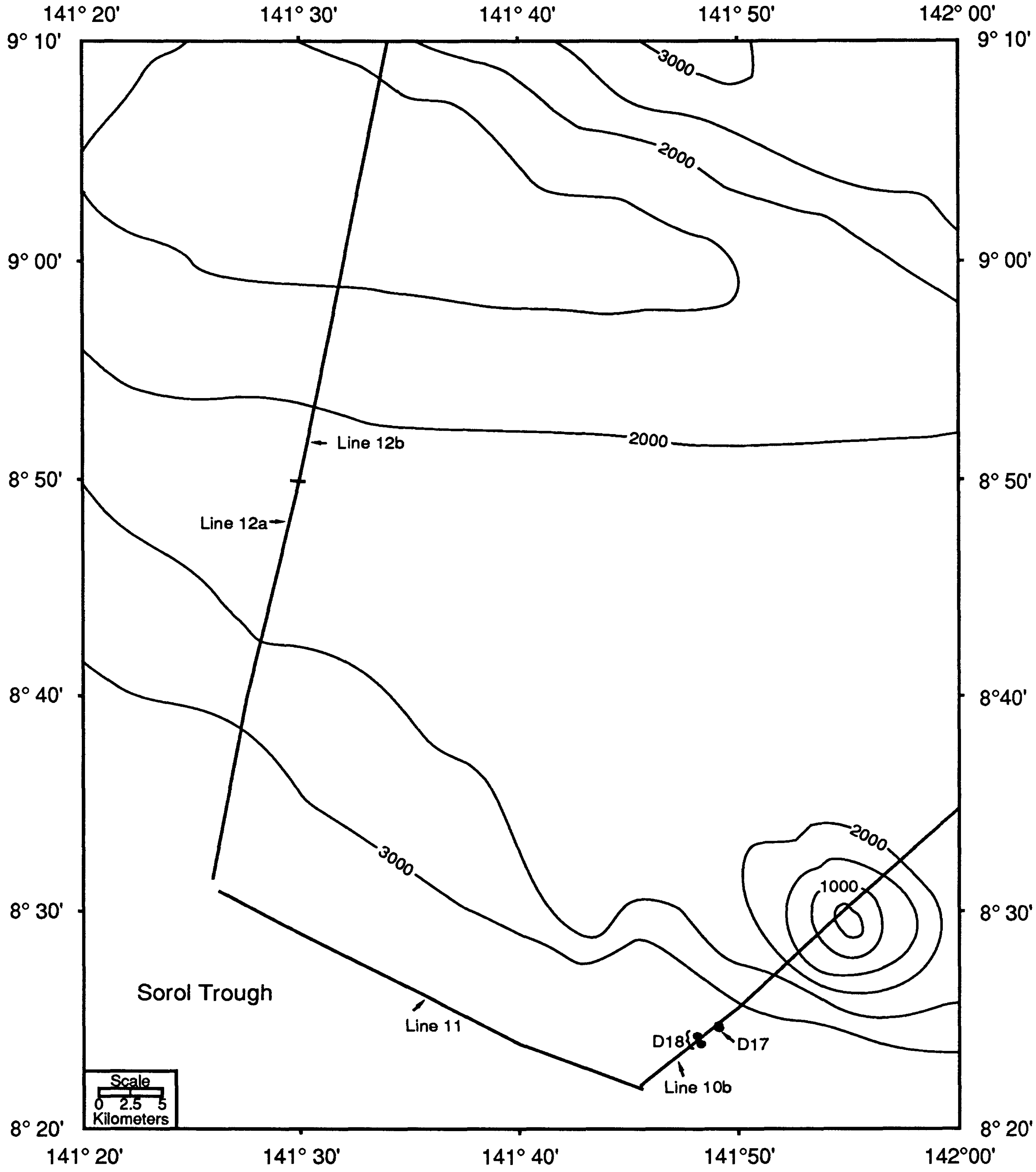

Figure 17. Trackline and Station map for Sorol Trough; bathymetry from Chase, Seekins, and Young (1988). Bathymetric lines indicate that the small seamount was mislocated and should be shifted about 5 km to the southwest. D = Dredge, a and b = Divisions of bathymetric lines. Contour interval is 500 m.

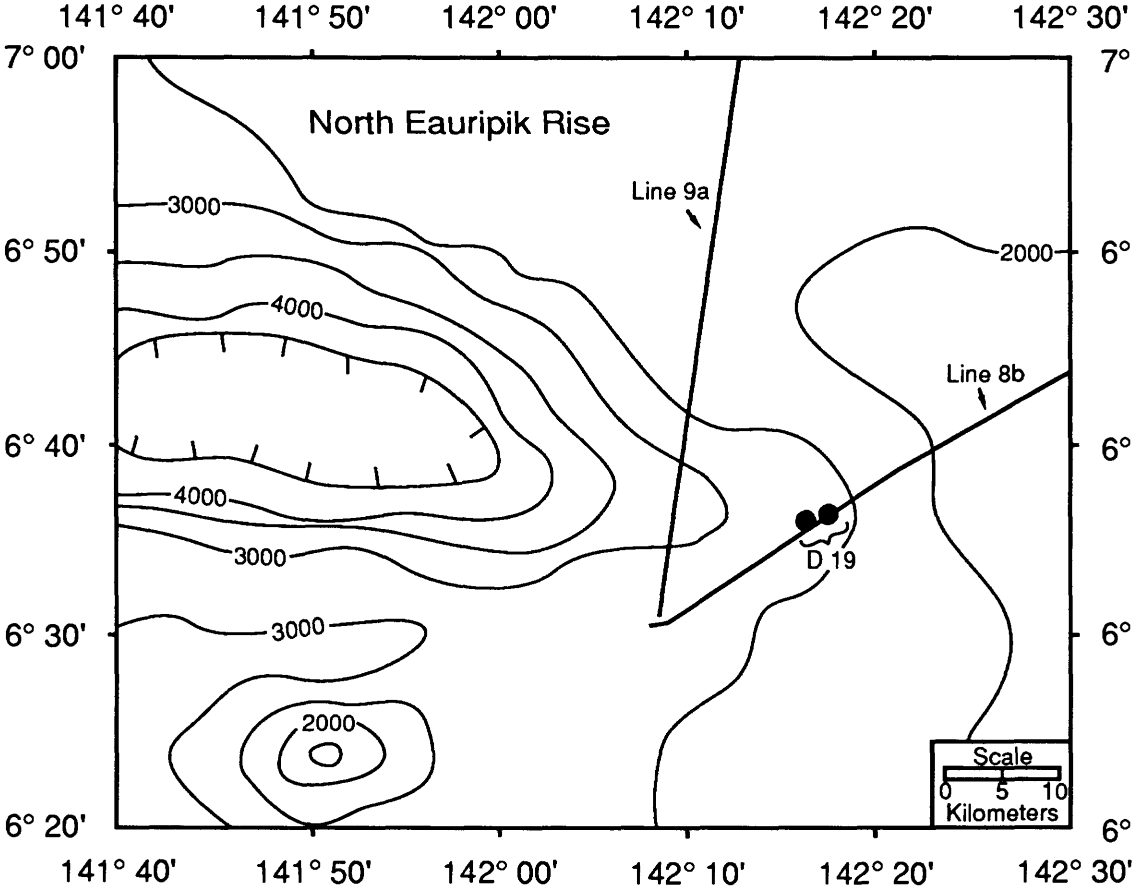

Figure 18. Trackline and station map for north Eauripik Rise; bathymetry from Chase, Seekins, and Young (1988). D = Dredge, a and b = division of bathymetry lines. Contour interval is 500 m.

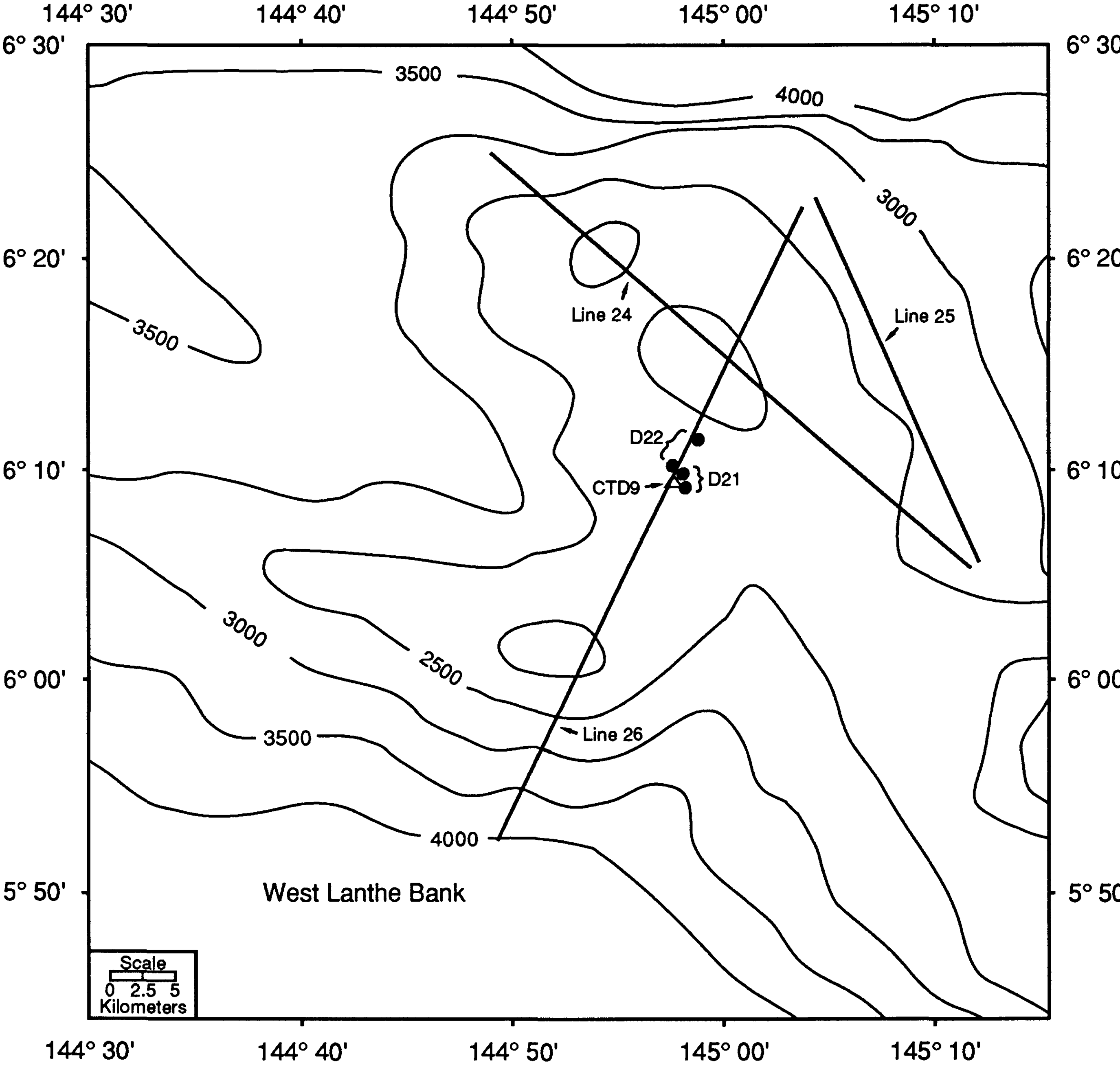

Figure 19. Trackline and station map for west Lanthe Bank; bathymetry modified from Chase, Seekins, and Young (1988). D = Dredge, CTD = Temperature-salinity-oxygen profile. Contour interval is 500 m.

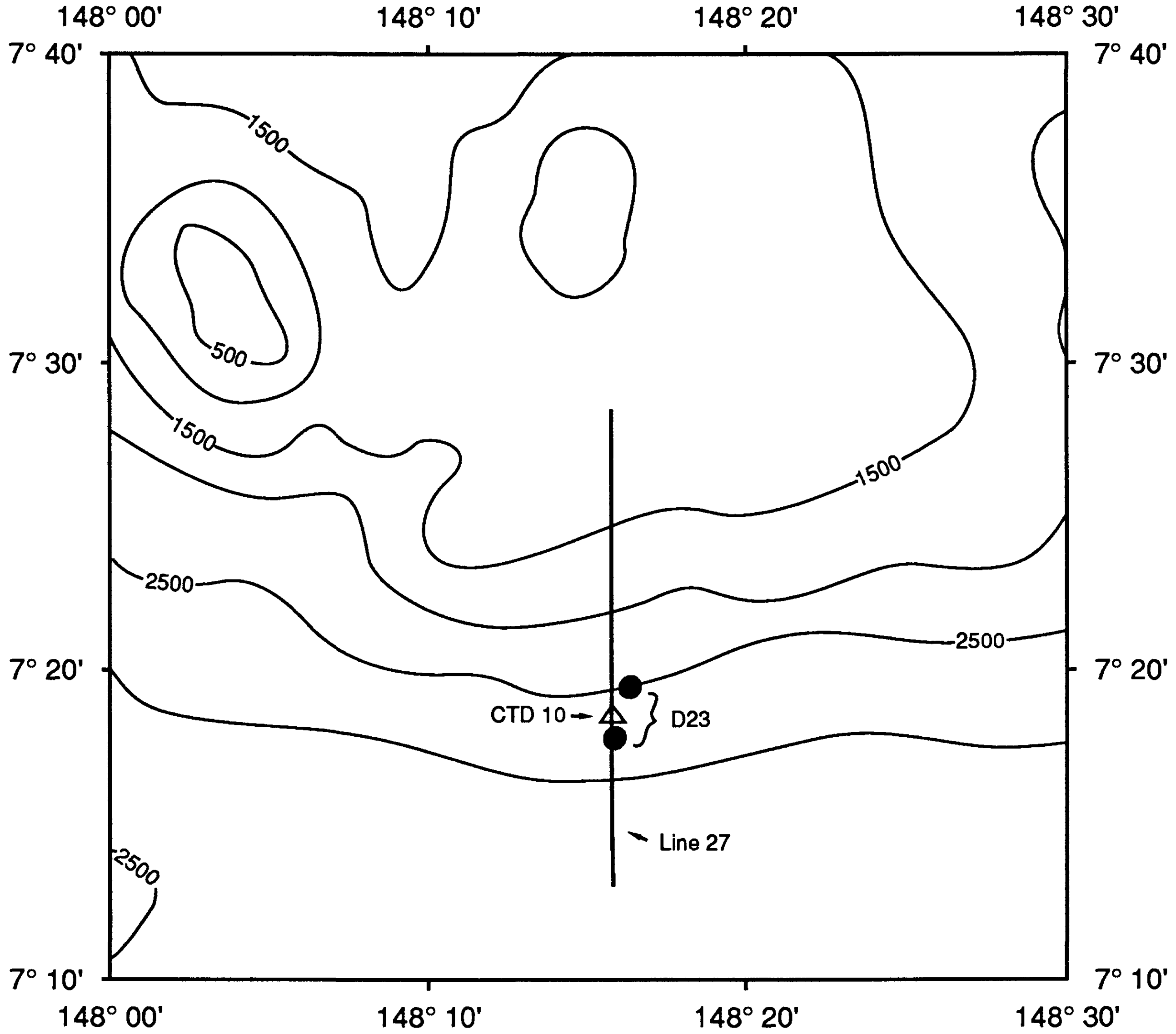

Figure 20. Trackline and station map for Condor Bank; bathymetry from Chase, Seekins and Young (1988). D = Dredge, CTD = Temperature-salinity-oxygen profile. Contour interval is 500 m.

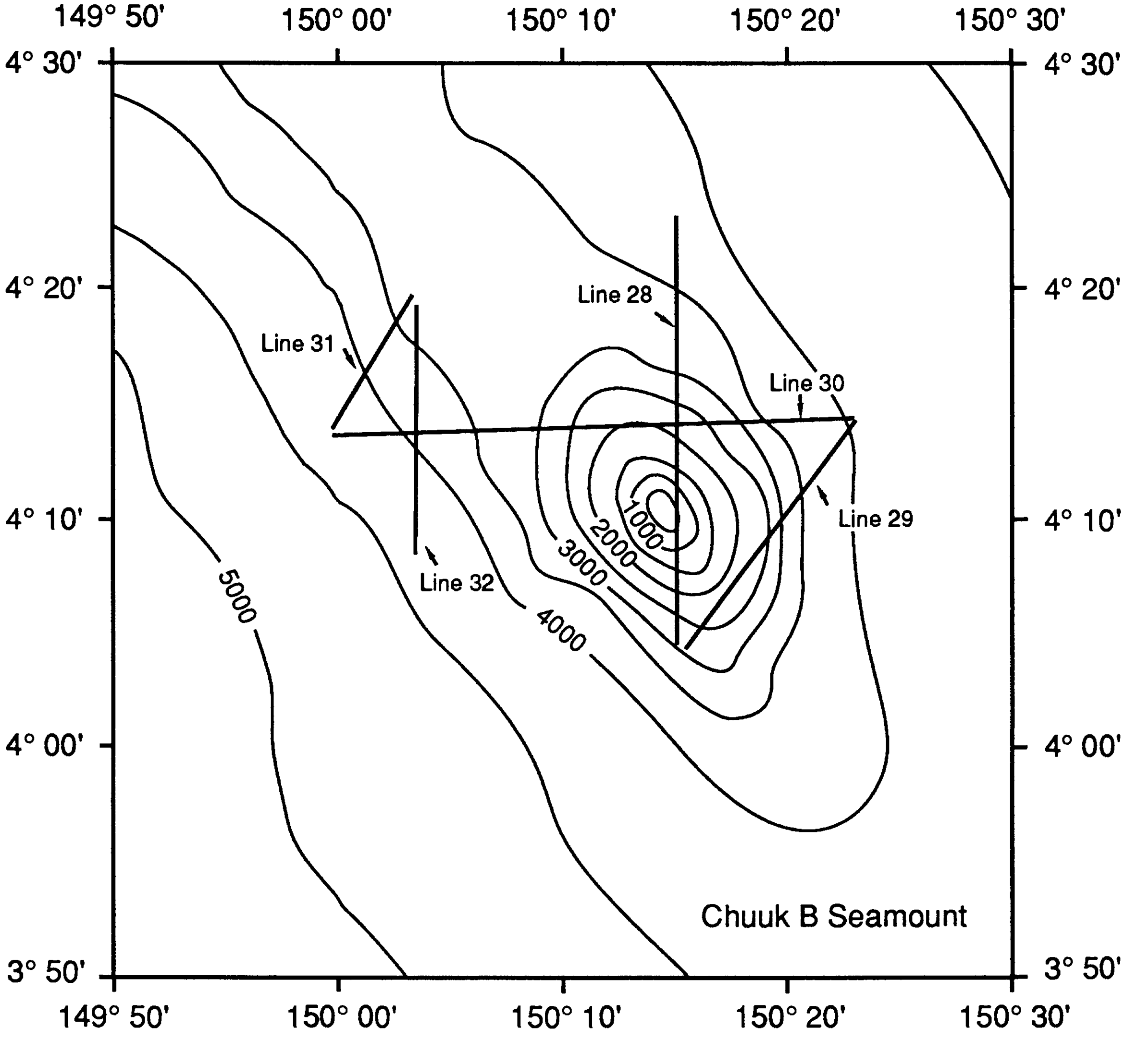

Figure 21. Trackline map for Chuuk B Seamount; the seamount was not located. Bathymetry from Chase, Seekins and Young (1988). Contour interval is 500 m.

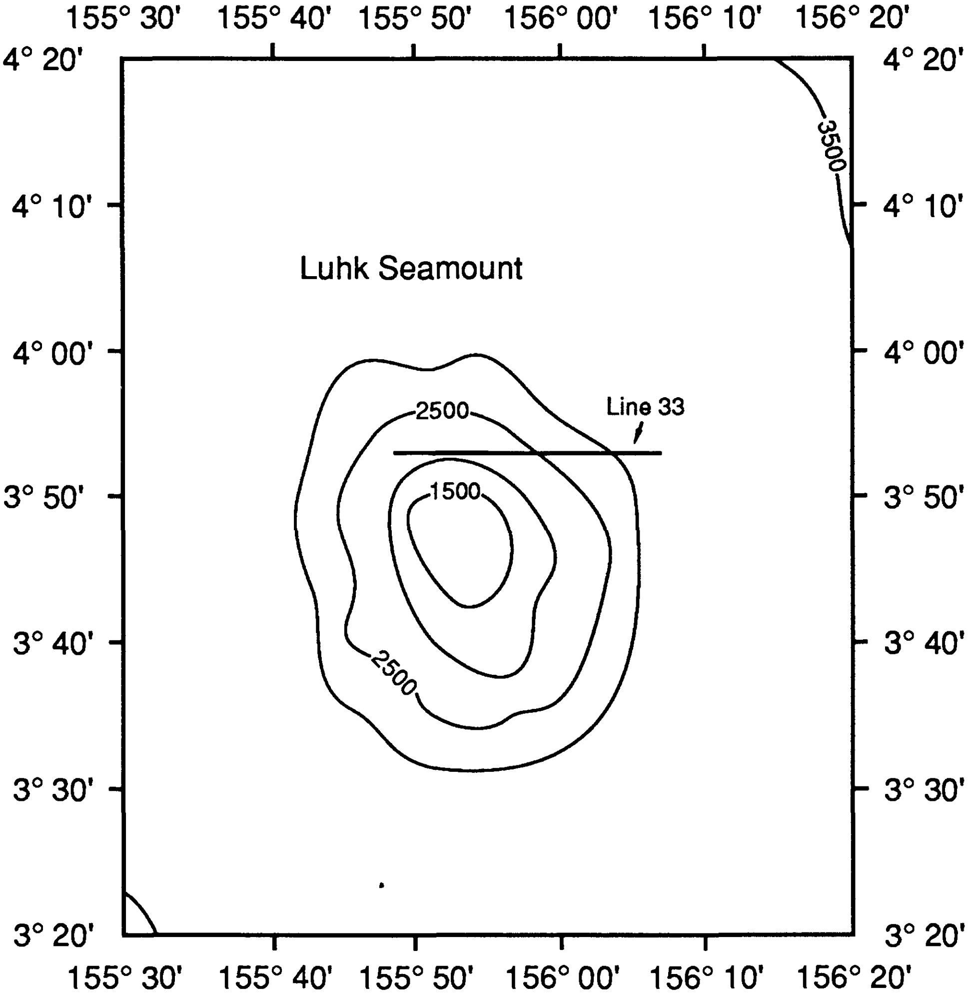

Figure 22. Trackline for Luhk Seamount; the seamount was not located. Bathymetry from Chase, Seekins and Young (1988). Contour interval is 500 m.

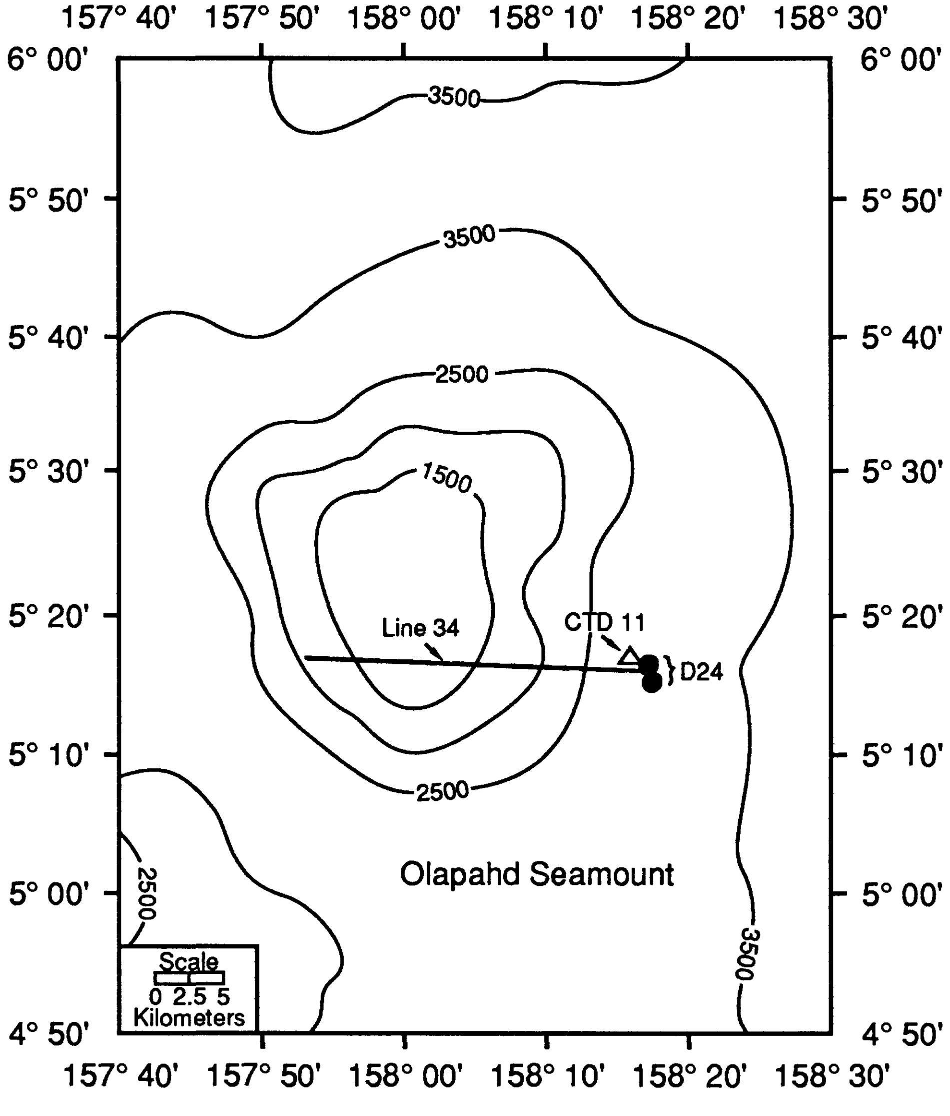

Figure 23. Trackline and station map for Olapahd Seamount; bathymetry from Chase, Seekins, and Young (1988). D = Dredge, CTD = Temperature-salinity-oxygen profile. Contour interval is 500 m.

S Pali Seamount N

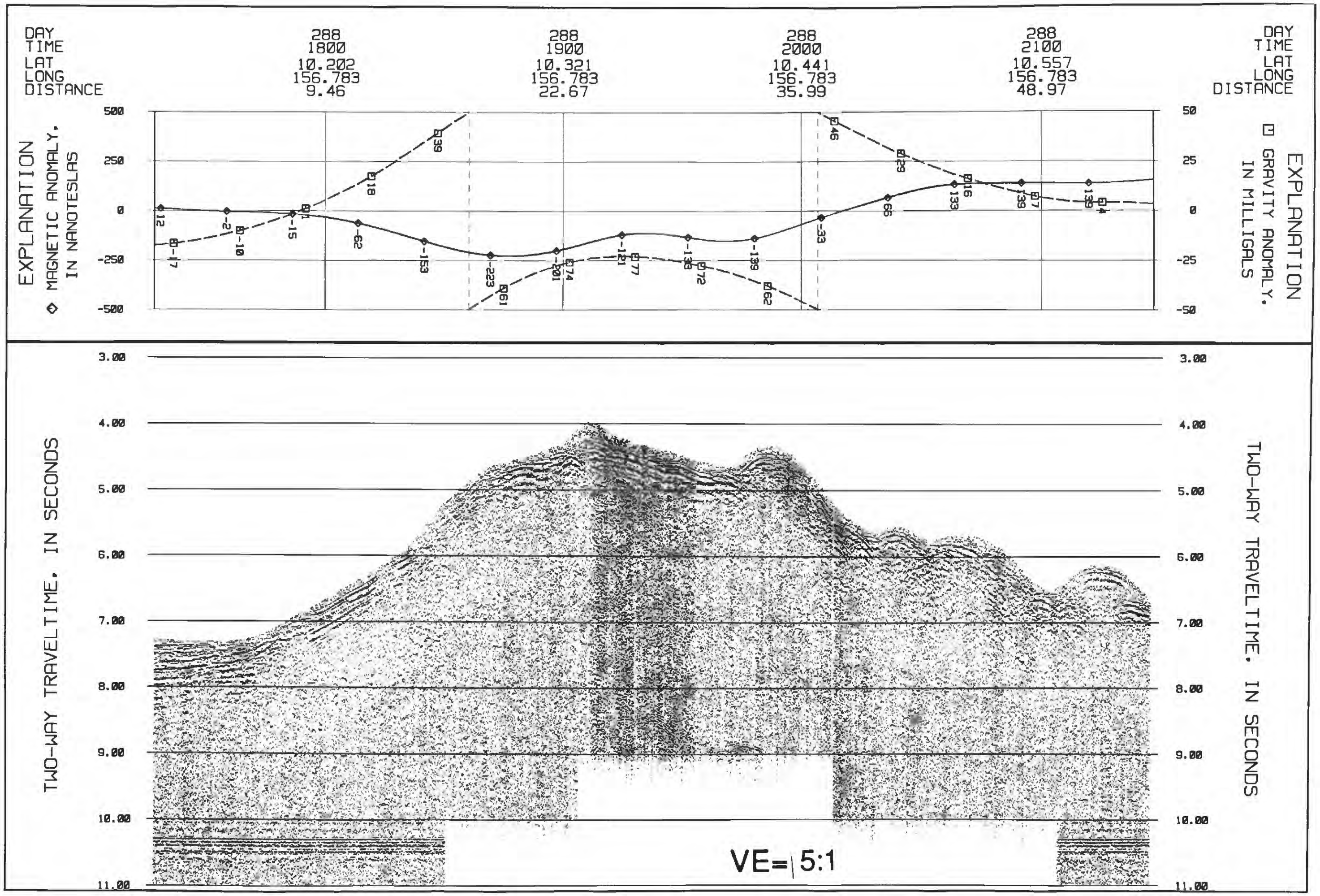

Figure 24. Pali Seamount, 195 in^3 single-channel airgun line 1 and associated gravity and magnetic profiles (See figure 4 for location).

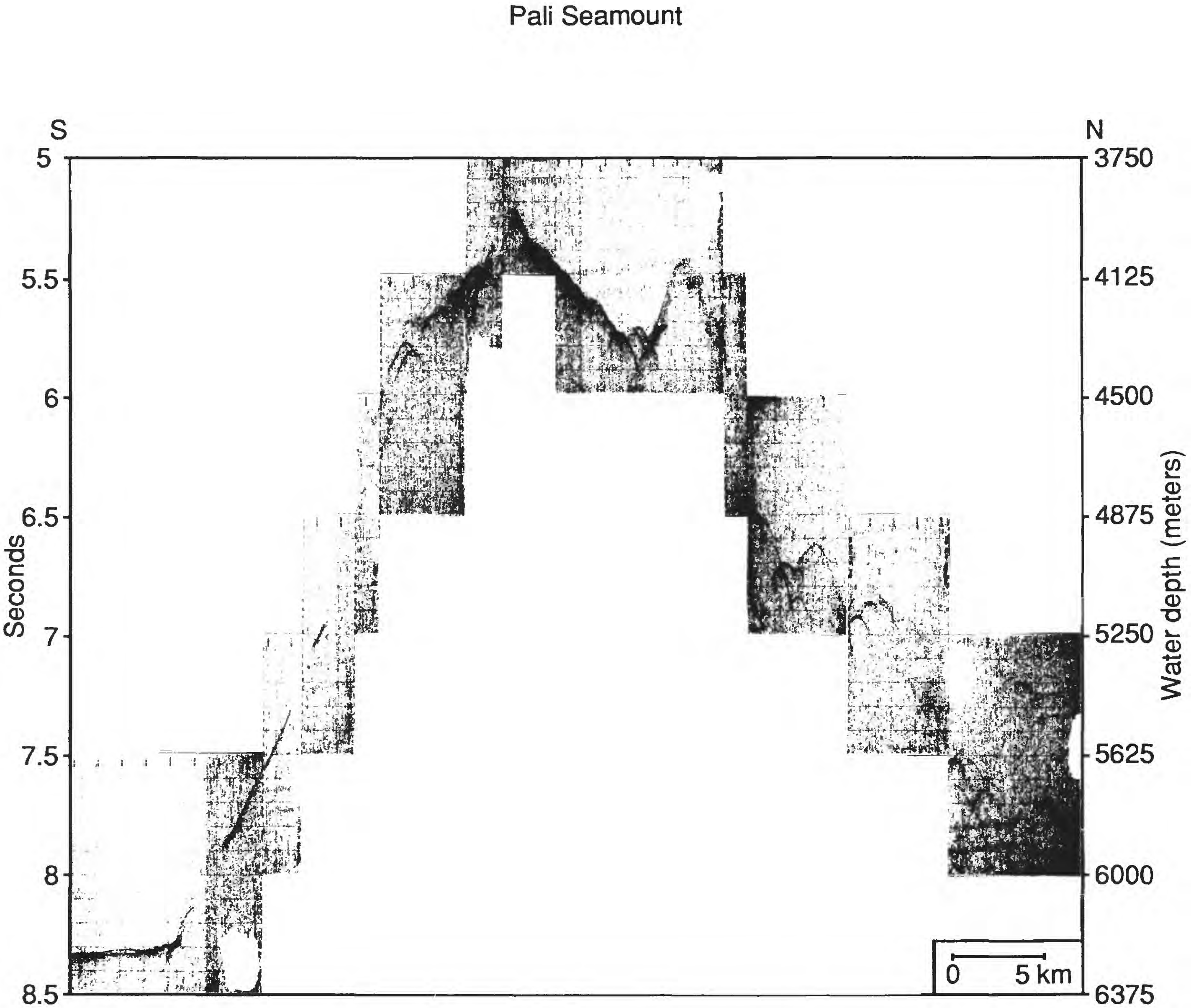

Figure 25. Pali Seamount, 3.5 kHz line 1 (see Fig. 4 for location).

North East Flank of Pali Seamount

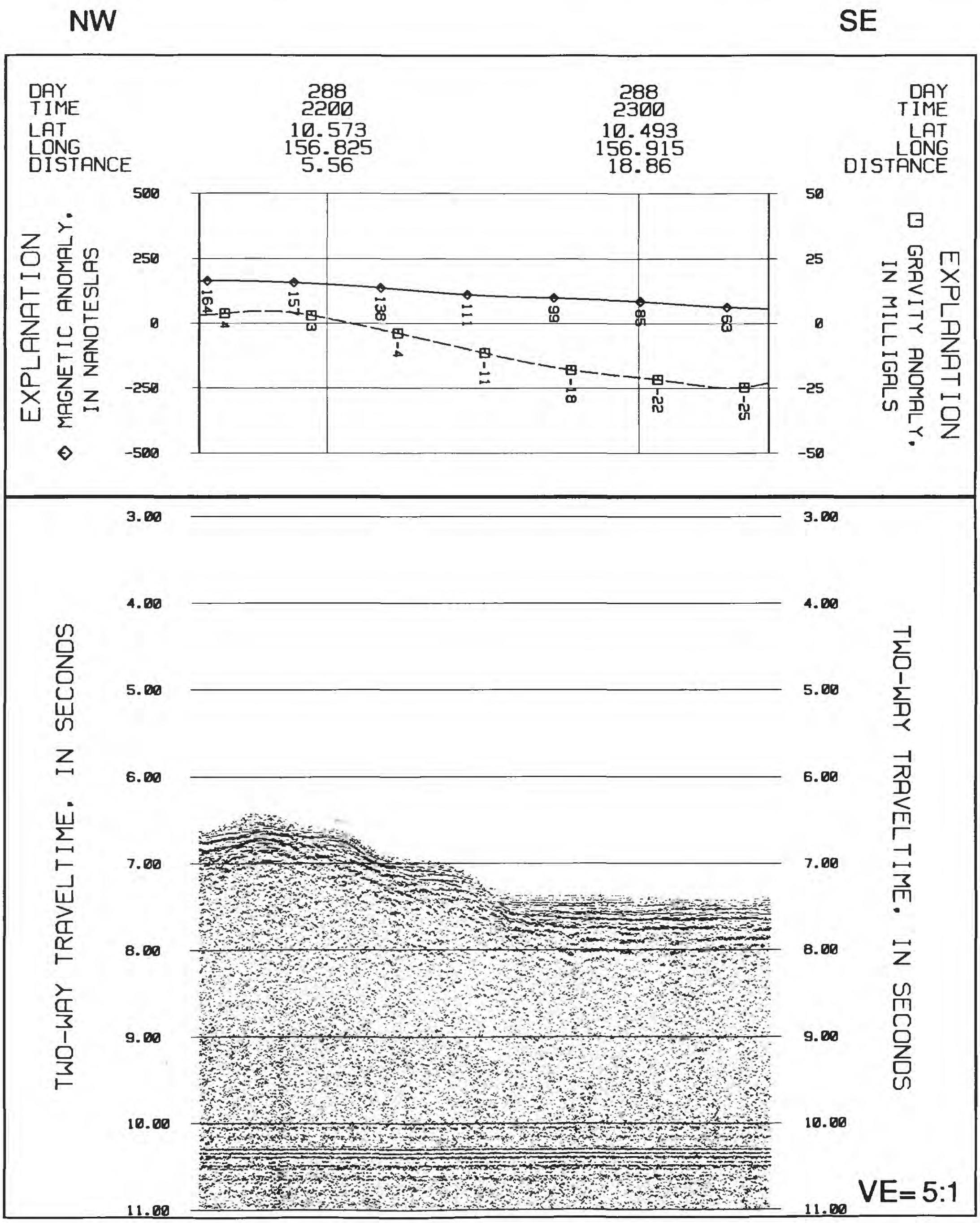

Figure 26. Pali Seamount, 195 in^3 single-channel airgun line 2 and associated gravity and magnetic profiles (see figure 4 for location).

North East Flank of Pali Seamount

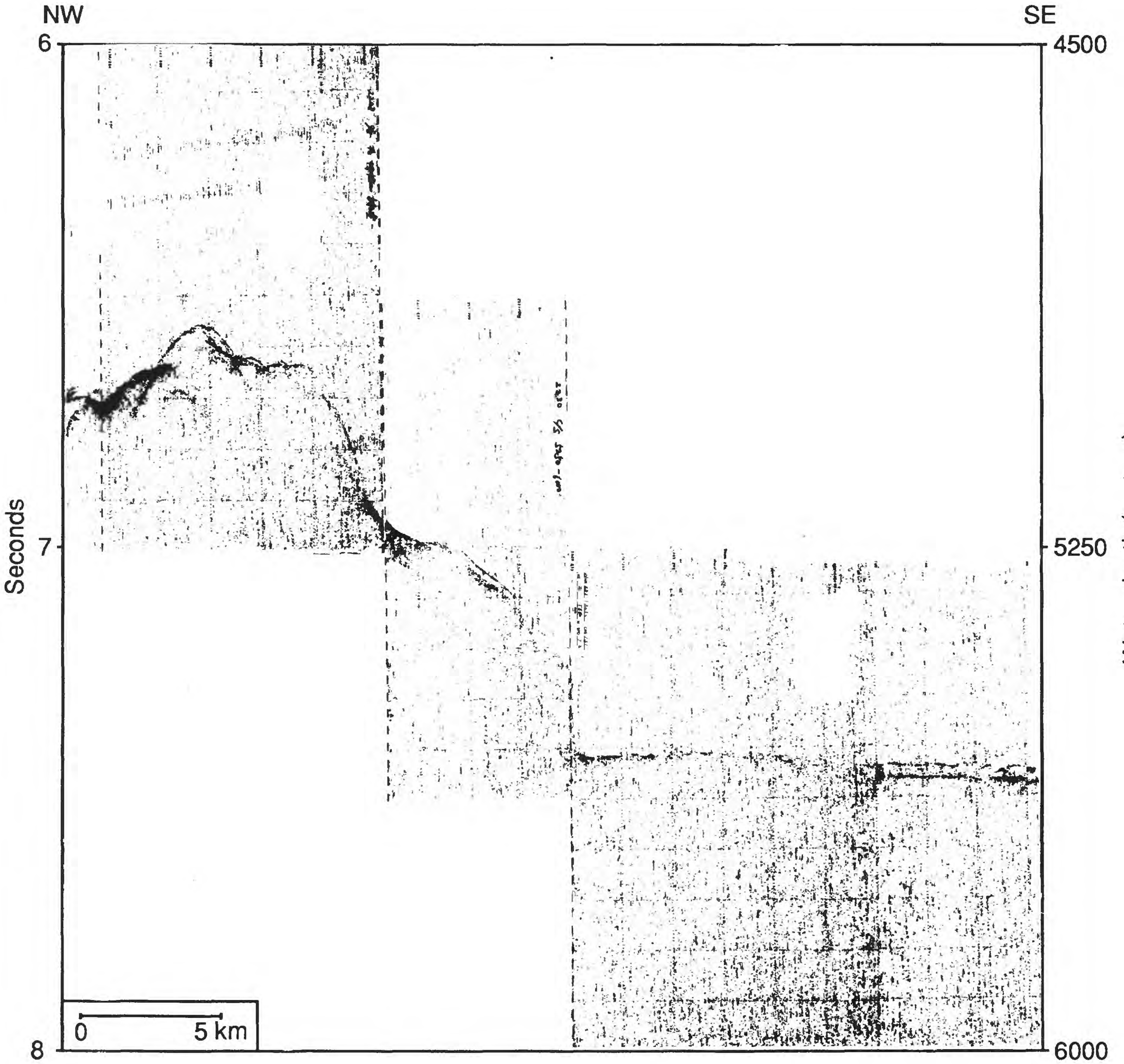

Figure 27. Pali Seamount, 3.5 kHz line 2 (see Fig. 4 for location).

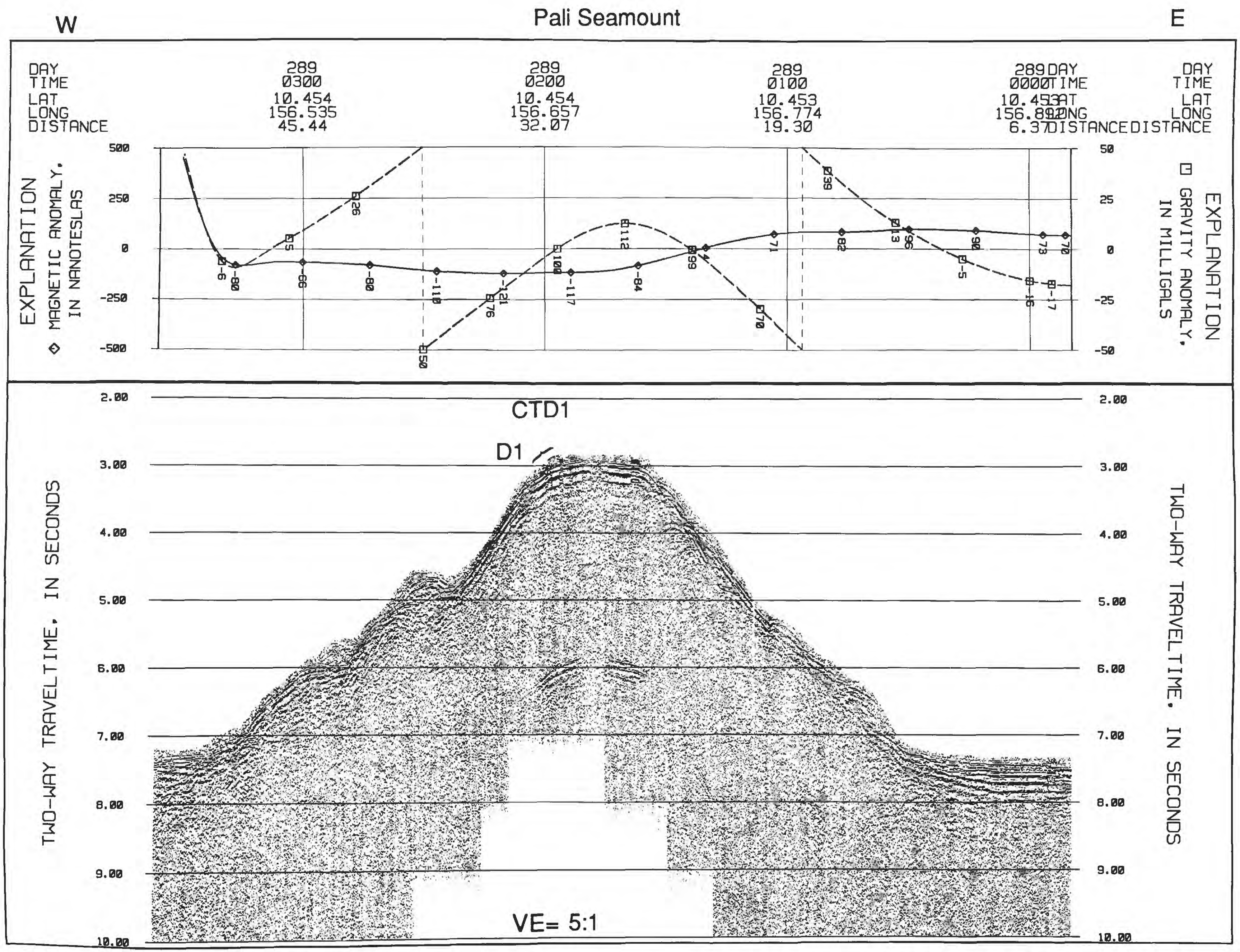

Figure 28. Pali Seamount, 195 in^3 single-channel airgun line 3 and associated gravity and magnetic profiles. Note location of Dredge 1 and CTD 1 (See Fig. 4 for location).

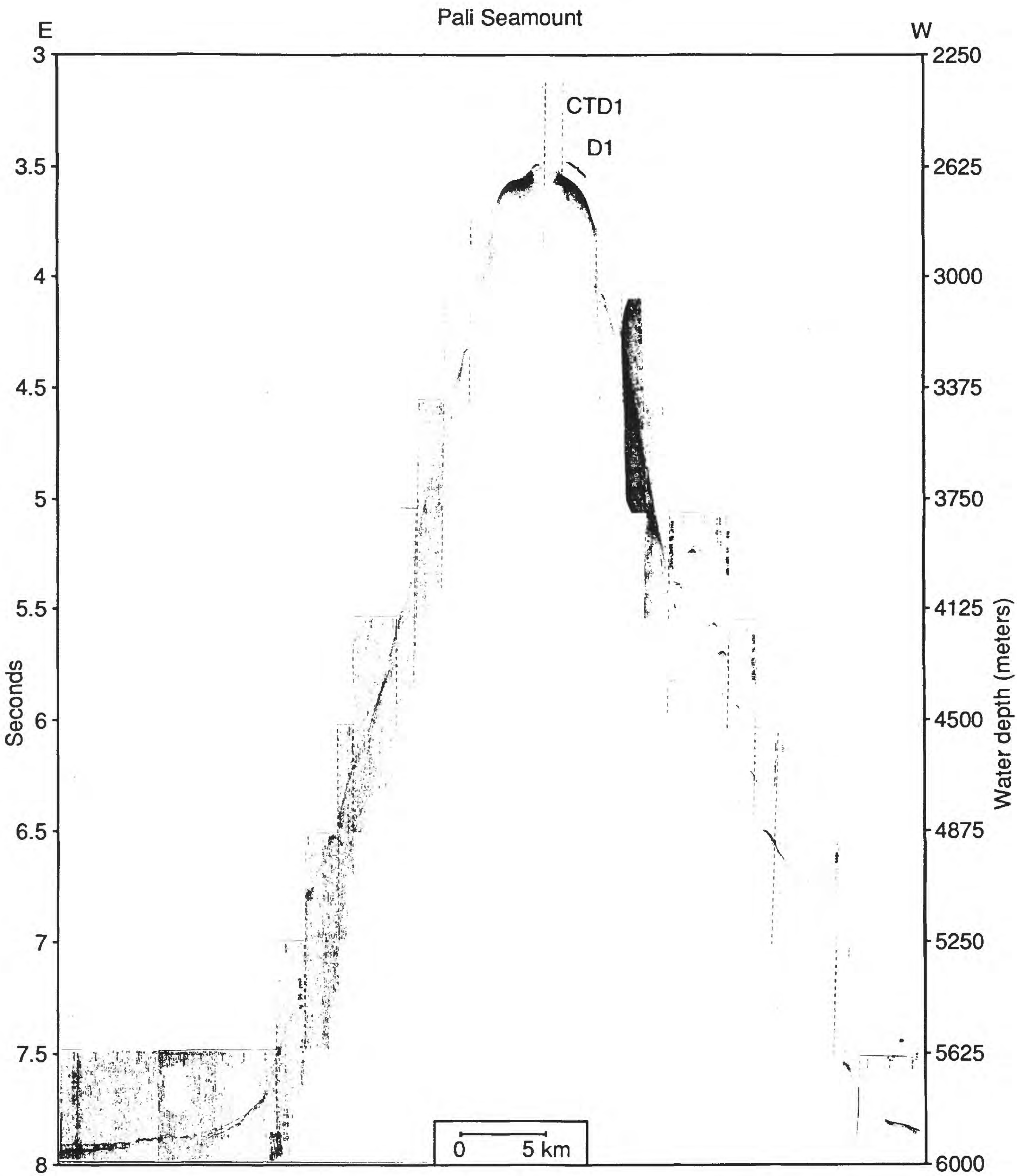

Figure 29. Pali Seamount, 3.5 kHz line 3. Note location of Dredge 1 and CTD 1. East and west directions are reversed from figure 28 (See Fig. 4 for location).

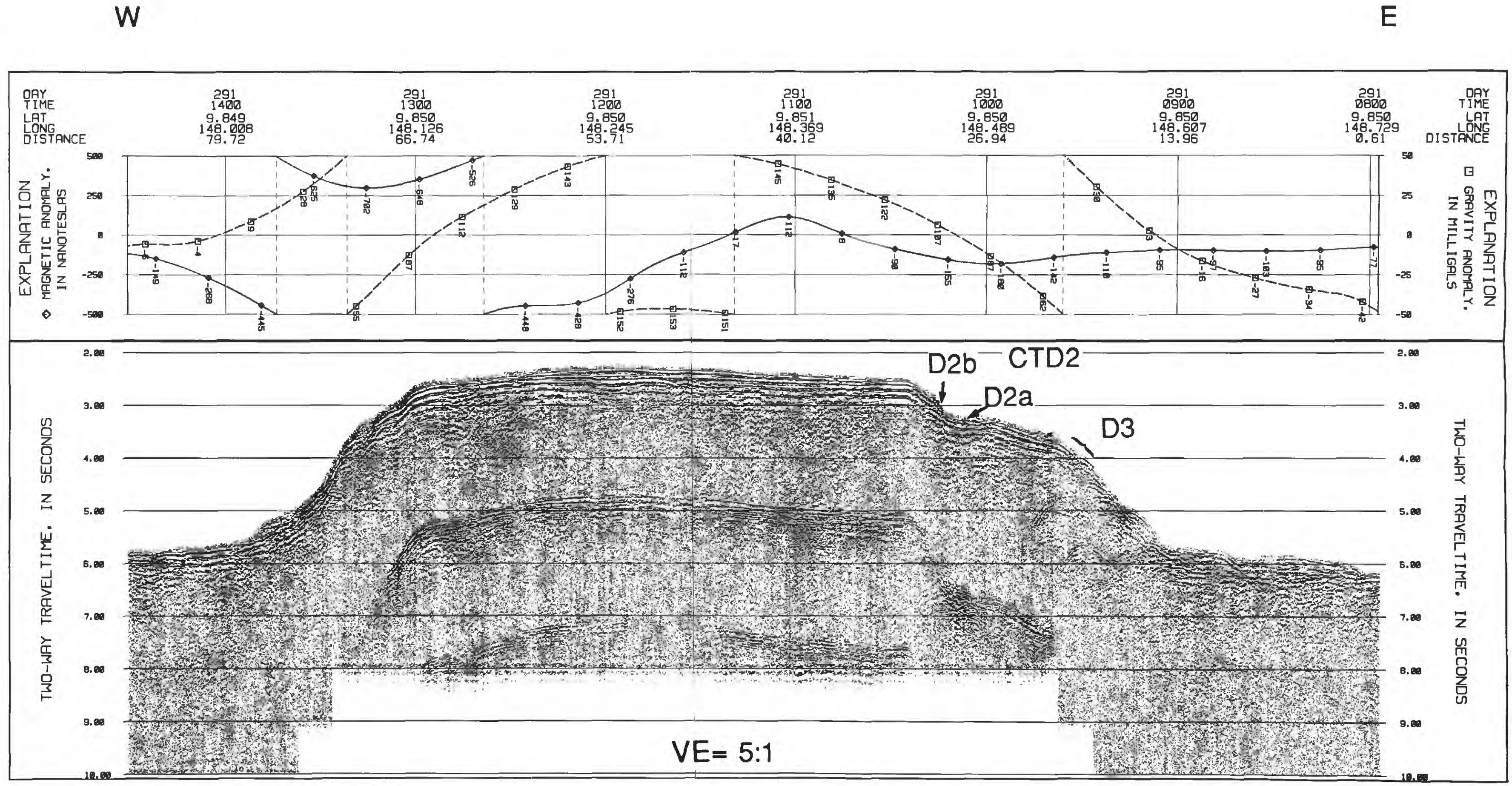

Figure 30. Namonuito Guyot, 195 in^3 single-channel airgun line 4 and associated gravity and magnetic profiles. Note locations of Dredges 2a, 2b and 3 and CTD 2 (see figure 5 for location).

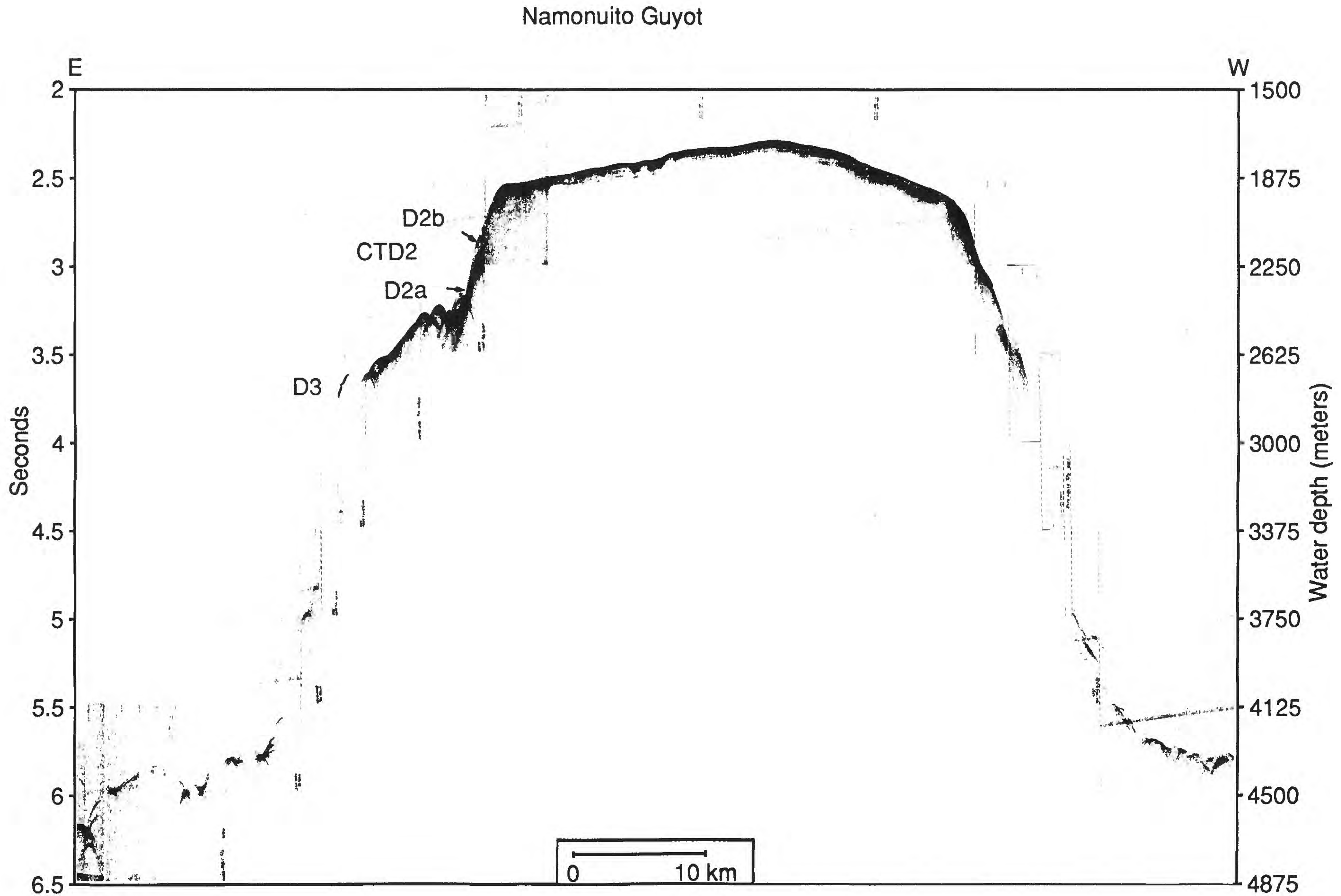

Figure 31. Namonuito Guyot, 3.5 kHz line 4. Note locations of Dredges 2a, 2b, and 3 and CTD 2. East and west directions are reversed relative to figure 30 (see figure 5 for location).

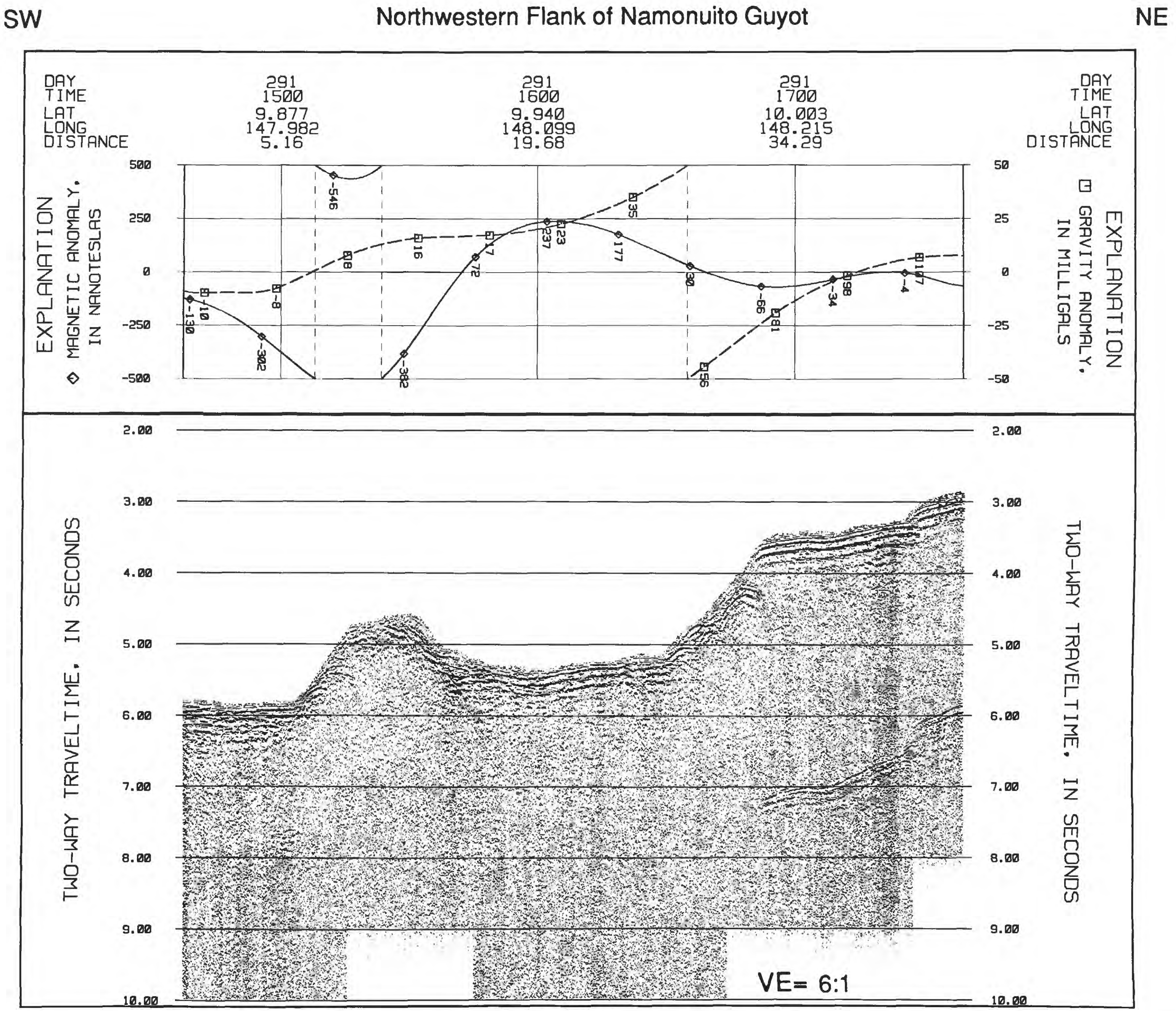

Figure 32. Northwest flank of Namonuito Guyot, 195 in^3 single-channel airgun line 5 and associated gravity and magnetic profiles (See figure 5 for location).

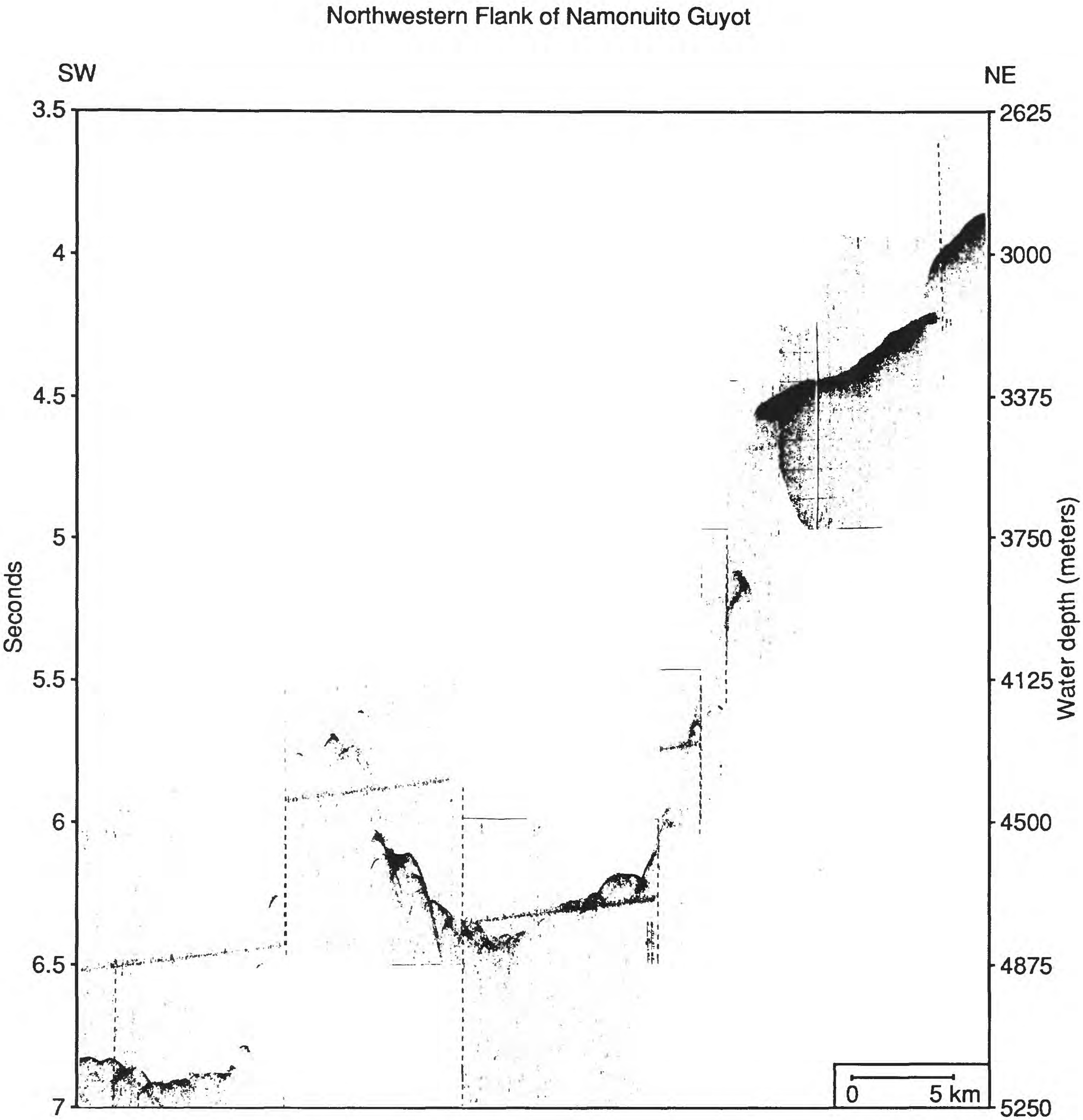

Figure 33. Northwest flank of Namonuito Guyot, 3.5 kHz line 5 (see Fig. 5 for location).

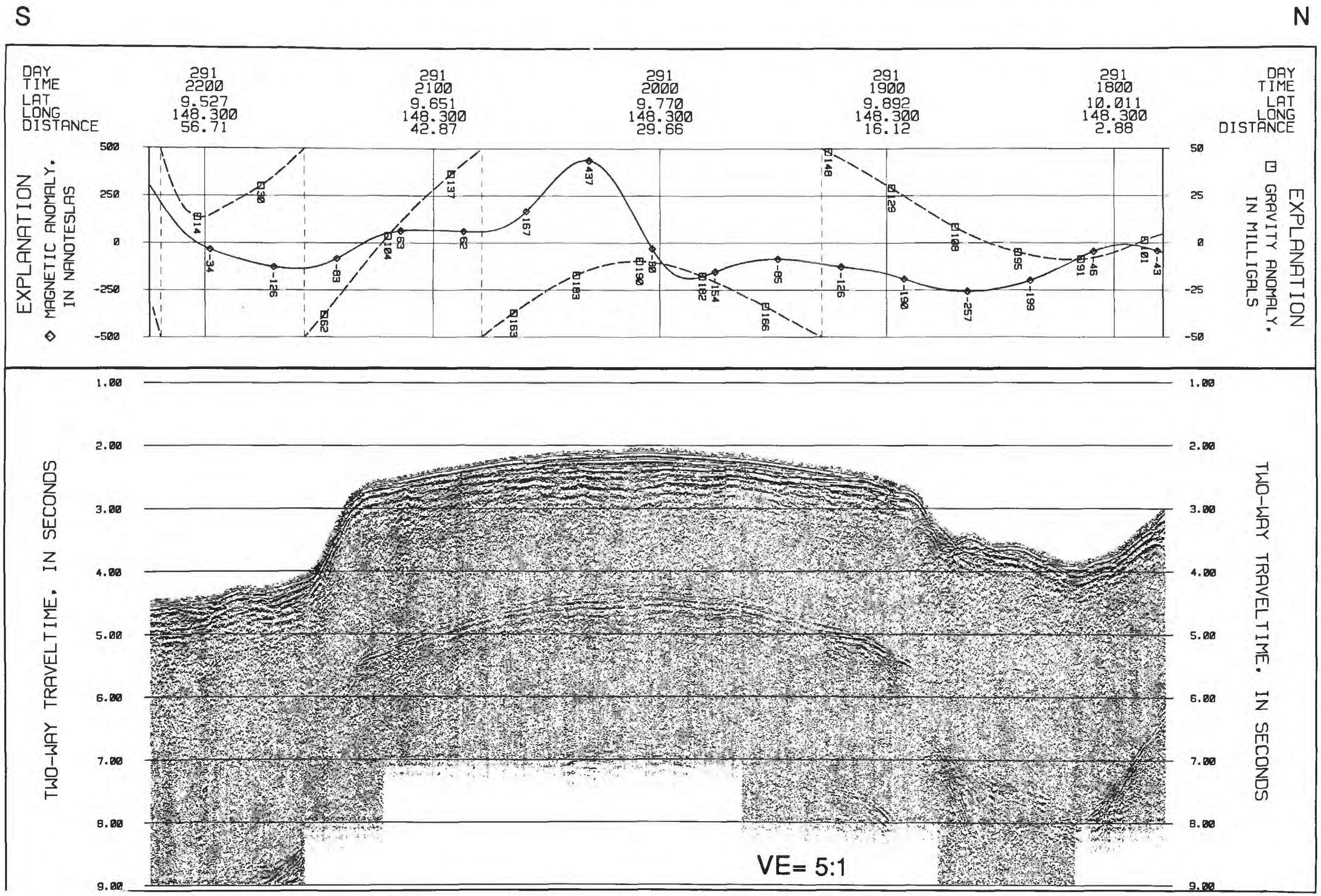

Figure 34. South-north cross section of Namonuito Guyot, 195 in^3 single-channel airgun line 6 and associated gravity and magnetic profiles (see figure 5 for location).

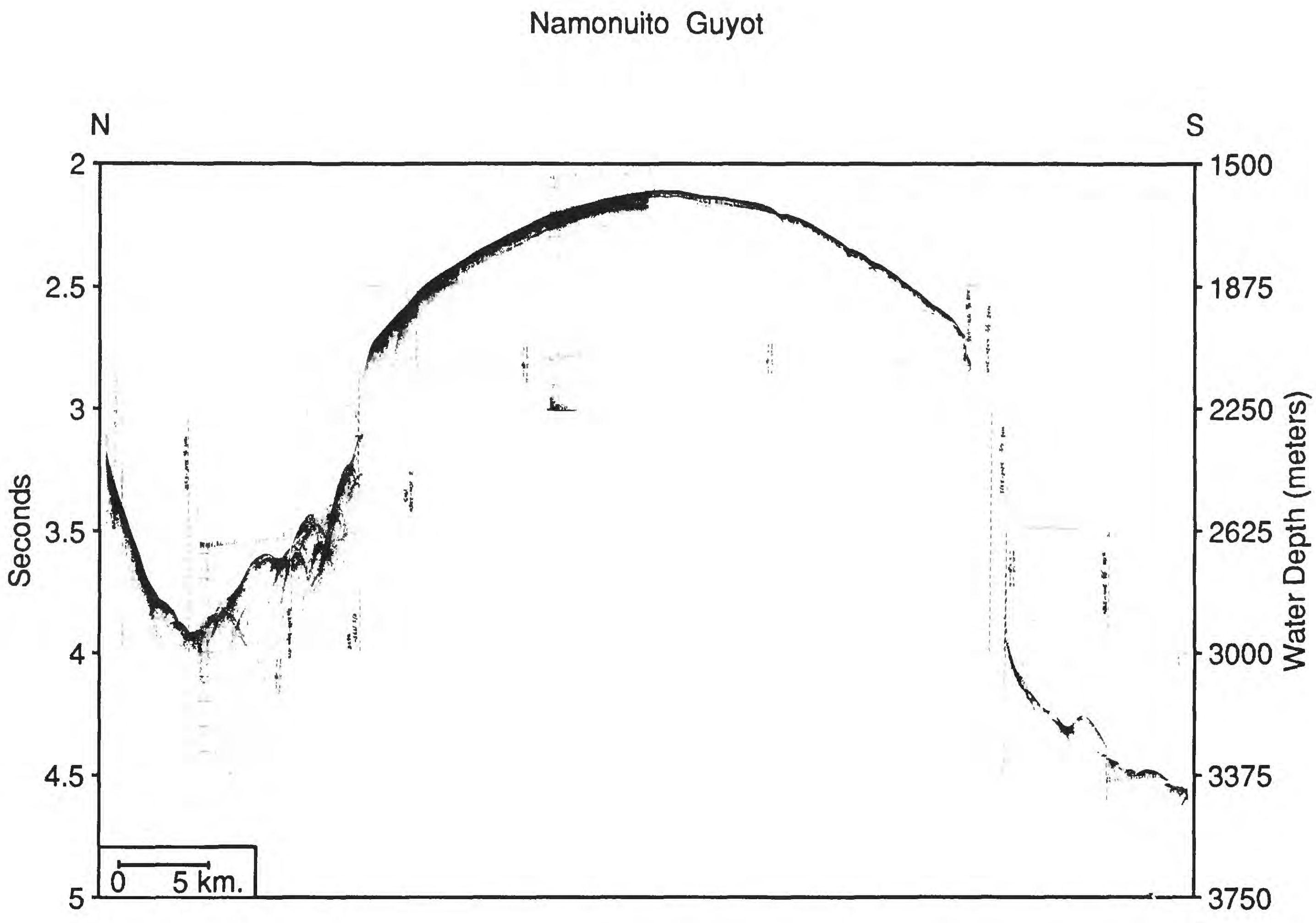

Figure 35. North-south cross section of Namonuito Guyot , 3.5 kHz line 6. North and south directions are reversed from figure 34 (see figure 5 for location).

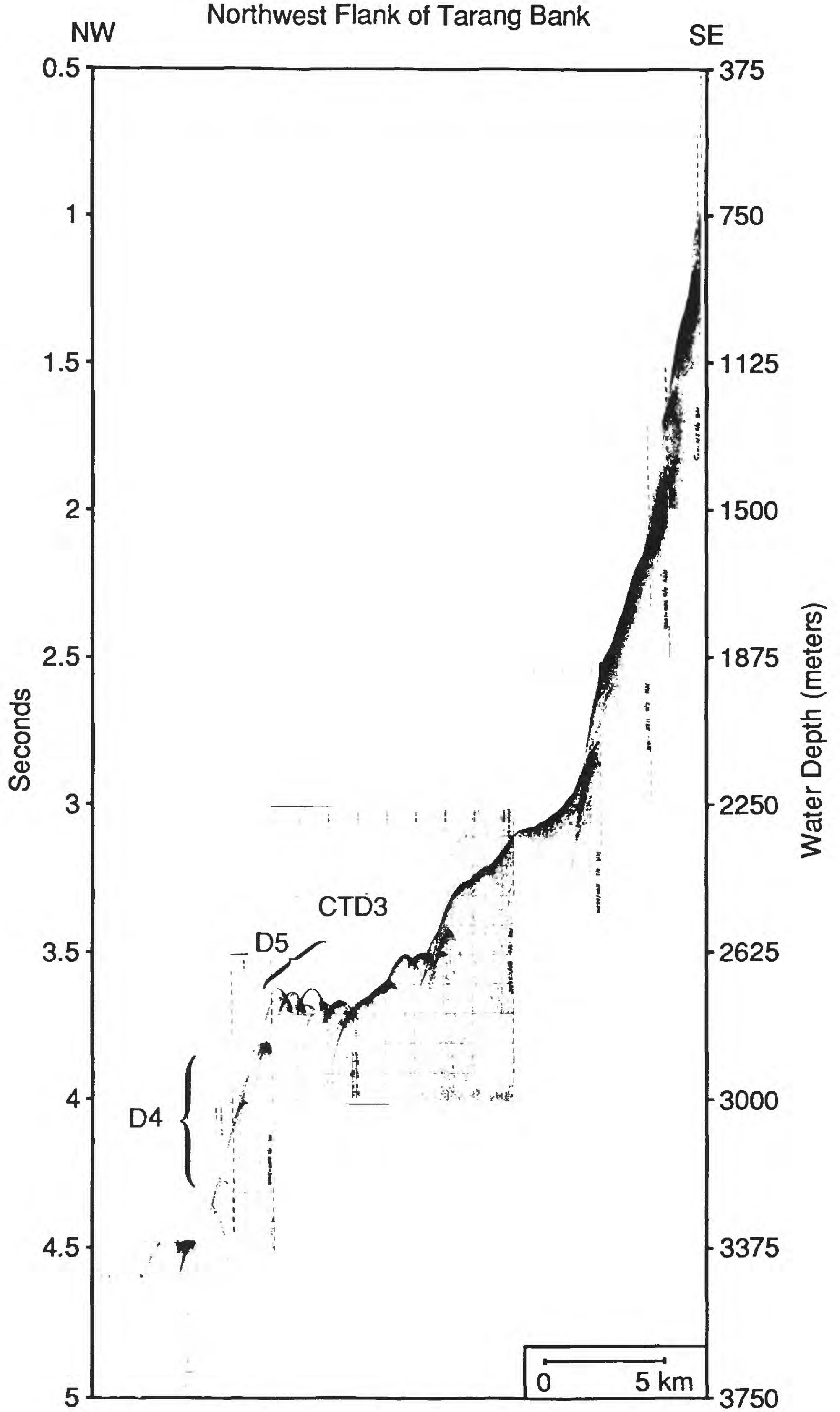

Figure 36. Northwest flank of Tarang Bank, 3.5 kHz line 7. Note location of Dredges 4 and 5 and CTD 3 (See Fig. 6 for location).

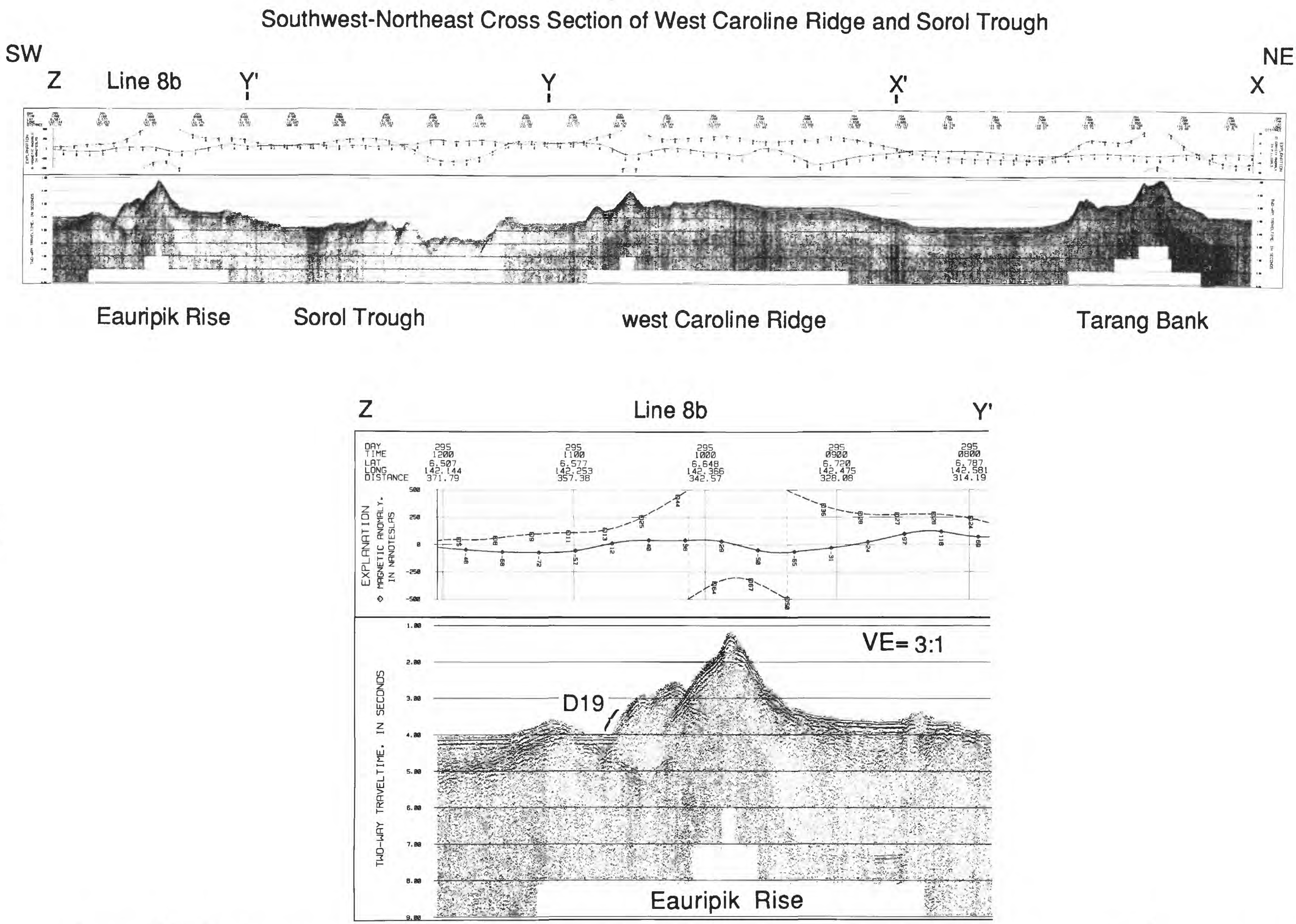

Figure 37A. Southwest to northeast cross section of west Caroline Ridge from Eauripik Rise to Tarang Bank, 195 in^3 single-channel airgun Line 8 and the associated gravity and magnetic profiles. Divisions correspond to Figs. 37A-37D and 38A-38D. Note location of Dredge 19 (See Figs. 7 and 18 for location).

Sorol Trough
Y'-Y

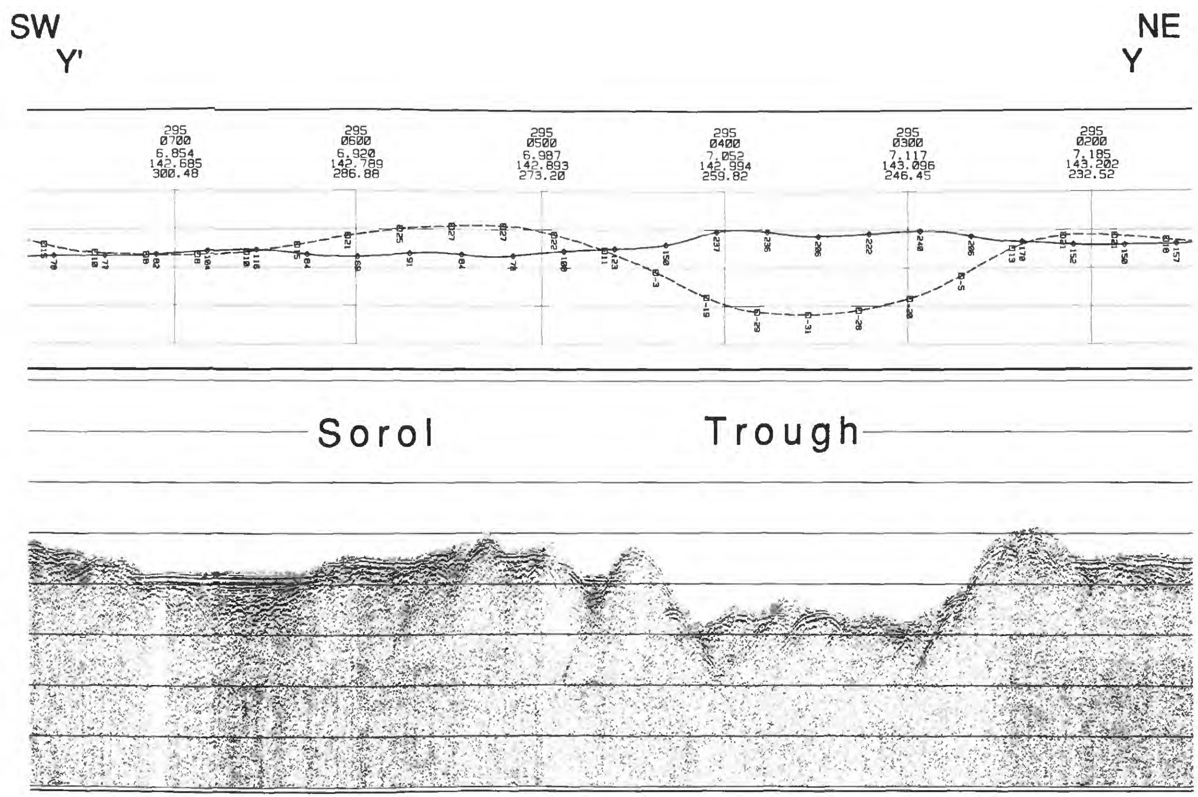

Figure 37B. Southwest to northeast cross section of Sorol Trough, 195 in^3 single-channel airgun line 8 (Y'-Y) and associated gravity and magnetic profiles (See Fig. 7 for location).

Caroline Ridge
Y-X'

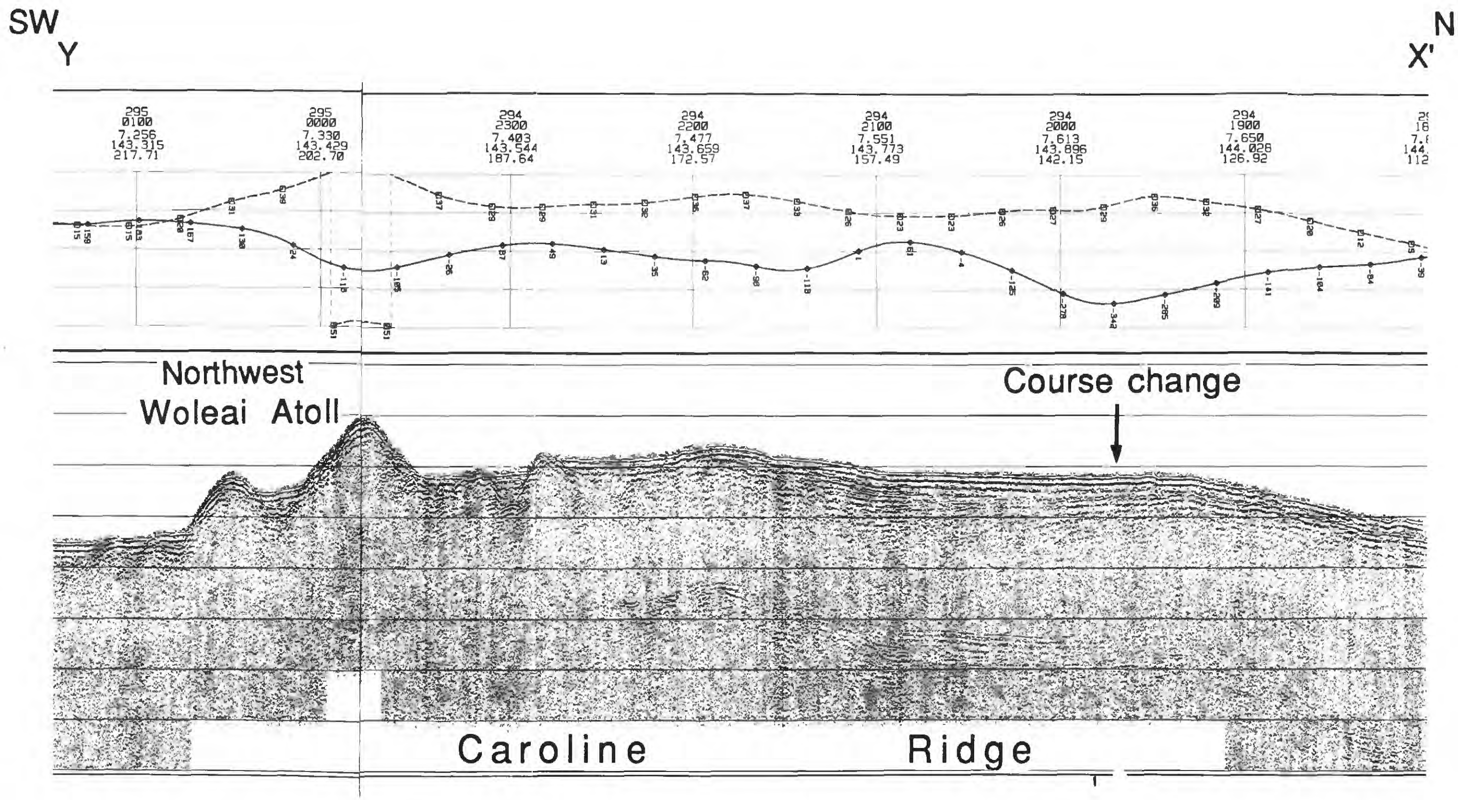

Figure 37C. Southwest to northeast cross section of Caroline Ridge, 195 in^3 single-channel airgun line 8 (Y-X') and associated gravity and magnetic profiles (See Fig. 7 for location).

Tarang Bank
X'-X

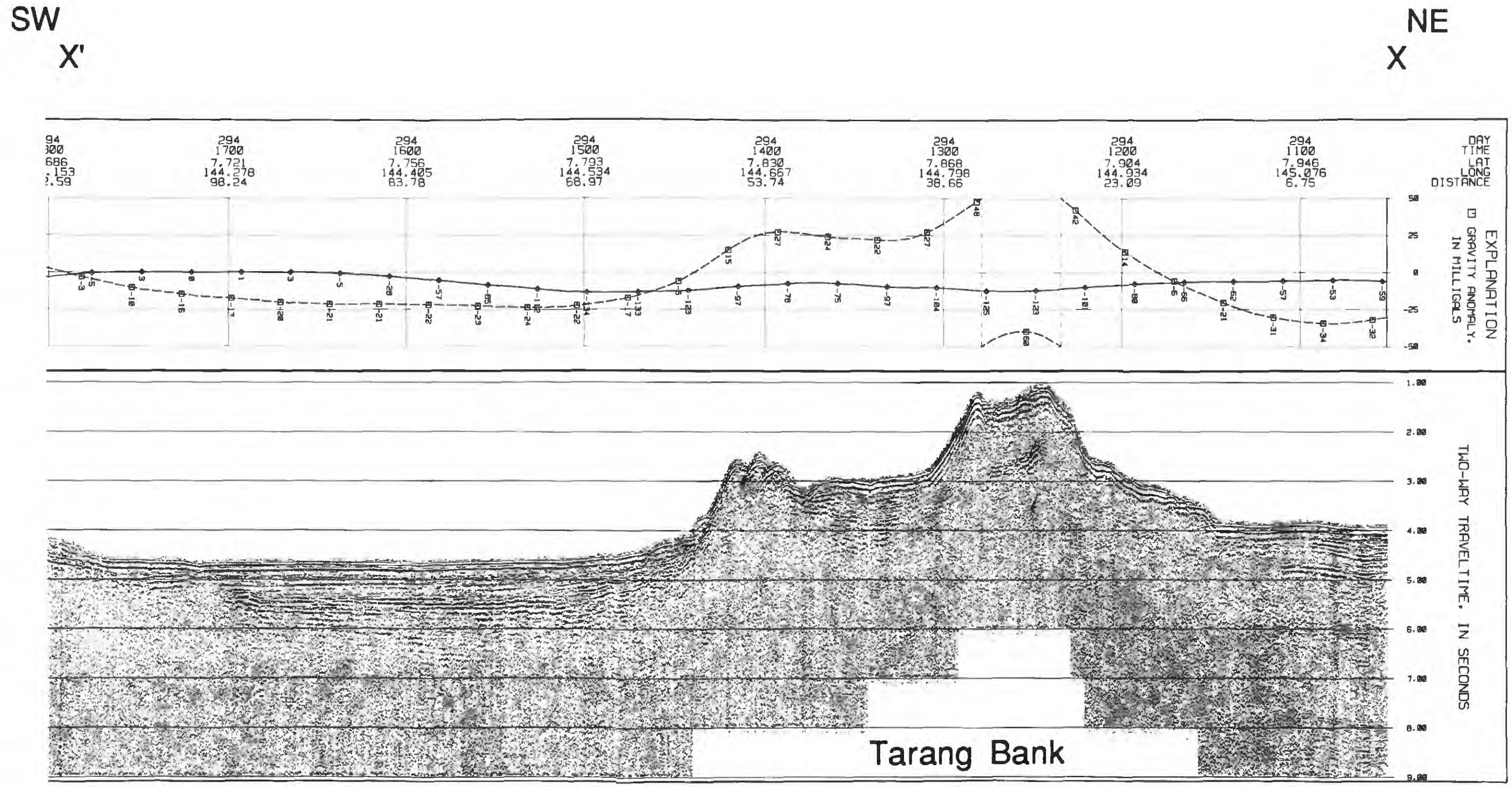

Figure 37D. Southwest to northeast cross section of abyssal plain and Tarang Bank, 195 in^3 single-channel airgun line 8 (X'-X) and associated gravity and magnetic profiles (See Fig. 7 for location).

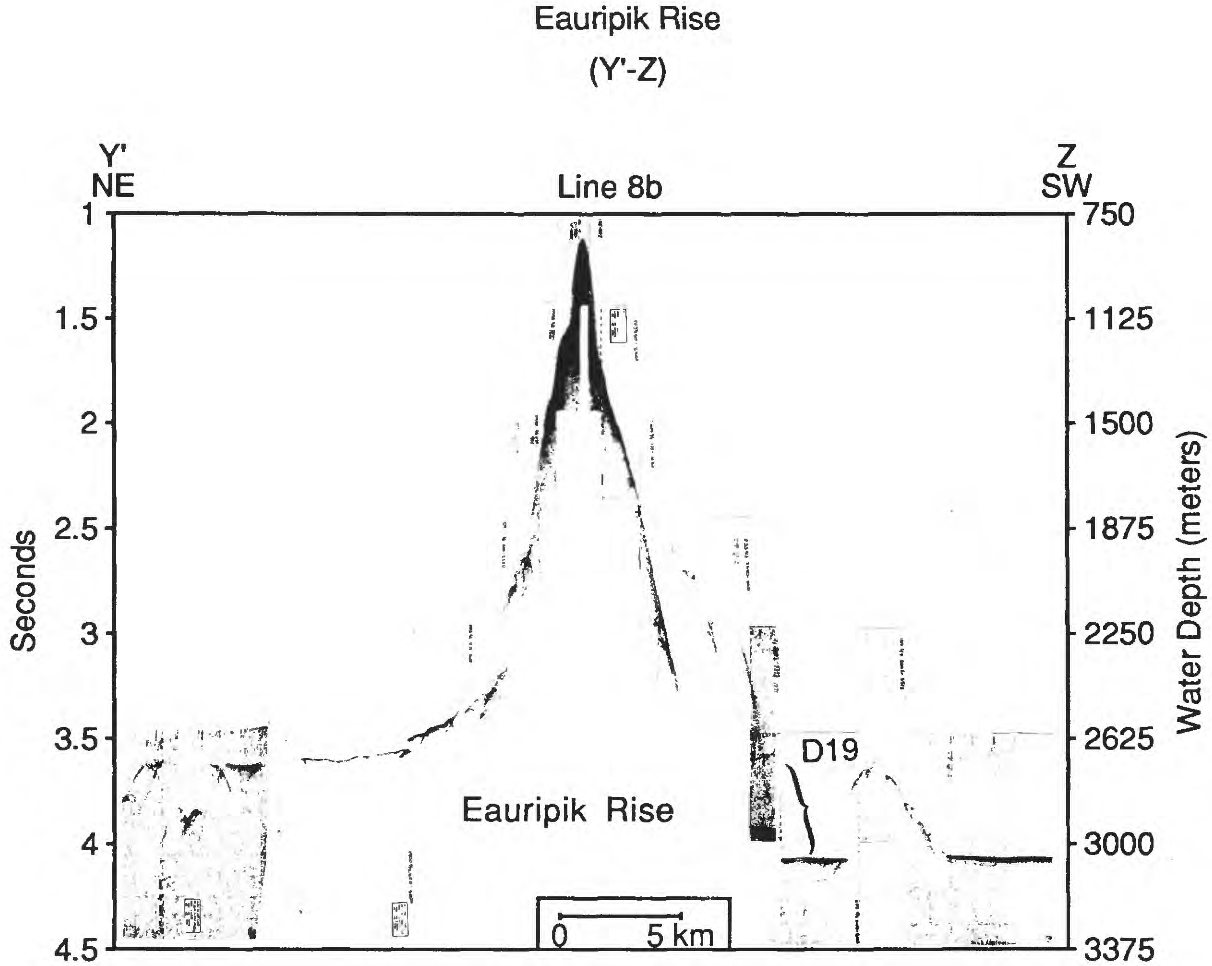

Figure 38A. Northeast-Southwest cross section of Eauripik Rise, 3.5 kHz Line 8b (Y'-Z). Note location of Dredge 19. Direction of line is reversed relative to figure 37A (See Fig. 7 and 18 for location).

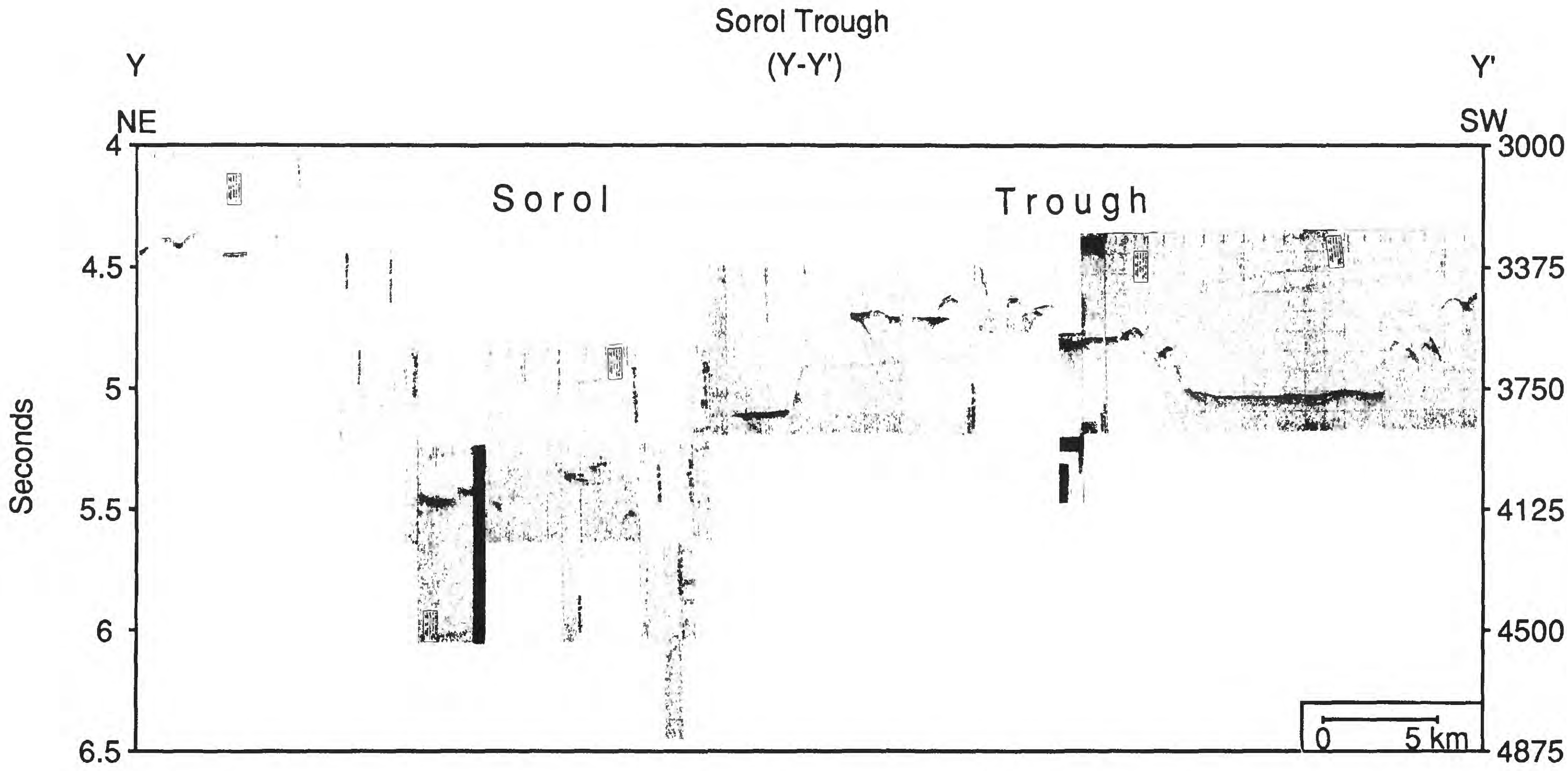

Figure 38B. Northeast-Southwest cross section of Sorol Trough, 3.5 kHz Line 8 (Y-Y'). Direction of line is reversed relative to figure 37B (See Fig. 7 for location).

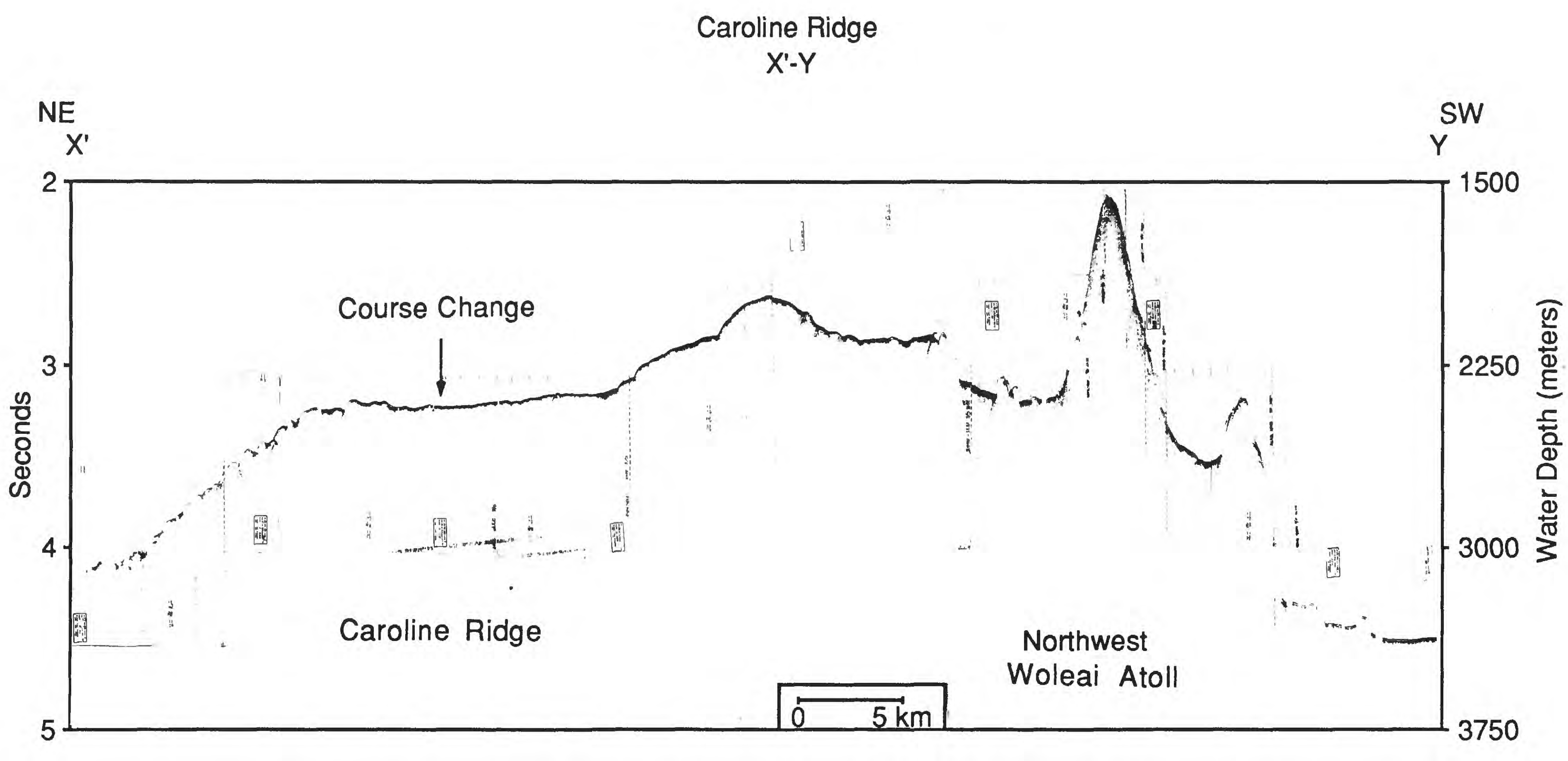

Figure 38C. Northeast-Southwest cross section of Caroline Ridge, 3.5 kHz Line 8 (X'-Y). Direction of line is reversed relative to figure 37C (See Fig. 7 for location).

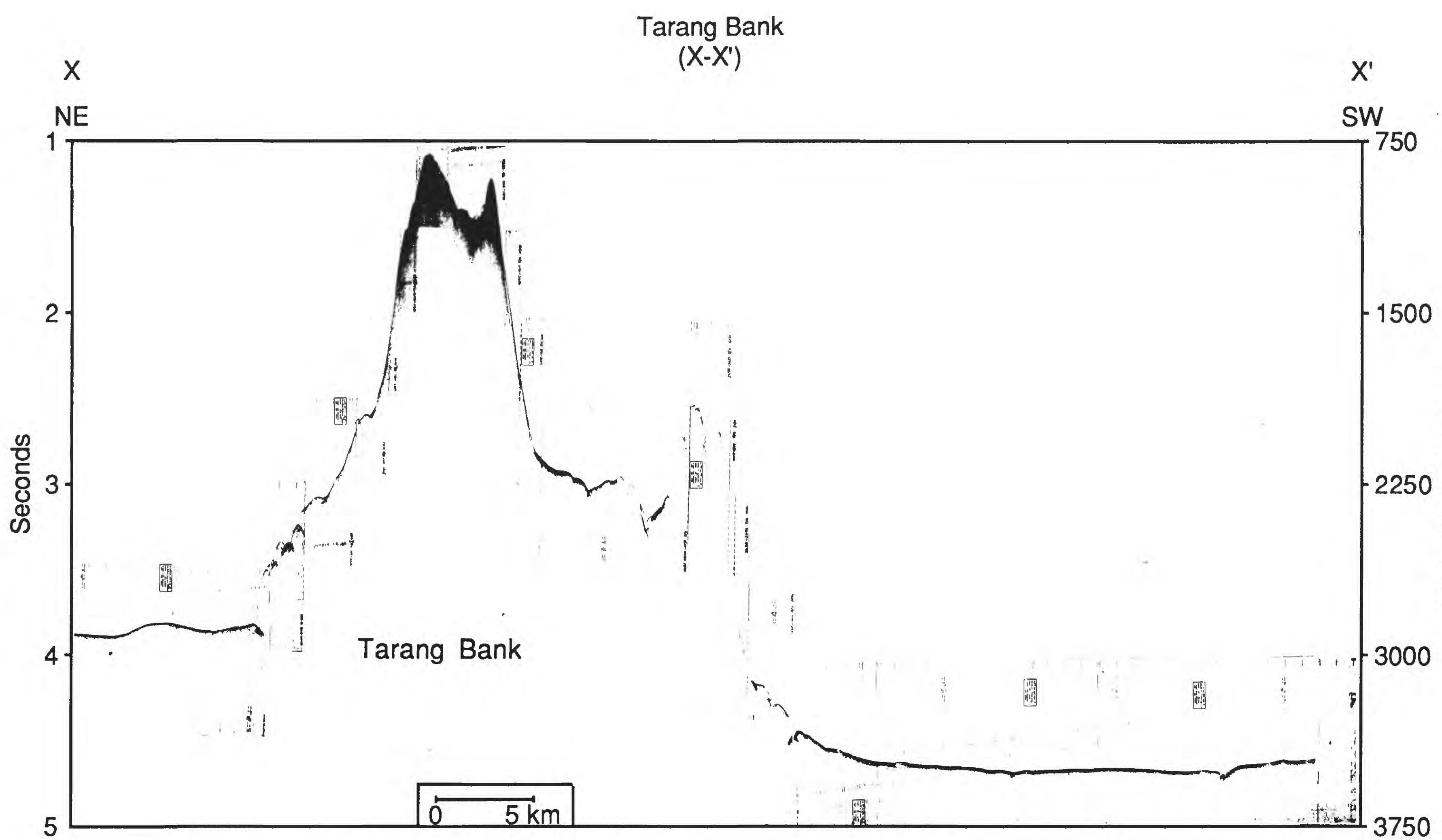

Figure 38D. Northeast-southwest cross section of abyssal plain and Tarang Bank, 3.5 kHz Line 8 (X-X'). Direction of line is reversed relative to figure 37D (See Fig. 7 for location).

West Caroline Ridge and Sorol Trough

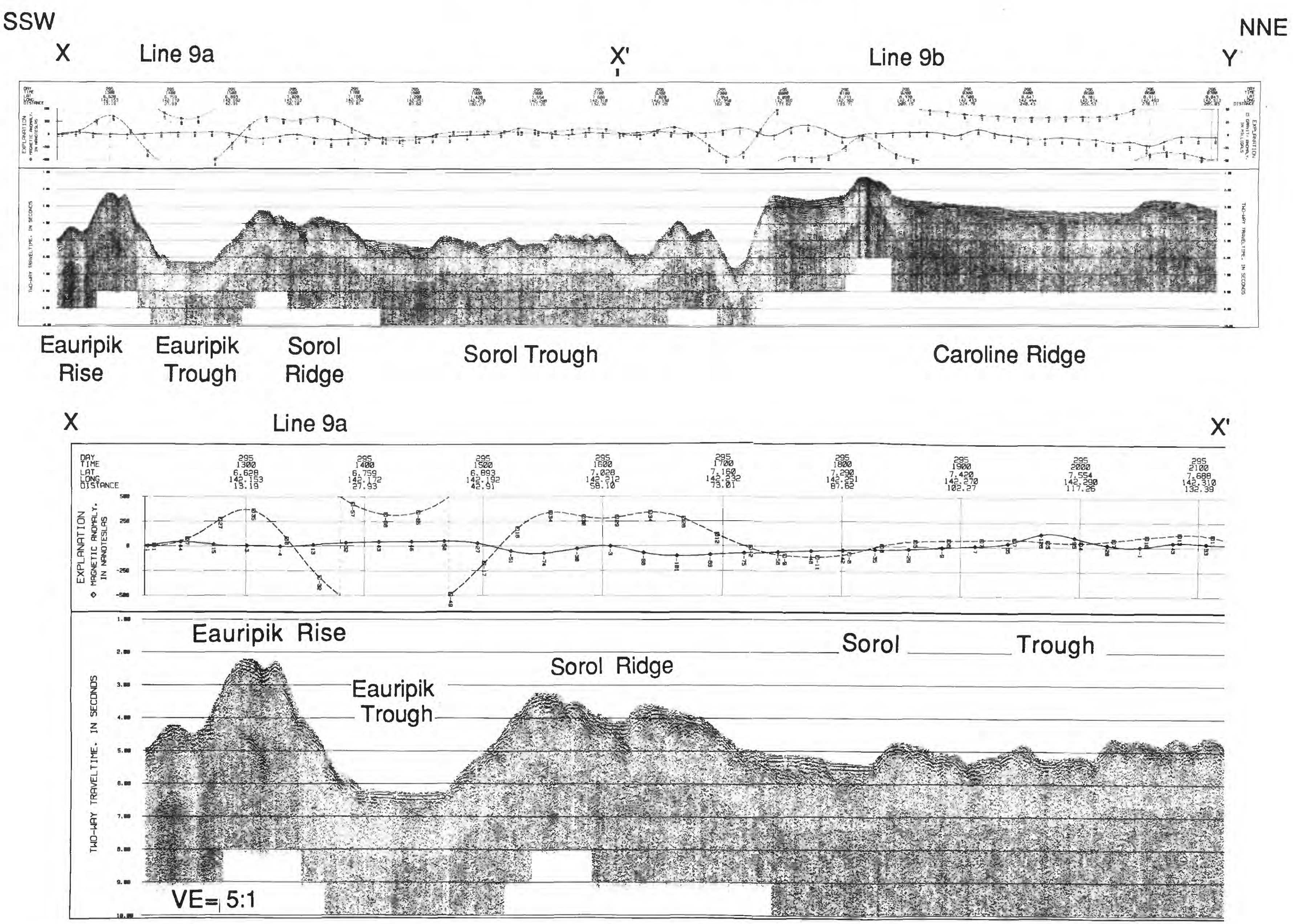

Figure 39A. Southwest to northeast cross section of Sorol Trough and Ridge, Eauripik Rise and Trough, and Caroline Ridge, 195 in^3 single-channel airgun line 9, and divisions of line 9, with associated gravity and magnetic profiles (See Figs. 7 and 18 for location).

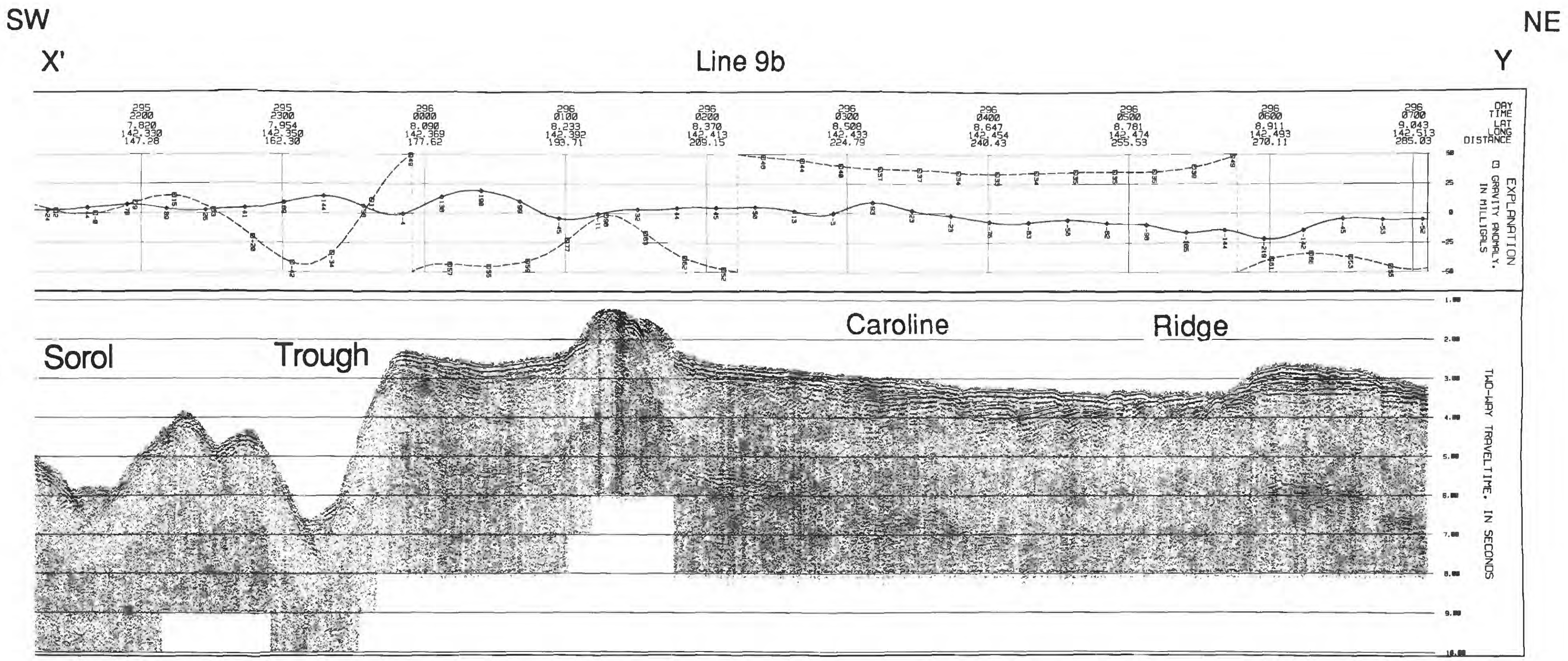

Figure 39B. Southwest to northeast cross section of Sorol Trough and Caroline Ridge, 195 in^3 single-channel airgun line 9b, X'-Y, and associated gravity and magnetic profiles (See Fig. 7 for location).

Eauripik Rise and Trough and Sorol Trough and Ridge

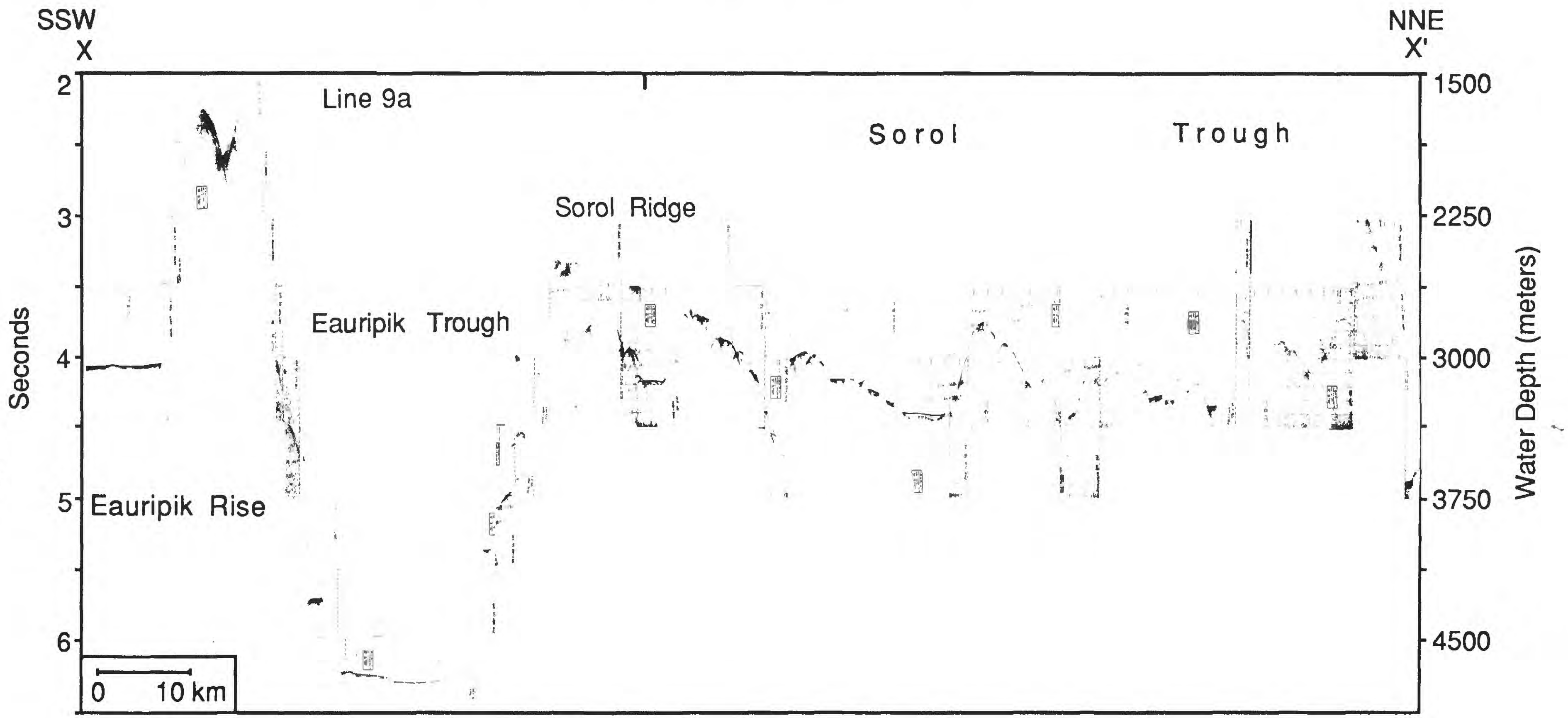

Figure 40A. Southwest-northeast cross section of Sorol Trough and Ridge and Eauripik Rise and Trough, 3.5 kHz line 9a (X-X'). (See Figs. 7 and 18 for location).

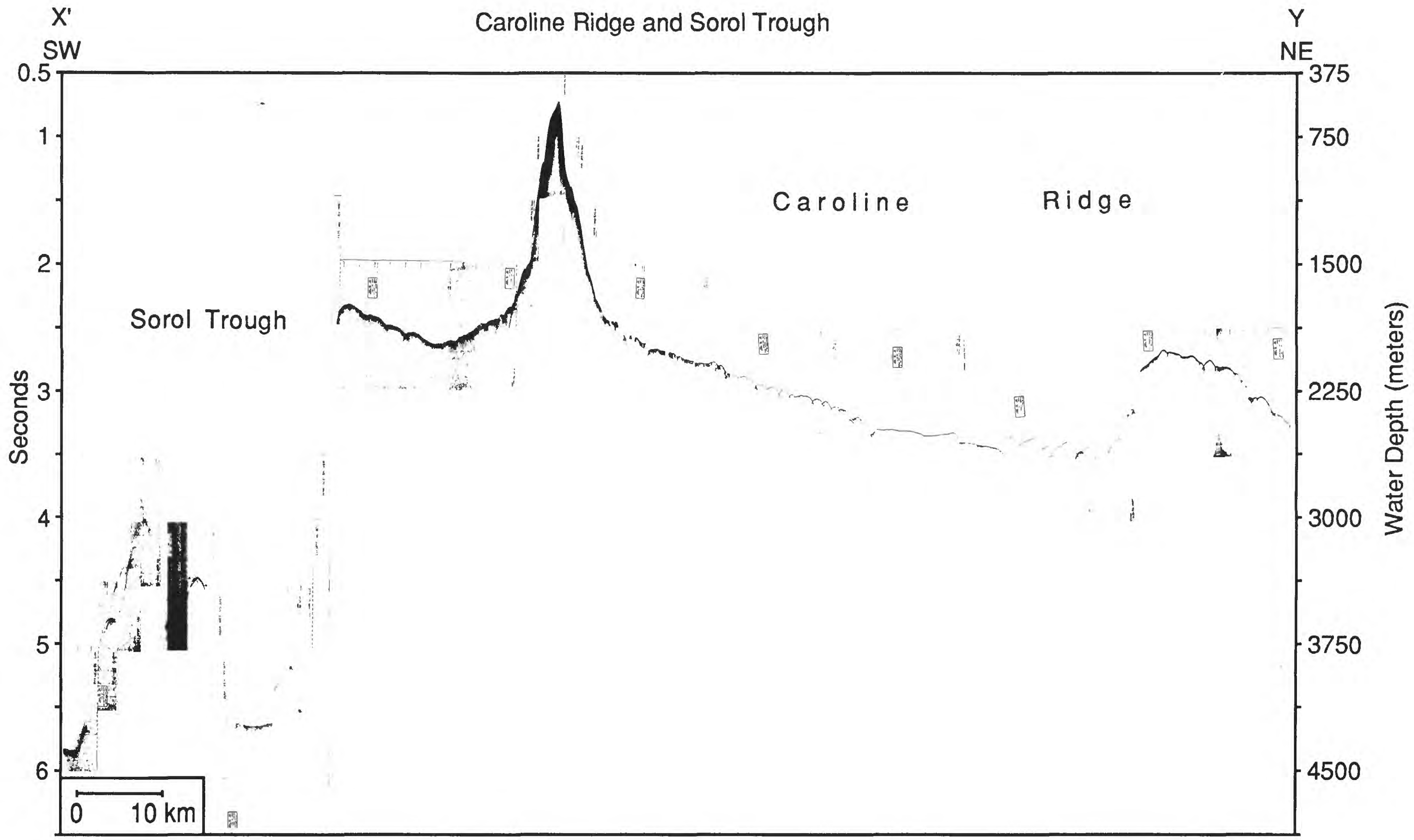

Figure 40B. Southwest to northeast cross section of Sorol Trough and Caroline Ridge, 3.5 kHz Line 9b (X'-Y) (See Fig. 7 for location).

Caroline Ridge

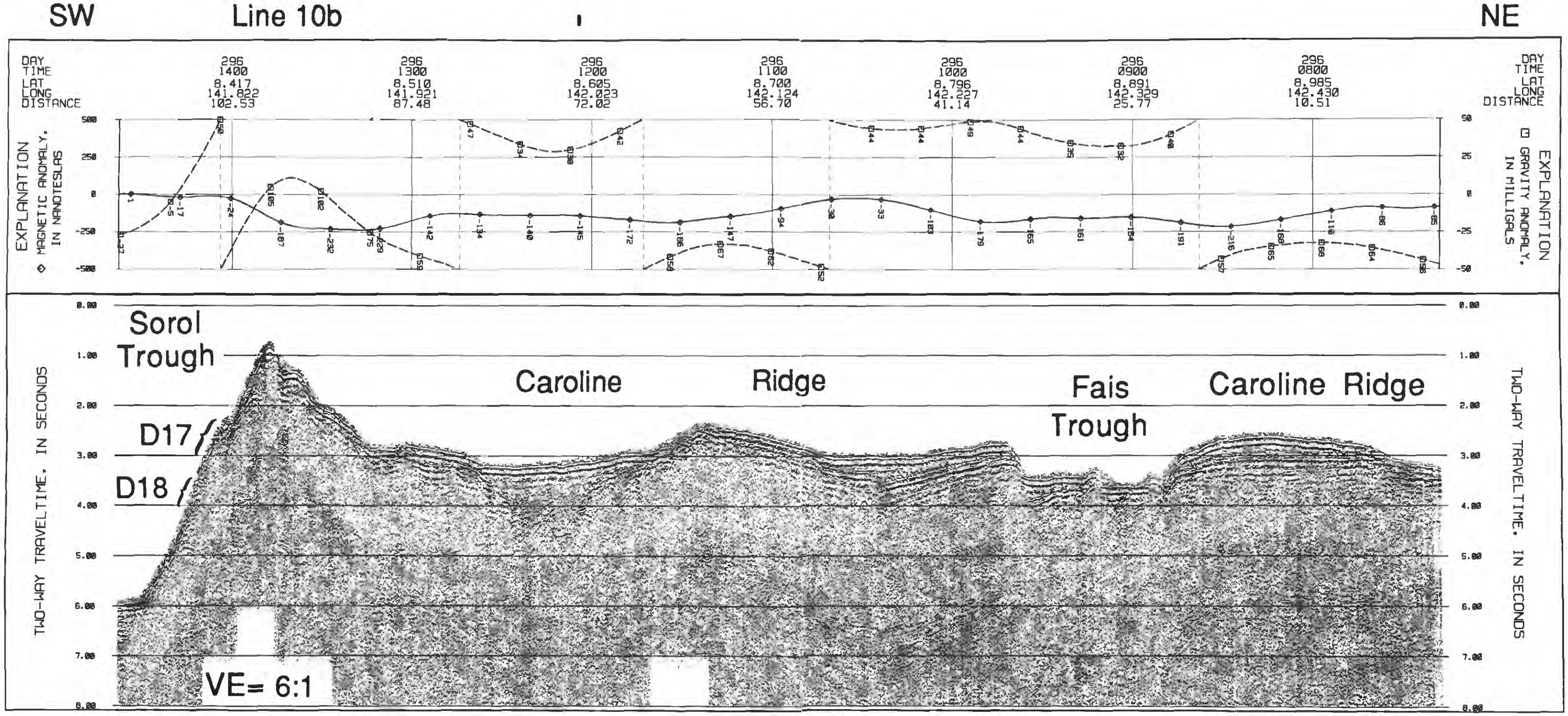

Figure 41. Southwest to northeast cross section of Caroline Ridge, 195 in^3 single-channel airgun line 10 and associated gravity and magnetic profiles. Note location of Dredges 17 and 18 (See Figs. 7 and 17 for location).

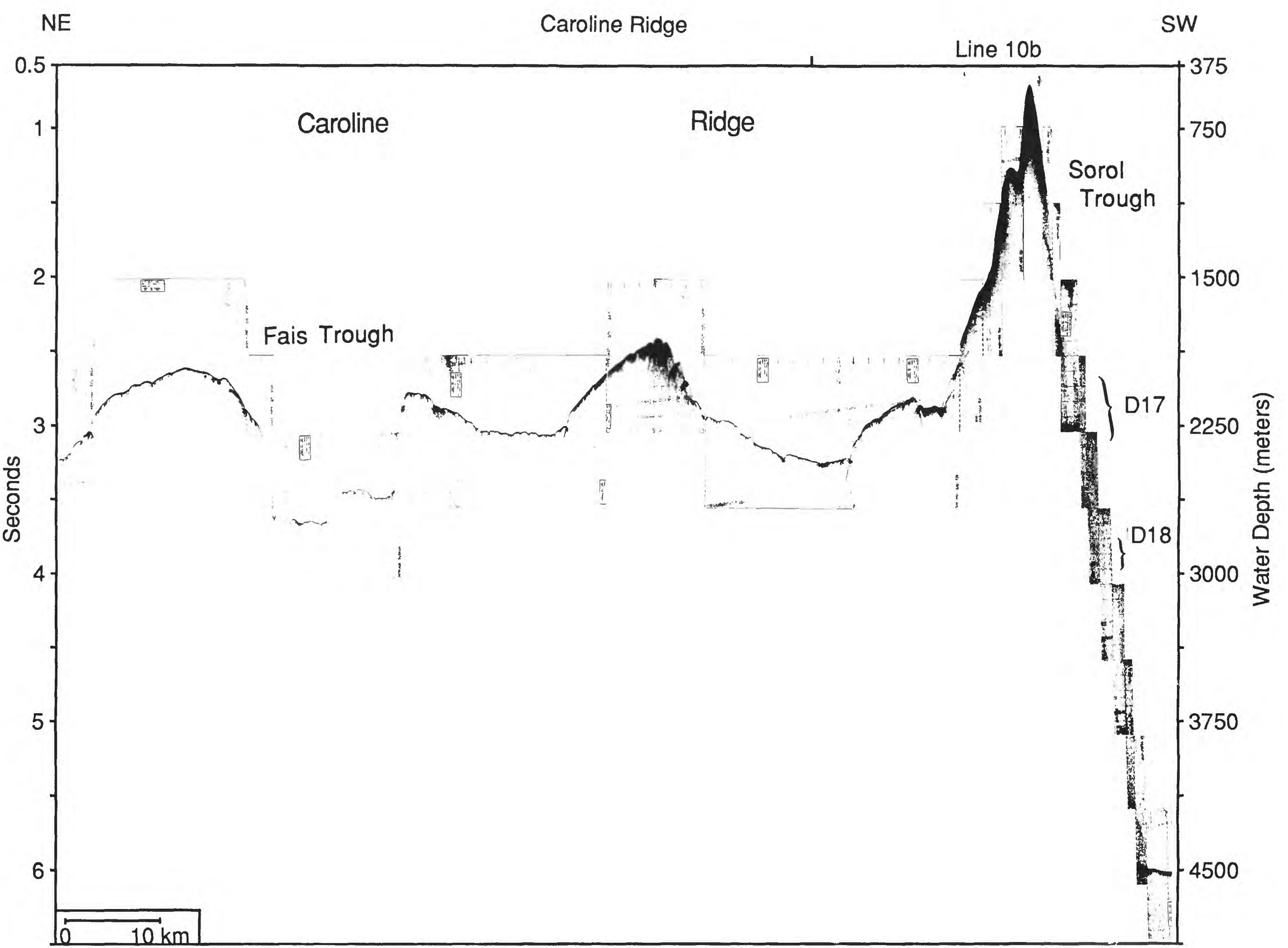

Figure 42. Southwest-northeast cross section of Caroline Ridge, 3.5 kHz Line 10. Note location of Dredges 17 and 18. Southwest and northeast directions are reversed from figure 41 (See Figs. 7 and 17 for location).

Northeast Flank of the Sorol Trough

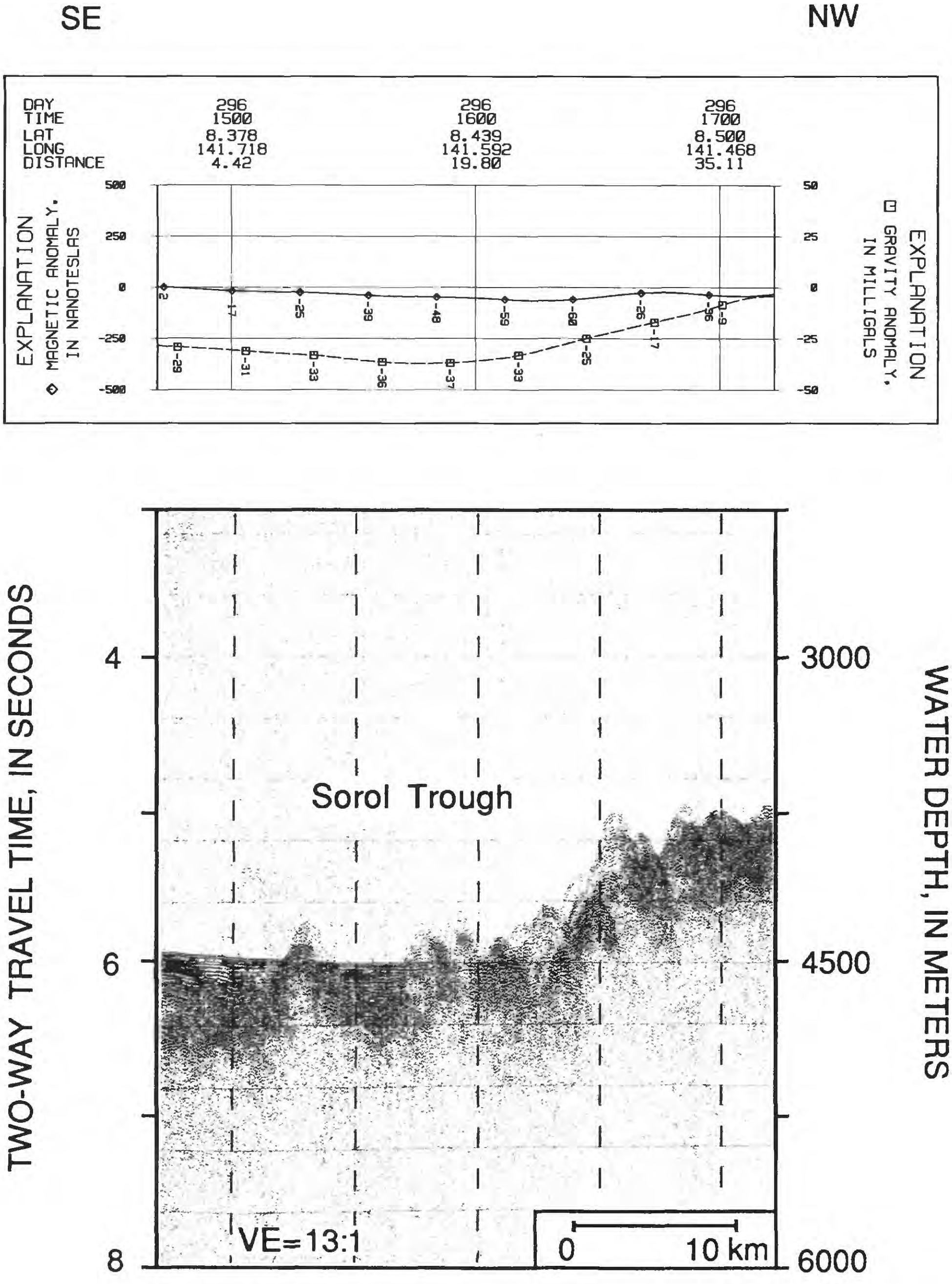

Figure 43. Northeast flank of the Sorol Trough, 195 in^3 single-channel airgun Line 11, and associated gravity and magnetic profiles (See Fig. 17 for location).

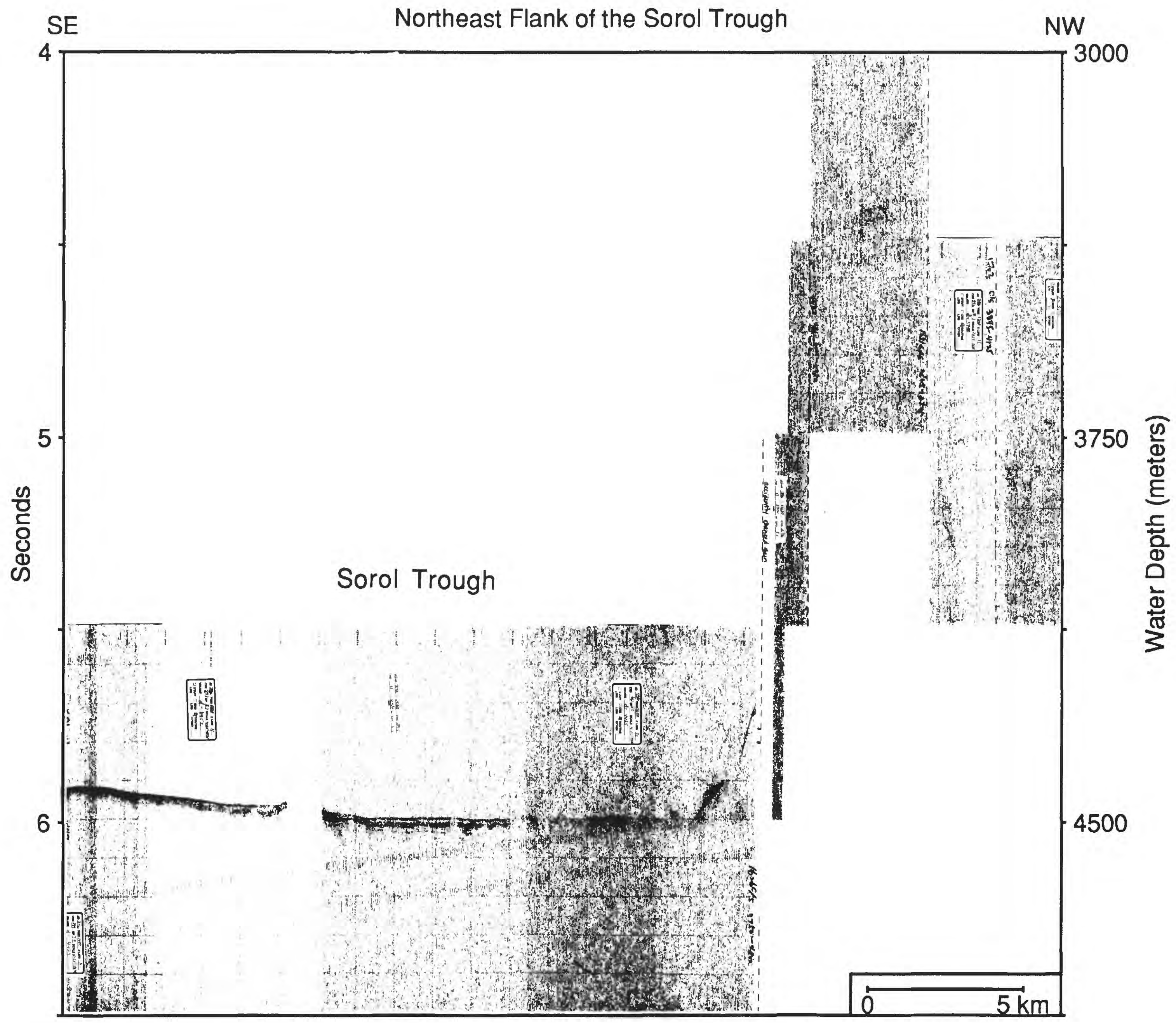

Figure 44. Northeast flank of the Sorol Trough, 3.5 kHz Line 11 (See Figs. 7 and 17 for location).

Caroline Ridge and Fais Trough

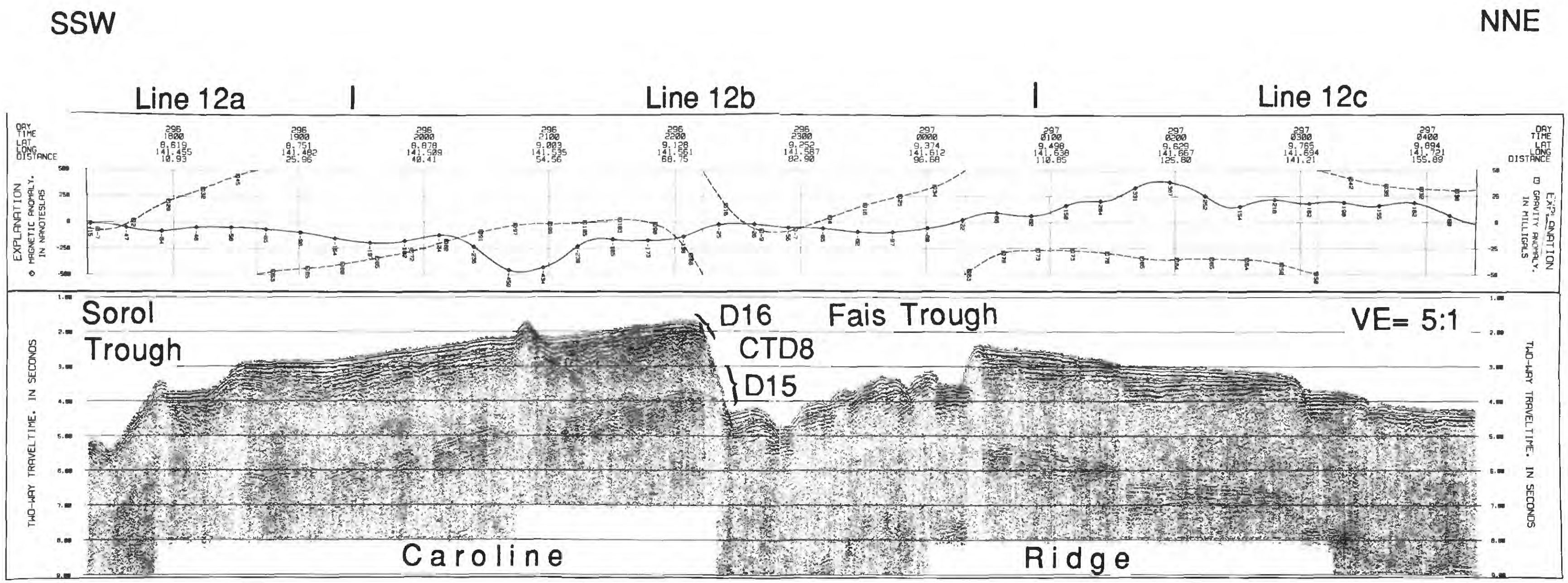

Figure 45. South-southwest-north-northeast cross section of Caroline Ridge and Fais Trough, 195 in^3 single-channel airgun line 12, with the divisions of line 12, and associated gravity and magnetic profiles. Note location of Dredges 15 and 16 and CTD 8 (See Fig. 7 for location of the entire line, Fig. 16 for line 12b and Fig. 17 for lines 12a and 12b).

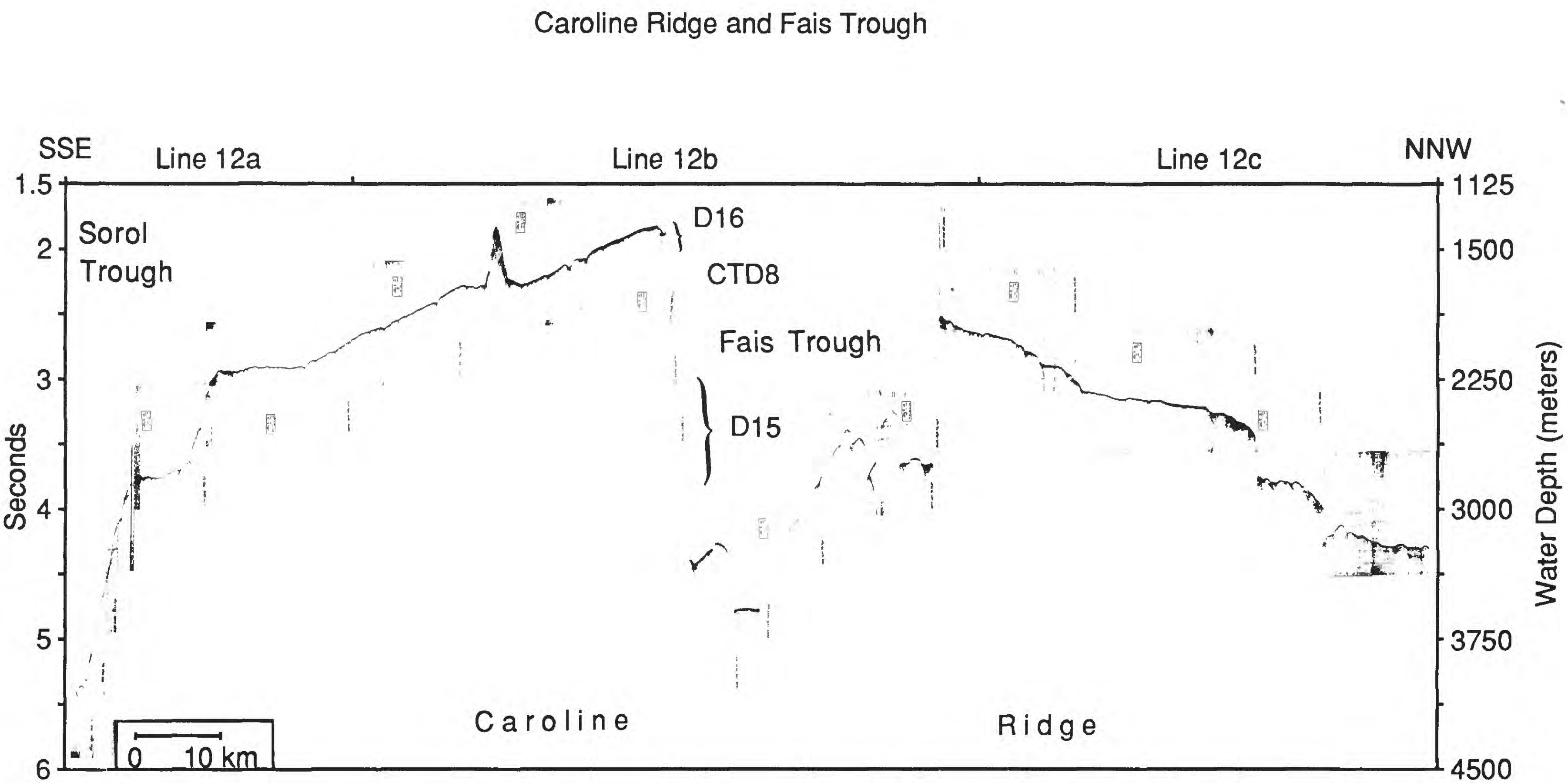

Figure 46. South-southeast to north-northwest cross section of Caroline Ridge and Fais Trough, 3.5 kHz Line 12 and the divisions of Line 12. Note location of Dredges 15 and 16 and CTD 8 (See Fig. 7 for location of the entire line, Fig. 16 for Line 12b, and Fig.17 for Lines 12a and 12b).

Fais Island and Caroline Ridges

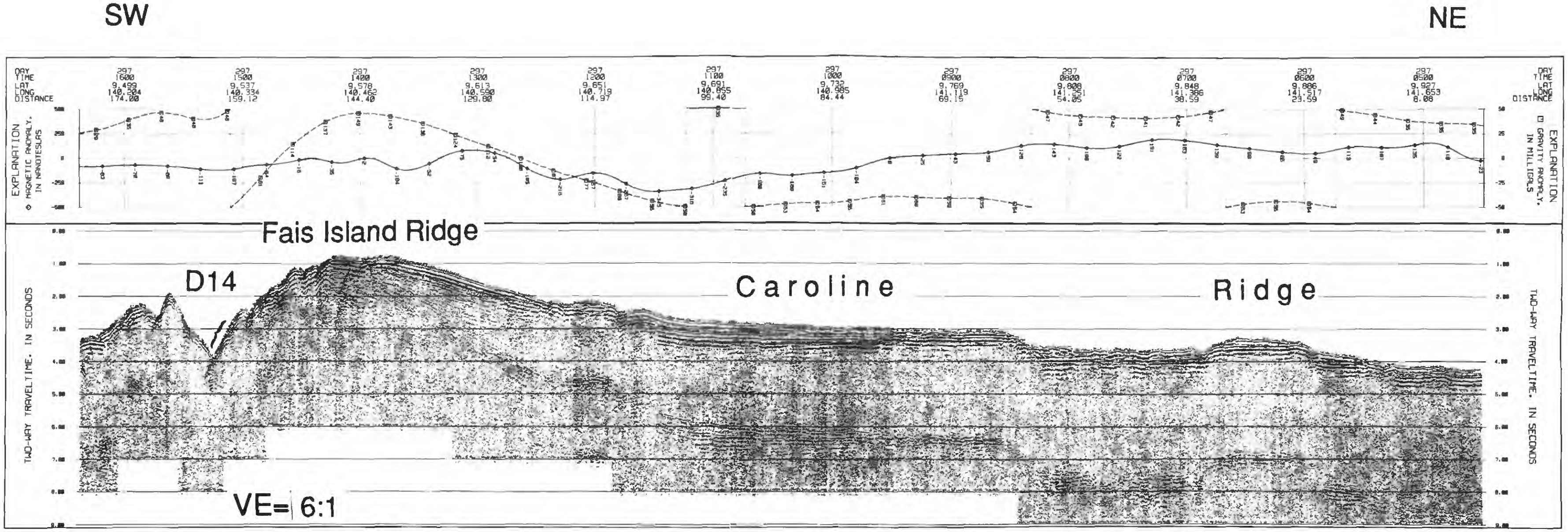

Figure 47. Southwest to northeast cross section of Fais Island and Caroline Ridges, 195 in^3 single-channel airgun line 13 and associated gravity and magnetic profiles. Note location of Dredge 14 (See Fig. 7 for entire line and Fig. 15 for dredge location).

Fais Island and Caroline Ridges

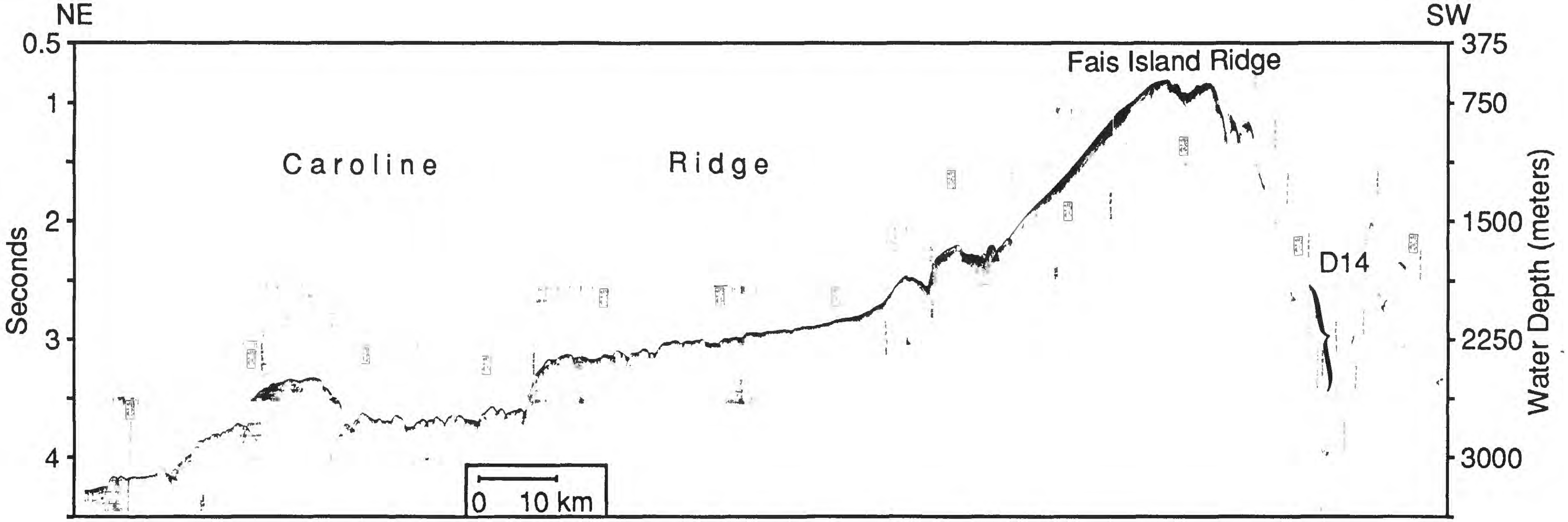

Figure 48. Northeast-southwest cross section of Fais Island and Caroline Ridges, 3.5 kHz Line 13. Note location of Dredge 14. Northeast and southwest directions are reversed from figure 47 (See Fig. 7 for entire line and Fig. 15 for dredge location).

Cross Section of a Trough on Caroline Ridge

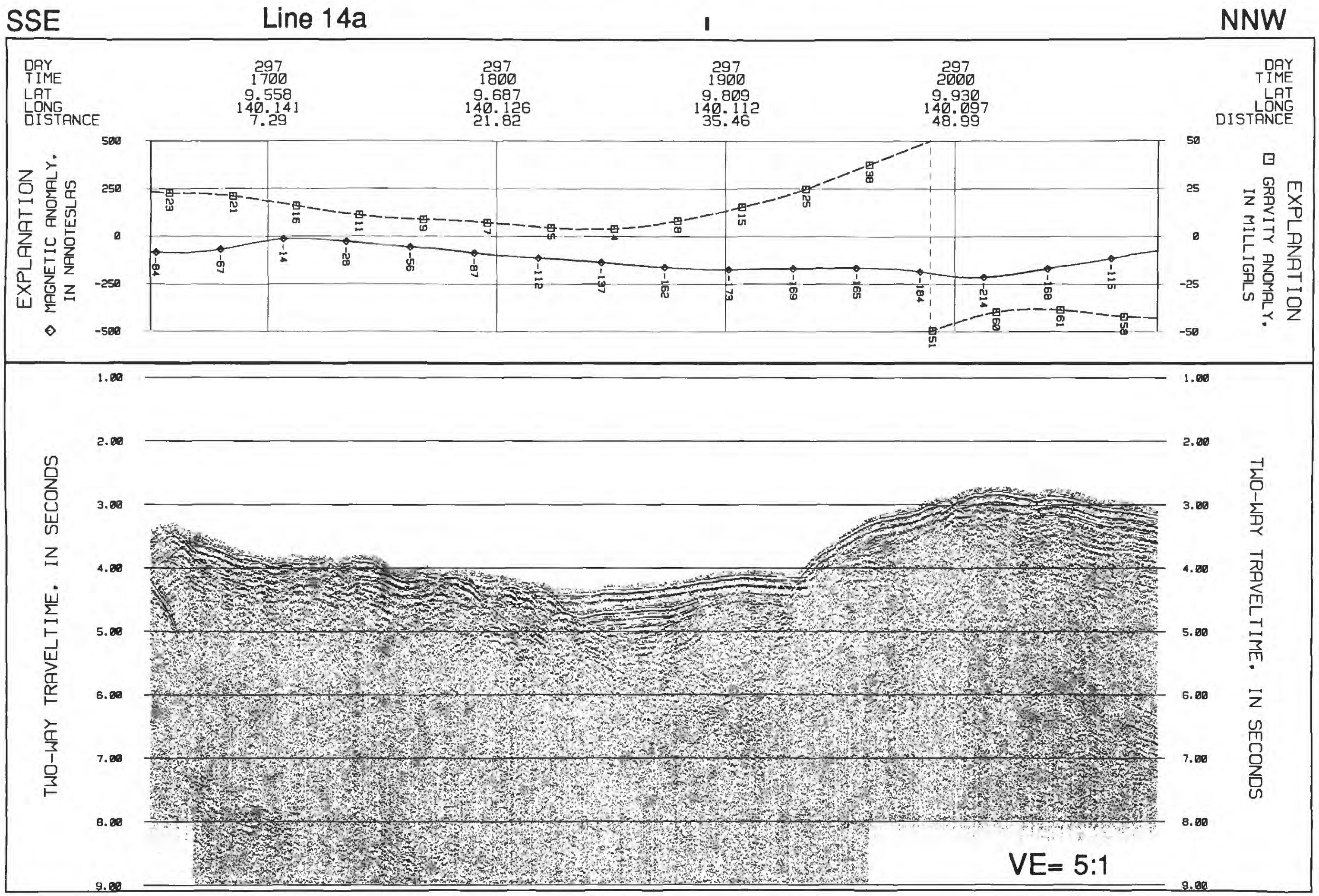

Figure 49. Southeast-northwest cross section of a trough on Caroline Ridge between Ulithi Atoll and Fais Island Ridge, 195 in^3 single-channel airgun line 14 and associated gravity and magnetic profiles. Note division of line 14 (See Fig. 7 for location of entire line and Fig. 15 for line 14a).

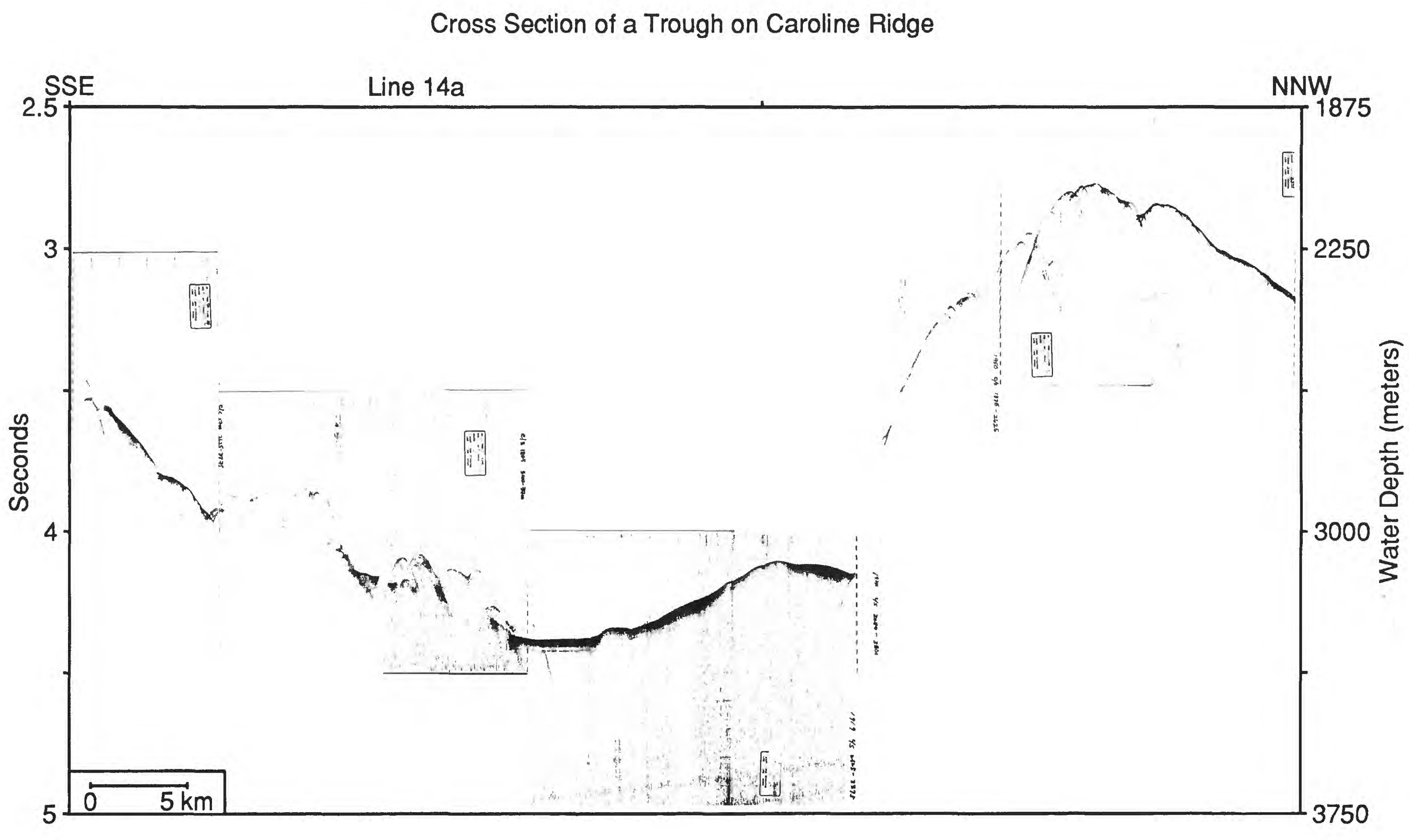

Figure 50. Southeast-northwest cross section of a trough on Caroline Ridge between Ulithi Atoll and Fais Island Ridge, 3.5 kHz line 14. Note division of line 14 (See Fig. 7 for location of entire line and Fig. 15 for line 14a).

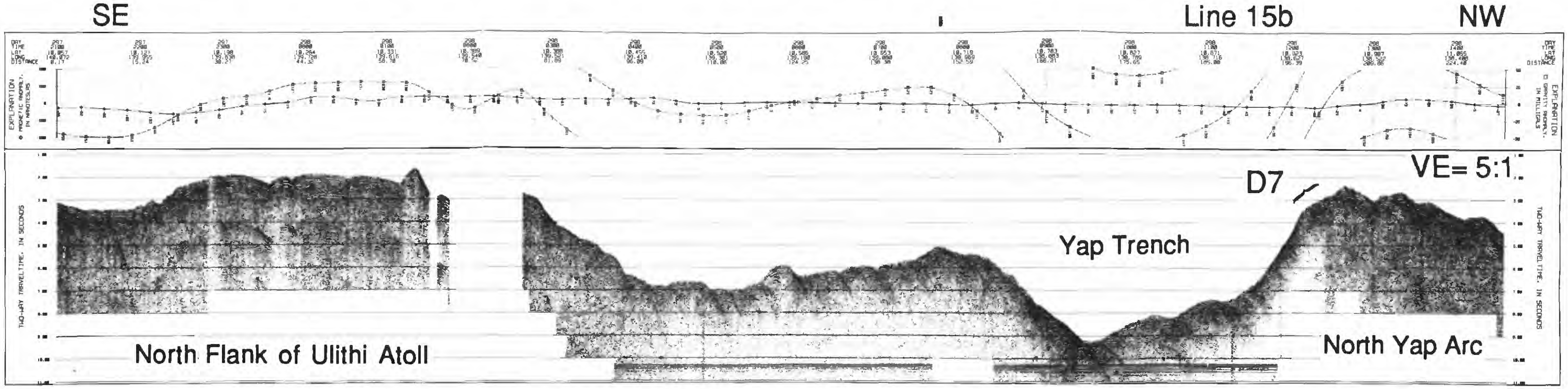

Figure 51. Southeast to northwest cross section of the north fank of Ulithi Atoll, northern Yap Trench, and north Yap Arc, 195 in^3 single-channel airgun Line 15, with divisions for line 15, and associated gravity and magnetic profiles. Note location of Dredge 7 and line 15b (See Figs. 7 and 11 for locations).

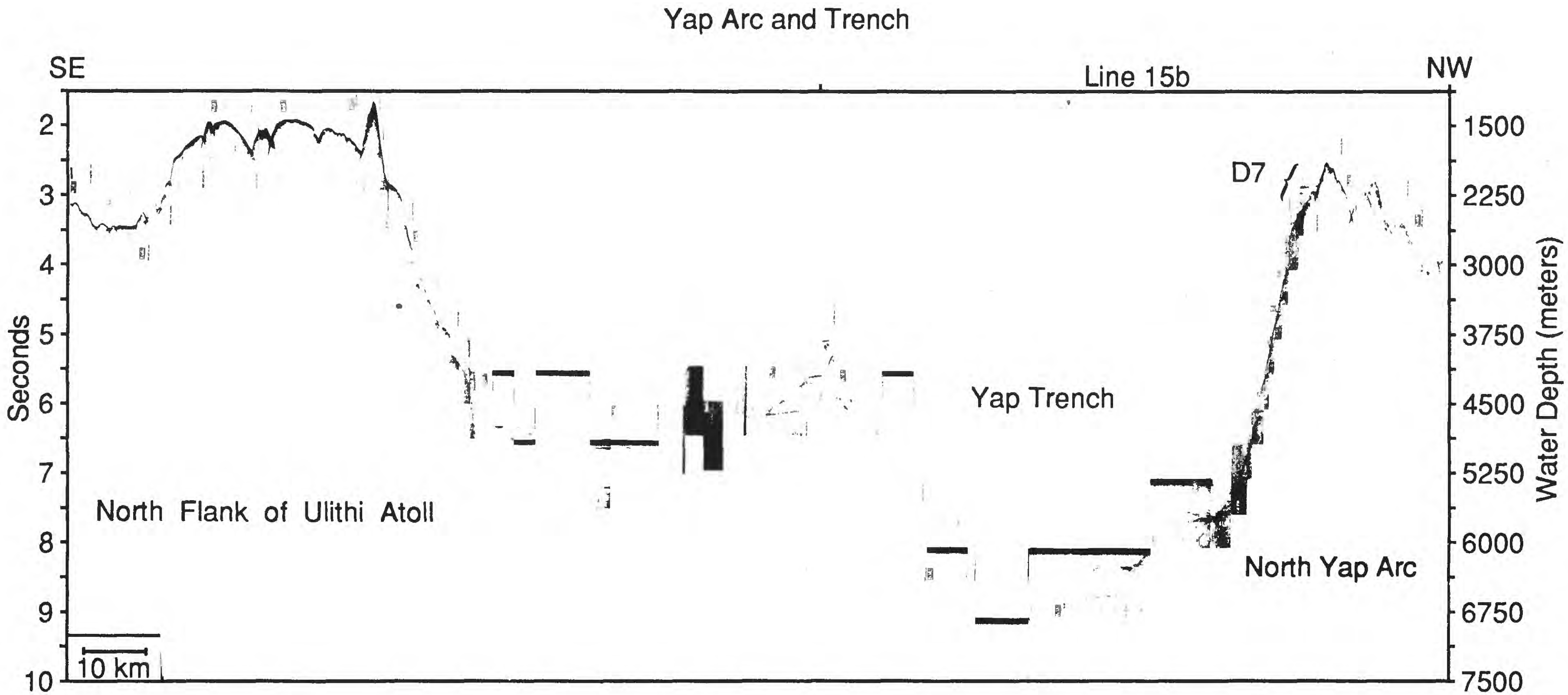

Figure 52. Southeast-northwest cross section of the north flank of Ulithi Atoll, northern Yap Trench, and north Yap Arc, 3.5 kHz Line 15 and divisions of Line 15. Note location of D7 and Line 15b (See Figs. 7 and 11 for location).

Juncture of Mariana-Yap Arcs and Trenches

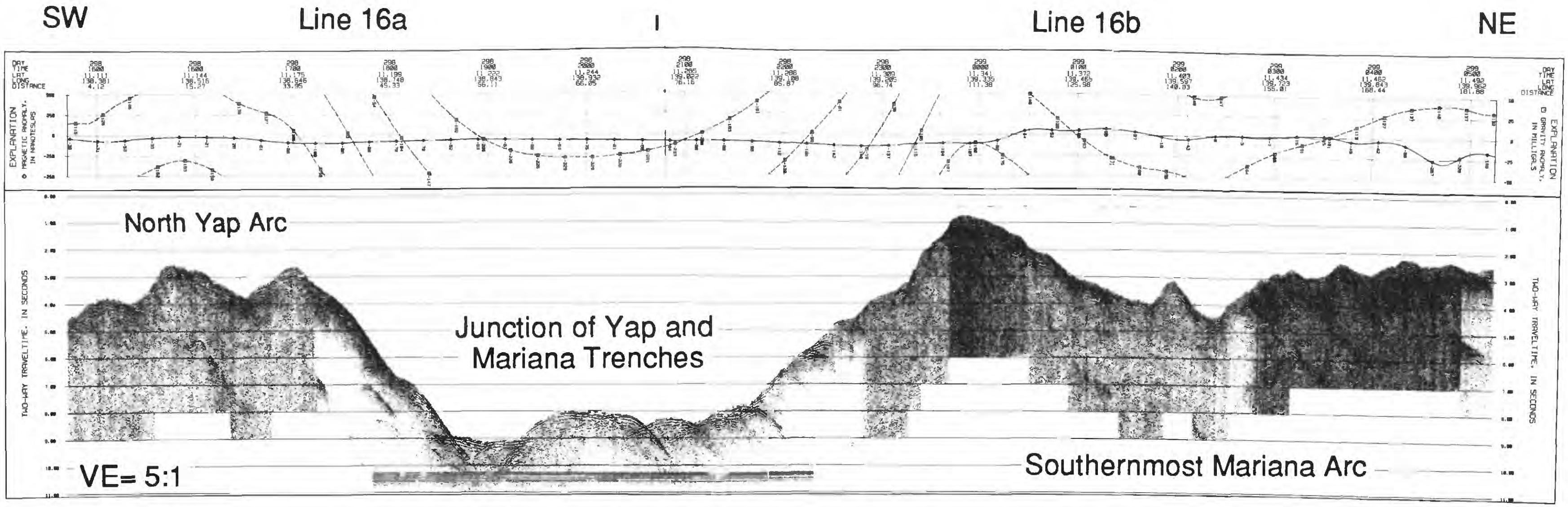

Figure 53. Juncture of Mariana-Yap Arcs and Trenches, 195 in^3 single-channel airgun line 16, with the divisions of line 16, and associated gravity and magnetic profiles (See Figs. 10 and 11 for location).

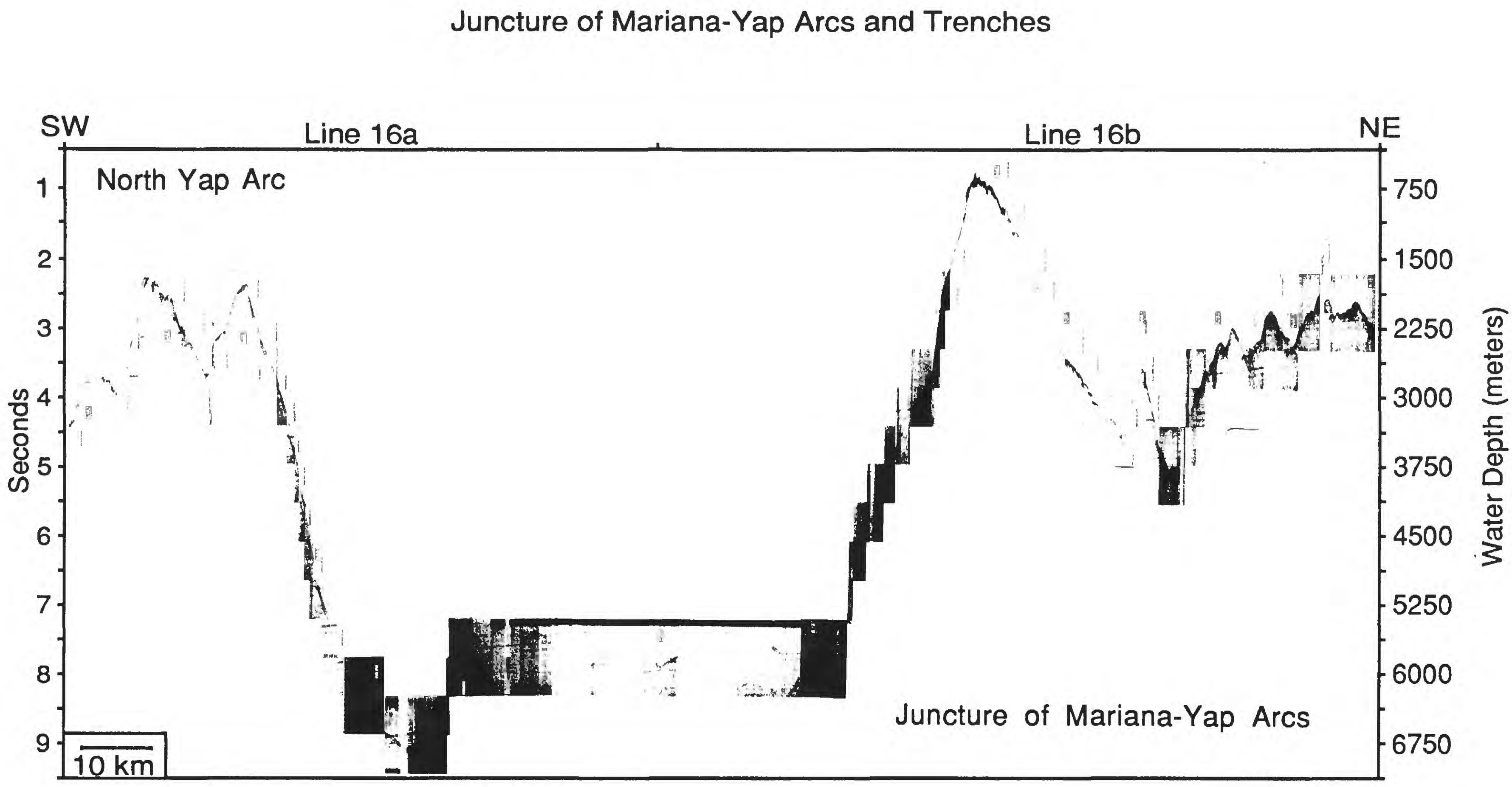

Figure 54. Juncture of Mariana-Yap Arcs and Trenches, 3.5 kHz line 16, with divisions for line 16 (See Figs. 10 and 11 for location).

Northeast Mariana-Yap Juncture

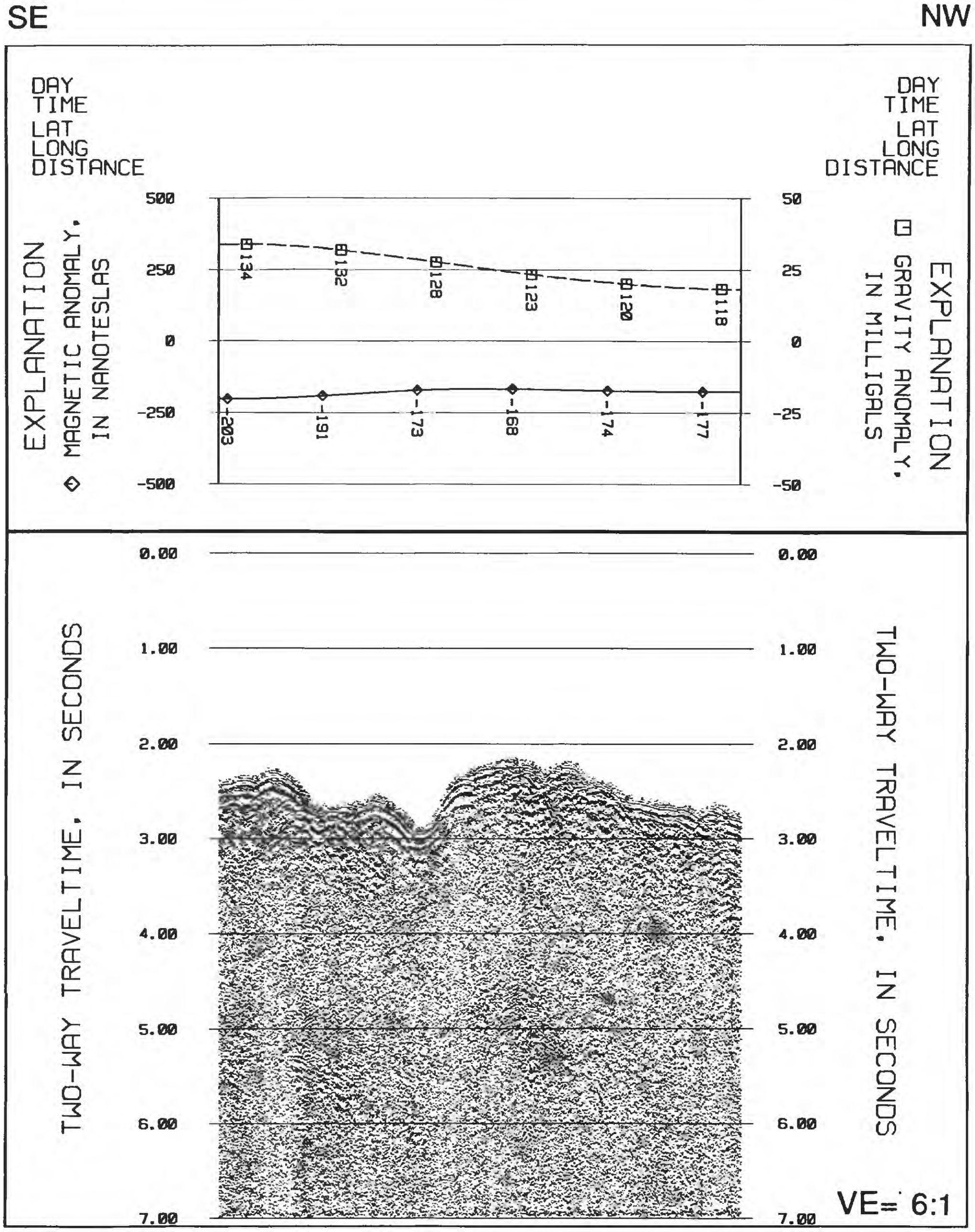

Figure 55. Northeast of the Mariana-Yap Arc Juncture, 195 in^3 single-channel airgun line 17 and associated gravity and magnetic profiles (see figure 10 for location).

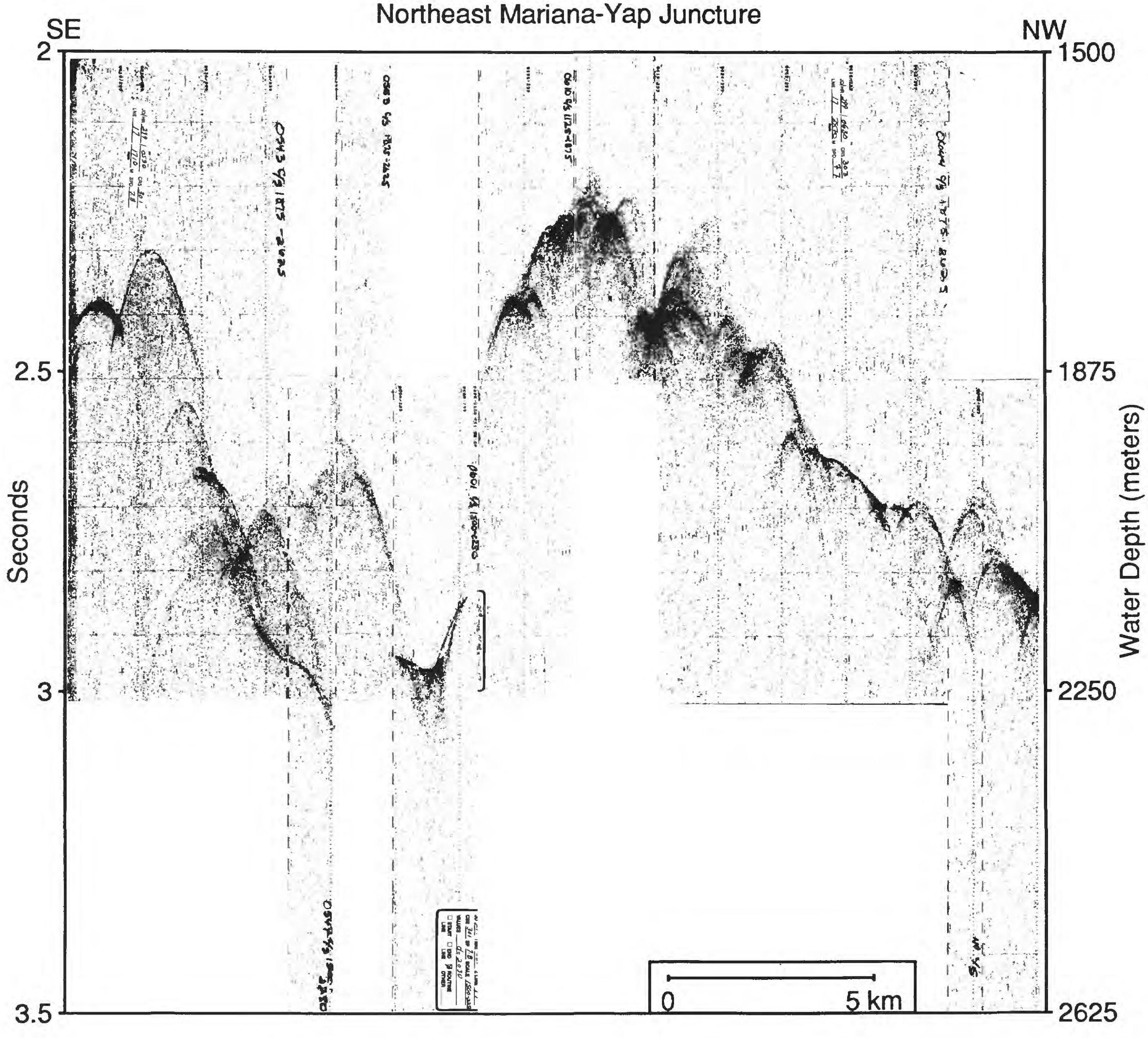

Figure 56. Northeast of the Mariana-Yap Arc juncture 3.5 kHz Line 17 (See Fig. 10 for location).

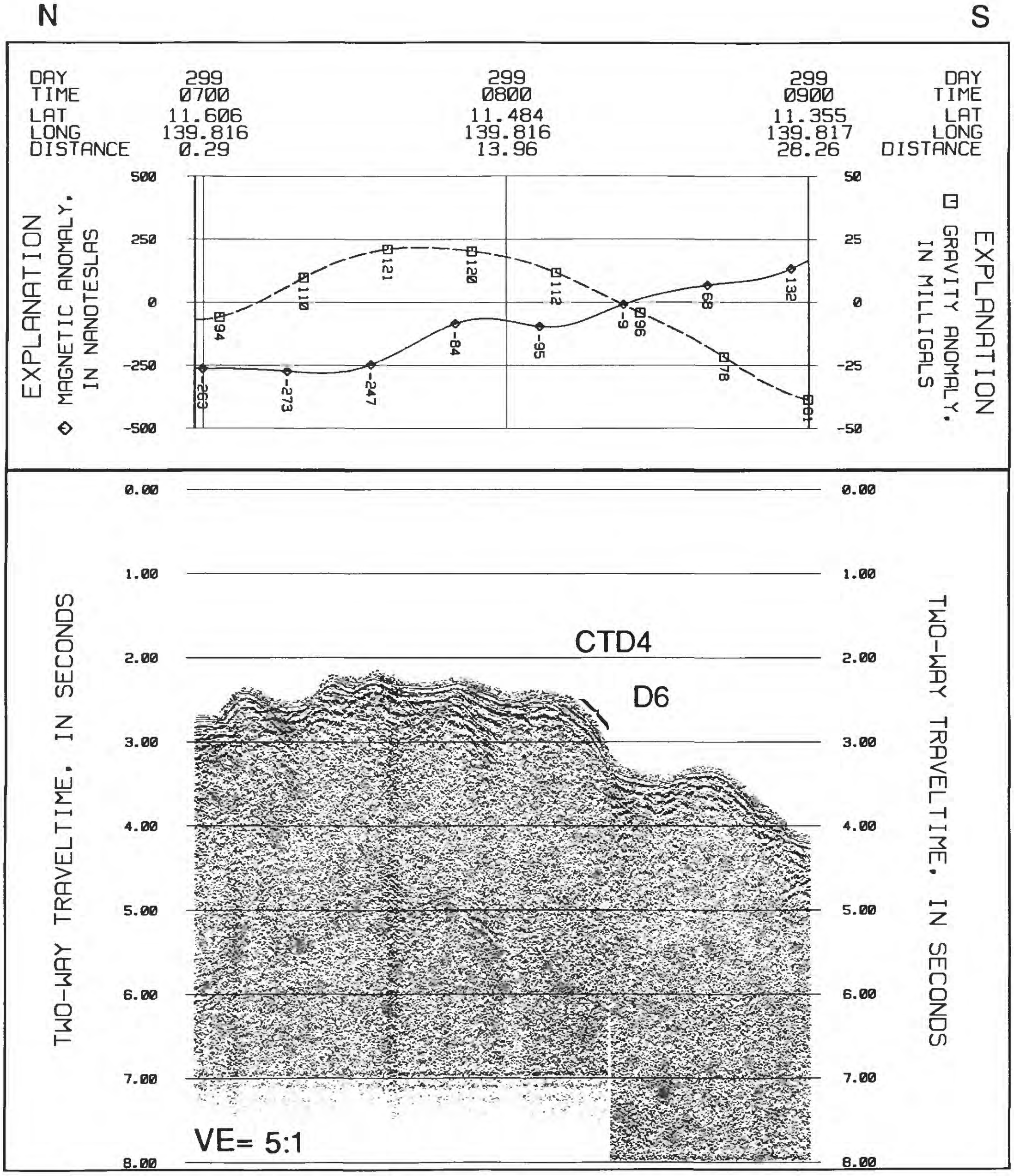

Figure 57. Juncture of Mariana and Yap Arcs, 195 in^3 single-channel airgun line 18 and associated gravity and magnetic profiles. Note location of Dredge 6 and CTD 4 (see figure 10 for location).

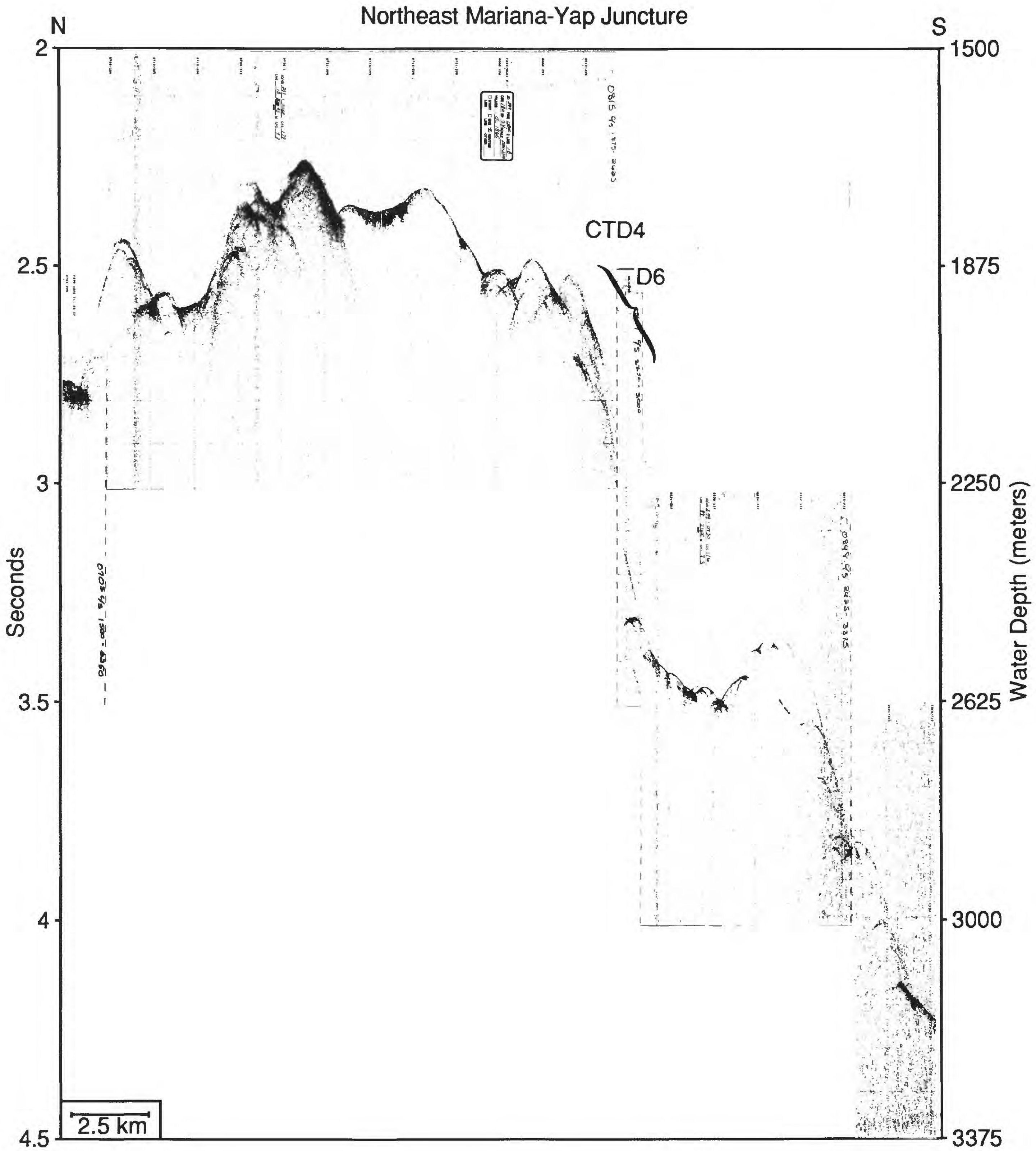

Figure 58. Juncture of the Mariana and Yap Arcs, 3.5 kHz Line 18. Note location of D6 and CTD 4 (See Fig. 10 for location).

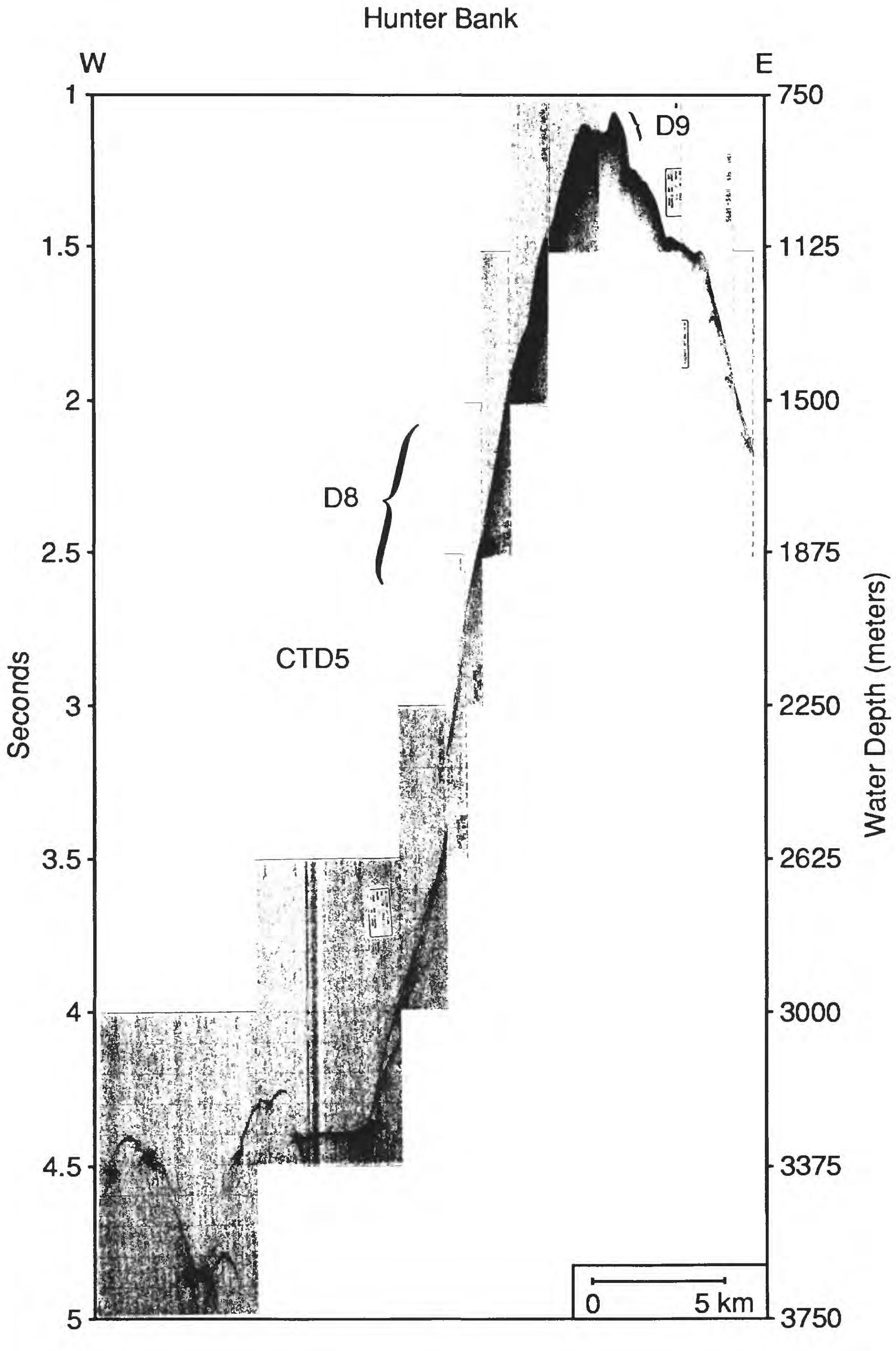

Figure 59. West-east cross section of Hunter Bank 3.5 kHz Line 19. Note location of Dredges 8 and 9 and CTD 5 (See Fig. 12 for location).

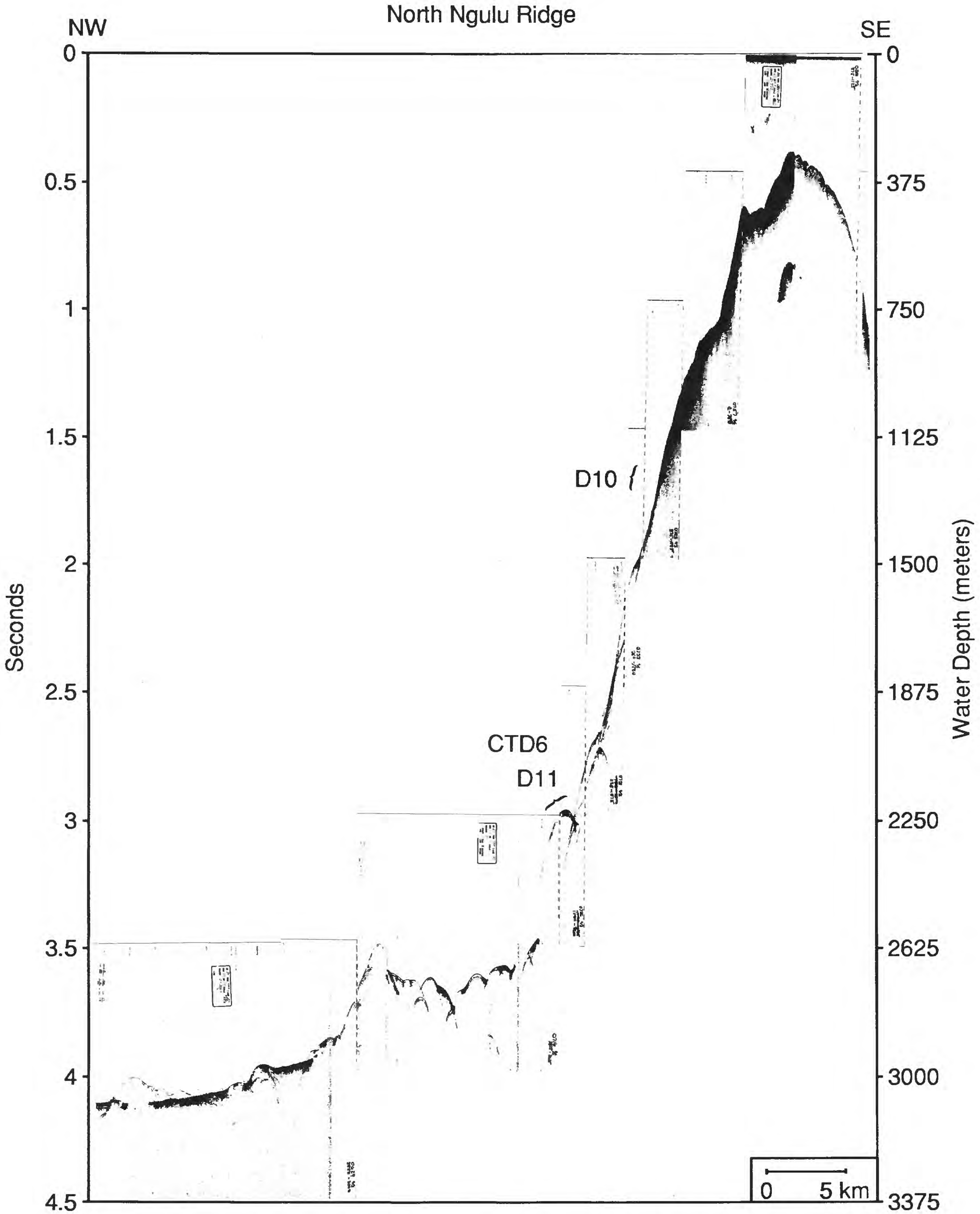

Figure 60. Northwest-southeast cross section of north Ngulu Ridge, 3.5 kHz Line 20. Note locations of Dredges 10 and 11 and CTD 11 (See Fig. 13 for location).

W E

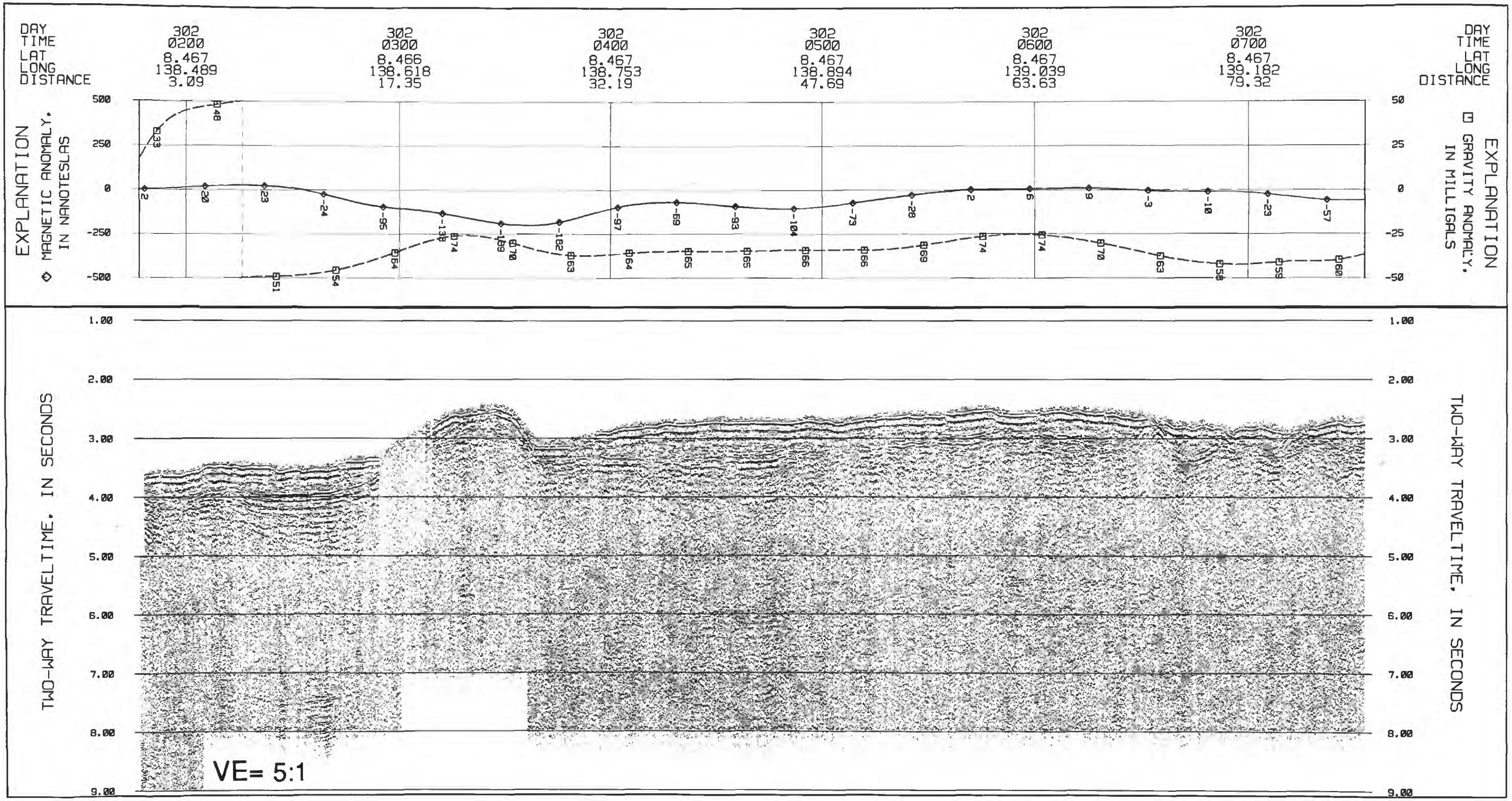

Figure 61. West-east cross section of Sorol Guyot, 195 in^3 single-channel airgun Line 21 and associated gravity and magnetic profiles (See Fig.14 for location).

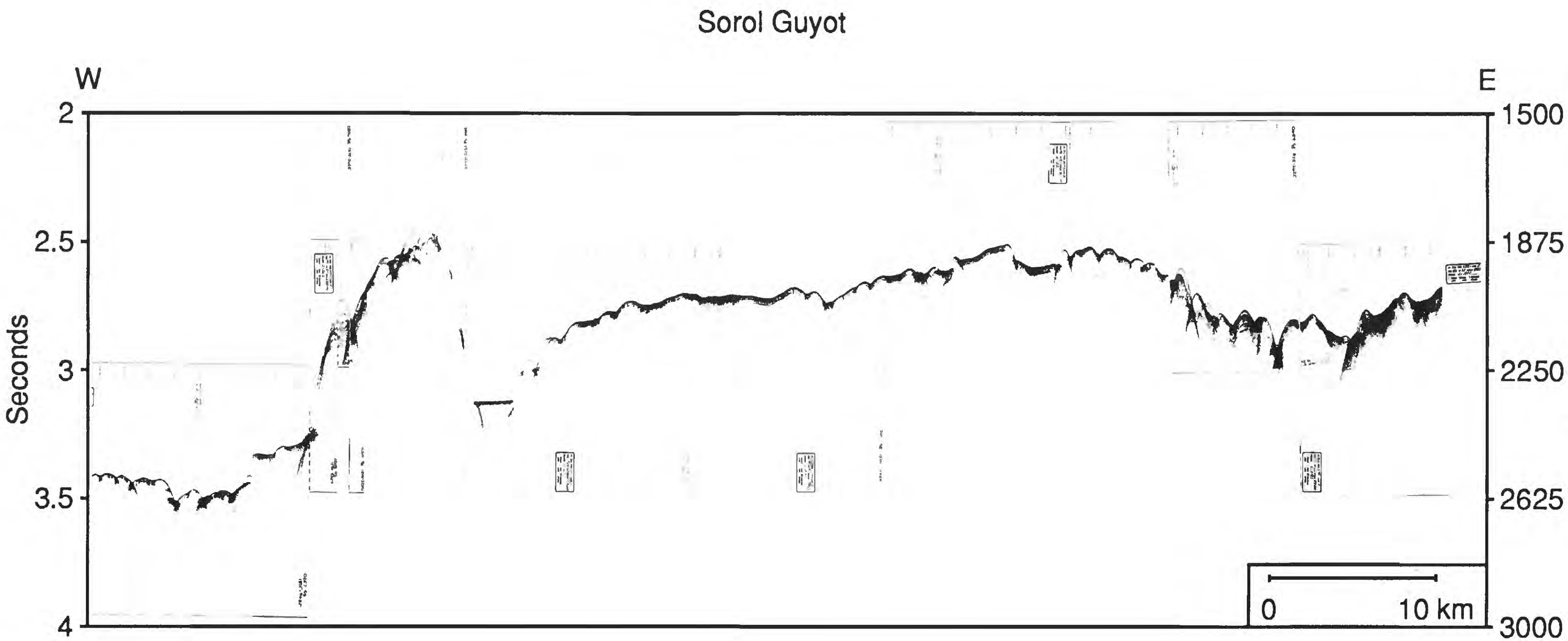

Figure 62. West-east cross section of Sorol Guyot, 3.5 kHz Line 21 (See Fig. 14 for location).

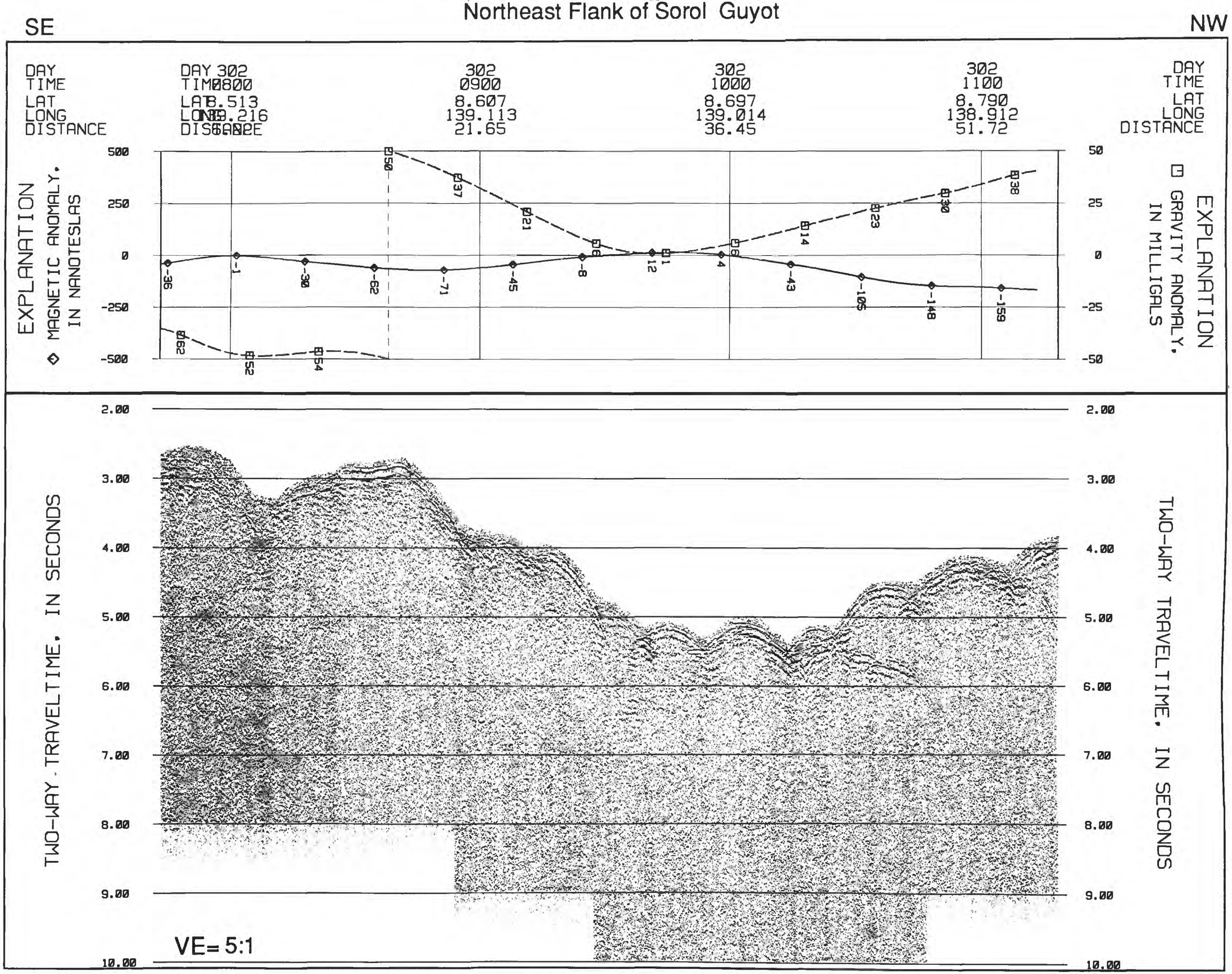

Figure 63. Northeast flank of Sorol Guyot, 195 in^3 single-channel airgun line 22 and associated gravity and magnetic profiles (See Fig. 14 for location).

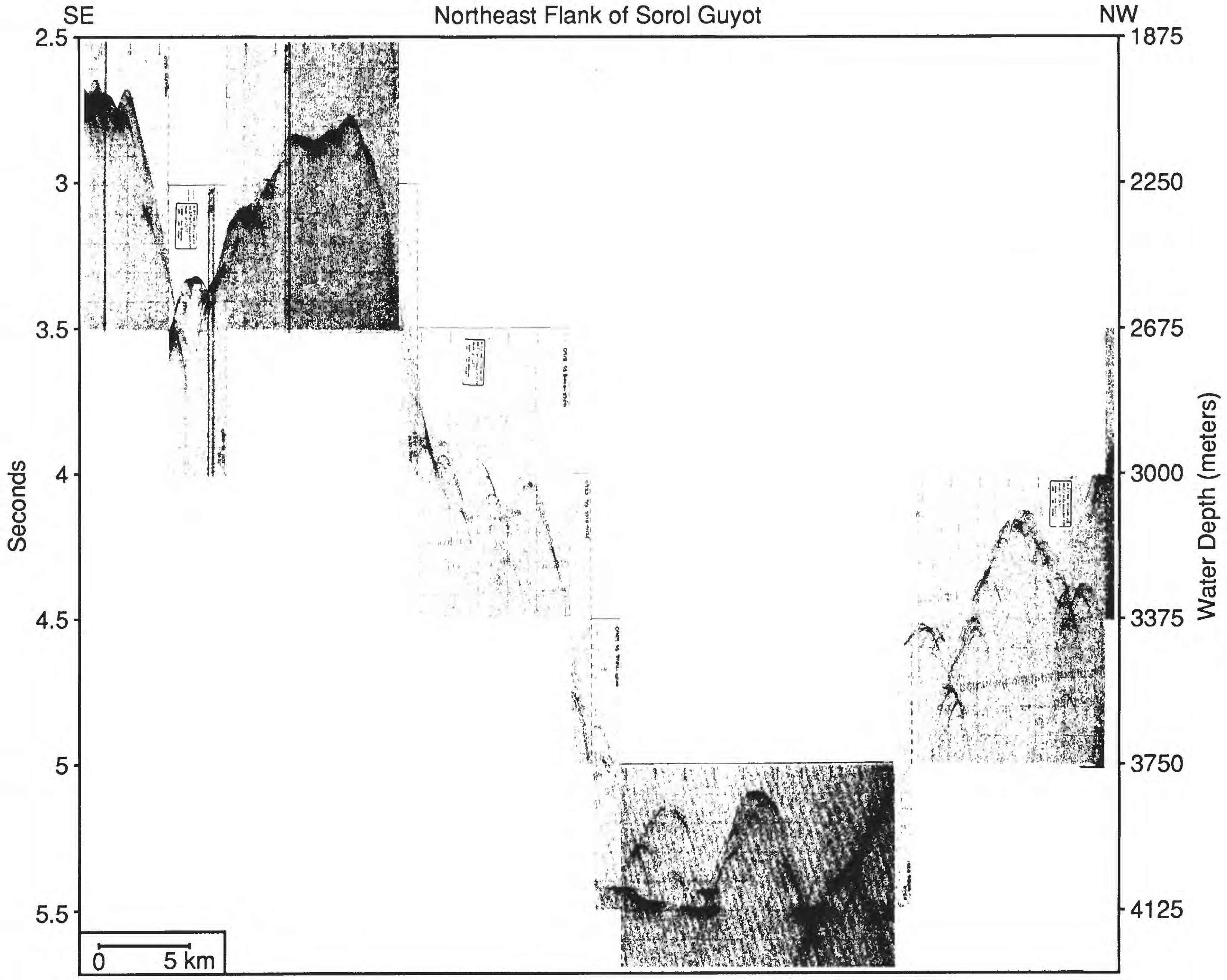

Figure 64. Northeast flank of Sorol Guyot, 3.5 kHz Line 22 (See Fig. 14 for location).

Sorol Guyot

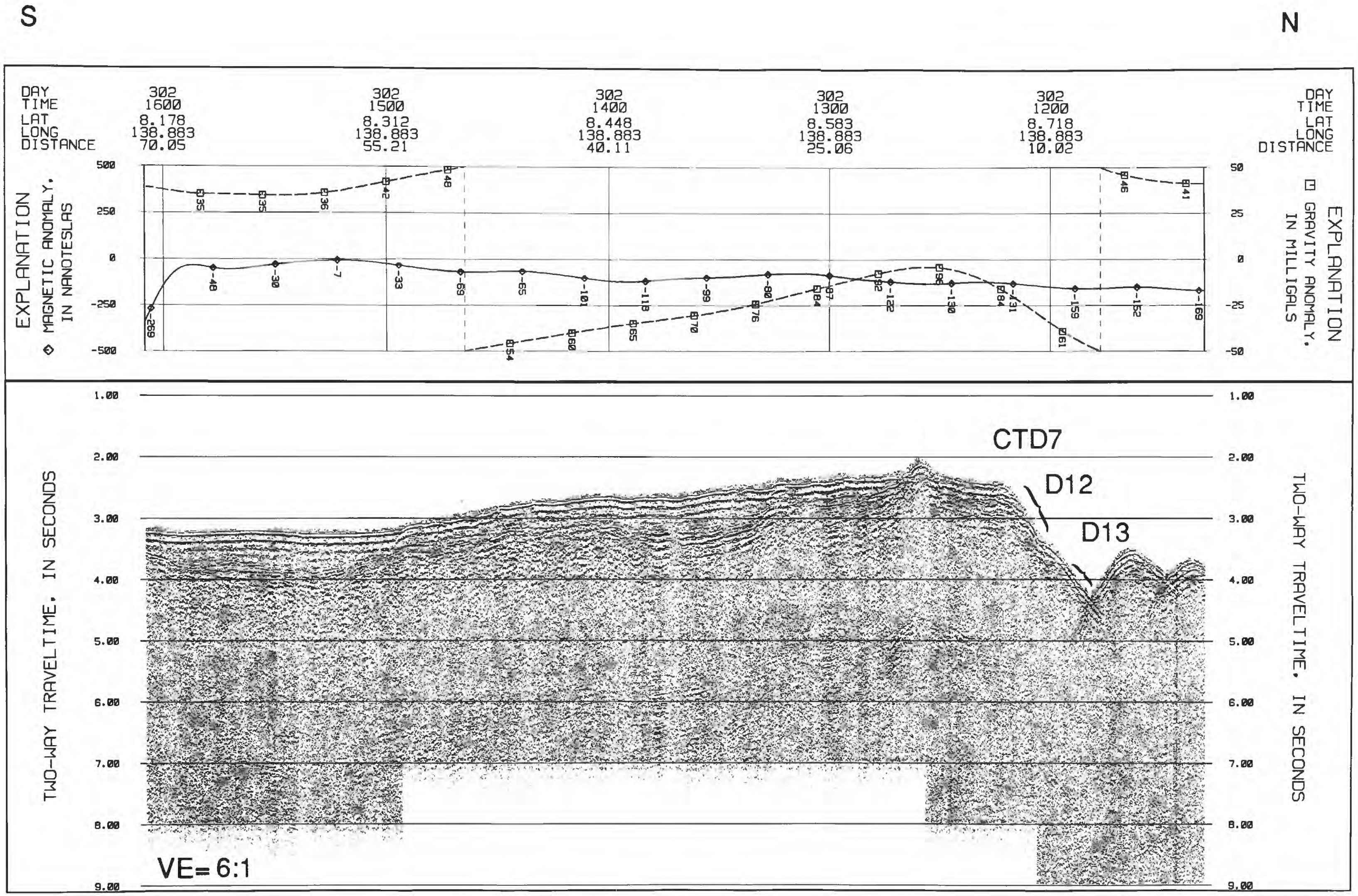

Figure 65. South-north cross section of Sorol Guyot, 195 in^3 single-channel airgun line 23 and associated gravity and magnetic profiles. Note location of Dredges 12 and 13 and CTD7 (see figure 14 for location).

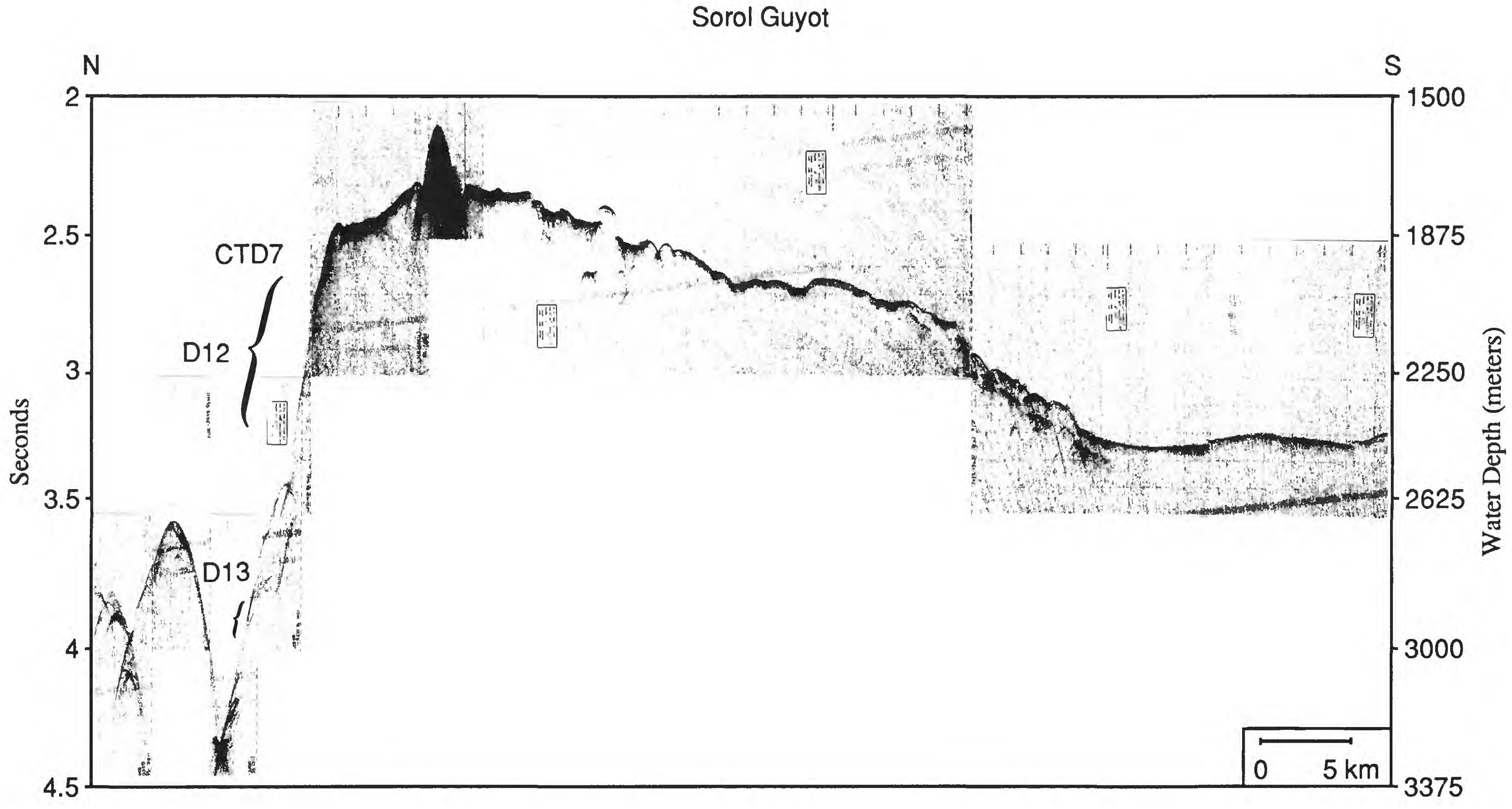

Figure 66. North-south cross section of Sorol Guyot, 3.5 kHz Line 23. Note location of Dredges 12 and 13 and CTD 7. North and south directions are reversed from figure 65 (see figure 14 for location).

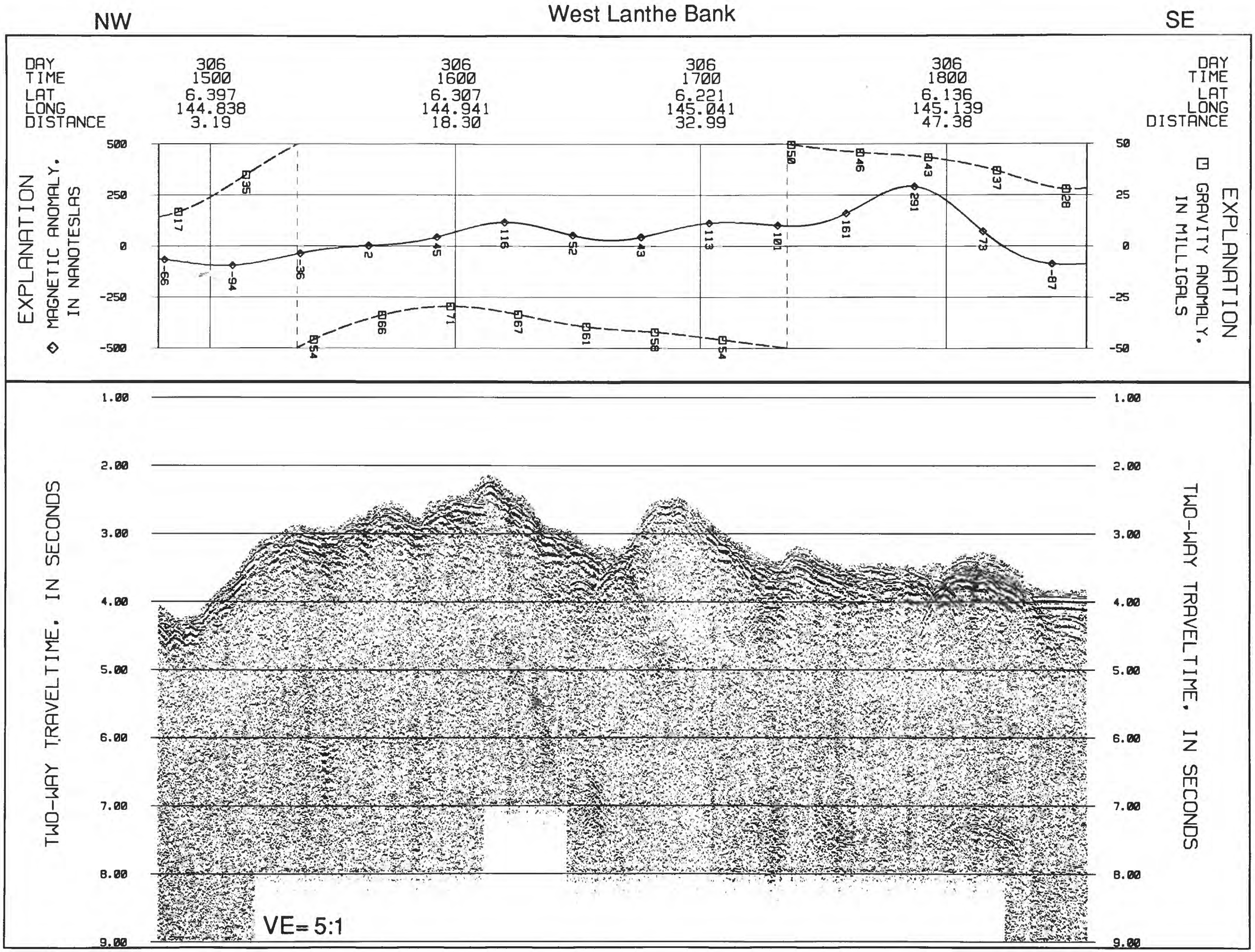

Figure 67. Northwest-southeast cross section of west Lanthe Bank, 195 in^3 single-channel airgun Line 24 and associated gravity and magnetic profiles (See Fig. 19 for location).

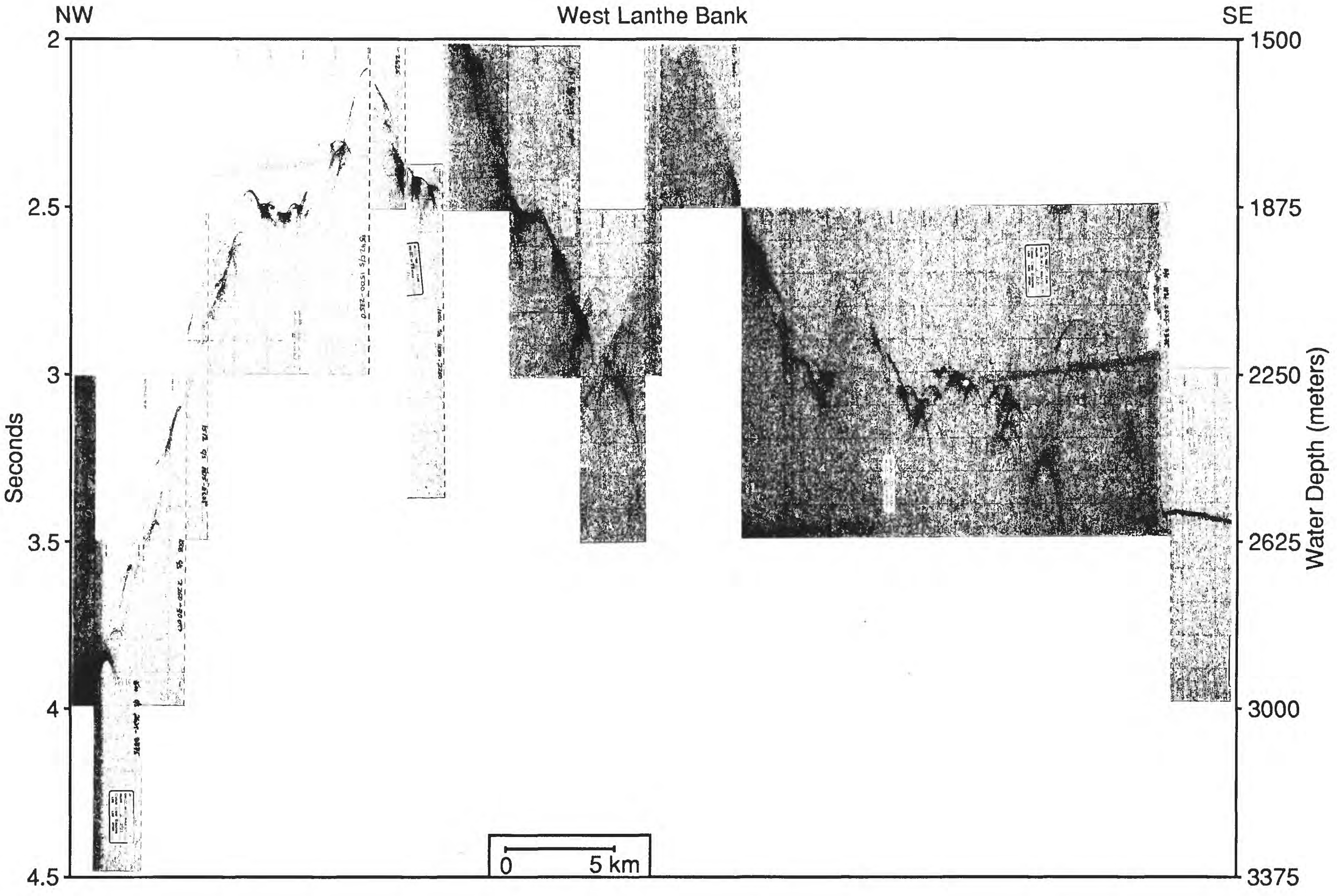

Figure 68. Northwest-southeast cross section of west Lanthe Bank, 3.5 kHz Line 24 (See Fig.. 19 for location).

Northeast Flank of West Lanthe Bank

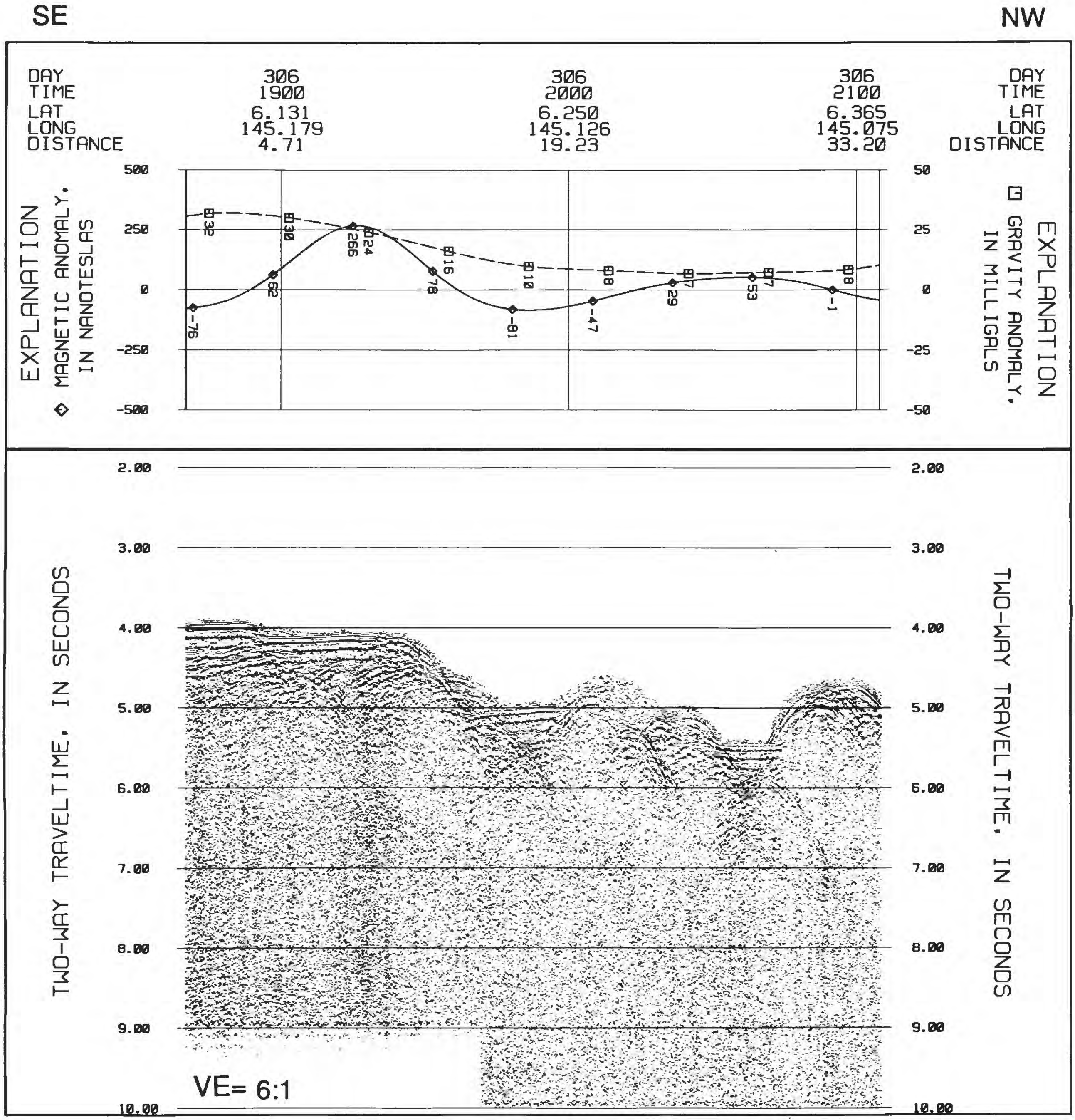

Figure 69. Northeast flank of West Lanthe Bank, 195 in^3 single-channel airgun line 25 and associated gravity and magnetic profiles (see figure 19 for location).

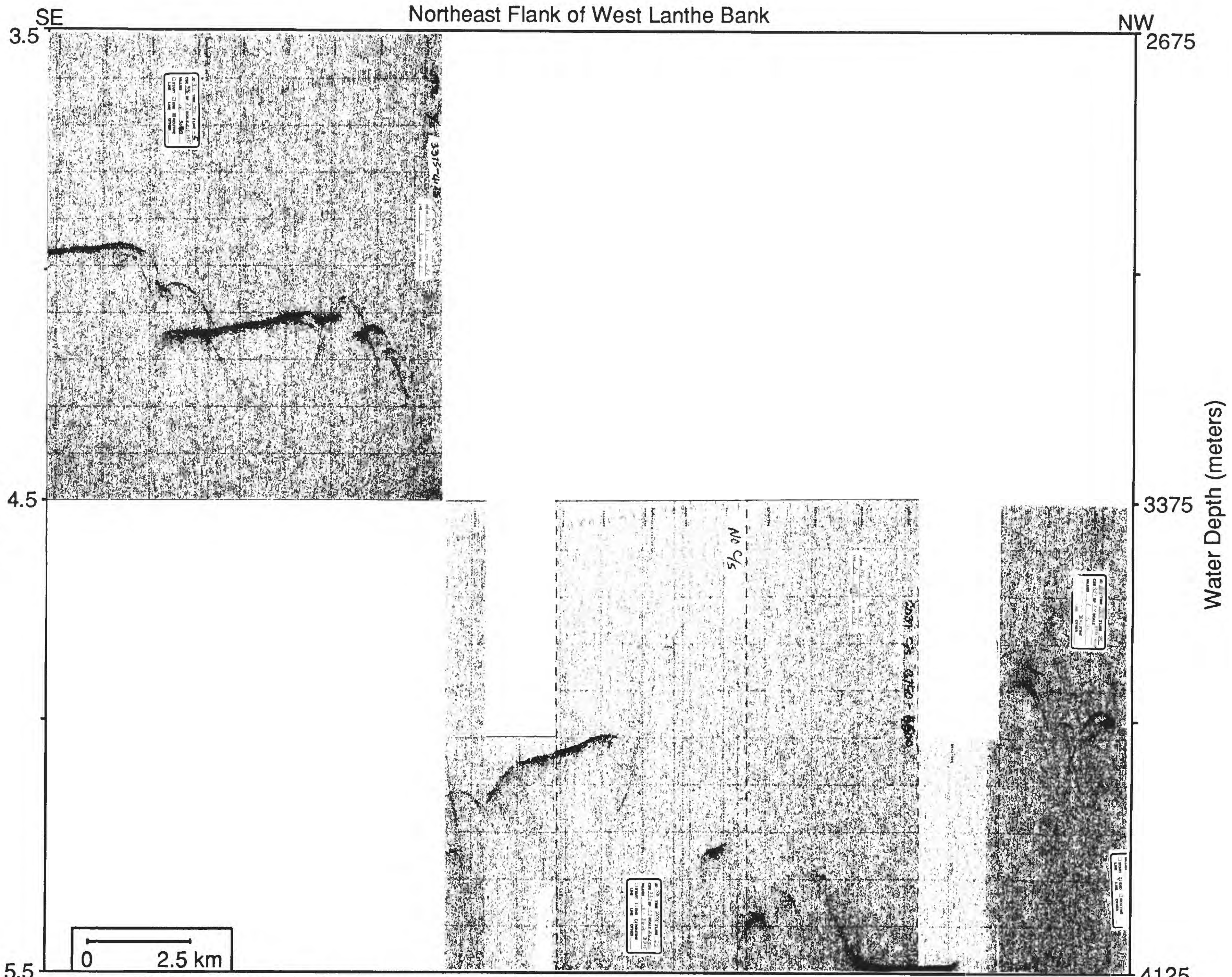

Figure 70. Northeast flank of west Lanthe Bank, 3.5 kHz Line 25 (See Fig. 19 for location).

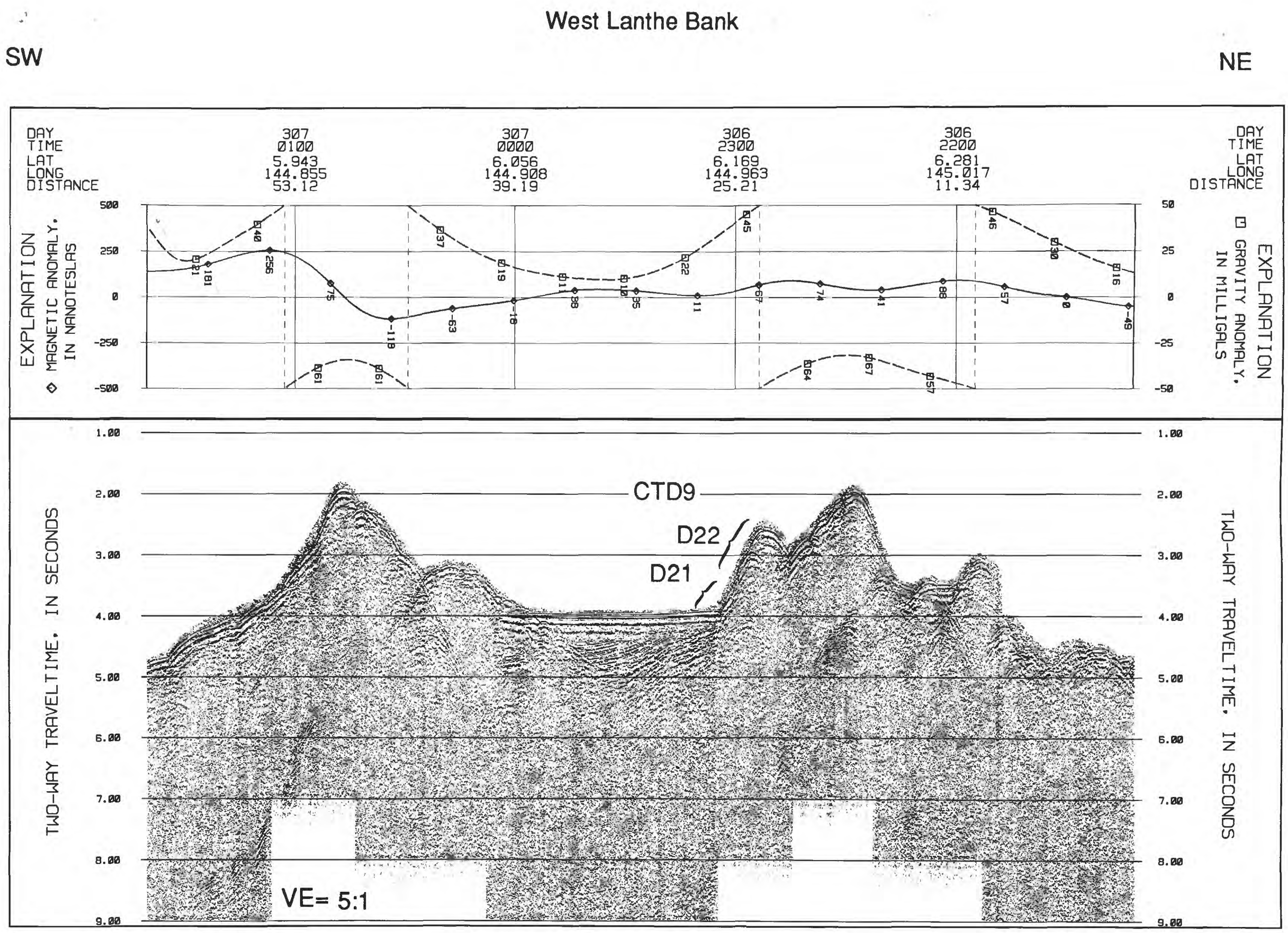

Figure 71. West Lanthe Bank, 195 in^3 single-channel airgun line 26 and associated gravity and magnetic profiles. Note location of Dredges 21 and 22 and CTD 9 (see figure 19 for location).

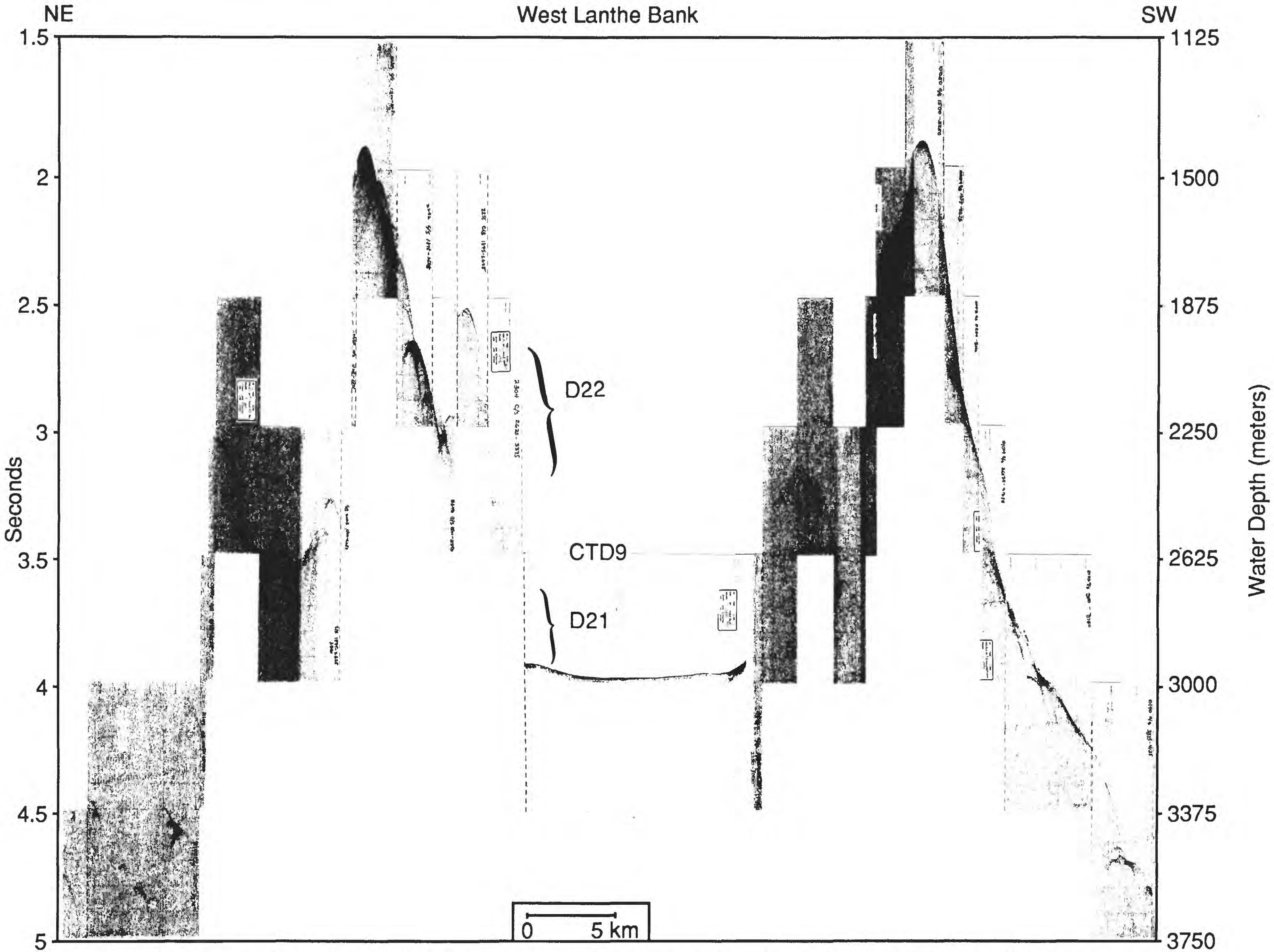

Figure 72. West Lanthe Bank, 3.5 kHz Line 26. Note location of Dredges 21 and 22 and CTD 9. Northeast and southwest directions are reversed from figure 71 (see figure 19 for location).

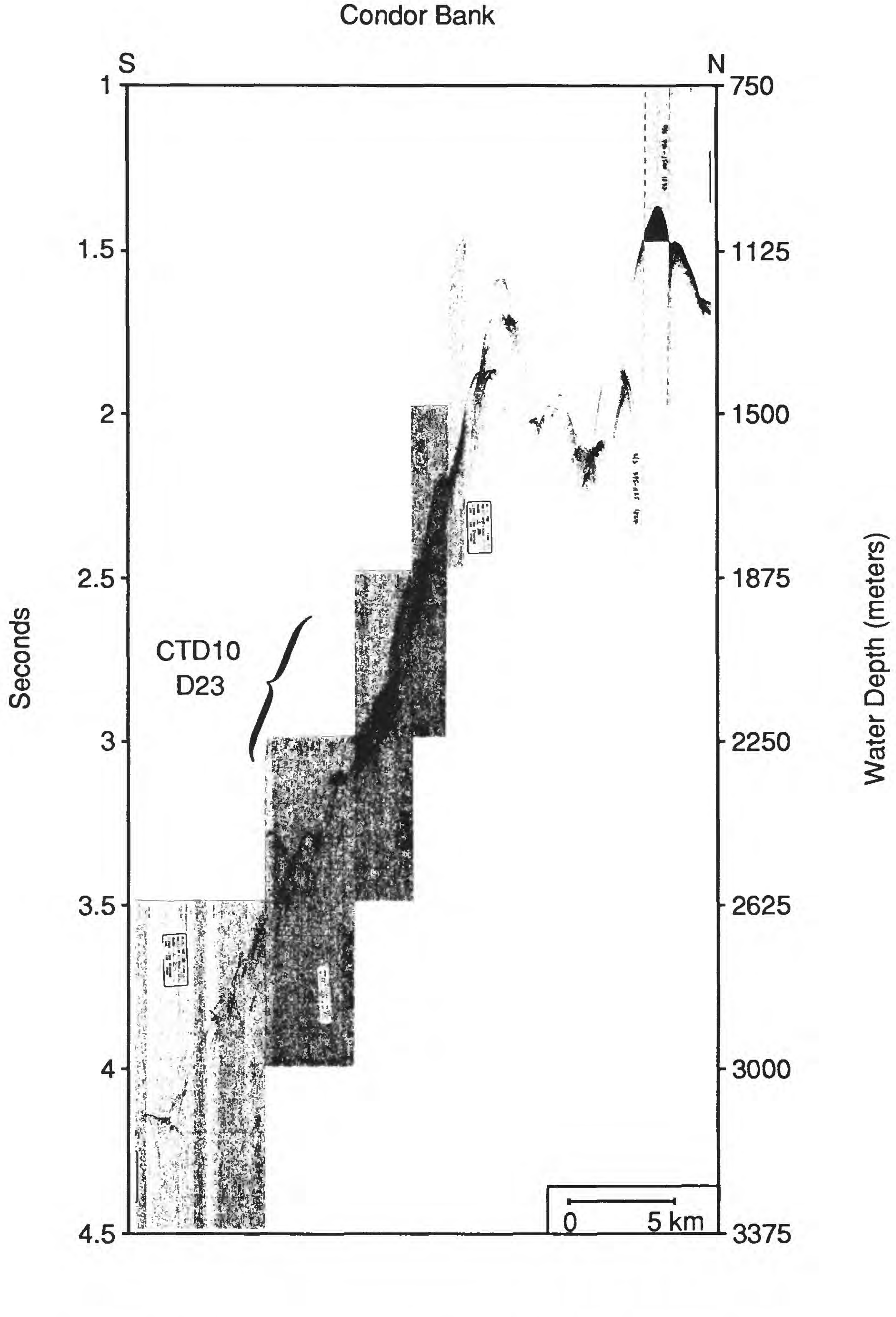

Figure 73. North-south cross section of Condor Bank, 3.5 kHz Line 27. Note location of Dredge 23 and CTD 10 (See Fig. 20 for location).

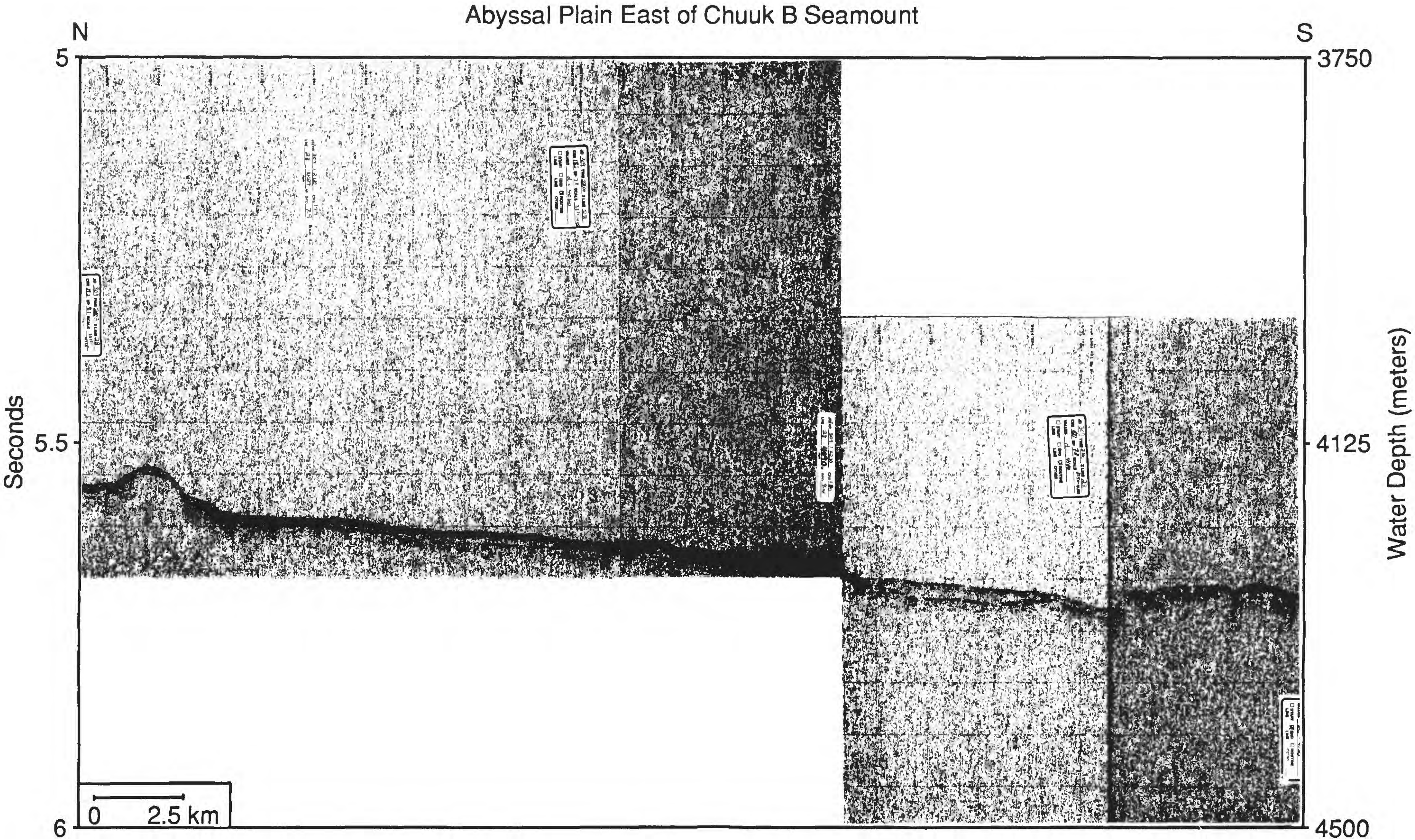

Figure 74. North-south cross section of Abyssal plain east of Chuuk B Seamount, 3.5 kHz Line 28 (See Fig. 21 for location).

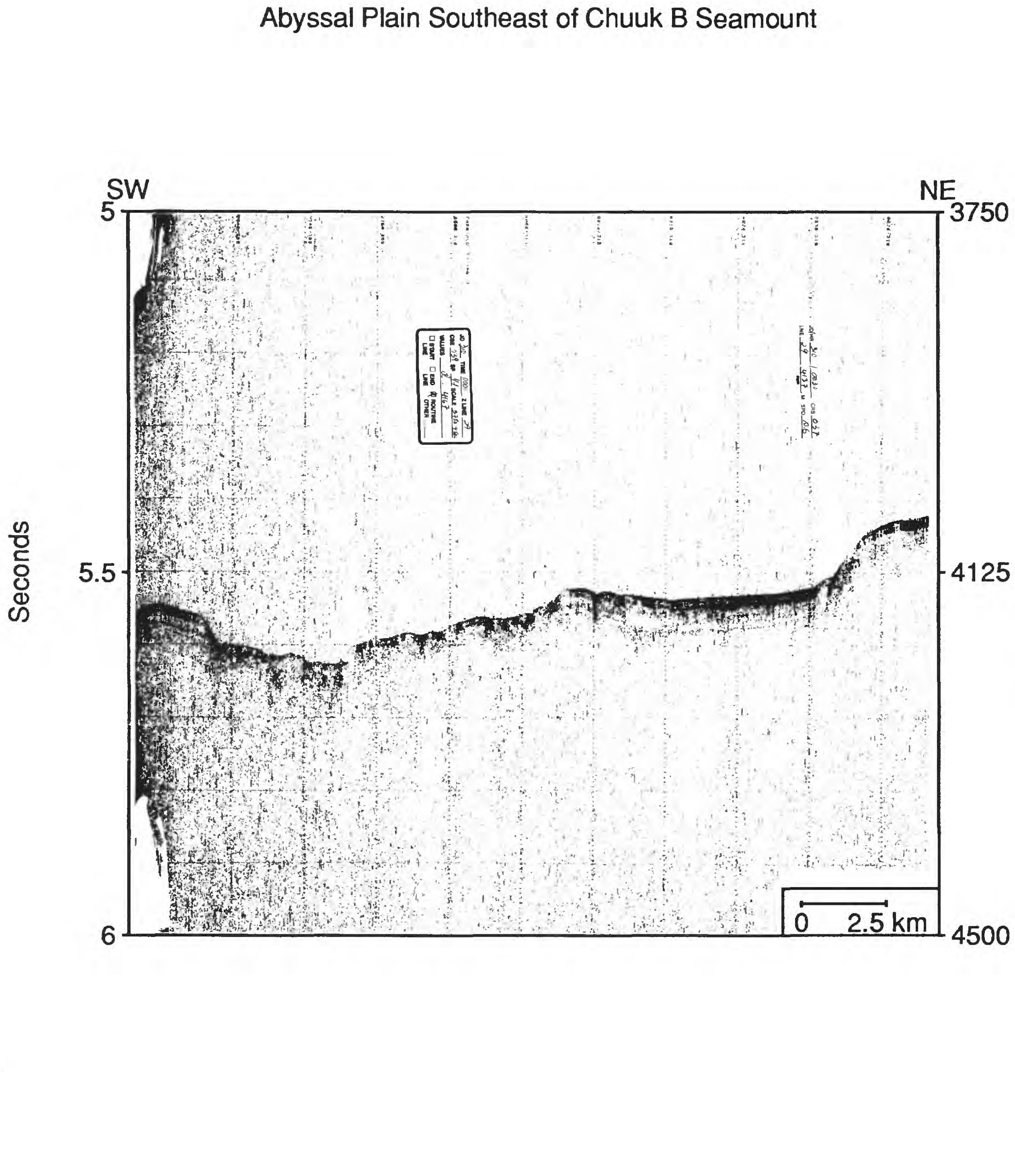

Figure 75. Abyssal plain southeast of Chuuk B Seamount, 3.5 kHz Line 29 (See Fig. 21 for location).

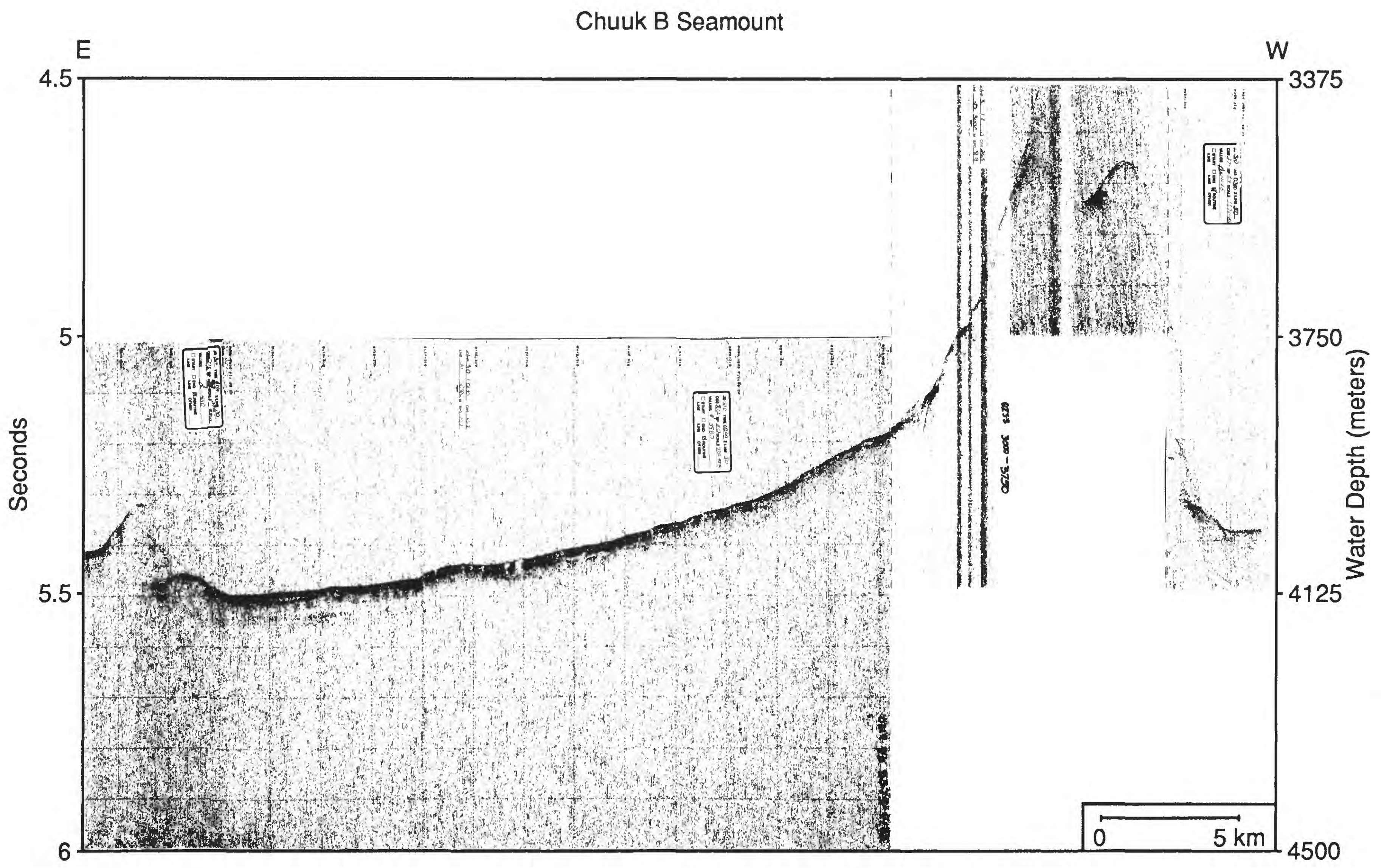

Figure 76. East-west cross section of Chuuk B Seamount, 3.5 kHz Line 30 (See Fig. 21 for location).

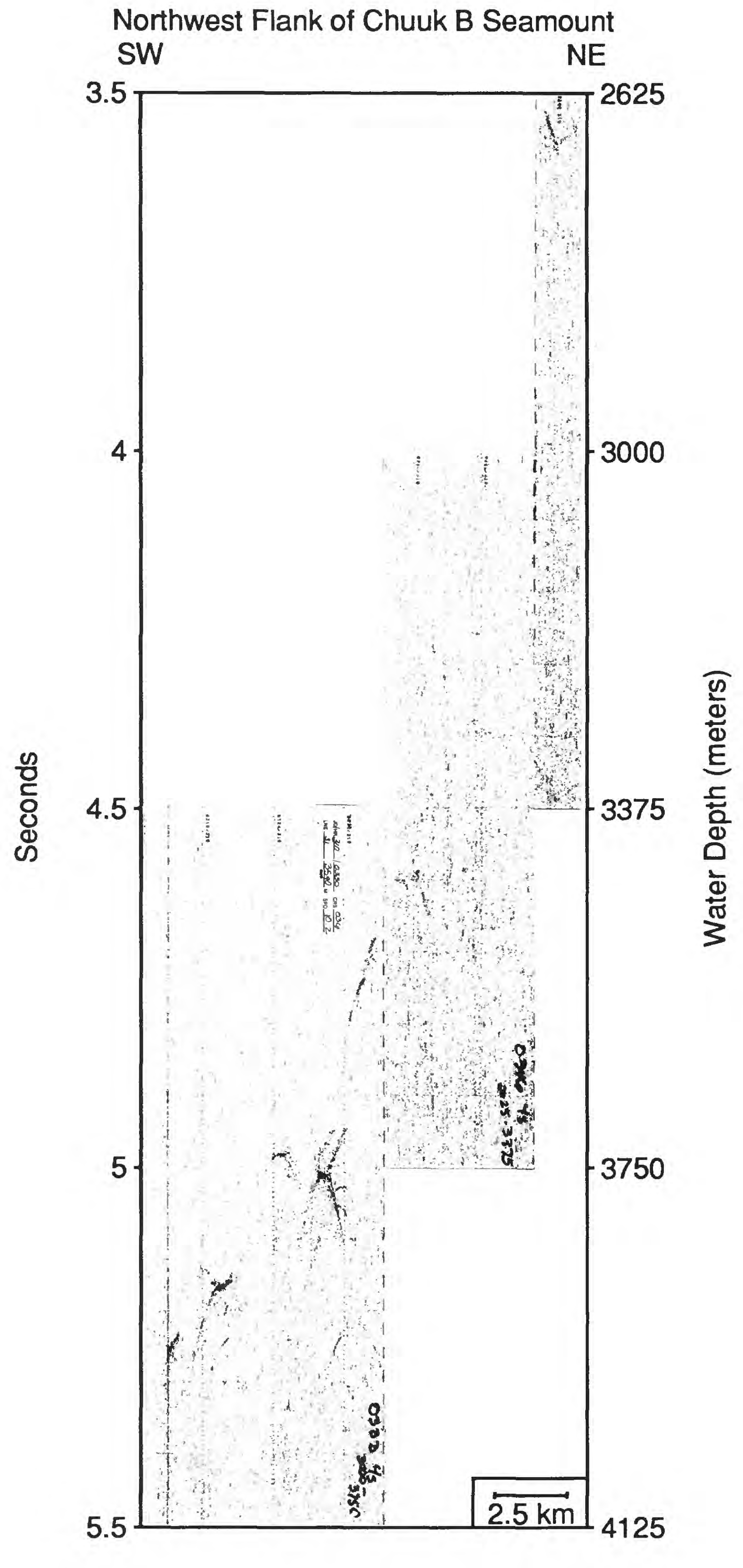

Figure 77. Northwest flank of Chuuk B Seamount, 3.5 kHz Line 31 (See Fig. 21 for location).

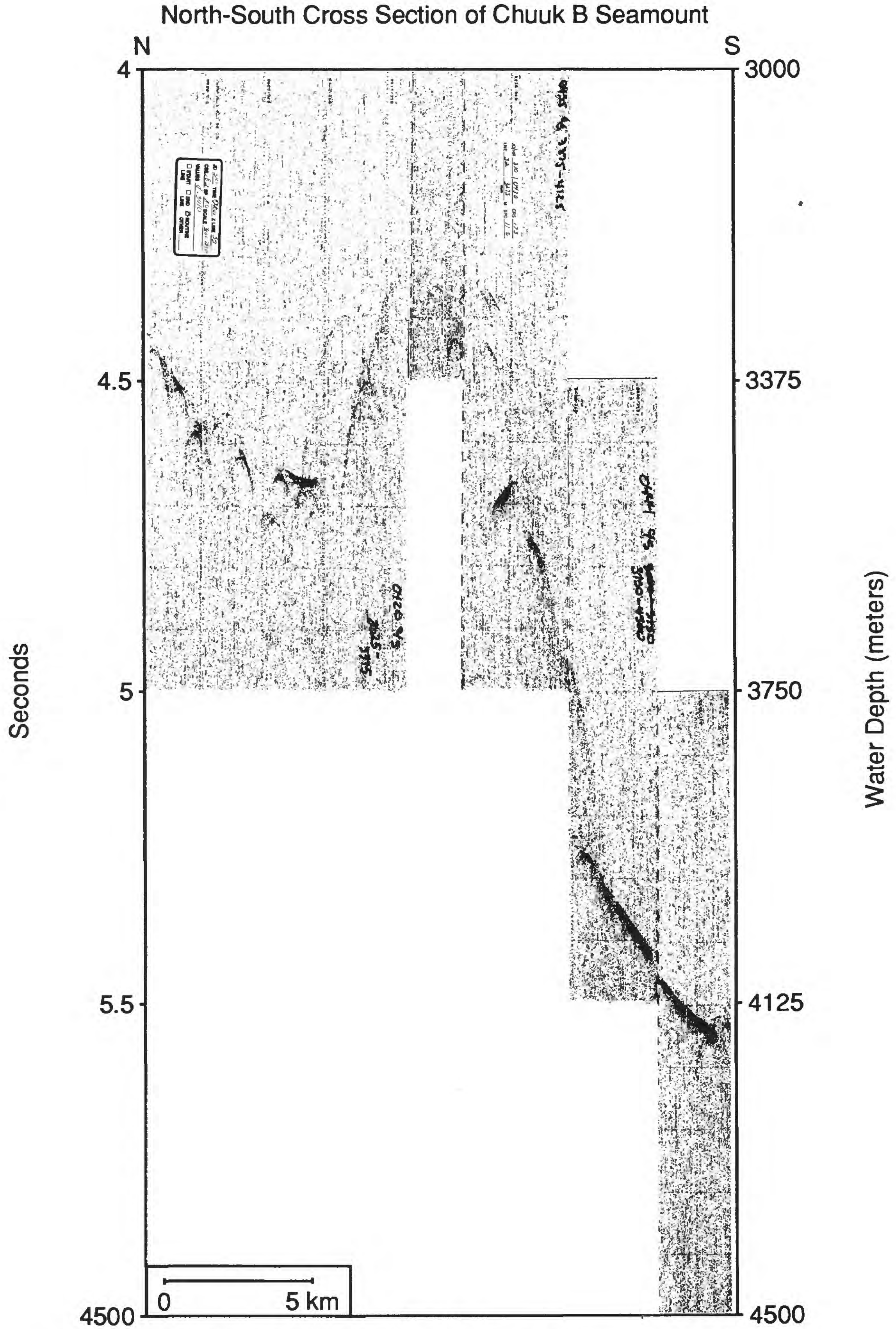

Figure 78. North-south cross section of Chuuk B Seamount, 3.5 kHz Line 32 (See Fig. 21 for location).

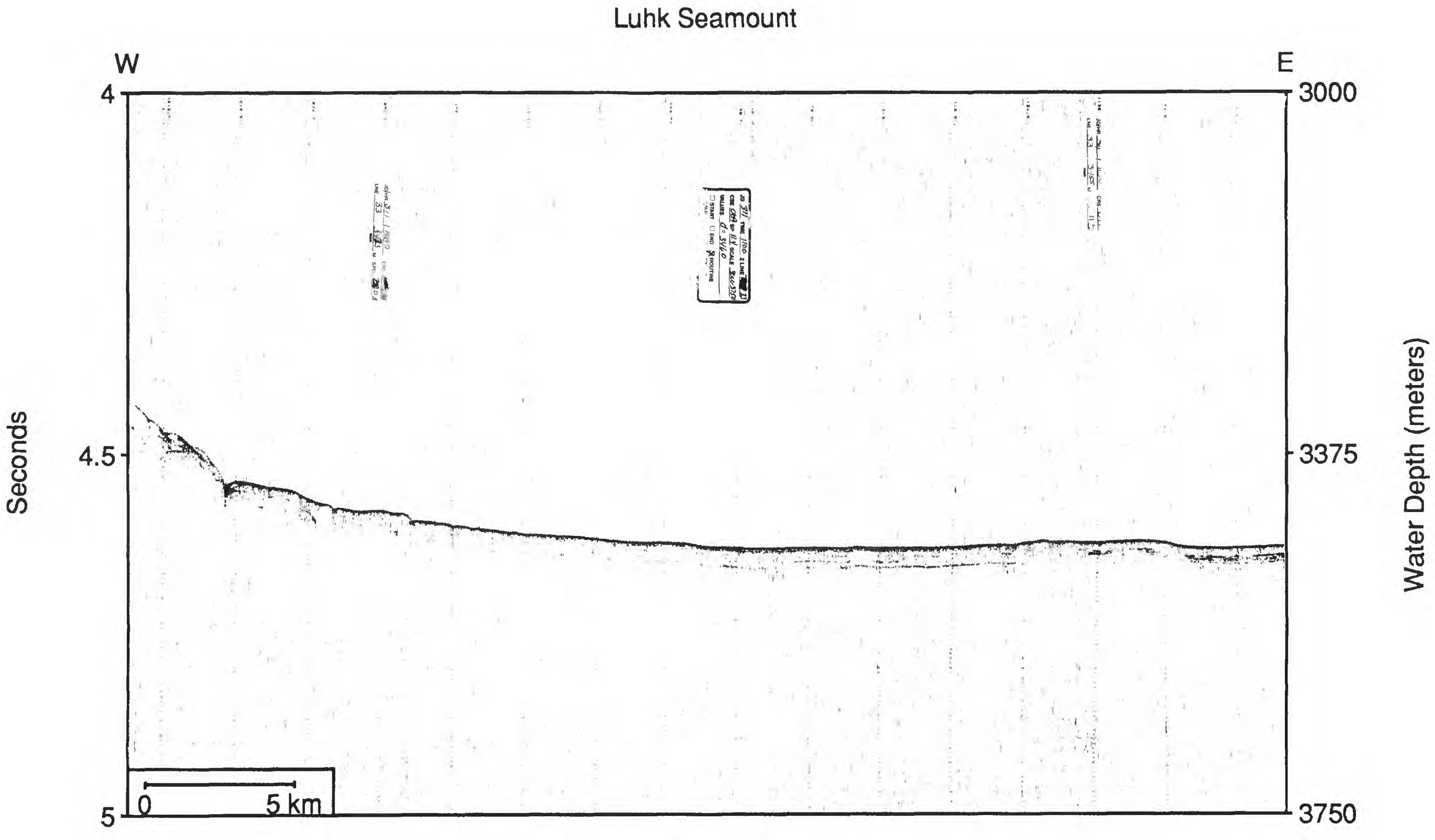

Figure 79. Abyssal plain and lower east flank(?) of Luhk Seamount, 3.5 kHz Line 33 (See Fig. 22 for location).

Olapahd Seamount

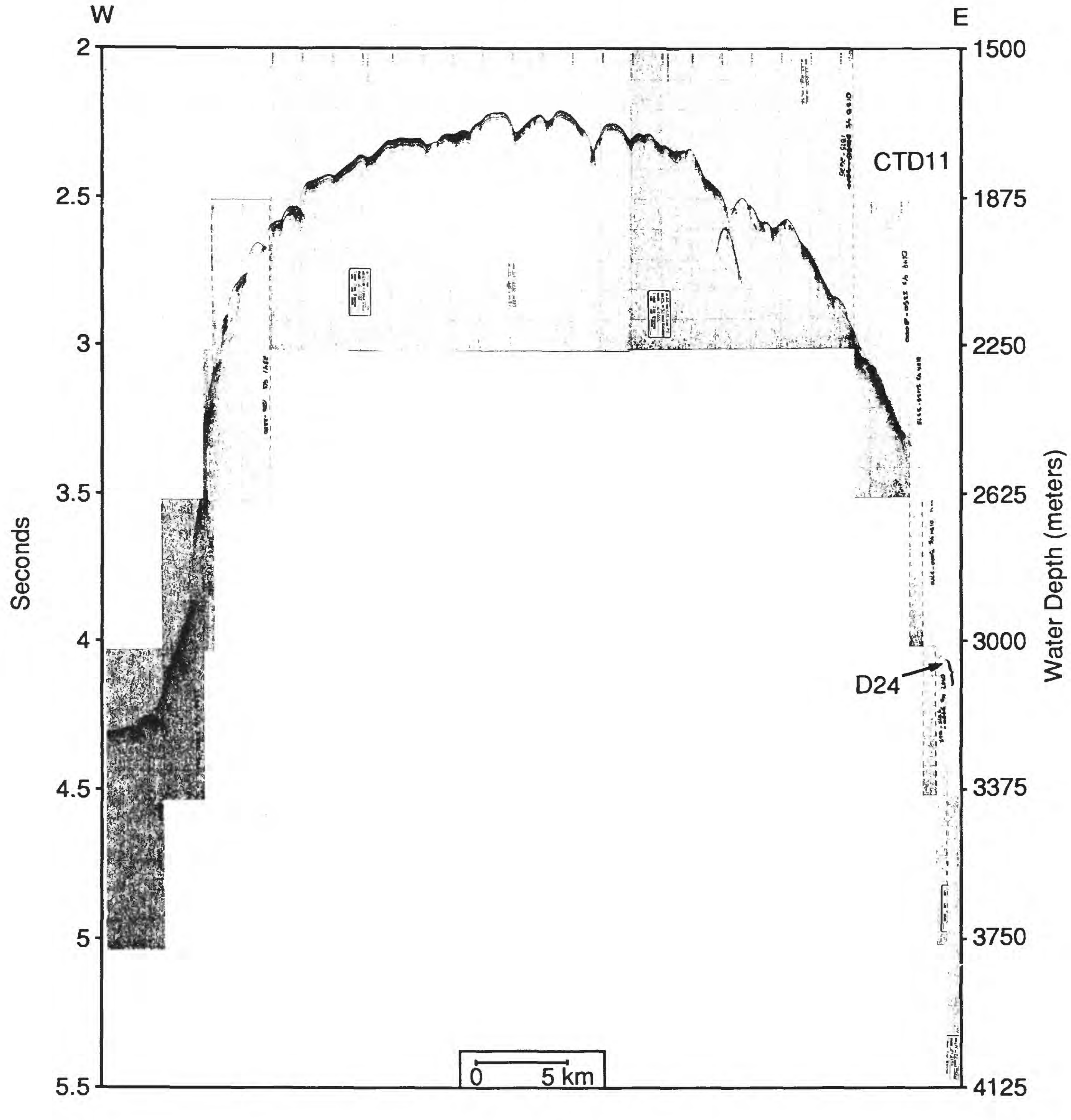

Figure 80. Olapahd Seamount, 3.5 kHz Line 34. Note location of Dredge 24 and CTD 11 (See Fig. 23 for location).

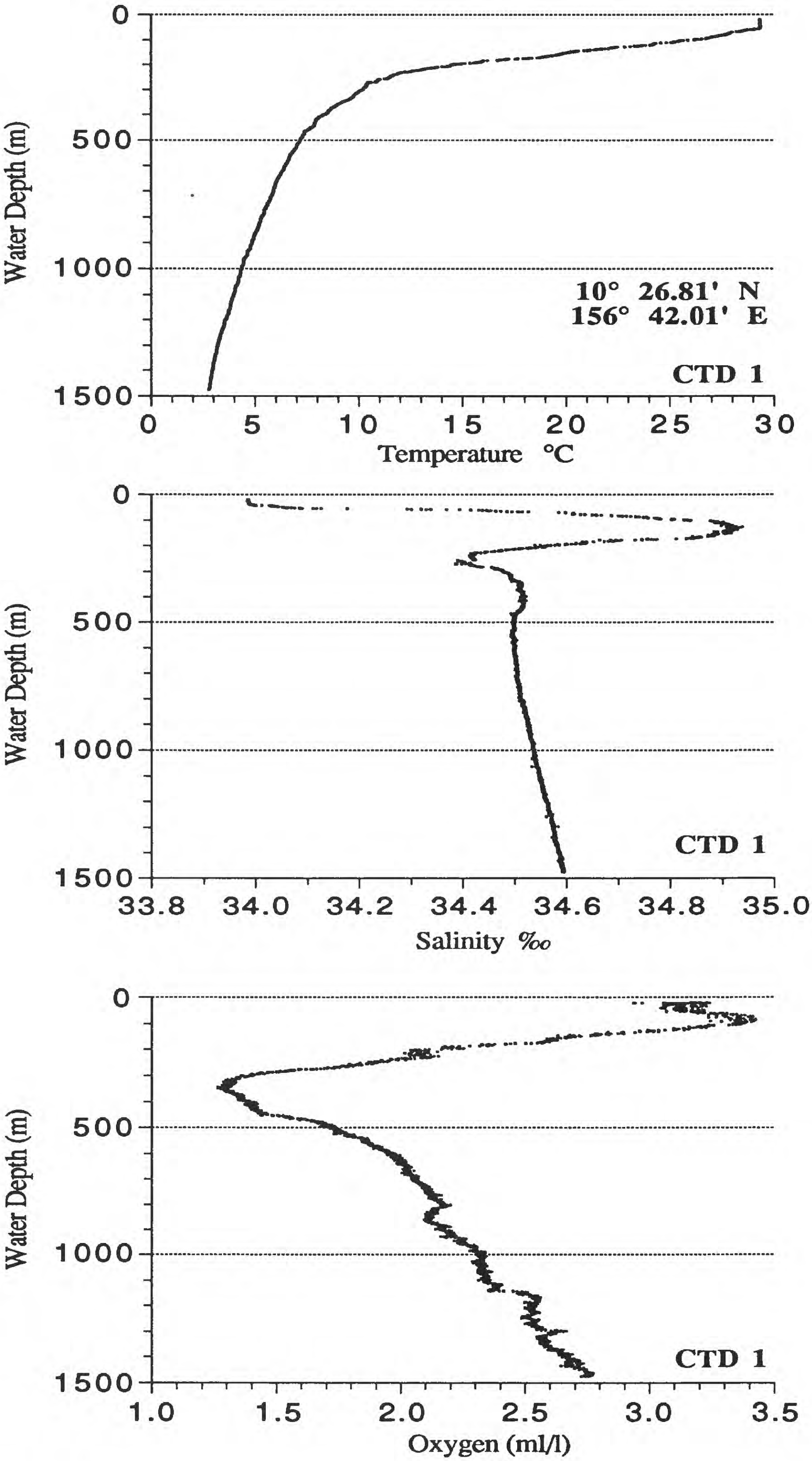

Figure 81. Temperature, salinity, and oxygen content versus water depth for CTD 1, Pali Seamount; water depth at station is 2147 meters. We believe that oxygen values above the oxygen minimum zone are higher than those presented here, due to problems with the oxygen sensor temperature probe.

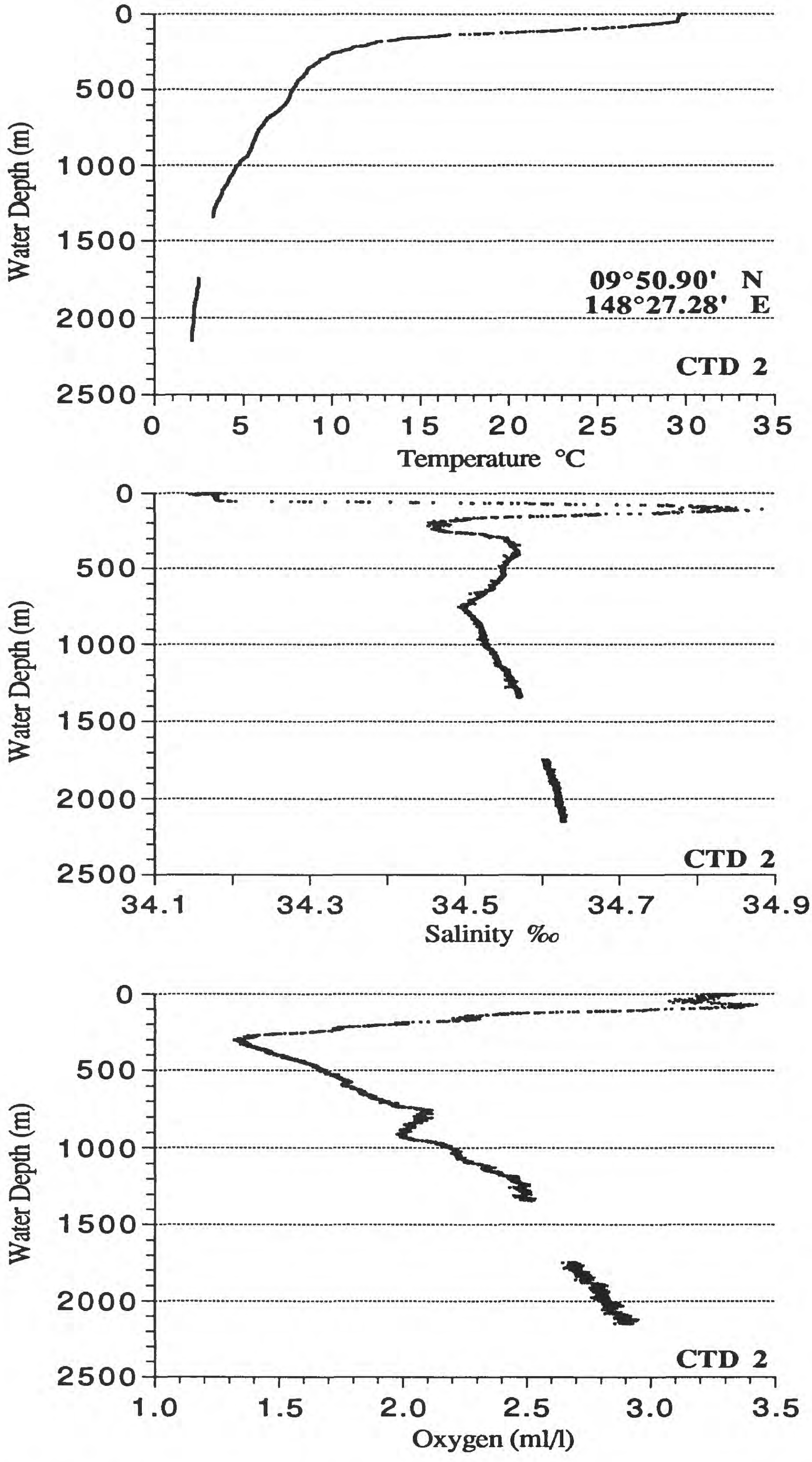

Figure 82. Temperature, salinity, and oxygen content versus water depth for CTD 2, Namonuito Guyot; water depth at station is 2230 meters. We believe that oxygen values above the oxygen minimum zone are higher than those presented here, due to problems with the oxygen sensor temperature probe.

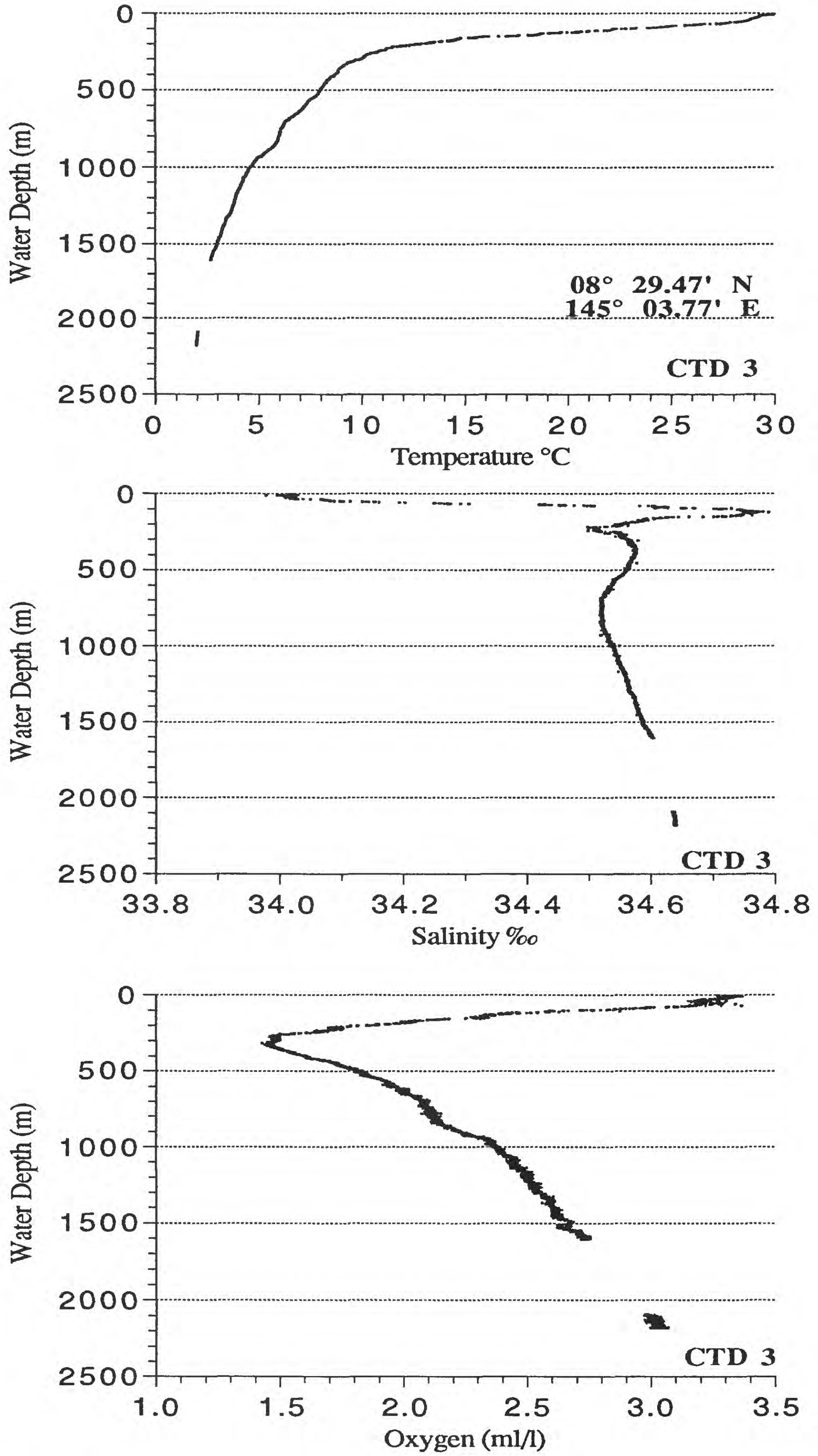

Figure 83. Temperature, salinity, and oxygen content versus water depth for CTD 3, Tarang Bank; water depth at station is 2590 meters. We believe that oxygen values above the oxygen minimum zone are higher than those presented here, due to problems with the oxygen sensor temperature probe.

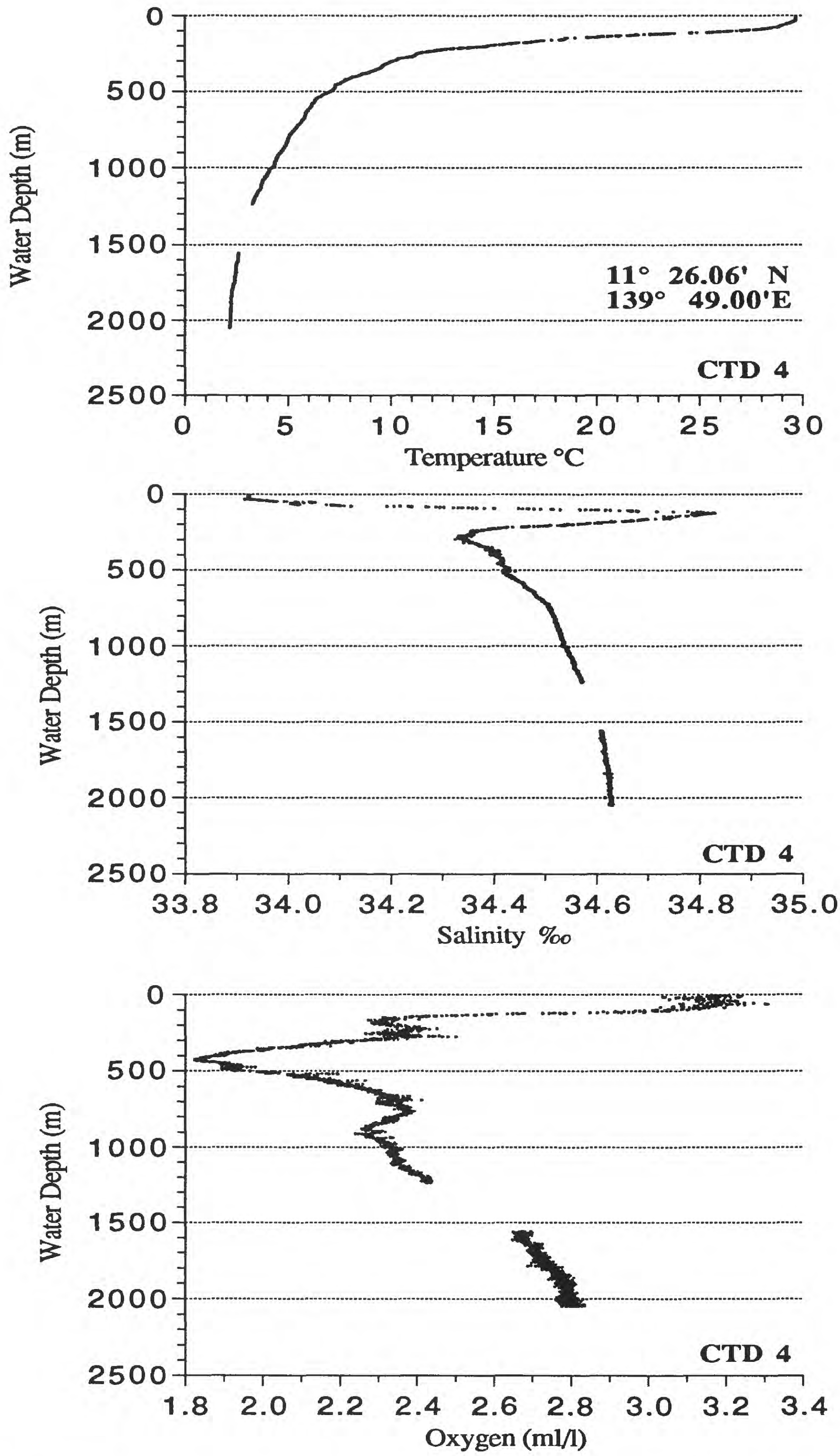

Figure 84. Temperature, salinity, and oxygen content versus water depth for CTD 4, Mariana-Yap arcs juncture; water depth at station is 2200 meters. We believe that oxygen values above the oxygen minimum zone are higher than those presented here, due to problems with the oxygen sensor temperature probe.

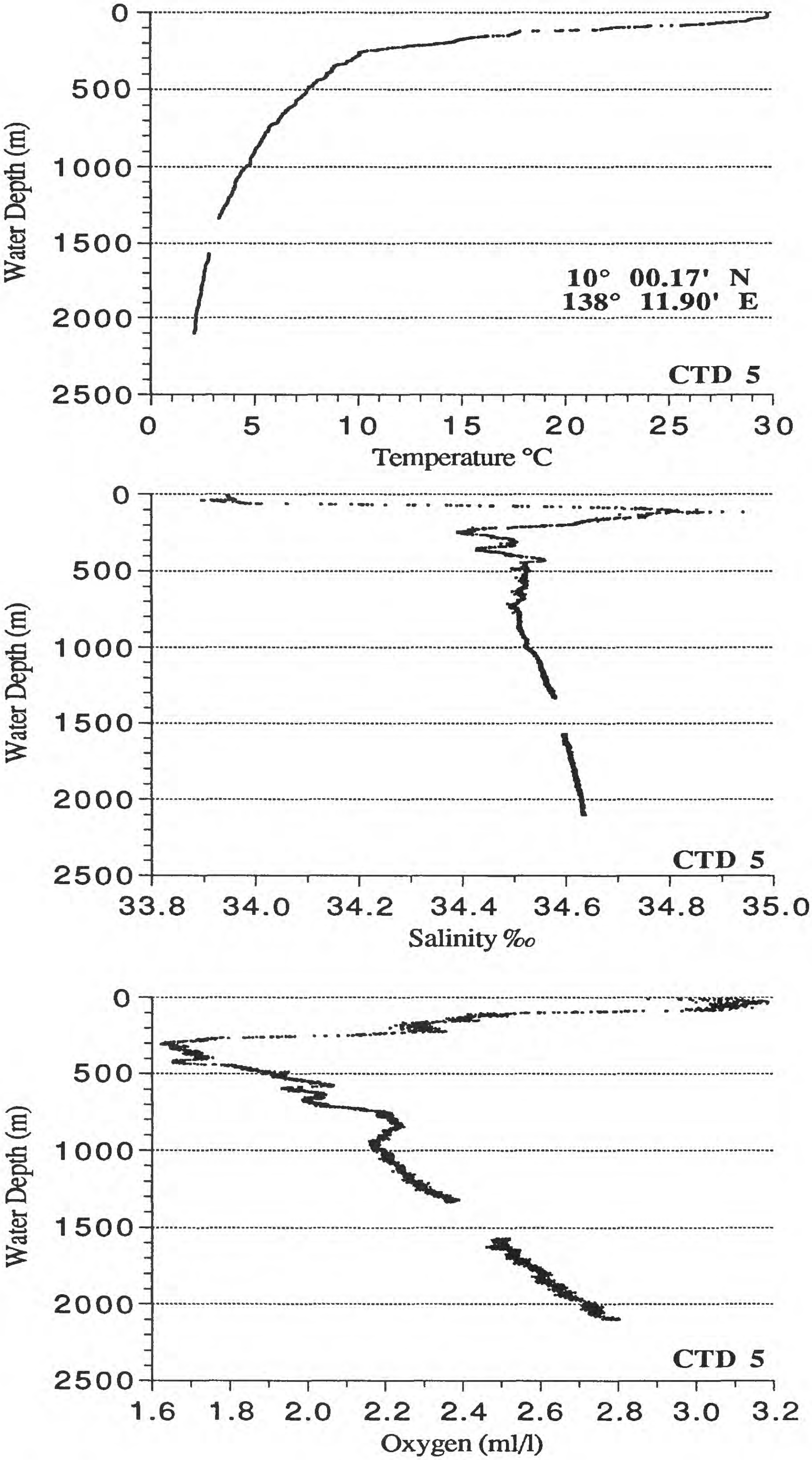

Figure 85. Temperature, salinity, and oxygen content versus water depth for CTD 5, Hunter Bank, Yap arc; water depth at station is 2230 meters. We believe that oxygen values above the oxygen minimum zone are higher than those presented here, due to problems with the oxygen sensor temperature probe.

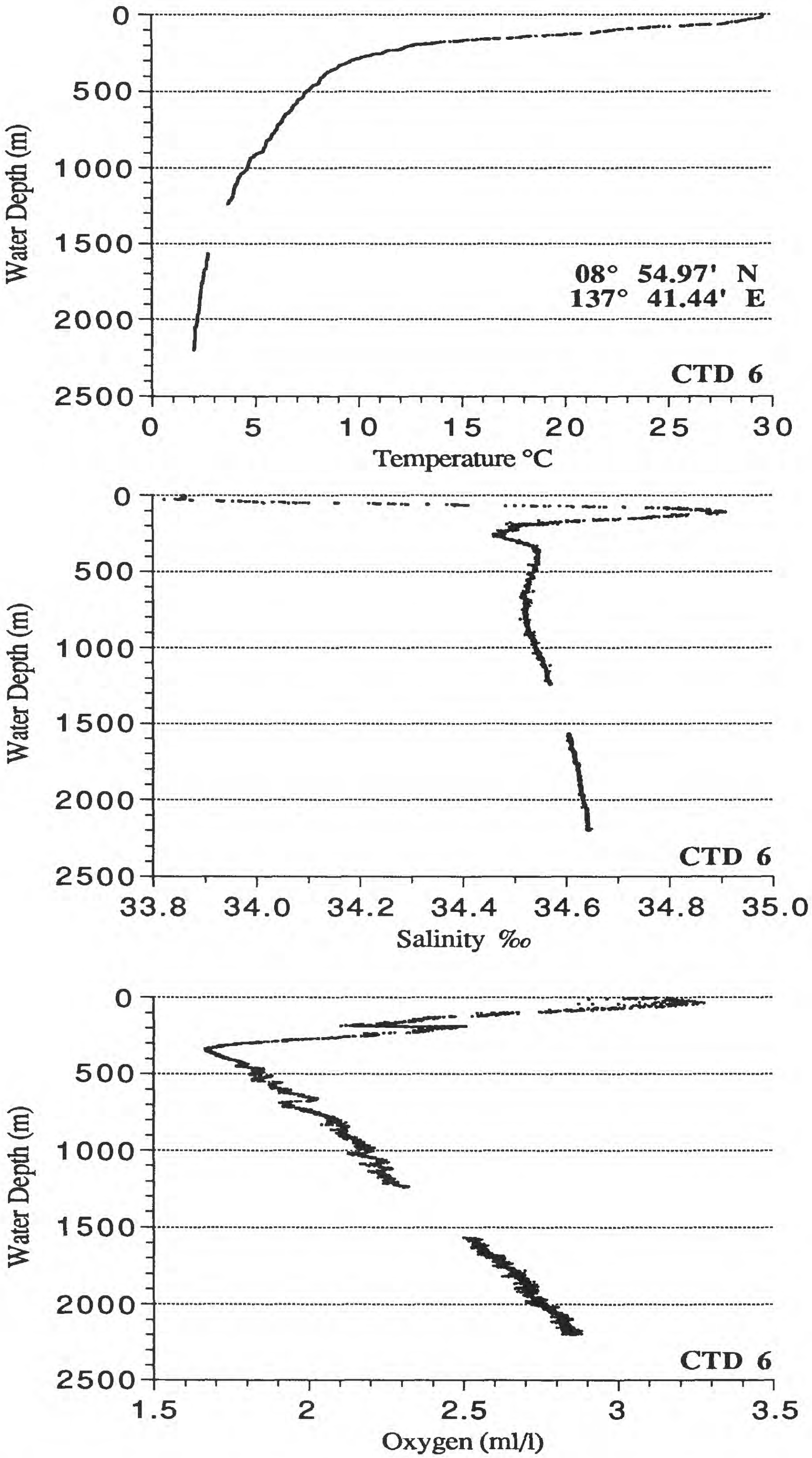

Figure 86. Temperature, salinity, and oxygen content versus water depth for CTD 6, north Ngulu Ridge, Yap arc; water depth at station is 2285 meters. We believe that oxygen values above the oxygen minimum zone are higher than those presented here, due to problems with the oxygen sensor temperature probe.

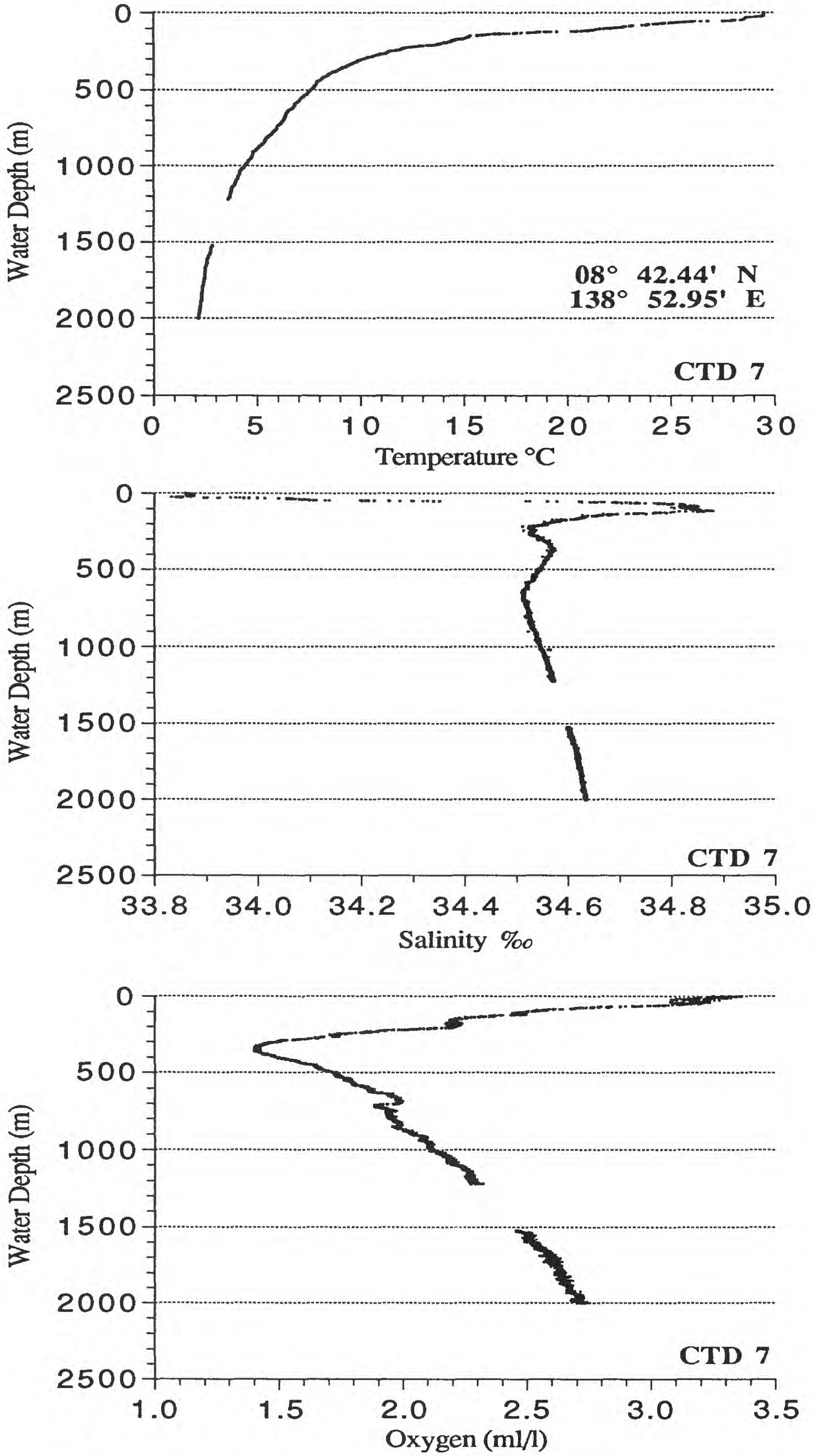

Figure 87. Temperature, salinity, and oxygen content versus water depth for CTD 7, Sorol Guyot; water depth at station is 2205 meters. We believe that oxygen values above the oxygen minimum zone are higher than those presented here, due to problems with the oxygen sensor temperature probe.

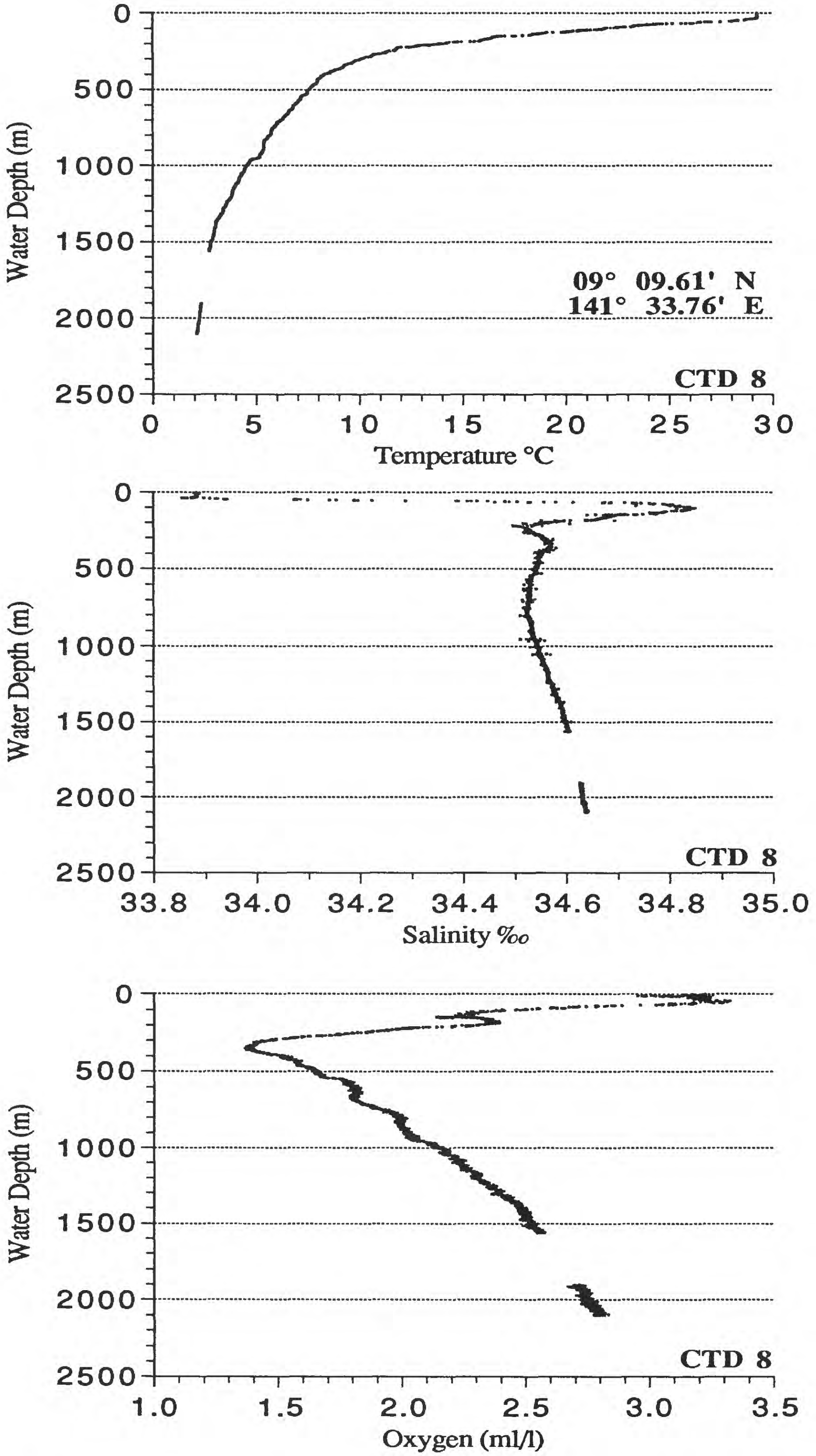

Figure 88. Temperature, salinity, and oxygen content versus water depth for CTD 8, Fais Trough on west Caroline Ridge; water depth at station is 2277 meters. We believe that oxygen values above the oxygen minimum zone are higher than those presented here, due to problems with the oxygen sensor temperature probe.

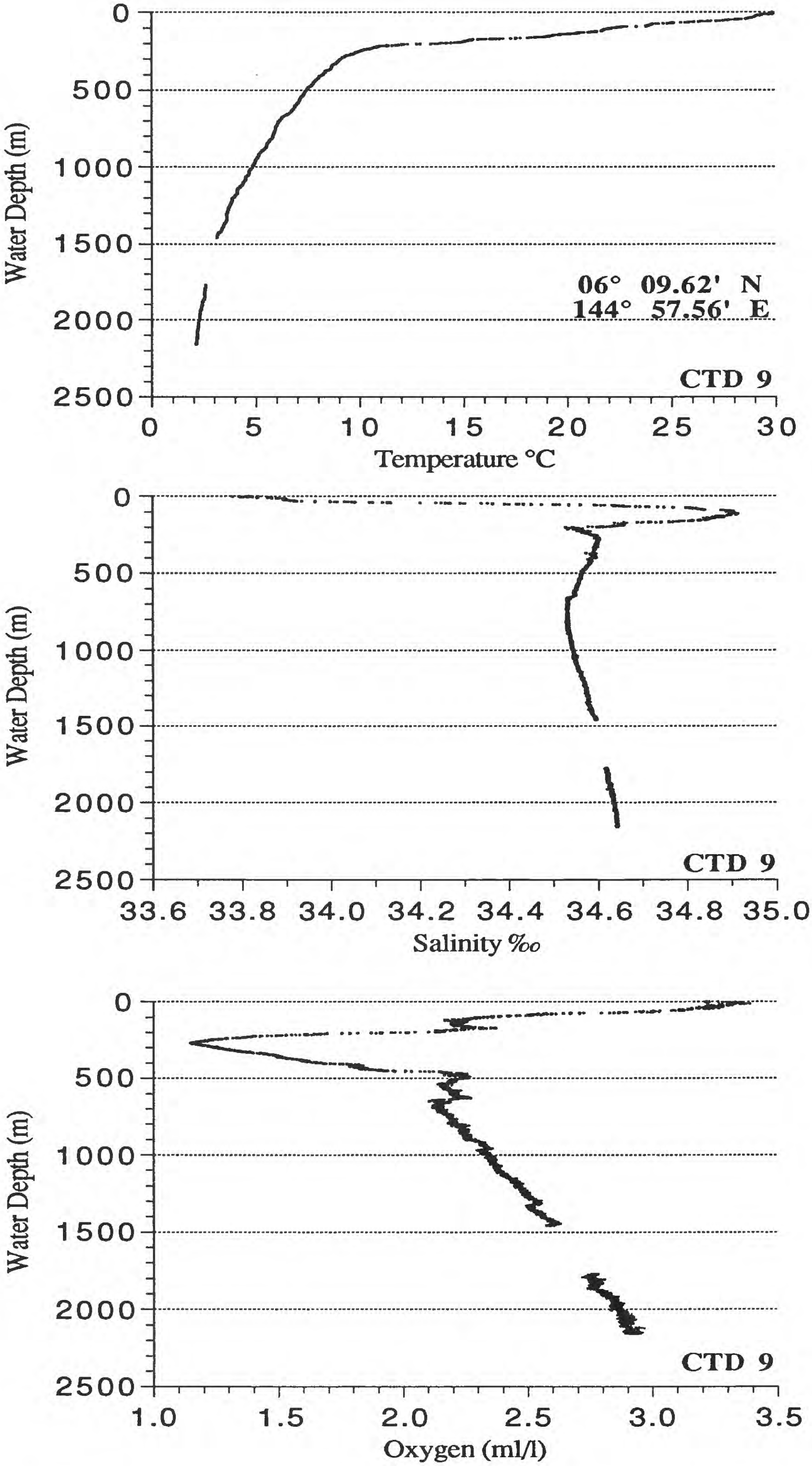

Figure 89. Temperature, salinity, and oxygen content versus water depth for CTD 9, west Lanthe Bank; water depth at station is 2930 meters. We believe that oxygen values above the oxygen minimum zone are higher than those presented here, due to problems with the oxygen sensor temperature probe.

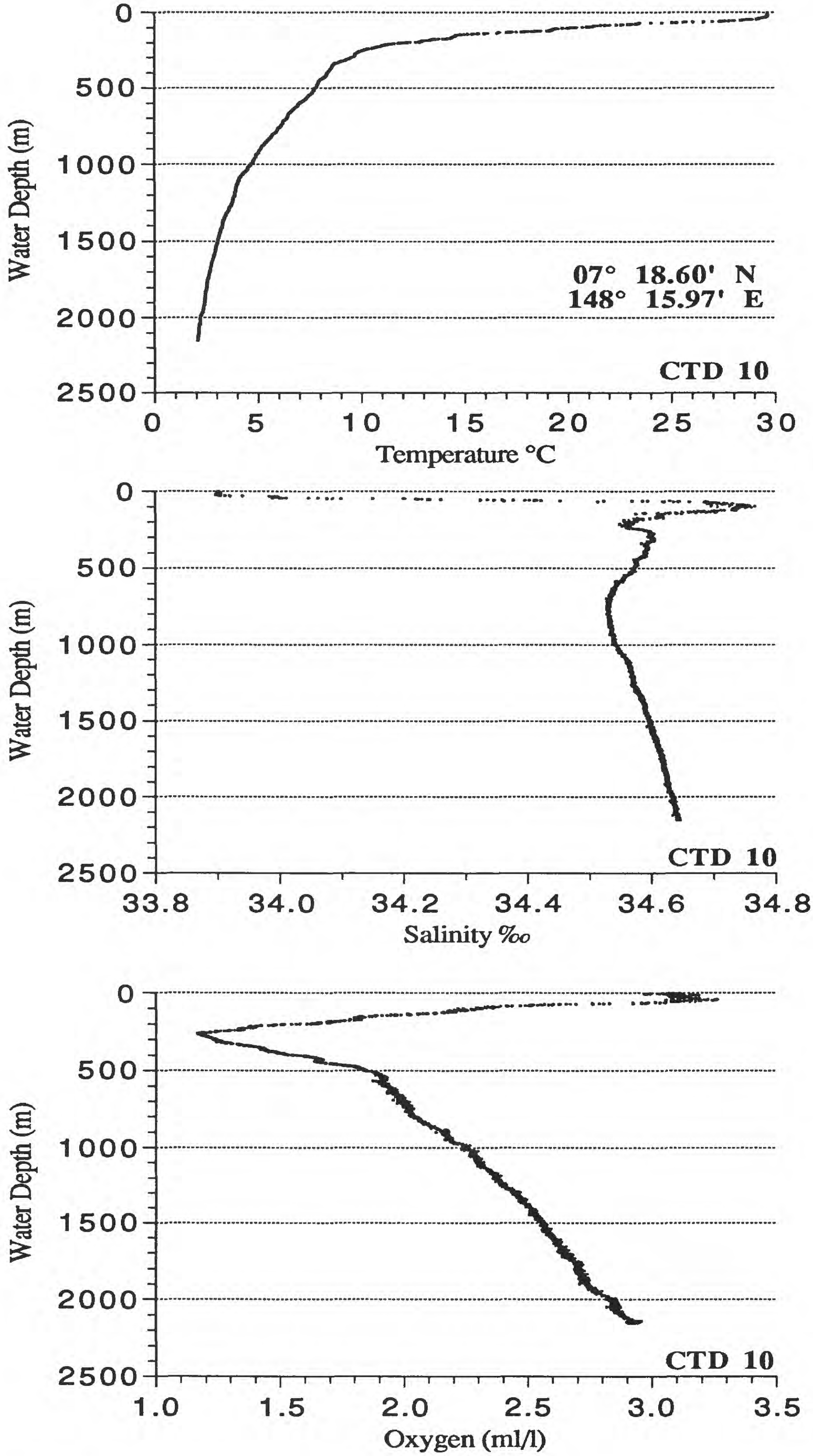

Figure 90. Temperature, salinity, and oxygen content versus water depth for CTD 10, Condor Bank; water depth at station is 2230 meters. We believe that oxygen values above the oxygen minimum zone are higher than those presented here, due to problems with the oxygen sensor temperature probe.

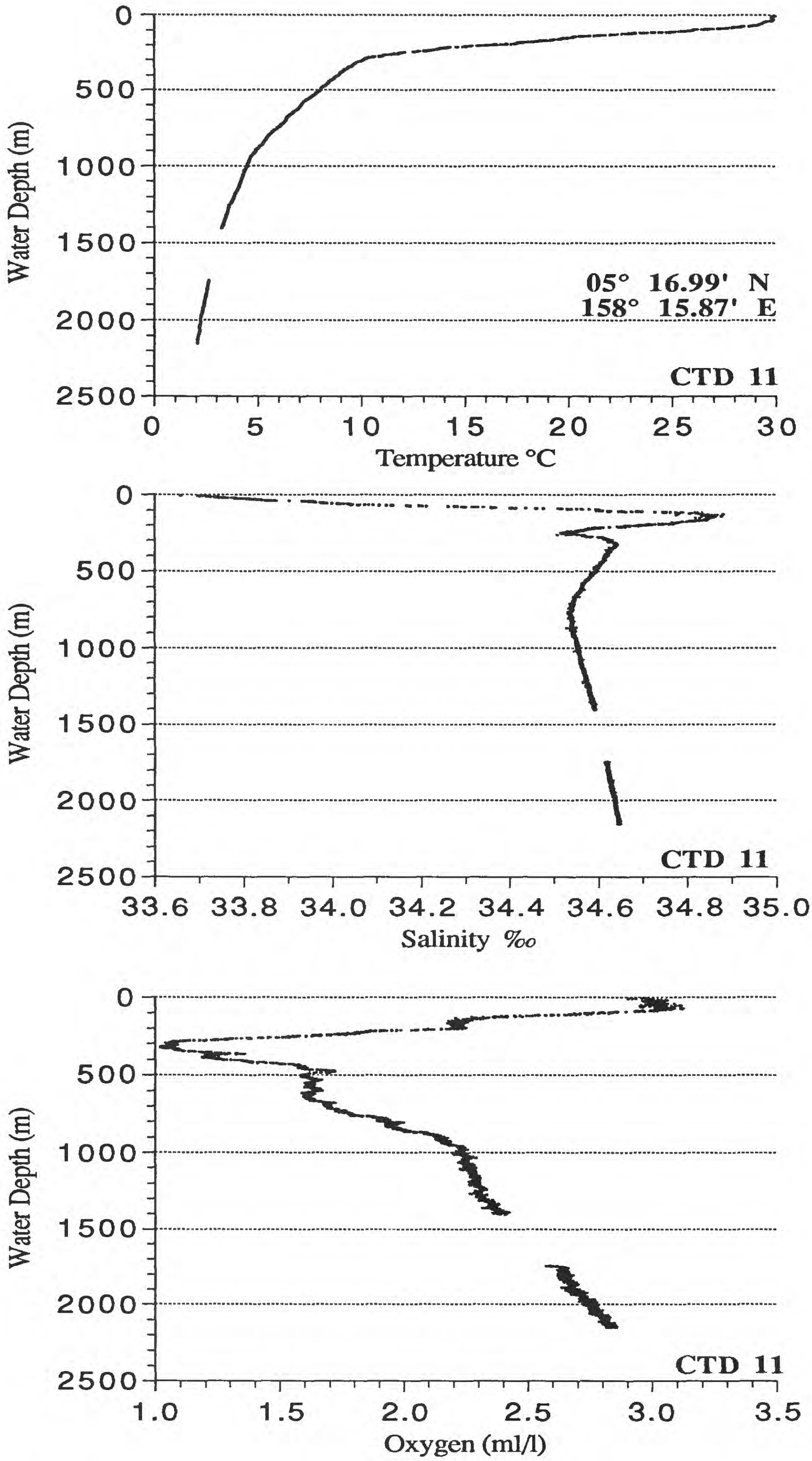

Figure 91. Temperature, salinity, and oxygen content versus water depth for CTD 11, Olapahd Seamount; water depth at station is 2360 meters. We believe that oxygen values above the oxygen minimum zone are higher than those presented here, due to problems with the oxygen sensor temperature probe.

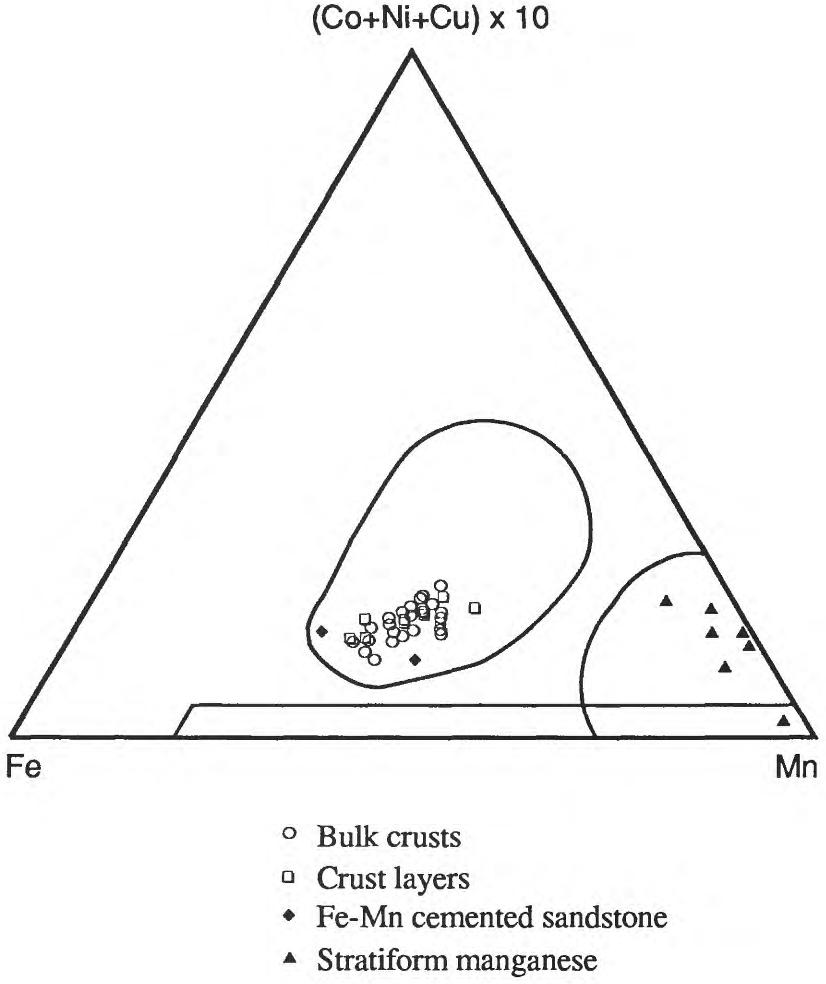

Figure 92. Ternary diagram after Bonatti et al., (1972) for 24 bulk crusts, 11 crust layers, 7 submetallic stratiform Mn layers and 2 Fe-Mn cemented sandstone samples. The central field is for 308 bulk hydrogenetic crusts from the central Pacific (Hein et al., 1991), the linear field along the base is for hydrothermal deposits, and the field around the Mn apex is a hydrothermal and diagenetic field (after Bonatti et al., 1972).

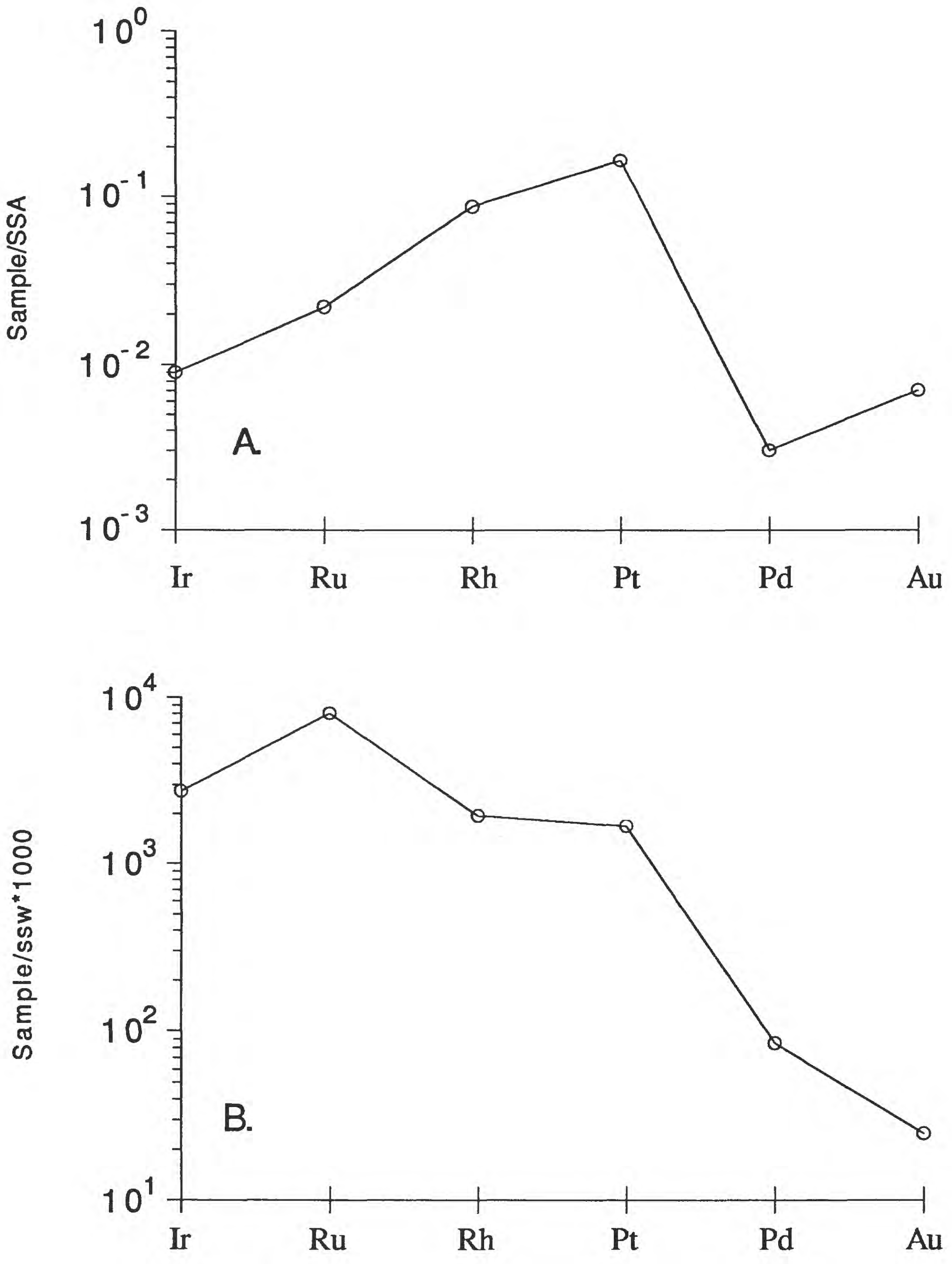

Figure 93. **A.** Mean PGE and Au concentrations in bulk crusts normalized to their solar system abundances (same as C1 chondrite concentrations) taken from Anders and Ebihara (1982). **B.** Mean PGE and Au concentrations in bulk crusts normalized to their surface seawater abundances taken from Goldberg (1987), except Rh which is set to 6 pg/l (see Hein, Kang, et al., 1990). Au is <10 ppb for all crust analyzed and is arbitrarily set at 1.0 ppb in both plots.

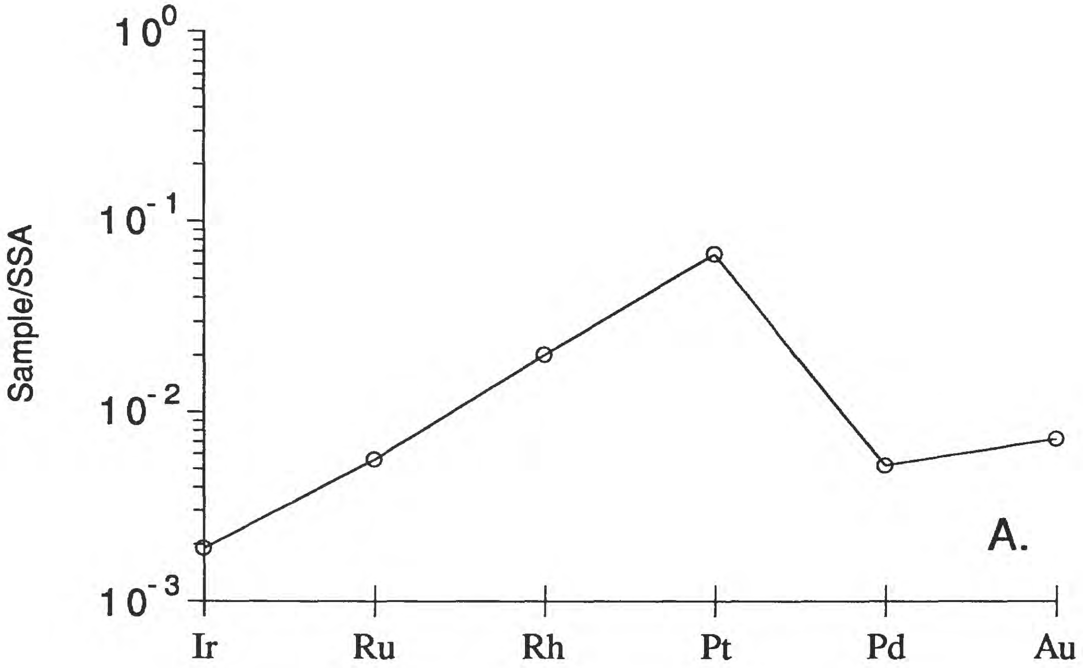

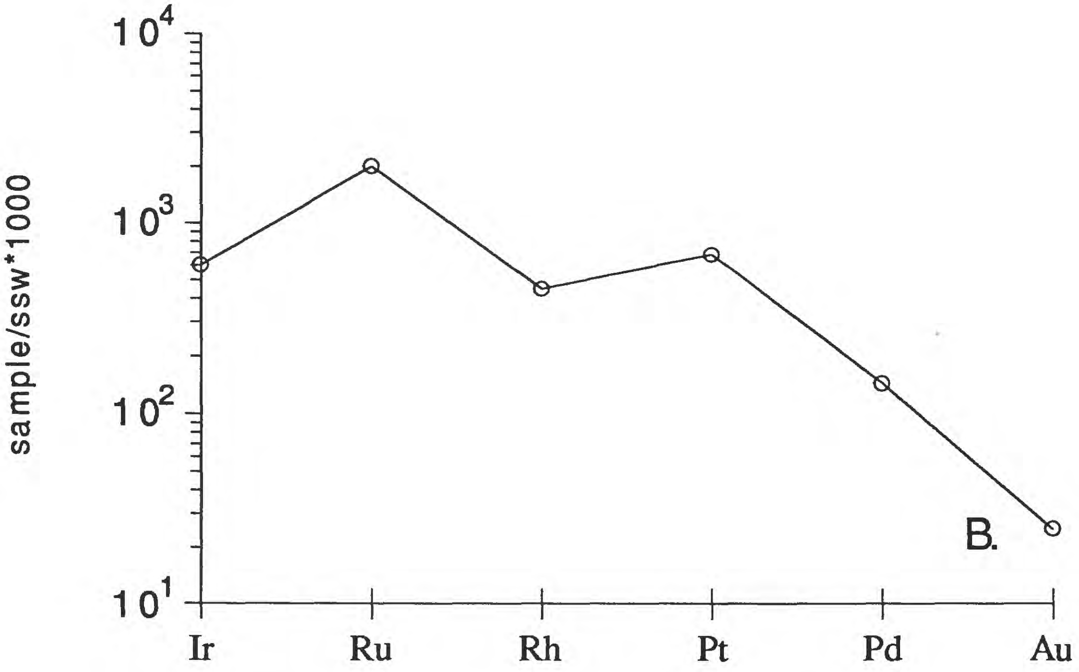

Figure 94. **A.** Mean PGE and Au concentrations in submetallic stratiform manganese normalized to their solar system abundances (same as C1 chondrite concentrations) taken from Anders and Ebihara (1982). **B.** Mean PGE and Au concentrations in submetallic stratiform manganese normalized to their surface seawater abundances taken from Goldberg (1987), except Rh which is set to 6 pg/l (see Hein, Kang, et al., 1990). Au is <10 ppb for all samples analyzed and is arbitrarily set at 1.0 ppb in both plots.

Figure 95. Chondrite-normalized REE plot. Shaded fields represent complete data set of 16 crust samples and 5 hydrothermal samples (see Table 13). Chondrite compositon for Figures 95-100 from Haskin et al. (1968).

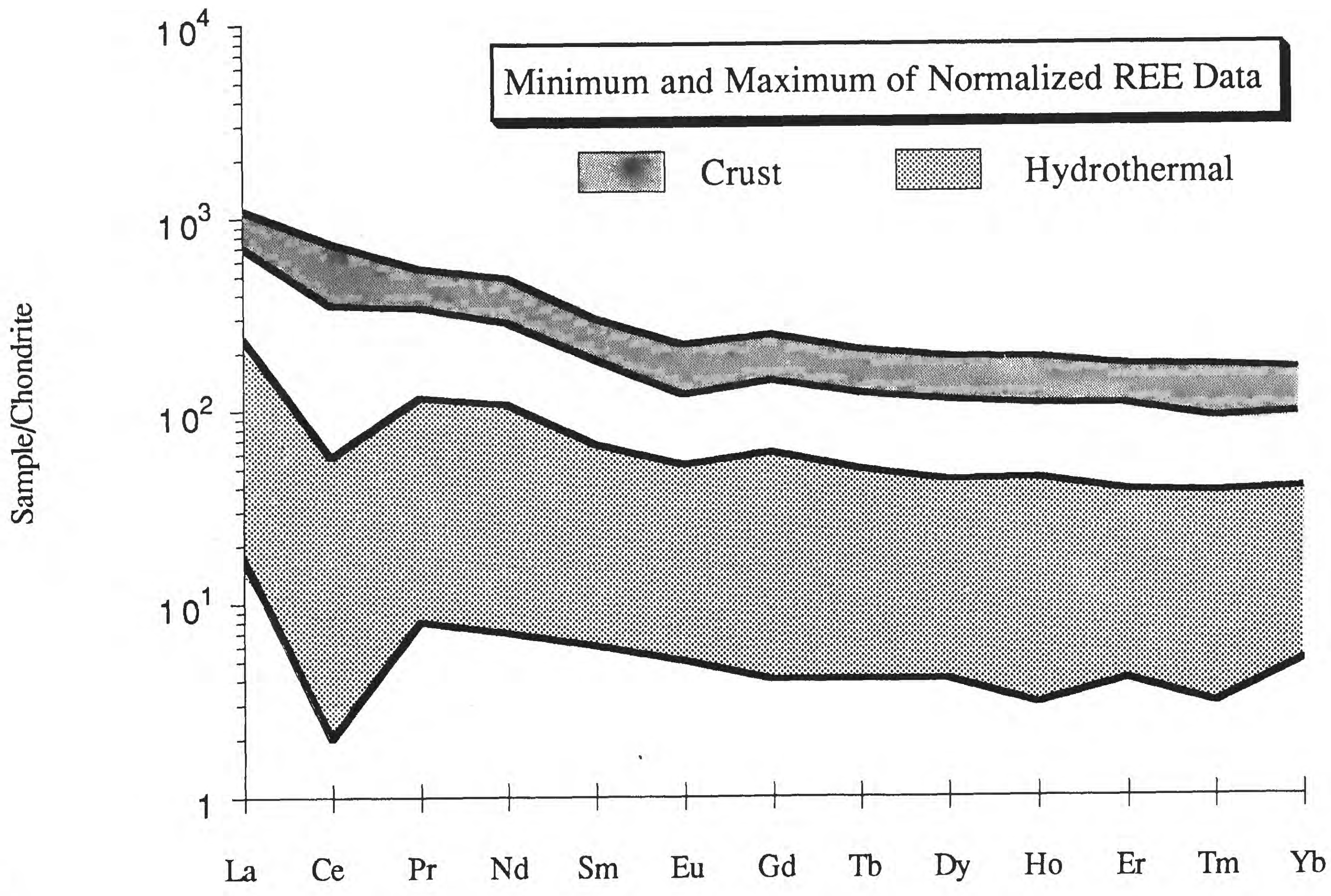

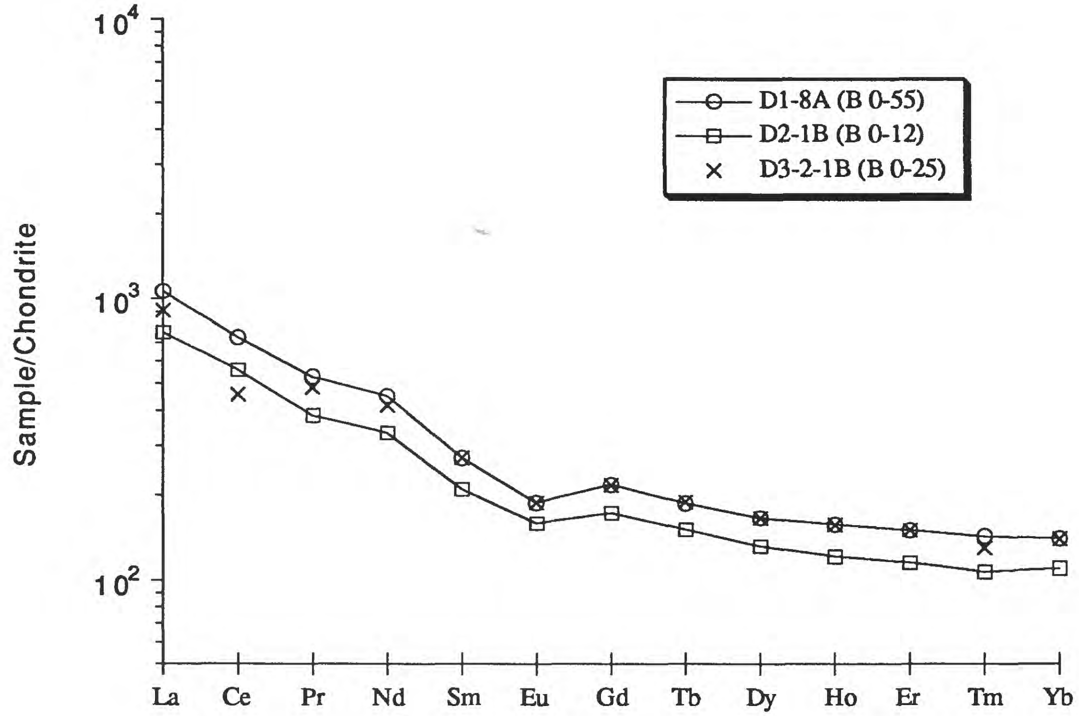

Figure 96. Chondrite-normalized REE plot of crusts from Dredges D1, D2, and D3. B = bulk, followed by sample interval in millimeters.

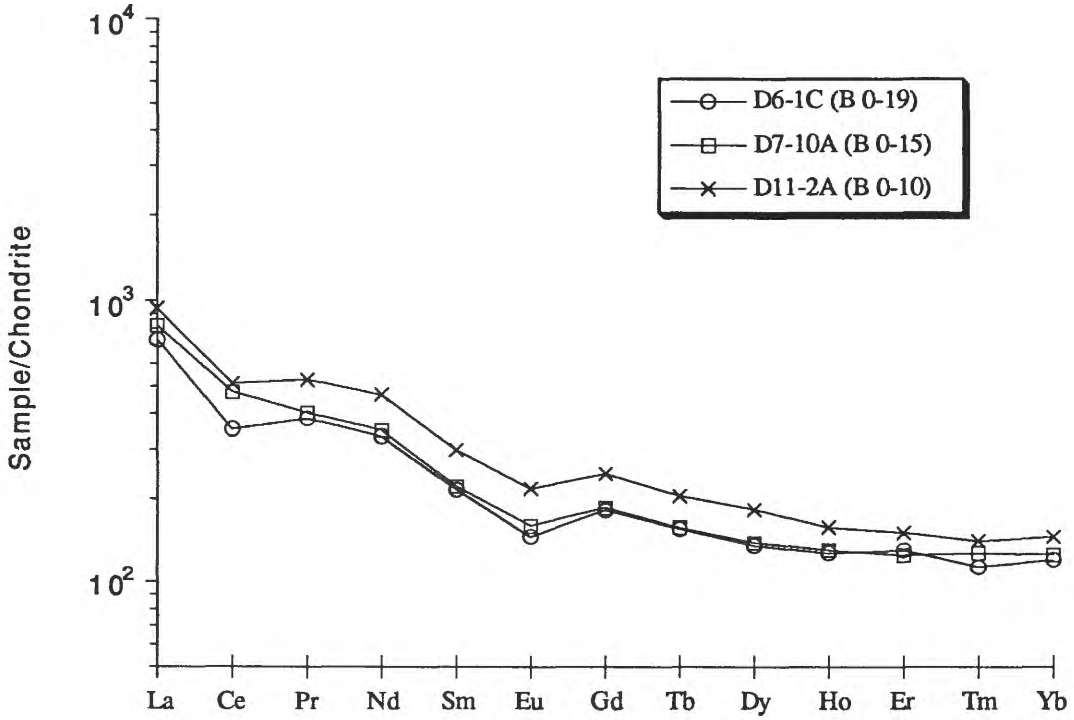

Figure 97. Chondrite-normalized REE plot of crusts from Dredges D6, D7, and D11. B = bulk, followed by sample interval in millimeters.

Figure 98. Chondrite-normalized REE plot of a layered crust from Dredge D1. L = layer, followed by sample interval in millimeters.

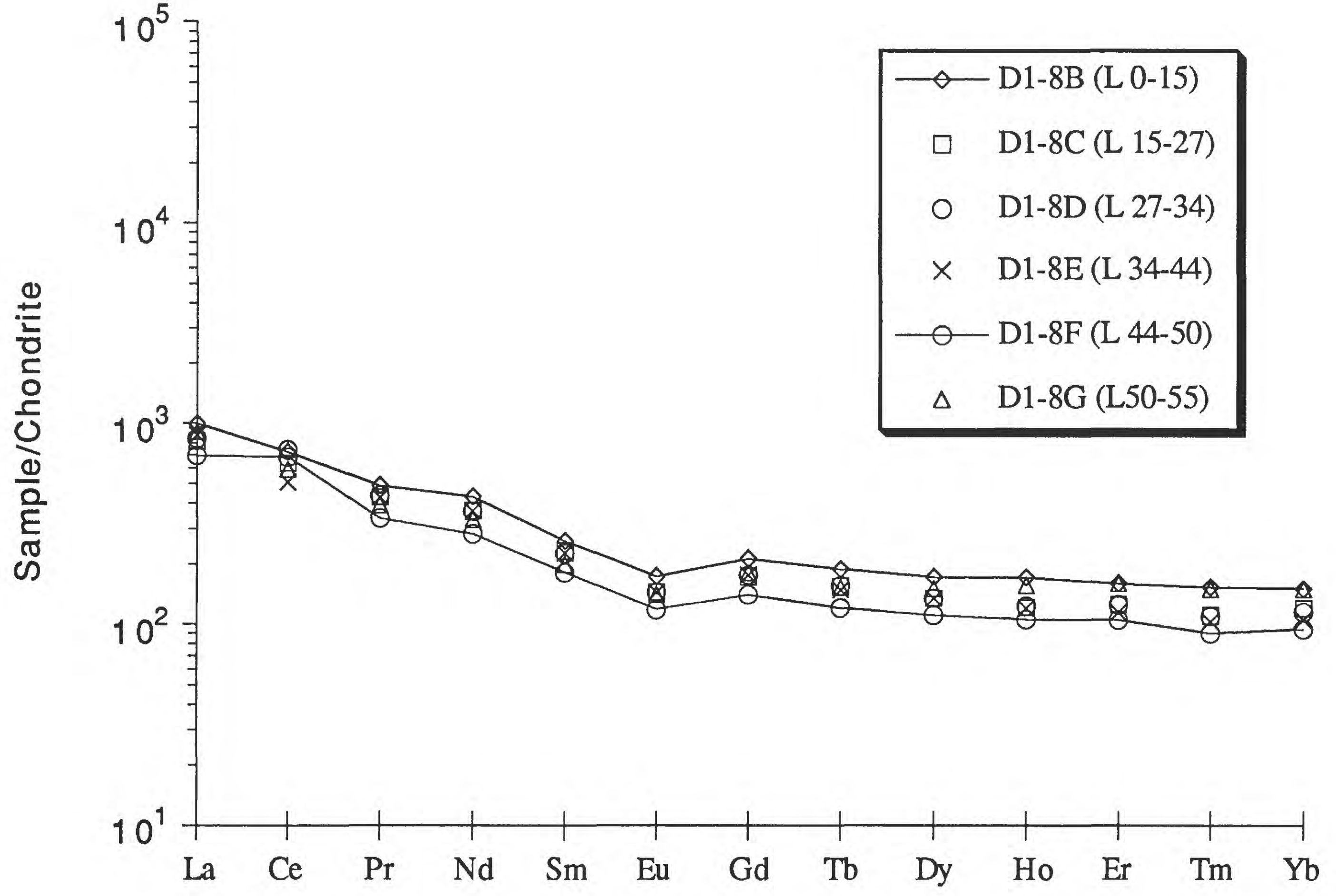

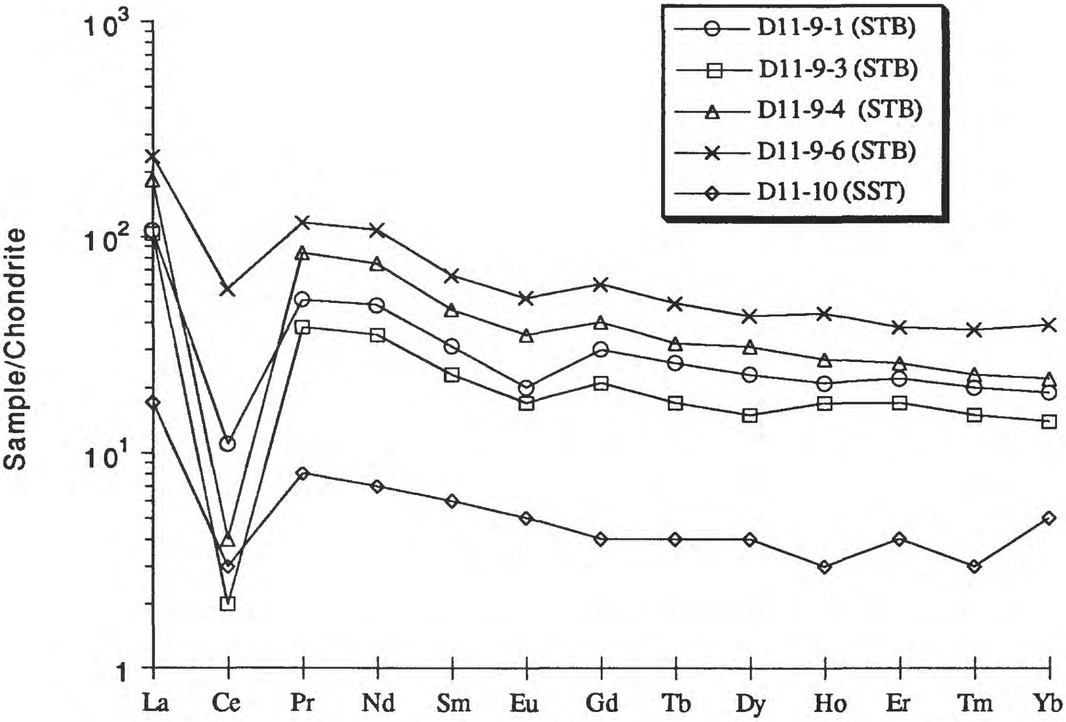

Figure 99. Chondrite-normalized REE plot of hydrothermal Mn deposits from Dredge D11. STB = submetallic stratiform, SST = Fe-Mn cemented sandstone.

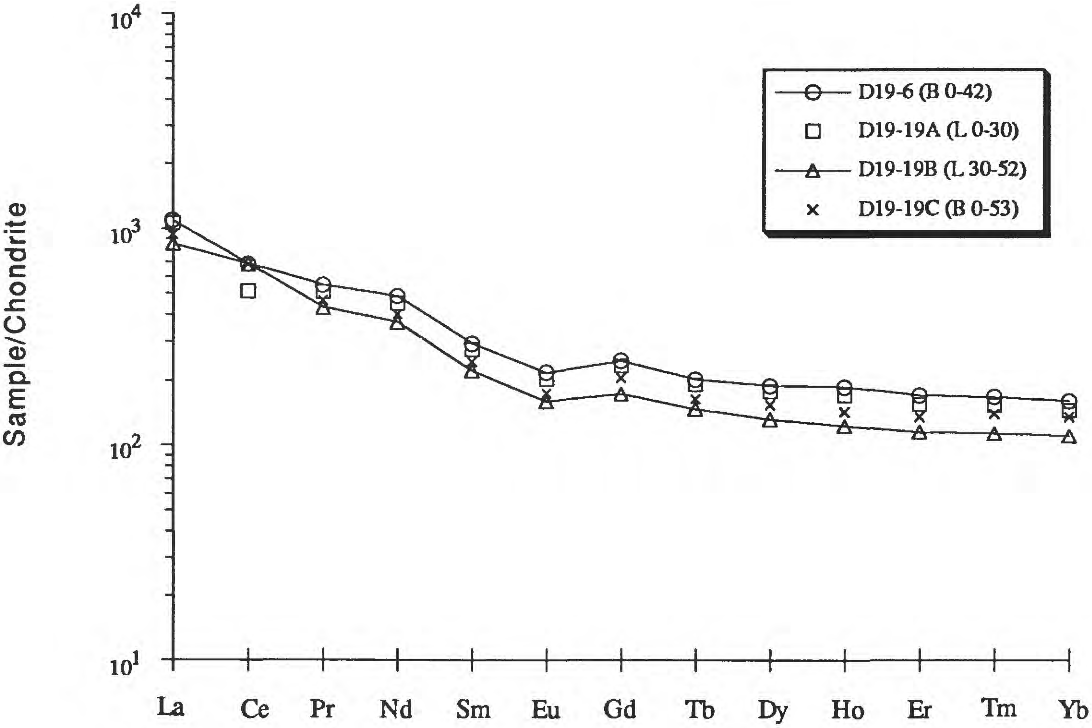

Figure 100. Chondrite-normalized REE plot of crusts from Dredge D19. B = bulk, L = layer, followed by sample interval in millimeters.

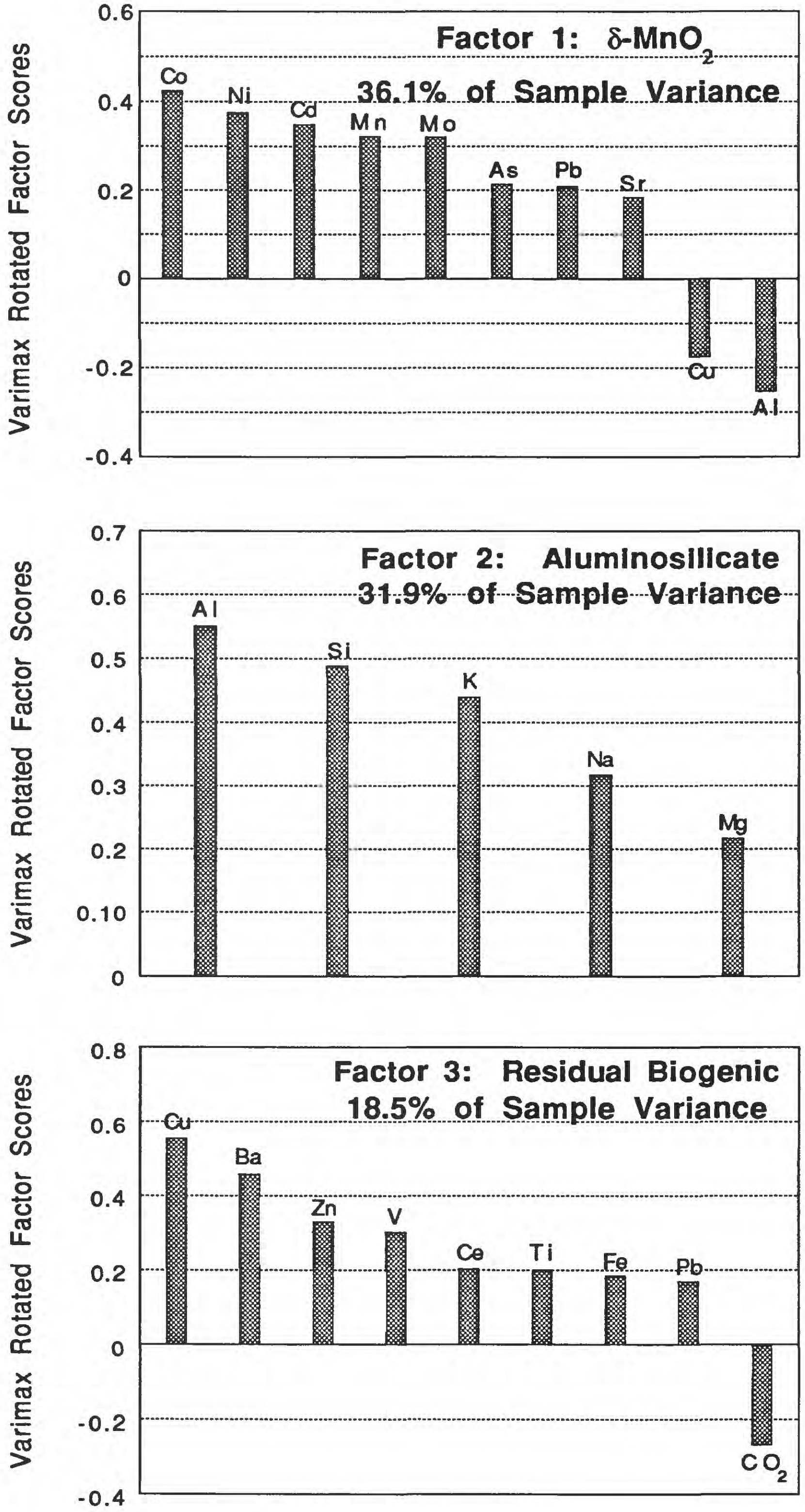

Figure 101. Three of five Q-mode factors for 24 bulk crusts (see Fig. 102 for other two). Factor scores between 0 and |0.160| are not included because random noise makes it difficult to resolve the orientation of the factor to within 10° of an absolute direction in variable space.

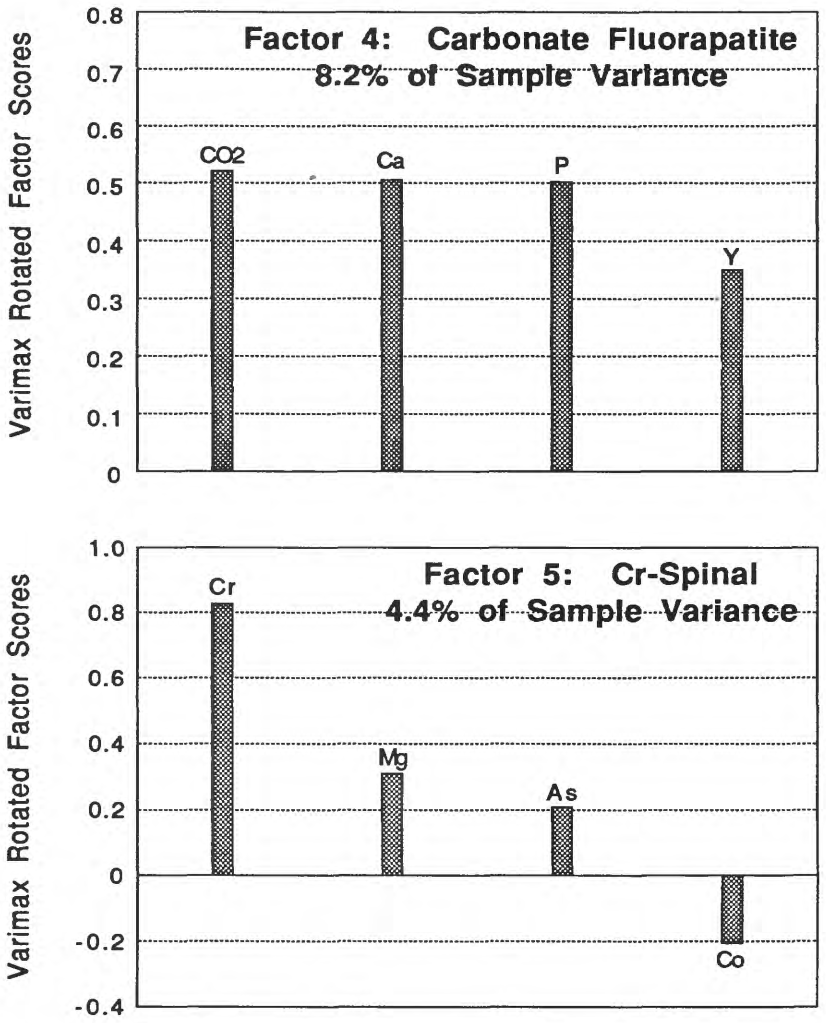

Figure 102. Two of five Q-mode factors for 24 bulk crusts (see Fig. 101 for other three). The five factors account for 99.1% of the data set.

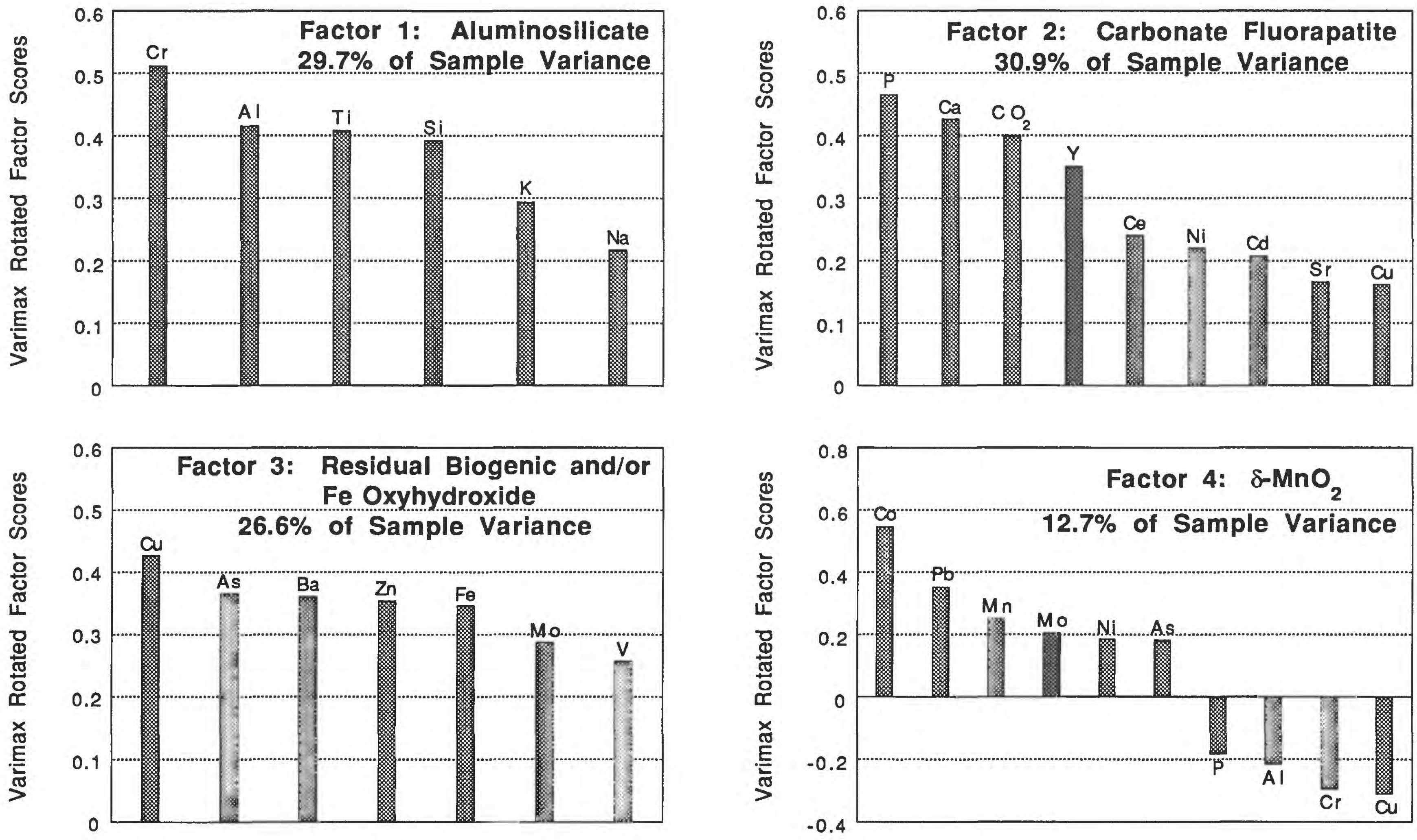

Figure 103. Q-mode factors for six layers from crust D1-8. Factor scores between 0 and |0.160| are not included because random noise makes it difficult to resolve the orientation of the factor to within 10° of an absolute direction in variable space. The four factors account for 99.7% of the data set.

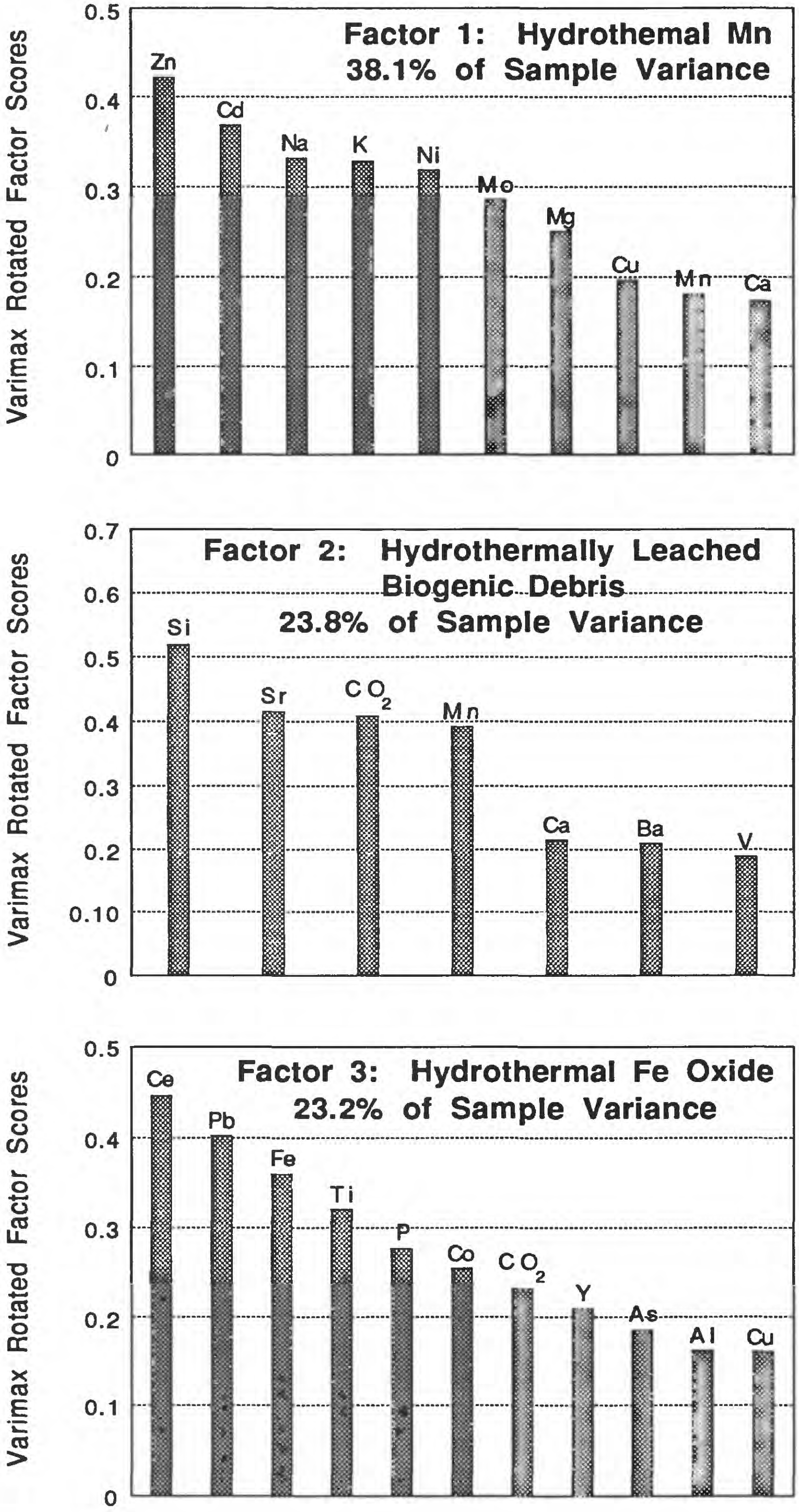

Figure 104. Three of five Q-mode factors for seven stratiform manganese layers (see Fig. 105 for other two). Factor scores between 0 and |0.160| are not included because random noise makes it difficult to resolve the orientation of the factor to within 10° of an absolute direction in variable space.

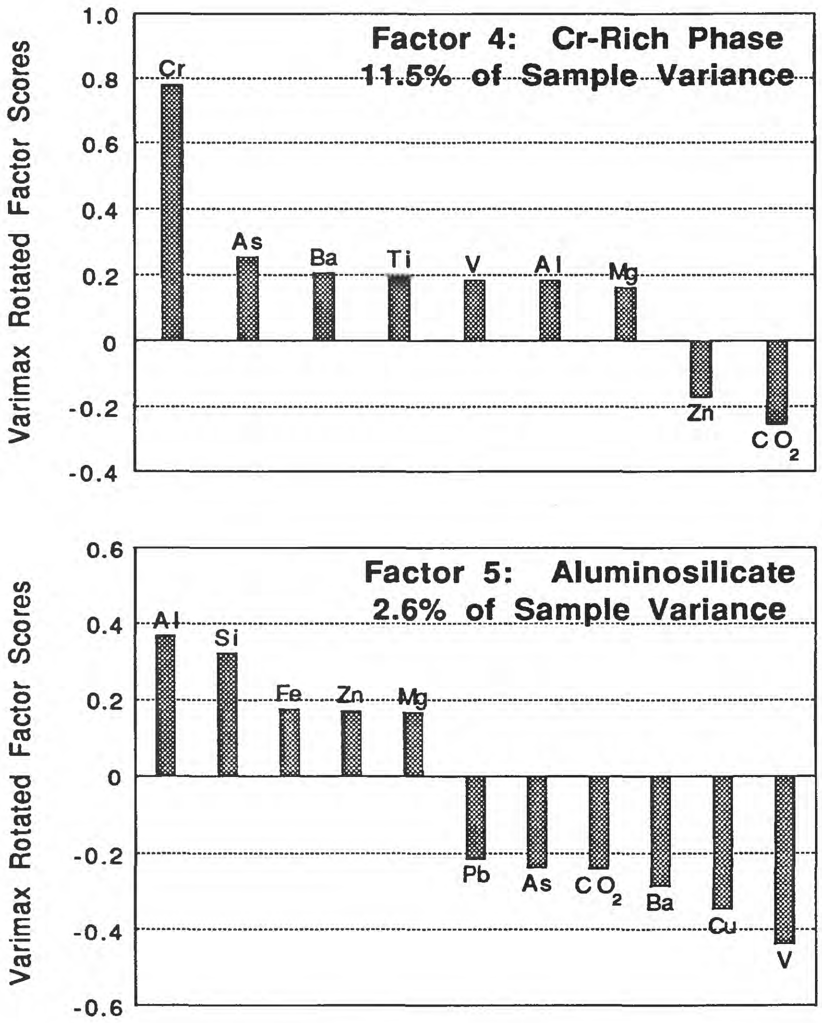

Figure 105. Two of five Q-mode factors for seven stratiform manganese layers (see Fig. 104 for other three). The five factors account for 99.2% of the data set.

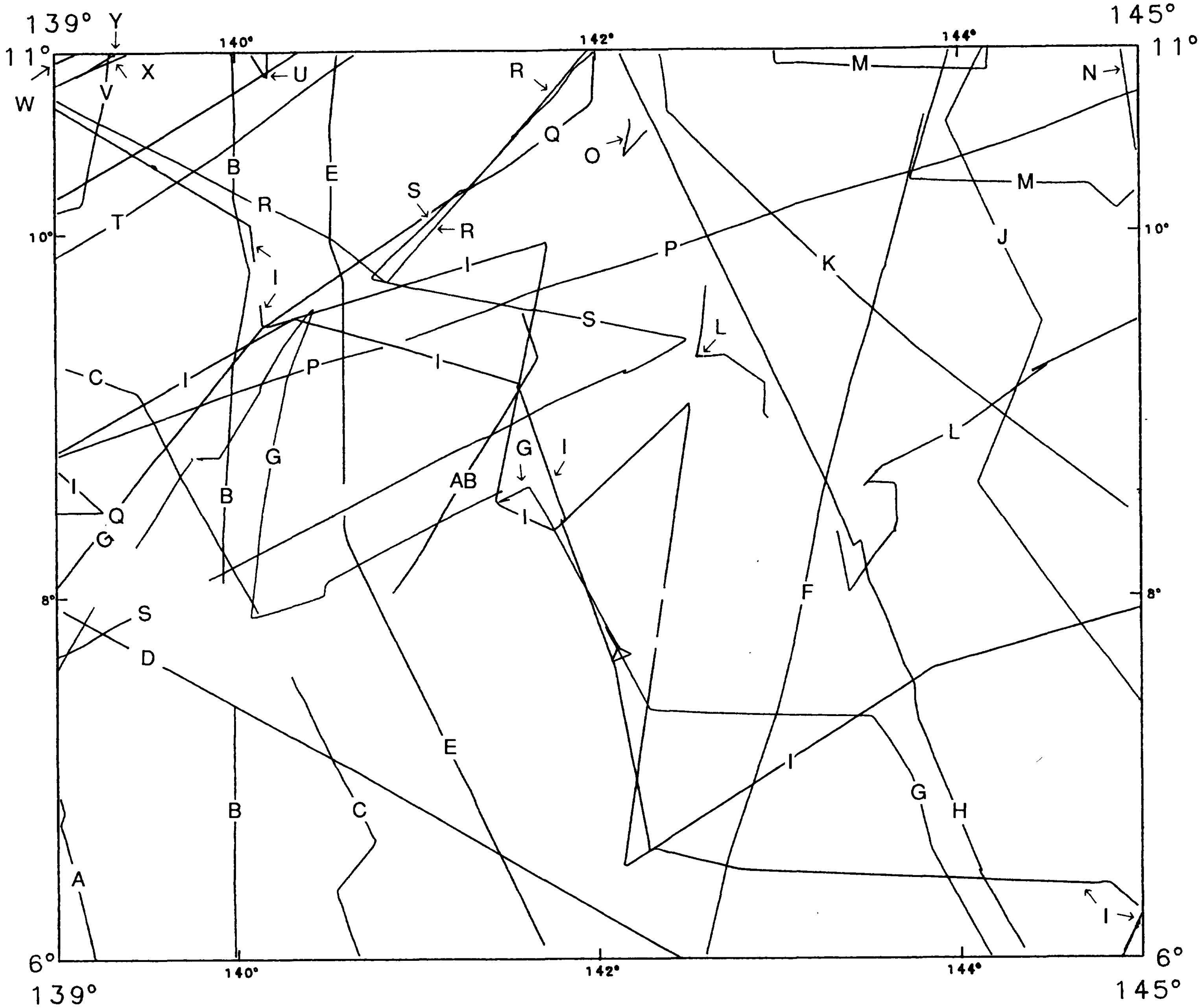

Appendix 1. Trackline map for the Caroline Ridge area. Bathymetric data used to construct Fig. 7 were obtained from this cruise and data from the National Geophysical Data Center (NGDC): **A.** University of Tokyo (UT) Hakuho Maru Cruise H4-69-SP, Chief unknown; **B.** Cruise U5-70-WP, Affiliation and Chief unknown; **C.** UT Hakuho Maru Cruise H4-71-NP, Chief unknown; **D.** China Xiangyanghong 5 Cruise X2-77-CP, Chief unknown; **E.** UT Umitaka Maru Cruise U1-67-SP, Chief unknown; **F.** Deep Sea Drilling Project (DSDP), Glomar Challenger Cruise G7-69-NP, E.L. Winterer and W. Riedel, Chiefs; **G.** Lamont-Doherty Geological Observatory (LDGO) Vema Cruise V3-77-NP, J. Yeissel, Chief; **H.** UT Umitaka Maru Cruise U2-64-SP, Chief unknown; **I.** USGS Farnella Cruise F11-90-CP, J. Hein and Jung-Ho Ahn, Chiefs; **J.** LDGO Vema Cruise V13-76-SP, Chief unknown; **K.** University of Hawaii (UH) Kana Keoki Cruise K3-76-SP, D. Hussong, Chief; **L.** DSDP, Glomar Challenger Cruise G6-69-NP, A.G. Fischer and B.C. Heezen, Chiefs; **M.** Scripps Institute of Oceanography (SIO) Thomas Wahington Cruise W5-78-NP, J. Hawkins, Chief; **N.** LDGO Vema Cruise V13-71-SP, D. Kent and J. Ladd, Chiefs; **O.** UH Kana Keoki Cruise K3-83-WP, E. Silver, Chief; **P.** Cruise M2-89-WP, Affiliation and Chief unknown; **Q.** NOAA/USCGS Pioneer Cruise P1-64-NP, H.B. Stewart, Chief; **R.** LDGO Vema Cruise V14-71-NP, J. Ladd, Chief; **S.** UH Moana Wave Cruise W7-88-CP, S. Stahl, S. Poulos, and M. Simpson, Chiefs; **T.** SIO Thomas Washington Cruise W5-78-NP, J. Hawkins, Chief; **U.** SIO Thomas Washington Cruise W3-76-WP, J. Reid, Chief; **V.** SIO Thomas Washington Cruise W4-76-WP, J. Hawkins, Chief; **W.** SIO Thomas Washington Cruise W10-77-SP, E. Silver, Chief; **X.** SIO Thomas Washington Cruise W5-80-SP, J. Curray and G. Moore, Chiefs; **Y.** SIO Thomas Washington Cruise W7-80-WP, A. Yayanos, Chief; **Z.** SIO Thomas Washington Cruise W9-79-SP, E. Silver, Chief; **AB.** UH Mahi Cruise M2B-70-SP, D. Hussong, Chief.

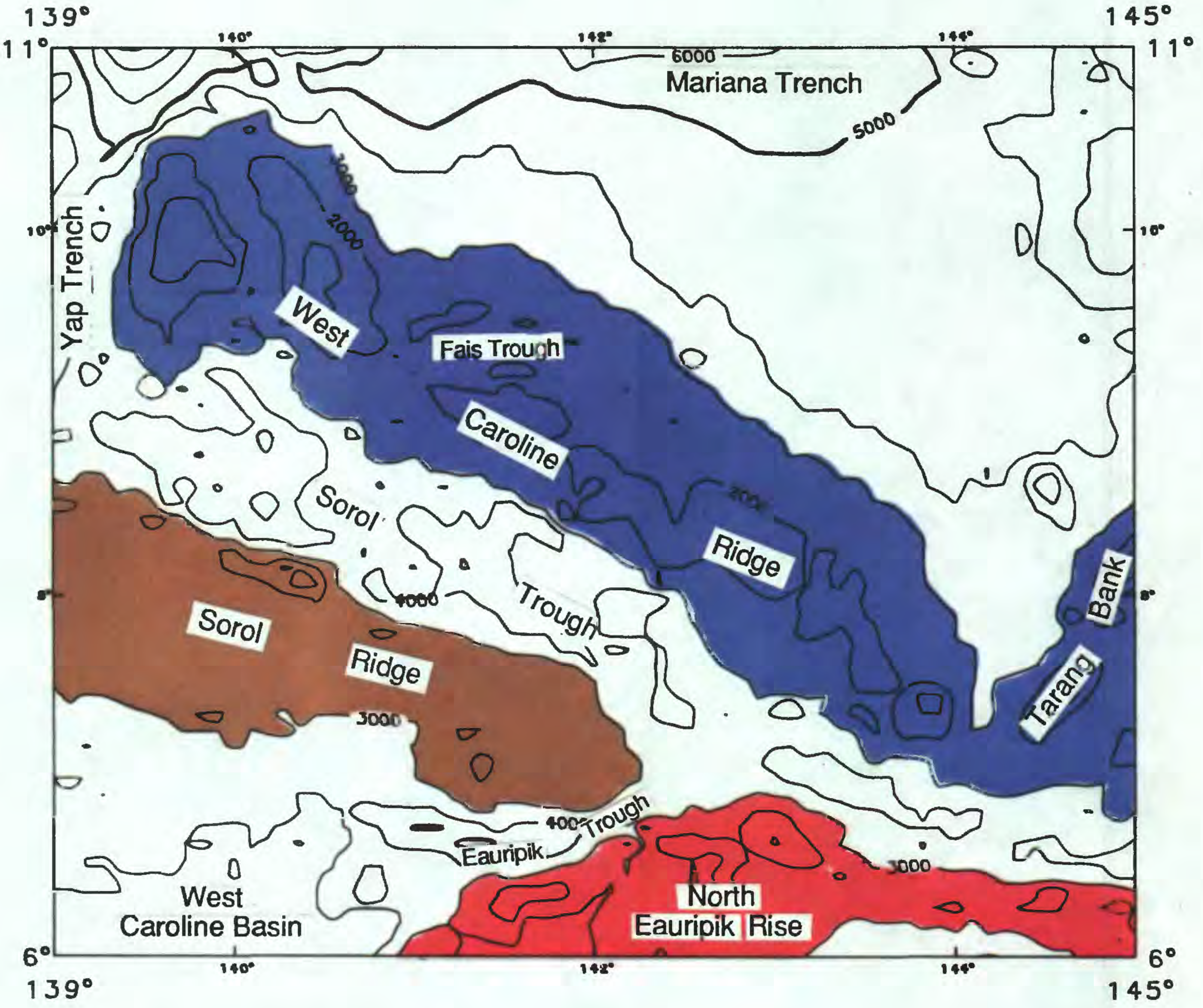

Appendix 2. Major structural units in the west Caroline Ridge area as defined by the 3000 m isobath. Tarang Bank is the westernmost part of central Caroline Ridge. Contour interval is 1000 m.